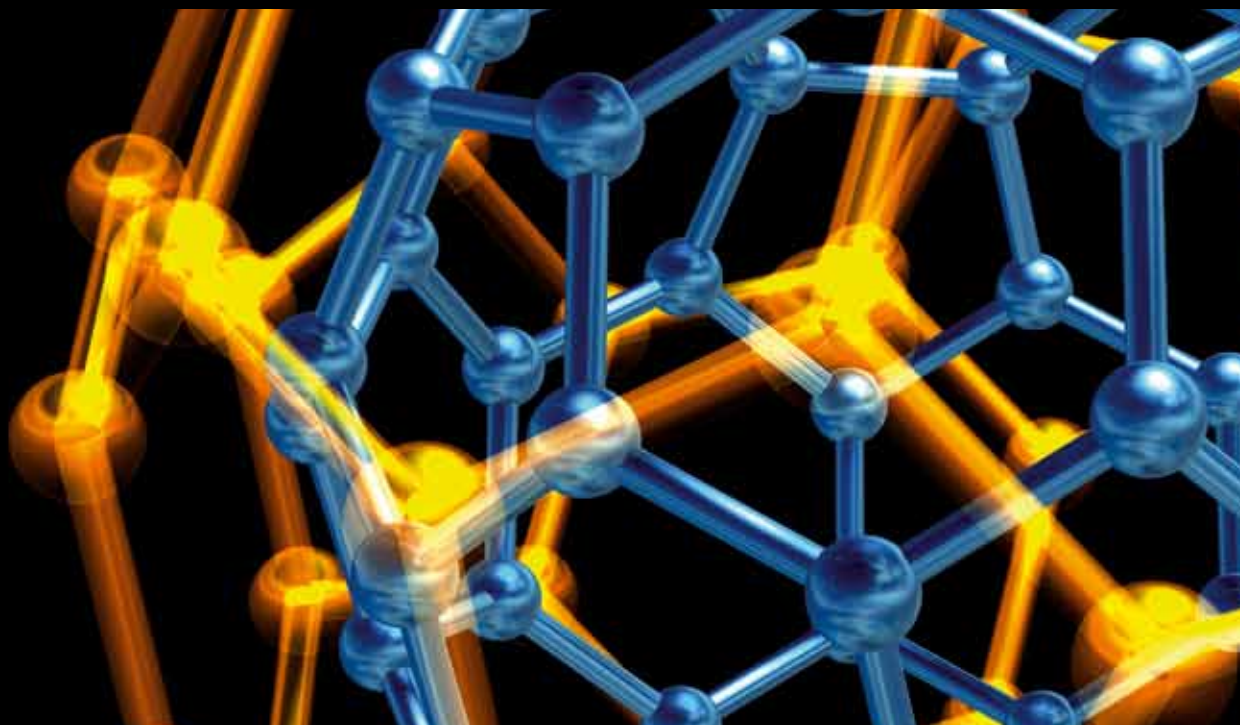


# NANOMATERIALS SYNTHESIS, APPLICATIONS, AND TOXICITY

GUEST EDITORS: MALLIKARJUNA NADAGOUDA, THOMAS F. SPETH,  
CHRISTOPHER IMPELLITTERI, AND YULIANG ZHAO





---

# **Nanomaterials Synthesis, Applications, and Toxicity**

Journal of Nanotechnology

---

**Nanomaterials Synthesis, Applications,  
and Toxicity**

Guest Editors: Mallikarjuna Nadagouda, Thomas F. Speth,  
Christopher Impellitteri, and Yuliang Zhao



---

Copyright © 2011 Hindawi Publishing Corporation. All rights reserved.

This is a special issue published in volume 2011 of "Journal of Nanotechnology." All articles are open access articles distributed under the Creative Commons Attribution License, which permits unrestricted use, distribution, and reproduction in any medium, provided the original work is properly cited.

## Editorial Board

Simon Joseph Antony, UK  
Y. Bando, Japan  
B. Bhushan, USA  
Felix A. Buot, USA  
Carlos R. Cabrera, Puerto Rico  
John A. Capobianco, Canada  
Franco Cerrina, USA  
Gan Moog Chow, Singapore  
Jeffery L. Coffey, USA  
Dmitriy A. Dikin, USA  
Dimitris Drikakis, UK  
H. D. Espinosa, USA  
John S. Foord, UK  
E. Goldys, Australia  
Lambertus Hesselink, USA  
Joseph Irudayaraj, USA

Niraj K. Jha, USA  
Miguel Jose-Yacamán, USA  
Valery Khabashesku, USA  
Yoke Khin Yap, USA  
Sakhrat Khizroev, USA  
Andrei Kolmakov, USA  
Charles M. Lieber, USA  
Charles M. Lukehart, USA  
Abdel S. H. Makhlof, Germany  
Constantinos Mavroidis, USA  
Vincent Meunier, USA  
Paolo Milani, Italy  
Oded Millo, Israel  
M. Grant Norton, USA  
R. Lee Penn, USA  
S. N. Piramanayagam, Singapore

A. M. Rao, USA  
Paresh Chandra Ray, USA  
Benjaram M. Reddy, India  
Federico Rosei, Canada  
Mehmet Sarikaya, USA  
Jorge M. Seminario, USA  
V. Shalaev, USA  
Mahi R. Singh, Canada  
Bobby G. Sumpter, USA  
Xiao Wei Sun, Singapore  
Weihong Tan, USA  
O. K. Tan, Singapore  
Thomas Thundat, USA  
Boris I. Yakobson, USA  
Nan Yao, USA  
Chuan Jian Zhong, USA

# Contents

**Nanomaterials Synthesis, Applications, and Toxicity**, Mallikarjuna Nadagouda, Thomas F. Speth, Christopher Impellitteri, and Yuliang Zhao  
Volume 2011, Article ID 218562, 2 pages

**Improving the Hydrophobicity of ZnO by PTFE Incorporation**, Meenu Srivastava, Bharathi Bai J. Basu, and K. S. Rajam  
Volume 2011, Article ID 392754, 6 pages

**Preparation and Characterization of Self-Assembled Manganese Dioxide Thin Films**, Suh Cem Pang, Suk Fun Chin, and Chian Ye Ling  
Volume 2011, Article ID 789305, 7 pages

**An Organic Acid-induced Synthesis and Characterization of Selenium Nanoparticles**, Charu Dwivedi, Chetan P. Shah, Krishankant Singh, Manmohan Kumar, and Parma Nand Bajaj  
Volume 2011, Article ID 651971, 6 pages

**Synthesis, Characterization and Catalytic Performance of  $H_3SiW_{12}O_{40}/SiO_2$  Prepared by Sol-Gel Technique**, W. N. R. W. Isahak, M. Ismail, N. M. Nordin, J. M. Jahim, and M. A. Yarmo  
Volume 2011, Article ID 507692, 6 pages

**Hydrothermal Synthesis of Ni/Al Layered Double Hydroxide Nanorods**, Yun Zhao, Fenfei Xiao, and Qingze Jiao  
Volume 2011, Article ID 646409, 6 pages

**Optical, X-Ray Diffraction, and Magnetic Properties of the Cobalt-Substituted Nickel Chromium Ferrites ( $CrCo_xNi_{1-x}FeO_4$ ,  $x=0, 0.2, 0.4, 0.6, 0.8, 1.0$ ) Synthesized Using Sol-Gel Autocombustion Method**, Sonal Singhal, Santosh Bhukal, Jagdish Singh, Kailash Chandra, and S. Bansal  
Volume 2011, Article ID 930243, 6 pages

**Structure and Magnetic Properties of  $Y_{3-x}Er_xFe_5O_{12}$  ( $x=0.2, 1.0, \text{ and } 2.0$ ) Thin Films Prepared by Sol-Gel Method**, Ramadan Shaiboub, Noor Baa'yah Ibrahim, Mustaffa Abdullah, and Ftema Abdilhade  
Volume 2011, Article ID 365378, 5 pages

**Magnetic Properties of  $Co_{0.5}Zn_{0.5}Fe_2O_4$  Nanoparticles Synthesized by a Template-Assisted Hydrothermal Method**, H. Y. He  
Volume 2011, Article ID 182543, 5 pages

**Green Synthesis of Silver Nanoparticles Using *Polyalthia longifolia* Leaf Extract along with D-Sorbitol: Study of Antibacterial Activity**, S. Kaviya, J. Santhanalakshmi, and B. Viswanathan  
Volume 2011, Article ID 152970, 5 pages

**Selective Oxidation Using Flame Aerosol Synthesized Iron and Vanadium-Doped Nano-TiO<sub>2</sub>**, Zhong-Min Wang, Endalkachew Sahle-Demessie, and Ashraf Aly Hassan  
Volume 2011, Article ID 209150, 11 pages

**Nano-Scale Hydroxyapatite: Synthesis, Two-Dimensional Transport Experiments, and Application for Uranium Remediation**, S. R. Kanel, T. P. Clement, M. O. Barnett, and M. N. Goltz  
Volume 2011, Article ID 462382, 5 pages



---

**Microwave-Assisted Combustion Synthesis of Nano Iron Oxide/Iron-Coated Activated Carbon, Anthracite, Cellulose Fiber, and Silica, with Arsenic Adsorption Studies**, Mallikarjuna N. Nadagouda and Darren A. Lytle  
Volume 2011, Article ID 972486, 8 pages

## Editorial

# Nanomaterials Synthesis, Applications, and Toxicity

**Mallikarjuna Nadagouda,<sup>1</sup> Thomas F. Speth,<sup>2</sup> Christopher Impellitteri,<sup>3</sup> and Yuliang Zhao<sup>4</sup>**

<sup>1</sup> National Risk Management Research Laboratory, US Environmental Protection Agency, 26 West MLK Drive, Cincinnati, OH 45268, USA

<sup>2</sup> Water Supply and Water Resources Division, US EPA, 26 West Martin Luther King Drive, Cincinnati, OH 45268, USA

<sup>3</sup> Water Quality Management Branch, US Environmental Protection Agency, ORD/NRMRL/WSWRD-MS 679, 26 West Martin Luther King Drive, Cincinnati, OH 45268, USA

<sup>4</sup> The Research Center for Cancer Nanotechnology, National Center for Nanosciences and Technology of China, Tianjin Cancer Hospital & CAS, P.O. Box 918, Beijing 100049, China

Correspondence should be addressed to Mallikarjuna Nadagouda, nadagouda.mallikarjuna@epa.gov

Received 11 August 2011; Accepted 11 August 2011

Copyright © 2011 Mallikarjuna Nadagouda et al. This is an open access article distributed under the Creative Commons Attribution License, which permits unrestricted use, distribution, and reproduction in any medium, provided the original work is properly cited.

This issue presents a wide variety of insightful work in the synthesis, characterization, and properties of nanomaterials.

Researchers continuously strive to improve material properties and develop novel methods for nanosynthesis. For example, M. Srivastava et al. report a novel method for increasing hydrophobicity of ZnO surfaces through the incorporation of polytetrafluoroethylene (PTFE). The modification of ZnO with PTFE results in a decreased treatment time, and such a material is easily modified by either stearic acid or fluoroalkylsilane to give a low-energy superhydrophobic material. Polymeric materials have also been found useful in nanoscale templates. S. L. Pang et al. present a novel route to the formation of thin-film MnO<sub>2</sub> by self-assembly of MnO<sub>2</sub> nanoparticles on nickel-coated polyethylene terephthalate utilizing a horizontal submersion process at room temperature. These materials exhibit high capacitance behavior, high cycling reversibility, and stability within the potential range of 0.0 to 0.9 V based on cyclic voltammetry. Furthermore, C. Dwivedi et al. report the synthesis of polyvinyl-alcohol-(PVA-) stabilized selenium nanoparticles by reaction of sodium selenosulfate with various organic acids in room-temperature aqueous media. Although a gamut of organic acids and various PVA concentrations were studied, no significant effects on structure were found. Simply, the spherical selenium nanoparticles ranged in size from about 40 to 100 nm, as readily seen in AFM and TEM imaging.

Soft matter has also played a role in nanoscale synthesis. In this issue, W. N. R. W. Isahak et al. present a comparative study of silicotungstic acid bulk (STAB) and STA-silica sol gel (STA-SG) and their efficacies, both in activity and selectivity, as catalysts in an esterification reaction. STA-SG resulted in lower conversion (96%) compared to STAB (100%) and control H<sub>2</sub>SO<sub>4</sub> (98%); however, STA-SG advantageously delivers selectivity of 95% compared to 89.9 and 81.6% by using STAB and H<sub>2</sub>SO<sub>4</sub>, respectively. Such attributes may result from the increased surface area obtained by the sol gel method.

In a different synthetic route, Y. Zhao et al. report the synthesis of Ni/Al layered double hydroxide (LDH) nanorods by a hydrothermal method. Such methods require a pH of 10.0 and temperature of 180°C for nanorod formation. Additionally, reaction time increases not only rod diameter, but also rod length.

The ability to tune magnetic properties of nanoparticles has recently garnered interest in many groups. S. Singhal et al. analyzed cobalt-substituted nickel chromium ferrites (CrCo<sub>x</sub>Ni<sub>1-x</sub>FeO<sub>4</sub>,  $x = 0, 0.2, 0.4, 0.6, 0.8,$  and  $1.0$ ) prepared by a sol gel autocombustion method at various annealing temperatures. Here, as annealing temperature increases, particle size increases up to 45 nm, and added Co<sup>3+</sup> content increases saturation magnetization and decreases coercivity.

Similarly, R. Shaiboub et al. discuss the demagnetization effects of increasing Er concentrations on nanoparticle Y<sub>3-x</sub>Er<sub>x</sub>Fe<sub>5</sub>O<sub>12</sub> ( $x = 0.2, 1.0,$  and  $2.0$ ) thin films synthesized

by a solgel method. Such films obtain a single-phase garnet and begin crystallization at 800°C, and with increased annealing temperature, the material displays larger crystallite sizes. The loss of magnetization with increased Er content was attributed to the reverse alignment between  $\text{Er}^{3+}$  and  $\text{Fe}^{3+}$ . In contrast to the sol gel method, H. Y. He reports that the properties of  $\text{Co}_{0.5}\text{Zn}_{0.5}\text{Fe}_2\text{O}_4$  nanoparticles formed by a carboxymethyl cellulose template hydrothermal method were analyzed by XRD, SEM, and vibrating sample magnetometer. The increase of template proportion in synthesis results in not only morphological change from granular to platelike but also an increase in superparamagnetic behavior (from 2.81 T without template to 3.13 T with template).

The application of reported nanomaterials is an important topic for researchers. S. Kaviya et al. report the utilization of *Polyalthia longifoli* leaf extract as both a reducing and capping agent with D-sorbitol for increased stabilization in the synthesis of silver nanoparticles (AgNPs). Additionally, UV-vis spectroscopy revealed a blue shift with increased reaction temperature. These synthesized materials were found to have a wider antimicrobial activity in gram-positive than gram-negative organisms.

Moreover, nanoparticles have found use not only as catalysts, but also as materials for environmental remediation. In the field of catalysis, Z. M. Wang et al. elucidate the important parameters in flame aerosol synthesis of pure  $\text{TiO}_2$  and  $\text{TiO}_2$  doped with Fe or V. Here, the photocatalytic properties of the synthesized material were studied by the selective oxidation of 1-phenyl ethanol to acetophenone. The introduction of a Fe or V dopant resulted in increased catalytic activity at lower concentrations of deposited metal ions. Additionally, the morphology of neat  $\text{TiO}_2$  alters with increased metal doping as witnessed in XRD analysis and the Raman spectroscopy. Researchers compared the efficacy of the photocatalyst in both acetonitrile and water and found the organic solvent to provide higher conversion.

In regards to remediation, S. R. Kanel et al. reports the synthesis of nanoscale (~20 to 50 nm) hydroxyapatite (NHA) through vigorous agitation of  $\text{Ca}(\text{NO}_3)_2 \cdot 4\text{H}_2\text{O}$  and  $(\text{NH}_4)_2\text{HPO}_4$  in alkaline solution. In uranium removal studies, the precipitate performed comparably to commercially available HA. Based on two-dimensional flow cell analysis, the synthesized NHA exhibits transport properties akin to tracers in aqueous environments; consequently, potential applications may include *in situ* U(VI) remediation. Additionally, M. N. Nadagouda and D. A. Lytle present the novel synthesis of iron oxide/iron-coated carbons like activated carbon, anthracite, cellulose fiber, and silica by combustion and their uses in arsenic adsorption. Generally, the spherical nanoparticles ranged in size from 50 to 400 nm. Such materials were found suitable for arsenic adsorption and may be suitable in environmental remediation, catalysis, and various other applications.

Mallikarjuna Nadagouda  
Thomas F. Speth  
Christopher Impellitteri  
Yuliang Zhao

## Research Article

# Improving the Hydrophobicity of ZnO by PTFE Incorporation

**Meenu Srivastava, Bharathi Bai J. Basu, and K. S. Rajam**

*Council of Scientific and Industrial Research, Surface Engineering Division, National Aerospace Laboratories, Bangalore 560 017, India*

Correspondence should be addressed to Meenu Srivastava, meenu\_srivas@yahoo.co.uk

Received 7 March 2011; Accepted 24 March 2011

Academic Editor: Mallikarjuna Nadagouda

Copyright © 2011 Meenu Srivastava et al. This is an open access article distributed under the Creative Commons Attribution License, which permits unrestricted use, distribution, and reproduction in any medium, provided the original work is properly cited.

The objective of the present study is to obtain a zinc oxide- (ZnO-) based superhydrophobic surface in a simple and cost-effective manner. Chemical immersion deposition being simple and economical has been adopted to develop modified ZnO coating on glass substrate. Several modifications of ZnO like treatment with alkanolic acid (stearic acid) and fluoroalkylsilane to tune the surface wettability (hydrophobicity) were attempted. The effect of thermal treatment on the hydrophobic performance was also studied. It was observed that thermal treatment at 70°C for 16 hrs followed by immersion in stearic acid resulted in high water contact angle (WCA), that is, a superhydrophobic surface. Thus, a modified ZnO superhydrophobic surface involves the consumption of large amount of electrical energy and time. Hence, the alternate involved the incorporation of low surface energy fluoropolymer polytetrafluoroethylene (PTFE) in the ZnO coating. The immersion deposited ZnO-PTFE composite coating on modification with either stearic acid or fluoroalkylsilane resulted in a better superhydrophobic surface. The coatings were characterized using Scanning Electron Microscope (SEM) for the surface morphology. It was found that microstructure of the coating was influenced by the additives employed. A flower-like morphology comprising of needle-like structure arranged in a radial manner was exhibited by the superhydrophobic coating.

## 1. Introduction

Superhydrophobic surfaces (water contact angle  $>150^\circ$ ) are gaining importance in industrial applications and academia due to their unique properties like self-cleaning, deicing, antisticking, and anticontamination. Some of the applications include self-cleaning paints, transparent antireflective coatings, self-cleaning glass, and wiperless windshields. In recent times, their usage in aerospace sector is also being explored, particularly in the tail and wings of the aircraft to reduce drag and thereby improve the efficiency of the engine. Superhydrophobicity can be achieved by obtaining a surface of micro- to nanoscale architecture [1]. Empirical models have been proposed on the basis of experimental data to explain the surface wetting properties and to understand the phenomenon of superhydrophobicity. Interest in this phenomenon increased in 1997 when the origin and the universal principle of “Lotus Effect” in nature were explained by Zhang et al. [1]. Since then, research has been focused on mimicking nature and trying to fabricate such surfaces artificially.

Various methods have been recommended for the fabrication of such a surface. Broadly, they have been classified as top-down approach, bottom-up approach, and a combined approach. Solution immersion process, which is a bottom-up method, has been adopted in the present study. The advantage of this method is that it is simple, economical and can be easily scaled up for large area applications. ZnO has been chosen because of its antimicrobial property, easy availability, and nontoxic nature [2]. Also it has other properties like photocatalytic ability, electrical conductivity, UV absorption, and photo-oxidizing capacity for chemical and biological species. Very recently, preparation of cotton bandages with antibacterial properties by immobilizing ZnO nanoparticles on the fabric surface has been reported [3]. Considerable work has been carried out on the immersion deposition of ZnO [4–12]. Shinde et al. have reported the structure, optical and electrical properties of heat-treated ZnO [4]. Similar aspect of Sr-doped ZnO film has also been studied [5]. The effect of thermal desorption of stearic acid on the superhydrophobic performance of ZnO has been reported by Saleema and Farzaneh [6]. ZnO nanorods have

been synthesized by chemical route by some investigators [7]. Yin and Sato have reported novel superstructures of ZnO, namely, nanoscrew and nanodisk obtained from the solution route [8]. Other modified superhydrophobic surfaces based on Cu, Ag, Co, Ni created through solution immersion process have also been reported [13–17]. In the present study, solution immersion deposited ZnO coating has been subjected to different modifications like heat treatment, immersion in alkanolic acid (stearic acid), combination of heat treatment and immersion in alkanolic acid, and immersion in fluoroalkylsilane. Stearic acid had been adopted as Wu et al. had reported that octadecanoic acid (C18 acid, stearic acid) imparted higher hydrophobicity compared to other acids of different chain lengths [9]. The influence of polytetrafluoroethylene (PTFE) on the hydrophobic nature was also studied by preparing ZnO-PTFE composite coating by immersion route. PTFE was chosen as it is a fluoropolymer with very low surface energy. The water contact angle of smooth PTFE film is about  $108^\circ$ , and by the axial extension of the crystals the water contact angle increases beyond  $150^\circ$  [18]. The PTFE-based coatings were also modified with alkanolic acid and fluoroalkylsilane. Thus, in this study, the investigators have attempted to improve the superhydrophobic behaviour of ZnO by PTFE incorporation, and a comparison with modified ZnO in terms of their microstructure and wettability behaviour has been made.

## 2. Materials and Methodology

ZnO was deposited on a glass substrate by immersion in a solution containing  $30\text{ g L}^{-1}$  zinc nitrate hexahydrate and  $53.3\text{ mL L}^{-1}$  ammonium hydroxide solution (25%). The chemical etching of the substrate was carried out to induce surface roughness. Surface roughness plays an important role in determining the wetting behaviour of solid surfaces [19]. The etchant and etching time was standardized. HF:HNO<sub>3</sub> mixture in the ratio 1:3 for a duration of 3 sec was adopted to obtain uniform ZnO coating on glass. The immersion time and temperature were also standardized. Deposition temperature of  $70^\circ\text{C}$  and an immersion time of 2 h after initiation of precipitate formation were employed. The as-prepared ZnO coatings were subjected to modifications such as heat treatment at  $350^\circ\text{C}$  (for 2 h and 4 h) and immersion in alkanolic acid-octadecanoic acid (stearic acid). The various concentrations of the acid solution in acetone used were 0.002 M, 0.01 M, 0.06 M, and 0.10 M. The other modifications included heating of ZnO coating at  $70^\circ\text{C}$  for 16 h followed by immersion in alkanolic acid and modification of the coating by immersion in fluoroalkylsilane, 1 wt% FAS-17 solution in ethanol for 1 h. The modified coatings were dried under ambient conditions.

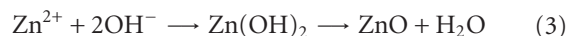
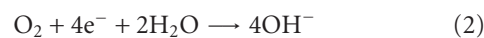
The ZnO-PTFE composite coatings were deposited by dispersing the PTFE ( $10\text{ mL L}^{-1}$ ) emulsion in the zinc nitrate solution, and the deposition was performed under similar conditions as that of ZnO. The composite coating was modified by immersion in 0.002 M stearic acid solution in acetone for 1 h and fluoroalkylsilane in ethanol for 1 h. These modified coatings were characterized for their surface

morphology and wetting behavior, and a comparison with modified ZnO has been made.

Static water contact angles (WCAs) of the coatings were measured using contact angle analyzer, model Phoenix 300 Plus from M/s Surface Electro Optics, Republic of Korea. Tangent fitting mode is used in this instrument for the determination of WCA. The drop volume was  $8\text{ }\mu\text{L}$  in this study. WCA is influenced by volume of water droplet and gravity force. Hence, WCA must be measured with the same volume of water droplet. Also, the same fitting method must be used for calculating WCA while comparing superhydrophobicity of different surfaces as explained by Zhang et al. [1]. They found that WCA values from  $156^\circ$  to  $179^\circ$  could be obtained for the same water droplet on a surface depending on different fitting modes such as ellipse fitting, circle fitting, tangent searching, or Laplace-Young fitting. Five measurements of WCA on the coating were taken, and the mean value was reported. The crystalline structure of the coatings was examined by X-ray diffraction (XRD) technique, Model Rigaku D/max 2200 powder diffractometer, using CuK<sub>α</sub> radiation of wavelength 0.154 nm. The diffraction patterns were scanned between  $20^\circ$  and  $100^\circ$  in steps of  $0.02^\circ$  at  $2\text{ deg min}^{-1}$  scan speed. The surface morphology of the coatings was studied using a scanning electron microscope, SEM Model LEO 440I.

## 3. Results and Discussion

*3.1. Microstructure and Hydrophobicity of Modified ZnO Coatings.* X-ray diffraction patterns of as-deposited ZnO coating and modified ZnO coating are shown in Figure 1. The diffraction peaks in Figure 1(a) indicate the presence of major amounts of ZnO with hexagonal wurtzite structure and smaller amounts of zinc hydroxide, Zn(OH)<sub>2</sub>. No other characteristic peak was observed for other impurities, and all the peaks are narrow indicating higher crystallinity. The probable reaction mechanism is



Zinc gets oxidized forming zinc cations (1), and oxygen gets reduced producing hydroxyl ions (2). These hydroxyl anions react with zinc cations to form zinc hydroxide (reaction (2)) which under slightly acidic condition transforms to the stable ZnO that is insoluble and appears as white precipitate on the surface [19]. This mechanism can be correlated with the presence of ZnO and Zn(OH)<sub>2</sub> in the diffractogram.

Surface morphology of various modified ZnO coatings is shown in Figure 2. It can be seen from Figure 2(a) that the morphology of as-deposited ZnO coating consists of uniform flower-like pattern. Every flower-like structure is composed of many rods with a sharp tip, and these rods are aligned in a radial pattern from the centre. The growth mechanism can be interpreted as an epitaxial growth wherein the ZnO nuclei initially formed a seed layer. The ammonium ions adsorbed on the surface of the ZnO nuclei promoted

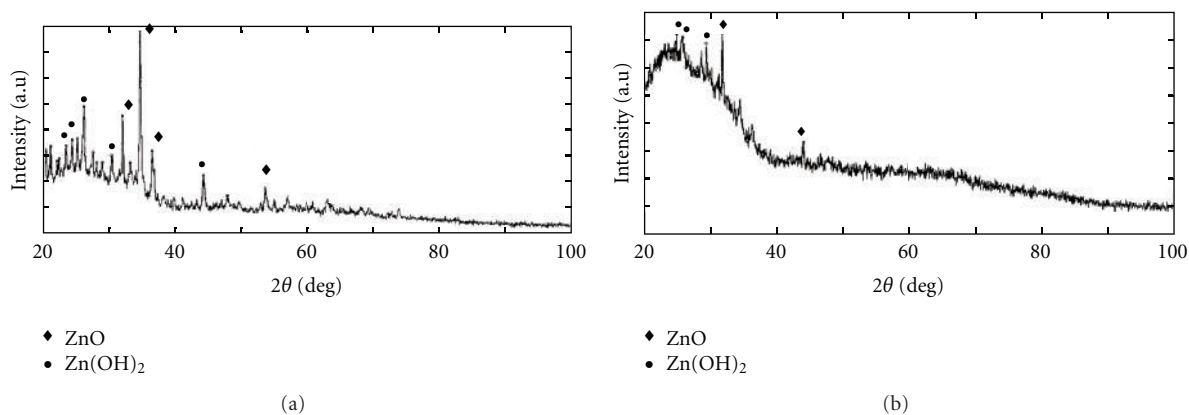


FIGURE 1: X-ray diffractograms of (a) as-deposited ZnO coating and (b) ZnO coating heat treated at 70°C and immersed in stearic acid (0.002 M).



FIGURE 2: Surface morphology of ZnO coating immersed in stearic acid (a), ZnO heat treated at 70°C and immersed in stearic acid (0.002 M) (b). Insets show the profiles of the water droplet on the film surface.

the growth of the crystallites [9, 20]. Similar structure has been reported by Wang et al. for ZnO powder synthesized from ZnSO<sub>4</sub> and NaOH solution [21]. However, Shinde et al. have reported a cone-like structure for ZnO deposited from an alkaline Zn(NO<sub>3</sub>)<sub>2</sub> solution [4]. Thus, by varying the alkalinity of the solution, different morphologies can be obtained. Strong alkaline solution results in a structure comprising of discrete nanorods, while a weak alkaline solution produces an assembled nanorod structure [21]. Zhang et al. have also reported the influence of pH on the surface morphology and wettability [19].

ZnO is basically a highly hydrophilic material with WCA < 5°. After heat treatment at 350°C for 2 h and 4 h, the ZnO coatings did not exhibit any change in their wetting behaviour and remained hydrophilic. Hence, their detailed characterization has not been discussed. However, Shinde et al. have reported that the ZnO coating annealed at 350°C for 2 h displayed superhydrophobic nature and its structure appeared as well-defined cones [4]. Thus, the wettability of solid surface is governed by both the chemical composition and the geometrical microstructure of the surface.

ZnO coatings were hydrophobically modified by immersing in varying concentrations of stearic acid for different durations of time, and their WCA values were measured. It was observed that the as-deposited ZnO coating after immersion in 0.01 M stearic acid for 6 days displayed a WCA of 145°. The surface morphology and diffraction pattern of the coating modified with stearic acid was similar to that of the as-deposited ZnO coating. In order to render hydrophobicity to the coating, a prolonged immersion time of 6 days was required. On the other hand, if ZnO coating was heated to 70°C for 16 h and subsequently immersed in stearic acid, superhydrophobicity was achieved in much shorter immersion time. The heat-treated ZnO coating was immersed in stearic acid of different concentrations and for various time durations. It was found that a low concentration of 0.002 M and short immersion time of 30 minutes was optimum to obtain superhydrophobicity. The morphology appears as sword-like nanorods with sharp tips, arranged in a flower-like arrangement (Figure 2(b)). In addition, cluster of flowers grouped over one another was also observed. EDX analysis revealed that the Zn content was slightly lower

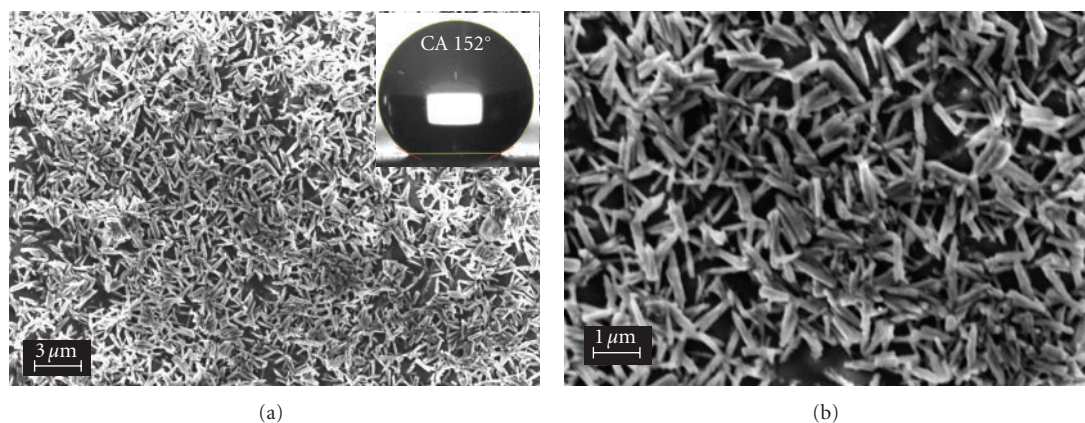


FIGURE 3: Surface morphology of ZnO coating treated with fluoroalkylsilane at 2500X (a) and 5000X (b). Inset shows the image of water drop on the film surface.

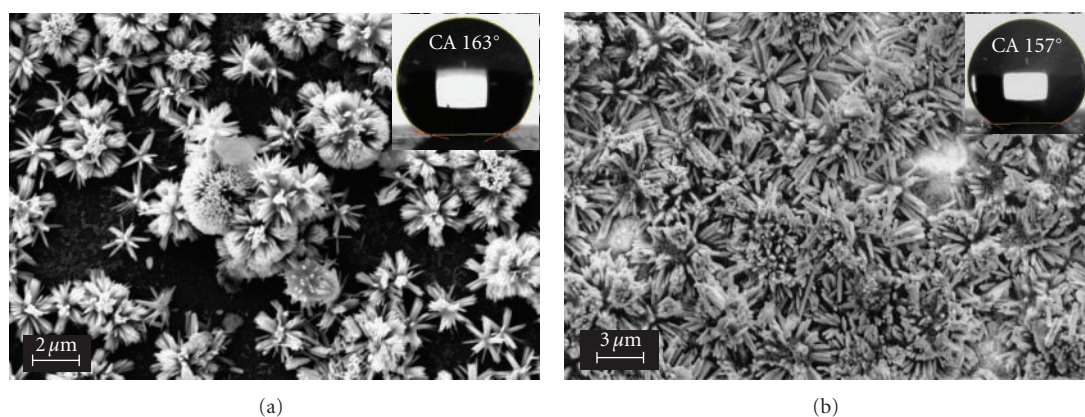


FIGURE 4: Surface morphology of ZnO-PTFE coating treated with stearic acid (a) and fluoroalkyl silane (b). Insets show the image of the water drop on the film surface.

on these clusters (65 wt%) as compared to single flower (72 wt%). Further, a marginal rise in carbon and oxygen content was observed on the floral cluster. This may be due to the contribution from the stearic acid. The X-ray diffractogram shows the presence of ZnO and  $\text{Zn}(\text{OH})_2$  (Figure 1(b)). The effect of fluoroalkylsilane modification on the hydrophobic behaviour of ZnO was also studied. The morphology of fluoroalkylsilane-modified ZnO coating is depicted in Figure 3. The structure appears as discrete rods distributed uniformly throughout the surface. The X-ray diffraction studies showed the presence of only  $\text{Zn}(\text{OH})_2$ .

The wettability of the coatings is expressed as water contact angle, and this angle is inversely proportional to the wettability. Figure 2 shows the water drop profile for (a) alkanolic acid-modified coating, (b) heat-treated followed by alkanolic acid modification and Figure 3 shows the profile of fluoroalkylsilane-modified coating. As-deposited ZnO coating was observed to be hydrophobic, with a WCA of  $120^\circ$ . However, on immersion in 0.10 M stearic acid, an improvement in the hydrophobic behaviour was observed with an enhancement in the contact angle values to  $145^\circ$  (Figure 2(a)). However, a combined treatment of heating

at  $70^\circ\text{C}$  and immersion in 0.002 M stearic acid rendered the coating superhydrophobic. It exhibited a contact angle of  $156^\circ$ , and the shape of the water droplet is shown in Figure 2(b). The hydrophobicity imparted by stearic acid can also be attributed to the fact that stearic acid chemically bonded to the surface of  $\text{Zn}^{2+}$  ions leading to the ZnO surface being covered by a monolayer of organic molecules with their nonpolar tails exposed to air [9]. The fluoroalkylsilane modified ZnO coating also exhibited superhydrophobic behaviour with a moderate reduction in the contact angle values to  $152^\circ$  (Figure 3). The higher contact angle ( $156^\circ$ ) of the coupled heat treatment and stearic acid modification of ZnO coating may be due to the less air entrapment in the clustered floral structure compared to the rod-like structure of silane-modified coating. Thus, different WCAs are due to the different surface structures. It can also be inferred that fluorosilane imparts higher degree of hydrophobicity ( $152^\circ$ ) due to its low surface free energy compared to exclusive alkanolic acid treatment ( $145^\circ$ ).

The above studies showed that superhydrophobic ZnO surface can be achieved, by heating for long hours (16 h) followed by short duration (0.50 h) immersion in stearic

acid. Although the coating is superhydrophobic in nature, a long time was spent to attain this nonwetting property. Hence, an alternative ZnO-PTFE composite coating was produced by solution immersion method.

**3.2. Microstructure and Hydrophobicity of Modified ZnO-PTFE Composite Coating.** The ZnO-PTFE composite coating was developed in a similar manner as that of ZnO coating, and it was subsequently modified with stearic acid and fluorosilane. The surface morphology of the modified ZnO-PTFE composite coatings is depicted in Figure 4. The surface morphology of stearic acid-modified ZnO-PTFE coating appears as floral structures along with a clustered growth (Figure 4(a)). The EDX studies showed that the clustered structure was rich in fluorine (5 wt% on the cluster and 2 wt% on floral pattern) indicating that it was the contribution from PTFE. The X-ray diffraction studies revealed that the coating comprised of ZnO and Zn(OH)<sub>2</sub>. The silane-modified coating exhibited a structure comprising of compactly arranged rod-like structures distributed in a random manner (Figure 4(b)). The diffraction studies showed that the coating comprised of exclusively Zn(OH)<sub>2</sub>. It was seen from the wettability test that the contact angle for stearic acid-modified ZnO-PTFE coating is 163° while that for silane-modified coating is 157°. The water drop profiles are depicted in Figure 4. Thus, it is observed that the incorporation of low surface energy PTFE in ZnO helped to improve the hydrophobicity without the necessity of heat treatment or long immersion time. It is also seen that unlike the modified ZnO coating wherein the fluorosilane imparted higher hydrophobicity compared to alkanolic acid, in the case of ZnO-PTFE coating the alkanolic acid imparted higher degree of hydrophobicity compared to fluorosilane. This may be due to the difference in the interaction of PTFE with stearic acid and fluoroalkylsilane. Thus, modified ZnO-PTFE composite helps to obtain a superhydrophobic surface in a simple manner. This can be associated with the interaction between fluorine, the most effective element for lowering the surface free energy, because of its small atomic radius and high electronegativity, and the roughness of the substrate induced by etching.

The superhydrophobic behaviour of modified ZnO films can be explained in terms of the Cassie-Baxter model [22]. According to Cassie-Baxter equation,

$$\cos \theta_C = f_1(\cos \theta_1 + 1) - 1, \quad (4)$$

where  $\theta_C$  and  $\theta_1$ , respectively, are apparent WCA of the corresponding rough and smooth surfaces,  $f_1$  is the surface area fraction of the solid. A water drop on the modified ZnO film only contacts the tips of the clusters and flower-like structures on the rough surface resulting in a large water-air interface. Such composite surface prevents water droplets from penetrating into the cavities, leading to superhydrophobicity. However, in unmodified ZnO films, water penetrates into the gap between the clusters thereby displaying merely a hydrophobic behaviour.

## 4. Conclusions

ZnO being a widely adopted material to obtain superhydrophobic surface was deposited on glass substrate by immersion deposition method. Some of the modifications adopted by various investigators like alkanolic acid immersion, heat treatment, and fluoroalkylsilane modification were carried out for the ZnO coatings obtained in the present study. The observation made was that ZnO deposition followed by heat treatment at 70°C for 16 hours and immersion in a solution of stearic acid had resulted in a surface with the highest hydrophobicity (CA 156°). The studies conducted also revealed that the modification of ZnO with fluoroalkylsilane imparted superhydrophobicity but to a lesser extent (CA 152°). The prolonged heat treatment time (16 h) can be avoided by the incorporation of a low surface energy PTFE in the ZnO coating. The ZnO-PTFE composite coatings on modification with either stearic acid or fluoroalkylsilane imparted greater superhydrophobicity compared to modified ZnO coatings. It was also seen that the surface morphology of the coating was greatly influenced by the nature of low energy material used for hydrophobic modification.

It was inferred from the morphology and contact angle measurement studies that the incorporation of PTFE in ZnO matrix followed by modification with stearic acid or fluoroalkylsilane produced a superhydrophobic surface in a simple and cost effective manner.

## Acknowledgments

The authors would like to thank Dr. A. R. Upadhyaya, Director NAL, Dr. Kota Harinarayana, Raja Ramanna Fellow, NAL for their constant support and encouragement. They are grateful to Dr. Anjana Jain and Mr. Raghavendra for their technical assistance with XRD and SEM studies. The authors would also like to thank Ms. Nandita Ganesh for the assistance in carrying out the experiments.

## References

- [1] X. Zhang, F. Shi, J. Niu, Y. Jiang, and Z. Wang, "Superhydrophobic surfaces: from structural control to functional application," *Journal of Materials Chemistry*, vol. 18, no. 6, pp. 621–633, 2008.
- [2] X. M. Li, D. Reinhoudt, and M. Crego-Calama, "What do we need for a superhydrophobic surface? A review on the recent progress in the preparation of superhydrophobic surfaces," *Chemical Society Reviews*, vol. 36, no. 8, pp. 1350–1368, 2007.
- [3] I. Perelshtein, G. Applerot, N. Perkas et al., "Antibacterial properties of an in situ generated and simultaneously deposited nanocrystalline ZnO on fabrics," *ACS Applied Materials & Interfaces*, vol. 1, no. 2, pp. 361–366, 2009.
- [4] V. R. Shinde, C. D. Lokhande, R. S. Mane, and S.-H. Han, "Hydrophobic and textured ZnO films deposited by chemical bath deposition: annealing effect," *Applied Surface Science*, vol. 245, no. 1–4, pp. 407–413, 2005.
- [5] T. A. Vijayan, R. Chandramohan, S. Valanarasu, J. Thirumalai, and S. P. Subramanian, "Comparative investigation on nanocrystal structure, optical, and electrical properties of ZnO

- and Sr-doped ZnO thin films using chemical bath deposition method,” *Journal of Materials Science*, vol. 43, no. 6, pp. 1776–1782, 2008.
- [6] N. Saleema and M. Farzaneh, “Thermal effect on superhydrophobic performance of stearic acid modified ZnO nanotowers,” *Applied Surface Science*, vol. 254, no. 9, pp. 2690–2695, 2008.
- [7] D. Li, Z. T. Liu, YU. H. Leung, A. B. Djuricic, M. H. Xie, and W. K. Chan, “Transition metal-doped ZnO nanorods synthesized by chemical methods,” *Journal of Physics and Chemistry of Solids*, vol. 69, no. 2-3, pp. 616–619, 2008.
- [8] S. Yin and T. Sato, “Mild solution synthesis of zinc oxide films with superhydrophobicity and superhydrophilicity,” *Journal of Materials Chemistry*, vol. 15, no. 43, pp. 4584–4587, 2005.
- [9] X. Wu, L. Zheng, and D. Wu, “Fabrication of superhydrophobic surfaces from microstructured ZnO-based surfaces via a wet-chemical route,” *Langmuir*, vol. 21, no. 7, pp. 2665–2667, 2005.
- [10] Y. Masuda and K. Kato, “Morphology control of zinc oxide particles at low temperature,” *Crystal Growth and Design*, vol. 8, no. 8, pp. 2633–2637, 2008.
- [11] K. E. Yu, Z. Jin, X. Liu, Z. Liu, and Y. Fu, “Synthesis of size-tunable ZnO nanorod arrays from  $\text{NH}_3 \cdot \text{H}_2\text{O}/\text{ZnNO}_3$  solutions,” *Materials Letters*, vol. 61, no. 13, pp. 2775–2778, 2007.
- [12] Z. Wang, M. Wang, Z. Lin, Y. Xue, G. E. Huang, and X. I. Yao, “Growth and interconversion of ZnO nanostructure films on different substrates,” *Applied Surface Science*, vol. 255, no. 9, pp. 4705–4710, 2009.
- [13] Q. I. Wang, B. Zhang, M. Qu, J. Zhang, and D. He, “Fabrication of superhydrophobic surfaces on engineering material surfaces with stearic acid,” *Applied Surface Science*, vol. 254, no. 7, pp. 2009–2012, 2008.
- [14] E. Hosono, S. Fujihara, I. Honma, and H. Zhou, “Superhydrophobic perpendicular nanopin film by the bottom-up process,” *Journal of the American Chemical Society*, vol. 127, no. 39, pp. 13458–13459, 2005.
- [15] A. Safaee, D. K. Sarkar, and M. Farzaneh, “Superhydrophobic properties of silver-coated films on copper surface by galvanic exchange reaction,” *Applied Surface Science*, vol. 254, no. 8, pp. 2493–2498, 2008.
- [16] M. Qu, B. Zhang, S. Song, L. Chen, J. Zhang, and X. Cao, “Fabrication of superhydrophobic surfaces on engineering materials by a solution-immersion process,” *Advanced Functional Materials*, vol. 17, no. 4, pp. 593–596, 2007.
- [17] M. Li, J. Xu, and Q. Lu, “Creating superhydrophobic surfaces with flowery structures on nickel substrates through a wet-chemical-process,” *Journal of Materials Chemistry*, vol. 17, no. 45, pp. 4772–4776, 2007.
- [18] H. Y. Kwong, M. H. Wong, Y. W. Wong, and K. H. Wong, “Superhydrophobicity of polytetrafluoroethylene thin film fabricated by pulsed laser deposition,” *Applied Surface Science*, vol. 253, no. 22, pp. 8841–8845, 2007.
- [19] J. Zhang, W. Huang, and Y. Han, “Wettability of zinc oxide surfaces with controllable structures,” *Langmuir*, vol. 22, no. 7, pp. 2946–2950, 2006.
- [20] R. Saravana Kumar, P. Sudhagar, R. Sathyamoorthy, P. Matheswaran, and Y. S. Kang, “Direct assembly of ZnO nanostructures on glass substrates by chemical bath deposition through precipitation method,” *Superlattices and Microstructures*, vol. 46, no. 6, pp. 917–924, 2009.
- [21] Y. Wang, X. Li, N. Wang, X. Quan, and Y. Chen, “Controllable synthesis of ZnO nanoflowers and their morphology-dependent photocatalytic activities,” *Separation and Purification Technology*, vol. 62, no. 3, pp. 727–732, 2008.
- [22] A. B. D. Cassie and S. Baxter, “Wettability of porous surfaces,” *Transactions of the Faraday Society*, vol. 40, pp. 546–551, 1944.

## Research Article

# Preparation and Characterization of Self-Assembled Manganese Dioxide Thin Films

Suh Cem Pang, Suk Fun Chin, and Chian Ye Ling

Department of Chemistry, Faculty of Resource Science and Technology, Universiti Malaysia Sarawak, 94300 Kota Samarahan, Sarawak, Malaysia

Correspondence should be addressed to Suh Cem Pang, suhcem@gmail.com

Received 5 May 2011; Accepted 20 June 2011

Academic Editor: Mallikarjuna Nadagouda

Copyright © 2011 Suh Cem Pang et al. This is an open access article distributed under the Creative Commons Attribution License, which permits unrestricted use, distribution, and reproduction in any medium, provided the original work is properly cited.

Thin films of manganese dioxide ( $\text{MnO}_2$ ) were prepared by self-assembly of  $\text{MnO}_2$  nanoparticles directly onto nickel-coated poly(ethylene terephthalate) flexible films using the newly developed horizontal submersion process. The thickness of deposited thin films was controllable by the deposition duration. This horizontal submersion deposition process for thin-film deposition is relatively easy, simple, and cost effective. Effects of deposition duration and calcination temperatures on the microstructure and electrochemical properties of self-assembled  $\text{MnO}_2$  thin films were investigated. Optimized  $\text{MnO}_2$  thin films exhibited high charge capacity, good cycling reversibility, and stability in a mild aqueous electrolyte and are thus promising electrode materials for the fabrication of thin-film electrochemical capacitors.

## 1. Introduction

Manganese dioxide- ( $\text{MnO}_2$ -) based thin film electrochemical capacitors have received numerous attentions since Pang et al. reported a specific capacitance value of 720 F/g for ultra-thin  $\text{MnO}_2$  films in a mild aqueous electrolyte [1, 2].  $\text{MnO}_2$  thin films appear to be a promising electrode material in batteries and electrochemical capacitors due to the low cost of raw materials, low toxicity and environmentally benign, and their excellent electrochemical properties [3, 4]. Many routes for the preparation of  $\text{MnO}_2$  thin films have currently been developed, which include the sol-gel process, electrodeposition [5–7], and atomic layer deposition [8]. More recently, the self-assembly technique has emerged as one of the most promising methods for thin film fabrication [9]. Self-assembly is the spontaneous adsorption process by which molecules or nanoparticles are arranged into organized aggregates, networks, or patterns onto a supporting substrate. It is characterized as being relatively simple, inexpensive, and requires low energy consumption.

In this study, we have attempted to prepare self-assembled manganese dioxide ( $\text{MnO}_2$ ) thin films directly on nickel-coated poly(ethylene terephthalate) (Ni/PET) flexible supporting substrate using the newly developed horizontal

submersion process under ambient conditions. This thin film deposition process is very cost effective, rapid, and conformal in the preparation of nanostructured thin films which are suitable for the fabrication of thin film electrochemical capacitors. Most notably, the thickness of deposited film is controllable simply by the duration of submersion or by repeating the deposition process a desired number of times. Physical and electrochemical characterization of manganese dioxide nanoparticles and self-assembled thin films was conducted using various established characterization techniques. The effect of deposition conditions on the microstructure and electrochemical properties of self-assembled manganese dioxide thin films were investigated.

## 2. Materials and Methods

**2.1. Preparation of  $\text{MnO}_2$  Colloidal Suspension (sol).** Stable  $\text{MnO}_2$  colloidal suspension (sol) was prepared based on a method reported in literature [10]. Typically,  $\text{MnO}_2$  sol was prepared by mixing 4 mL of  $\text{KMnO}_4$  ( $1.0 \times 10^{-1}$  mol/L) and 8 mL of  $\text{Na}_2\text{S}_2\text{O}_3$  ( $1.88 \times 10^{-2}$  mol/L) in 38 mL ultrapure water (18.2 M $\Omega$ ). The resulting dark-brown  $\text{MnO}_2$  sol was

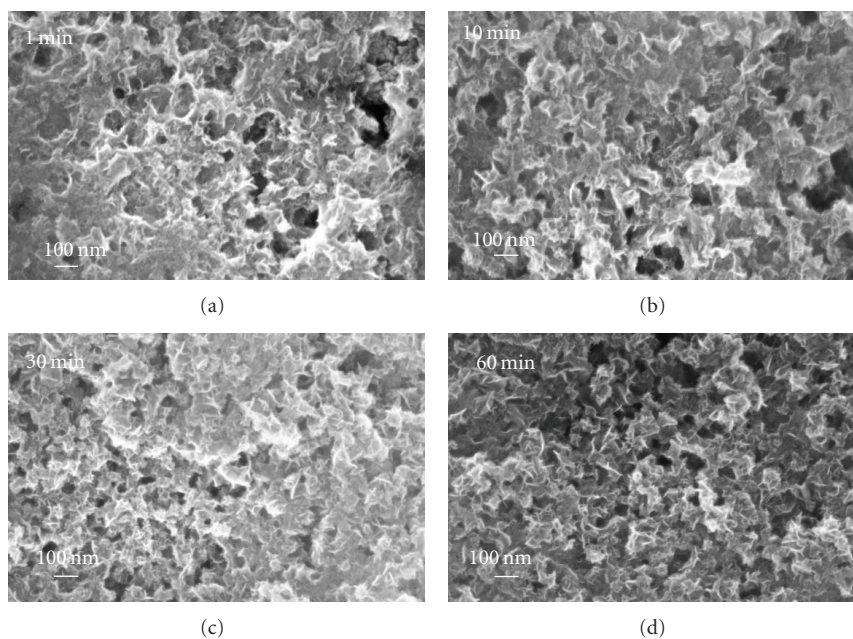


FIGURE 1: FESEM micrographs of self-assembled  $\text{MnO}_2$  thin films deposited on Ni/PET substrates at various submersion durations (a) 1 min, (b) 10 min, (c) 30 min, and (d) 60 min.

being dispersed by sonication in order to enhance dispersion to form a stable colloidal suspension.

**2.2. Preparation of Self-Assembled  $\text{MnO}_2$  Thin Films.** Self-assembled  $\text{MnO}_2$  thin films were prepared on nickel-coated poly(ethylene terephthalate) supporting substrate (Ni/PET) using the newly developed horizontal submersion process. Precleaned Ni/PET substrate with a surface area of  $\sim 3 \text{ cm}^2$  was positioned horizontally onto glass slides using adhesive tape and placed into petri dishes. The  $\text{MnO}_2$  sol was sonicated for 5 minutes to ensure well-dispersed nanoparticles before being poured into the petri dishes. A measured volume of  $\text{MnO}_2$  sol was then poured into each petri dish to completely submerge the substrate. Self-assembled  $\text{MnO}_2$  thin films were formed spontaneously on the substrates upon submersion within the sol for the desired duration. The relative film thickness was controlled by the duration of submersion in the sol. All deposited films were air dried at ambient temperature and subsequently calcined in a tube furnace at various temperatures in air for an hour.

**2.3. Characterizations of  $\text{MnO}_2$  Nanoparticles and Thin Films.** The surface morphology of  $\text{MnO}_2$  nanoparticles and self-assembled thin films were characterized using a scanning electron microscope (SEM) (JEOL Model JSM 6390LA) and a field emission scanning electron microscope (FESEM) (LEO Model 1535), respectively, at various magnifications. All samples were coated with platinum using a sputtering device JFC-1100 E to reduce the inherent charging effect. A transmission electron microscope (TEM) (Model JEM-1230) was used to study the surface morphology of  $\text{MnO}_2$  nanoparticles. The elemental composition of the  $\text{MnO}_2$  nanoparticles was analyzed by FESEM-associated energy

dispersive X-ray microanalysis (EDX) operated with a beam energy of 10 kV.

The electrochemical characterization of self-assembled  $\text{MnO}_2$  thin films was conducted using an advanced electrochemical analyzer (PARSTAT 2263). Sample evaluation by cyclic voltammetry (CV) was conducted using a standard three-electrode cell configuration. The reference electrode used was a saturated calomel electrode (SCE) fitted with a Vycor bridge, and the counter electrode was a platinum foil ( $\sim 2 \text{ cm}^2$ ). A geometric electrode area of  $0.1257 \text{ cm}^2$  of thin-film sample was being exposed to the electrolyte during all cyclic voltammetric experiments. Cyclic voltammograms were obtained by scanning over the potential range of 0.0 V–0.9 V (versus SCE), with a scan rate of 50 mV/s in 1.0 M  $\text{Na}_2\text{SO}_4$  aqueous solution as electrolyte.

The mass loading of various self-assembled  $\text{MnO}_2$  films was determined quantitatively by atomic absorption spectroscopy (AAS) after dissolving a known area of films in the  $\text{H}_2\text{O}_2/\text{HNO}_3$  solution mixture. Based on the measured Mn concentration, the mass loading of  $\text{MnO}_2$  per unit of electrode area was calculated using the formula weight of stoichiometric  $\text{MnO}_2$  of 86.94 g/mol.

### 3. Results and Discussion

**3.1. Effect of Submersion Duration.** Figure 1 shows SEM micrographs of self-assembled  $\text{MnO}_2$  thin films deposited on Ni/PET substrate by the horizontal submersion process at various submersion durations under ambient conditions. These films showed good adhesion to the substrate even without the addition of any binder. Self-assembled films deposited at shorter submersion duration were observed to be rather porous with loosely packed nanoclusters,

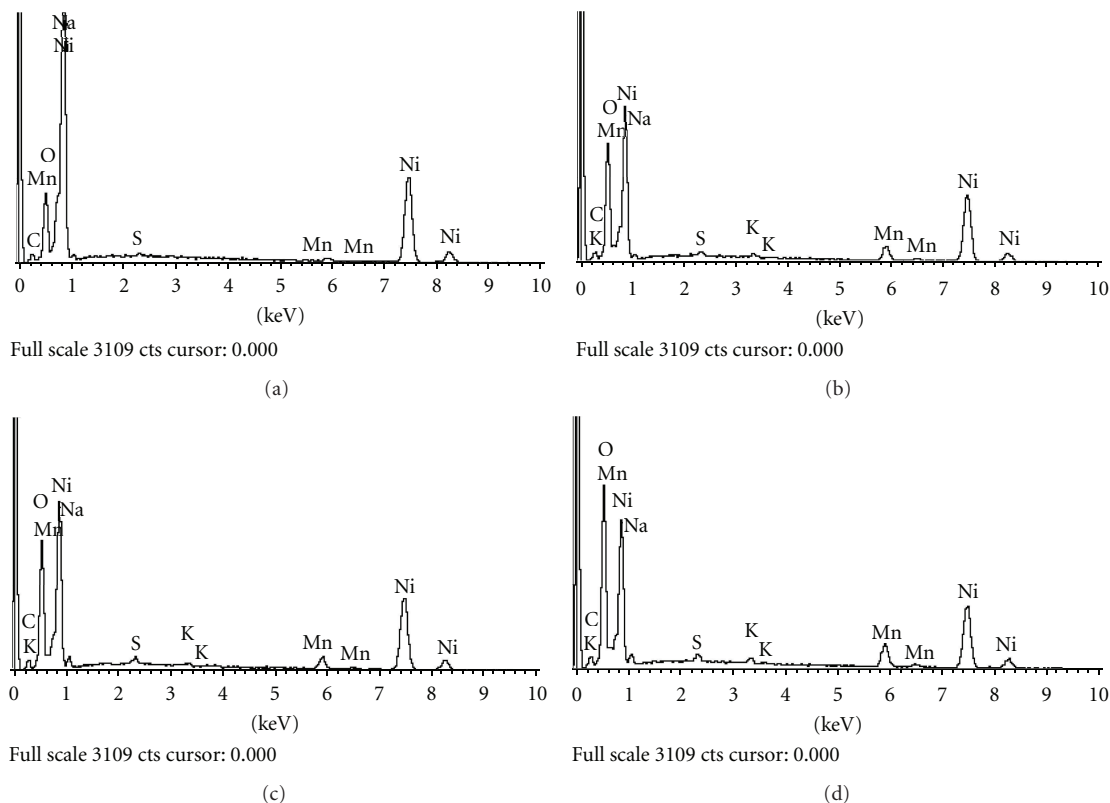


FIGURE 2: EDX spectra of self-assembled  $\text{MnO}_2$  thin films on Ni-coated PET films at submersion duration of (a) 1 min, (b) 10 min, (c) 30 min, and (d) 60 min.

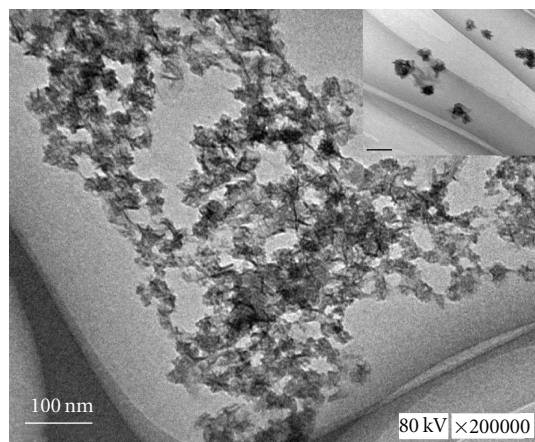


FIGURE 3: TEM micrographs of  $\text{MnO}_2$  self-assembled thin films as deposited on Ni/PET supporting substrate. Inset showed well-dispersed nanoclusters and individual nanoparticles.

whereas films deposited at longer submersion duration were denser with closely packed nanoclusters. Figure 2 shows the EDX spectra of self-assembled manganese oxide thin films on Ni/PET substrates. The presence of manganese and oxygen atoms in the elemental composition of deposited thin films confirmed the deposition of  $\text{MnO}_2$  thin films. Besides, the weight percentages of Mn and O elements

within the deposited films were observed to increase with increased submersion durations, indicating the deposition of thicker films. The weight percentage of Mn was observed to have increased from 1.42% to 8.74%, whereas that of O was increased from 10.85% to 25.56% as the submersion duration was increased from 1 minute to 60 minutes.

Figure 3 shows TEM micrographs of self-assembled  $\text{MnO}_2$  thin film as deposited on Ni/PET supporting substrate. Well-dispersed manganese dioxide nanoclusters and well-defined individual nanoparticles could be clearly discernable (insets of Figure 3). The mean average nanoparticle size was about 20–25 nm in diameter. Aggregated and dense nanofibrous structures were observed to radiate outward from the centre of each nanoparticle.

**3.2. Effect of Calcination.** The effect of calcination on the surface morphology of self-assembled  $\text{MnO}_2$  thin films on Ni/PET supporting substrates was studied by FESEM and shown in Figure 4. The heat treatment was observed to have substantial effect on the surface morphology of  $\text{MnO}_2$  thin films, with calcined films showing comparatively smoother surface morphology with densely packed nanoparticles. Apart from film densification, the calcination process could have effectively removed all physisorbed and chemisorbed water from  $\text{MnO}_2$  thin films, as evidenced by the porous microstructure and occurrence of cracks due to the shrinkage of films. Such porous microstructures could serve to enhance ionic transport and redox reactions which underlie the

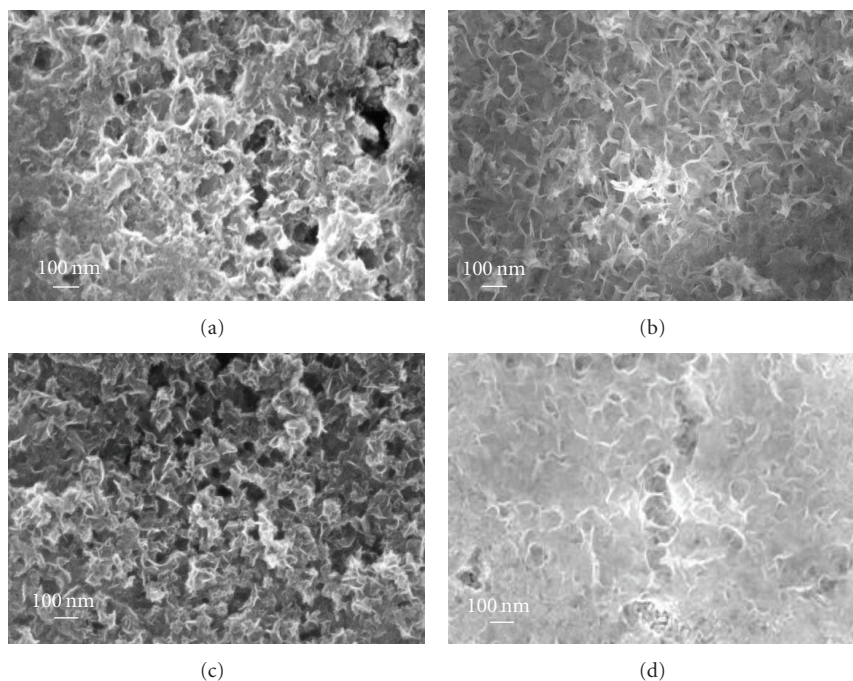


FIGURE 4: FESEM micrographs of  $\text{MnO}_2$  thin films on Ni-coated PET films at deposition duration of (a) 1 min, before, (b) 1 min, after, and (c) 60 min, before, (d) 60 min, after calcination at  $200^\circ\text{C}$  in air for 1 hour.

charge storage mechanism [11]. The electrolyte ions could penetrate into the porous microstructure of manganese dioxide thin-film electrode during electrochemical reactions.

### 3.3. Electrochemical Characterization of Self-Assembled $\text{MnO}_2$ Thin Films

**3.3.1. Effect of Calcination.** The effect of heat treatment on the capacitive behavior of self-assembled  $\text{MnO}_2$  thin films on Ni/PET films was investigated by heating them in air at various temperatures for 1 hour. The calcination temperature did not exceed  $200^\circ\text{C}$  since the melting point of pure PET was  $241^\circ\text{C}$  [12]. Calcination temperature was observed to have a positive effect on the charge capacity of  $\text{MnO}_2$  thin films as shown by the increase in areas of cyclic voltammograms for films calcined at higher temperatures (Figure 5). The charge capacities of  $\text{MnO}_2$  thin films were observed to increase moderately with increasing calcination temperatures up to  $200^\circ\text{C}$ . A maximum charge capacity of  $34\text{ mF/cm}^2$  was achieved for films calcined at  $200^\circ\text{C}$ . Previous studies reported that annealing temperature could affect the crystal structure of the electrochemically deposited manganese oxide [13]. Chemically bound water within the  $\text{MnO}_2$  films was thought to have played a major role in the observed variation of charge capacity. As chemically bound water is essential for the transportation of active ionic species, the pseudocapacitance of oxide material is dependent upon its water content [14]. Water content in manganese oxides is known to affect the electrochemical reactivity and thermodynamic stability of various manganese dioxide phases as it causes variation of crystal lattice and

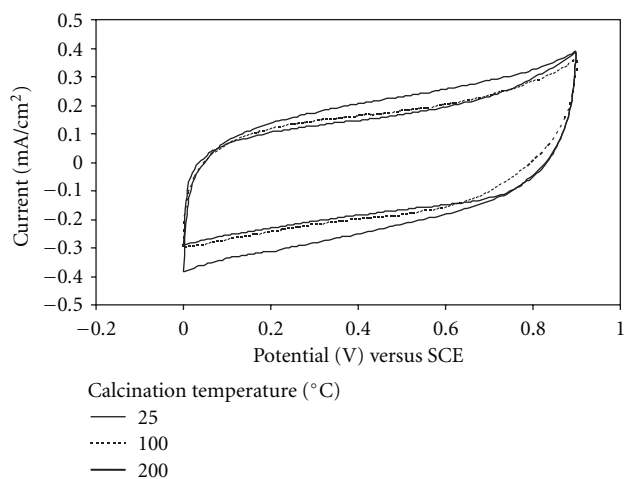


FIGURE 5: Cyclic voltammograms of self-assembled  $\text{MnO}_2$  thin films calcined at various temperatures.

consequently of electrical conductivity and electrode potential [15]. Although the presence of structural water promotes proton diffusivity in manganese oxide, its resistivity increases with increasing water content. As such, heat treatment of  $\text{MnO}_2$  films at  $200^\circ\text{C}$  in air for 1 hour could have resulted in lowering their structural water content within the oxide lattice and consequently led to increase in the electronic conductivity and hence the observed higher charge capacity.

**3.3.2. Effect of Film Thickness.** Figure 6 shows the cyclic voltammograms of  $\text{MnO}_2$  films coated on Ni/PET substrates

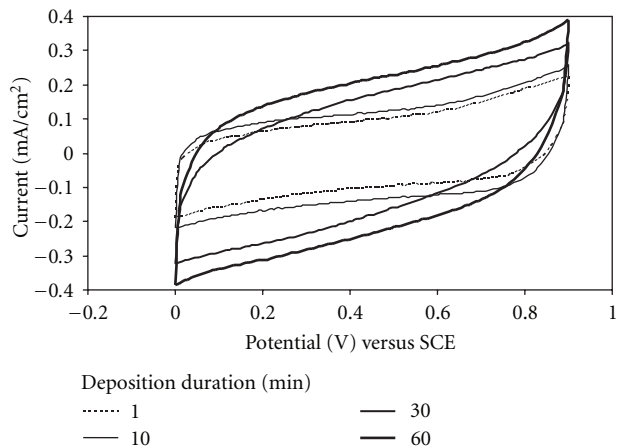


FIGURE 6: Cyclic voltammograms of self-assembled manganese dioxides thin films deposited at different submersion durations.

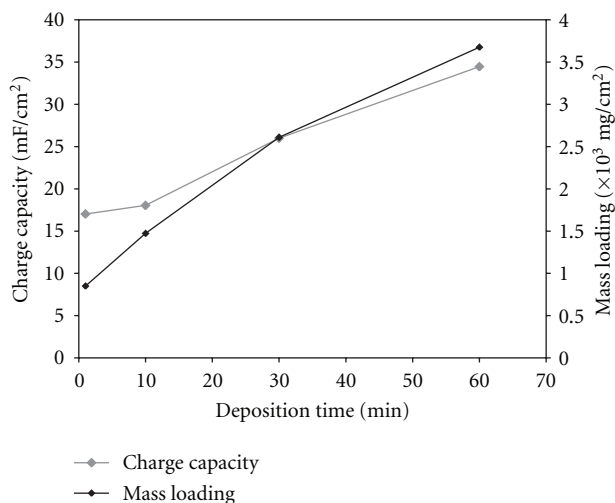


FIGURE 7: Charge capacity and mass loading of MnO<sub>2</sub> thin films deposited at various submersion durations.

at different submersion duration. The relative film thickness was controlled by the submersion duration which was being varied between 1 minute and 60 minutes. All cyclic voltammograms obtained were almost rectangular in shape with symmetrical anodic and cathodic halves. Such rectangular cyclic voltammograms indicated that self-assembled MnO<sub>2</sub> films exhibited almost ideal capacitive behaviors. It is clear from Figure 6 that there were no redox peaks observed within the potential range between 0 and 0.9 V (versus SCE) which could be attributed to the phase stability of electrode materials and the high reversibility of pseudocapacitive electrochemical reactions.

Figure 7 shows the average mass loading and charge capacities of self-assembled MnO<sub>2</sub> thin films deposited on Ni/PET substrates at various submersion durations. The mass loading of self-assembled MnO<sub>2</sub> films deposited on the supporting substrate was used as an indication of their relative film thickness. The mass loadings of MnO<sub>2</sub> films deposited on Ni/PET substrates were determined using AAS

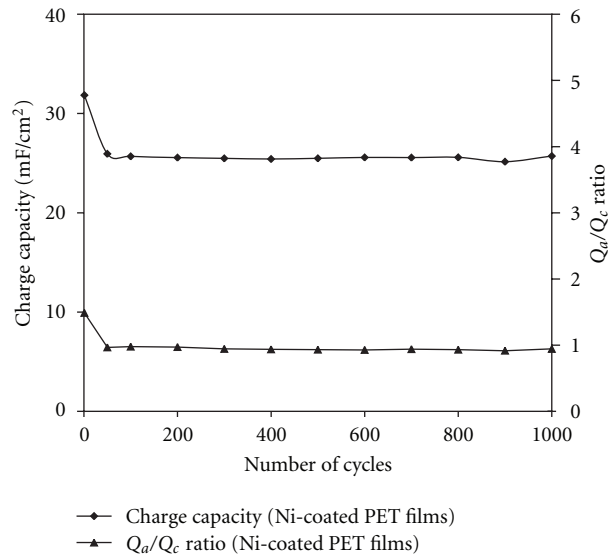
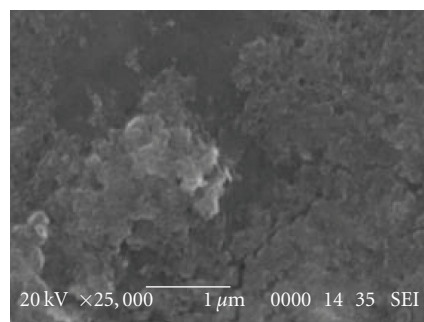
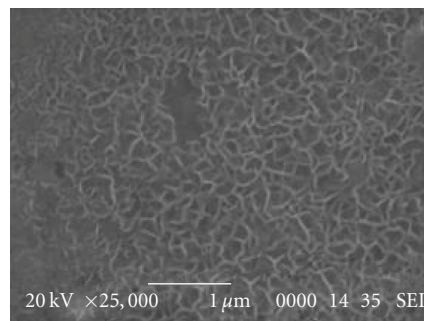


FIGURE 8: Charge capacity and cycling reversibility of self-assembled MnO<sub>2</sub> thin films as a function of cycle numbers.



(a)



(b)

FIGURE 9: Effect of voltammetric cycling on the microstructure of MnO<sub>2</sub> films (a) before cycling; (b) after cycling.

by dissolving these films in HNO<sub>3</sub>/H<sub>2</sub>O<sub>2</sub> mixture. Generally, the mass loading of MnO<sub>2</sub> was observed to increase in submersion durations. A maximum mass loading of 3.68 × 10<sup>-3</sup> mg/cm<sup>2</sup> of MnO<sub>2</sub> was deposited on Ni/PET substrates at the submersion duration of 60 minutes. Both mass loading and charge capacity of self-assembled MnO<sub>2</sub> thin films were observed to increase in tandem with submersion durations. Such increase in charge capacity was associated

with the higher mass loading of manganese dioxide for thicker films, as also evidenced by the higher weight % of Mn as determined by both the EDX and AAS analyses for films deposited at longer submersion durations (Figure 2). The voltammetric charge of the electrochemically oxidized MnO<sub>2</sub> films was observed to increase with increasing film thickness, which corresponded to increase in their charge capacity. It was observed that self-assembled MnO<sub>2</sub> films possessed highly porous microstructure with high specific surface area and hence favored the proton/cation diffusion and adsorption/desorption during the redox transitions.

**3.3.3. Effect of Long-Term Cycling.** The effect of long-term cycling of self-assembled MnO<sub>2</sub> thin films deposited on Ni/PET substrates in 1.0 M Na<sub>2</sub>SO<sub>4</sub> aqueous solution is shown in Figure 8. The charge capacity was observed to decline rather rapidly for the initial 100 cycles but only decreased gradually thereafter upon long-term cycling. The overall net loss in charge capacity of MnO<sub>2</sub> thin films was observed to be about 19% of their initial charge capacity upon cycling for 1,000 cycles. Such decline in charge capacity could be attributed to delamination and partial dissolution of manganese dioxide films into the electrolytes during cycling rather than any structural or chemical degradation. Dissolution of MnO<sub>2</sub> during discharge in neutral electrolyte occurred by both the disproportionation reaction and solid-phase diffusion [1]. However, it is speculated that other factors may also be involved, such as changes in the electronic conductivity of the film during cycling associated with changes in oxidation states or structural water content [2]. The decrease in capacity after cycling can also be attributed to increased electrode resistance with increasing cycle number [16]. The charge capacity was observed to decline rather rapidly for the initial 100 cycles but only decreased gradually thereafter upon long-term cycling. The overall net loss in charge capacity of self-assembled MnO<sub>2</sub> thin films was observed to be about 19% of their initial charge capacity upon cycling for 1,000 cycles.

Figure 9 shows the SEM micrographs of self-assembled MnO<sub>2</sub> thin films deposited on Ni/PET films before and after cycling for 1000 cycles. The surface morphology of MnO<sub>2</sub> film after cycling was more porous and fibrous in nature. Similar observations had been reported by Nagarajan et al. [17]. The higher porosity could be resulted from partial dissolution and redeposition of manganese oxide during cycling. Since the charge/discharge process in MnO<sub>2</sub> involves a redox reaction between the III and IV oxidation states of Mn, the reactivity (or utilization) of the oxide can be enhanced with increased accessibility of electrolyte ions within materials [16, 17]. In addition, some of the MnO<sub>2</sub> inevitably dissolved into the 1.0 M Na<sub>2</sub>SO<sub>4</sub> electrolyte and then redeposited onto the substrate. The redeposited oxide layer was highly porous and showed a distinctive petal-like surface morphology. This could be attributed to the anodized film caused by back and forth sweeps of the applied cycling potential.

## 4. Conclusion

Self-assembled manganese dioxide thin films have been successfully deposited onto Ni/PET films using the newly developed horizontal submersion process under ambient conditions. These films were shown by cyclic voltammetry to exhibit excellent capacitance behavior, high cycling reversibility, and stability within the potential range of 0.0 to 0.9 V versus SCE in mild NaSO<sub>4</sub> aqueous electrolyte. Thin film with desired thickness, good uniformity and tailored microstructure, and enhanced electrochemical properties could be prepared through optimizing deposition conditions such as submersion duration and calcination temperature.

## Acknowledgment

This work was supported in part by the Ministry of Higher Education Malaysia (MOHE) Fundamental Research Grant Scheme: FRGS/01(18)/747/2010(33).

## References

- [1] S. C. Pang, M. A. Anderson, and T. W. Chapman, "Novel electrode materials for thin-film ultracapacitors: comparison of electrochemical properties of sol-gel-derived and electrodeposited manganese dioxide," *Journal of the Electrochemical Society*, vol. 147, no. 2, pp. 444–450, 2000.
- [2] S. F. Chin, S. C. Pang, and M. A. Anderson, "Material and electrochemical characterization of tetrapropylammonium manganese oxide thin films as novel electrode materials for electrochemical capacitors," *Journal of the Electrochemical Society*, vol. 149, no. 4, pp. A379–A384, 2002.
- [3] S. F. Chin and S. C. Pang, "Tetrapropylammonium-manganese oxide/polypyrrole hybrid nanocomposite thin films as novel electrode materials for supercapacitors," *Materials Chemistry and Physics*, vol. 124, no. 1, pp. 29–32, 2010.
- [4] S. F. Chin, S. C. Pang, and M. A. Anderson, "Self-assembled manganese dioxide nanowires as electrode materials for electrochemical capacitors," *Materials Letters*, vol. 64, no. 24, pp. 2670–2672, 2010.
- [5] S. C. Pang and M. A. Anderson, "Novel electrode materials for electrochemical capacitors: part II. Material characterization of sol-gel-derived and electrodeposited manganese dioxide thin films," *Journal of Materials Research*, vol. 15, no. 10, pp. 2096–2106, 2000.
- [6] C. C. Hu and T. W. Tsou, "Capacitive and textural characteristics of hydrous manganese oxide prepared by anodic deposition," *Electrochimica Acta*, vol. 47, no. 21, pp. 3523–3532, 2002.
- [7] B. Babakhani and D. G. Ivey, "Anodic deposition of manganese oxide electrodes with rod-like structures for application as electrochemical capacitors," *Journal of Power Sources*, vol. 195, no. 7, pp. 2110–2117, 2010.
- [8] O. Nilsen, H. Fjellvåg, and A. Kjekshus, "Growth of manganese oxide thin films by atomic layer deposition," *Thin Solid Films*, vol. 444, no. 1-2, pp. 44–51, 2003.
- [9] X. Zhang, W. Yang, and D. G. Evans, "Layer-by-layer self-assembly of manganese oxide nanosheets/polyethylenimine multilayer films as electrodes for supercapacitors," *Journal of Power Sources*, vol. 184, no. 10, pp. 695–700, 2008.
- [10] J. F. Perez-Benito, C. Arias, and E. Amat, "A kinetic study of the reduction of colloidal manganese dioxide by oxalic acid,"

- Journal of Colloid and Interface Science*, vol. 177, no. 2, pp. 288–297, 1996.
- [11] S. C. Pang, W. H. Khoh, and S. F. Chin, “Nanoparticulate magnetite thin films as electrode materials for the fabrication of electrochemical capacitors,” *Journal of Materials Science*, vol. 45, no. 20, pp. 5598–5604, 2010.
- [12] Z. Fang, R. L. Smith, H. Inomata, and K. Arai, “Phase behavior and reaction of polyethylene terephthalate-water systems at pressures up to 173 MPa and temperatures up to 490°C,” *Journal of Supercritical Fluids*, vol. 15, no. 3, pp. 229–243, 1999.
- [13] M. S. Wu and R. H. Lee, “Nanostructured manganese oxide electrodes for lithium-ion storage in aqueous lithium sulfate electrolyte,” *Journal of Power Sources*, vol. 176, no. 1, pp. 363–368, 2008.
- [14] S. J. Bao, B. L. He, Y. Y. Liang, W. J. Zhou, and H. L. Li, “Synthesis and electrochemical characterization of amorphous MnO<sub>2</sub> for electrochemical capacitor,” *Materials Science and Engineering A*, vol. 397, no. 1-2, pp. 305–309, 2005.
- [15] A. Era, Z. Takehara, and S. Yoshizawa, “Discharge mechanism of the manganese dioxide electrode,” *Electrochimica Acta*, vol. 12, no. 9, pp. 1199–1212, 1967.
- [16] B. Babakhani and D. G. Ivey, “Anodic deposition of manganese oxide electrodes with rod-like structures for application as electrochemical capacitors,” *Journal of Power Sources*, vol. 195, no. 7, pp. 2110–2117, 2010.
- [17] N. Nagarajan, H. Humadi, and I. Zhitomirsky, “Cathodic electrodeposition of MnOx films for electrochemical supercapacitors,” *Electrochimica Acta*, vol. 51, no. 15, pp. 3039–3045, 2006.
- [18] J. K. Chang, C. H. Huang, W. T. Tsai, M. J. Deng, I. W. Sun, and P. Y. Chen, “Manganese films electrodeposited at different potentials and temperatures in ionic liquid and their application as electrode materials for supercapacitors,” *Electrochimica Acta*, vol. 53, no. 13, pp. 4447–4453, 2008.

## Research Article

# An Organic Acid-induced Synthesis and Characterization of Selenium Nanoparticles

**Charu Dwivedi, Chetan P. Shah, Krishankant Singh, Manmohan Kumar, and Parma Nand Bajaj**

*Radiation and Photochemistry Division, Bhabha Atomic Research Centre, Trombay, Mumbai 400 085, India*

Correspondence should be addressed to Manmohan Kumar, manmoku@barc.gov.in

Received 30 March 2011; Accepted 26 May 2011

Academic Editor: Mallikarjuna Nadagouda

Copyright © 2011 Charu Dwivedi et al. This is an open access article distributed under the Creative Commons Attribution License, which permits unrestricted use, distribution, and reproduction in any medium, provided the original work is properly cited.

A simple wet chemical method has been developed to synthesize selenium nanoparticles (size 40–100 nm), by the reaction of sodium selenosulphate precursor with different organic acids in aqueous medium, under ambient conditions. Polyvinyl alcohol has been used to stabilize the selenium nanoparticles. The synthesized nanoparticles can be separated from its sol by using a high-speed centrifuge and can be redispersed in aqueous medium with a sonicator. UV-visible optical absorption spectroscopy, X-ray diffraction, energy dispersive X-rays, differential scanning calorimetry, atomic force microscopy, and transmission electron microscopy techniques have been employed to characterize the synthesized selenium nanoparticles.

## 1. Introduction

The research on the synthesis and characterization of nanomaterials has been stimulated by their technological applications. The first few technological uses of these materials were as catalysts and pigments. Now, much of the hype surrounding these materials revolves around the enhanced electrical, mechanical, and optical properties. In this nanosize regime, the particles possess short-range structures that are essentially the same as that of the bulk, yet they have optical and/or electronic properties which are dramatically different from that of the bulk [1–3]. These represent a relatively new class of materials and have come under intensive investigations because of their quantum size effects, large surface-to-volume ratio, and the large difference in the properties of their surface atoms. An extensive reported literature exists on the synthesis and applications of nanoparticles of both metals, such as silver, gold, and platinum, and semiconductors, such as CdSe, ZnSe, TiO<sub>2</sub>. However, research on metalloid, like selenium, is scanty. Selenium is used in rectifiers, solar cells, photographic exposure meters, and xerography [4]. It is also used in the glass industry to eliminate bubbles and remove undesirable tints produced by iron. Linear and nonlinear

optical properties of selenium and its reactivity towards Cd, Zn, make this an important field of study. The research on selenium has attracted more and more attention not only because of its technological applications, but also due to its novel role in life sciences. Selenium is also an essential trace element in human body and has great importance in nourishment and medicine [5]. It exists in a number of crystalline structures, the principal ones being trigonal, consisting of helical chains, and the less stable monoclinic form, consisting of Se<sub>8</sub> rings [6]. Monoclinic Se (m-Se) comes in three forms,  $\alpha$ ,  $\beta$ , and  $\gamma$ , which differ only in the way the rings are packed [6, 7]. Amorphous selenium (a-Se) is composed of a mixture of disordered chains. Various forms of nanoselenium can be produced, using different synthetic methods [5, 8–12]. Reduction method is the most popular method for selenium nanoparticle preparation, which includes chemical reduction [13],  $\gamma$ -radiolytic reduction [14], bacterial reduction [15], and so forth. However, some literature on the formation of nanoselenium via oxidation method, such as reaction of selenourea with hydroxyl radical [16], electrochemical oxidation of selenide [17], and reaction of sodium selenosulphate with acrylonitrile [18], also exists.

Here, we have developed a new simple wet chemical method, employing protic acids, such as acetic acid, oxalic

acid, and gallic acid to synthesize polyvinyl alcohol-stabilized selenium nanoparticles from aqueous sodium selenosulphate as selenium precursor. The method is capable of producing spherical selenium nanoparticles of size 35 to 70 nm, under ambient conditions. The synthesized selenium nanoparticles were characterized by UV-visible optical absorption spectroscopy, X-ray diffraction (XRD), energy dispersive X-rays (EDAX), differential scanning calorimetry (DSC), atomic force microscopy (AFM), and transmission electron microscopy (TEM) techniques.

## 2. Experimental Details

High-purity polyvinyl alcohol (PVA) of molecular weight 1,25,000 was obtained from S.D. fine chemicals Ltd., Mumbai, India. All the other chemicals used were of GR grade, procured from local market. Selenium powder was purchased from Aldrich. Aqueous solutions were prepared, using water obtained from Millipore-Q water purification system (with conductivity of  $0.6 \mu\text{Scm}^{-1}$ , or less).

Sodium selenosulphate ( $\text{Na}_2\text{SeSO}_3$ ) solution was prepared by refluxing a mixture of selenium (2 g) and  $\text{Na}_2\text{SO}_3$  (20 g) in 100 mL water at  $70^\circ\text{C}$ , for about 7 hours [19]. This sodium selenosulphate ( $\text{Na}_2\text{SeSO}_3$ ) solution ( $\sim 0.25 \text{ mol dm}^{-3}$ ), containing unreacted  $\text{Na}_2\text{SO}_3$ , was used as a stock for Se precursor. An aqueous PVA stock solution, 1% by weight, was prepared by dissolving 1.0 g of PVA in 100 mL of water, while stirring at  $80^\circ\text{C}$ . The above stock solutions were diluted to the required concentrations for different experiments.

PVA-stabilized Se nanoparticles were synthesized by reaction of sodium selenosulphate (concentration  $1 \times 10^{-4}$  to  $1.0 \times 10^{-3} \text{ mol dm}^{-3}$ ) with different organic carboxylic acids ( $5 \times 10^{-3}$  to  $3 \times 10^{-2} \text{ mol dm}^{-3}$ ) in aqueous medium, in the presence of PVA as a stabilizer, in the concentration range from 0.01 to 0.1%. The formation of orange-red-coloured selenium nanoparticle sol was observed in less than one minute. However, in the absence of PVA stabilizer, a dark red-coloured precipitate of selenium was formed.

UV-visible optical absorption spectra of the selenium nanoparticle sols were recorded, using a double beam spectrophotometer, model Spectroscan 2600 from Chemito. XRD patterns of the nanoparticles were recorded with a Phillips X-ray diffractometer, model PW 1710, using a  $\text{Cu K}\alpha$  source ( $\lambda = 0.15406 \text{ nm}$ ). DSC measurements were carried out, using a Mettler TA 3000 thermal analysis system (model DSC-30). About 5–10 mg of the synthesized selenium nanoparticles and standard selenium powder were weighed into aluminum crucibles separately, and DSC measurements of both were carried out in  $\text{N}_2$  atmosphere, at a heating rate of  $10^\circ\text{C}/\text{min}$ , from  $50^\circ$  to  $250^\circ\text{C}$ . Selenium nanoparticles, separated from aqueous sols, using a high-speed centrifuge, at about 15000 rpm, washed with water, and dried at room temperature, were used for XRD and thermal analysis measurements. AFM analysis of the synthesized selenium nanoparticles was carried out, using a Solver P47 model from NT-MDT, Russia. TEM characterization was carried out with a TECNAI 20, FEI electron microscope, using the sample on a copper grid, coated with a thin amorphous carbon film.



FIGURE 1: Aqueous selenium nanoparticle sols obtained by the reaction of (A)  $2.0 \times 10^{-4}$  (B)  $5.0 \times 10^{-4}$  (C)  $1.0 \times 10^{-3} \text{ mol dm}^{-3}$  sodium selenosulphate with  $2.0 \times 10^{-2} \text{ mol dm}^{-3}$  acetic acid, in the presence of 0.05% PVA.

## 3. Results and Discussion

**3.1. Optical Absorption Studies.** The initial concentration of sodium selenosulphate determines the intensity of Se nanoparticle sols. Typical picture of the selenium sols, produced from three different initial concentrations of sodium selenosulphate, is shown in Figure 1.

Figure 2 shows the effect of sodium selenosulphate and PVA concentrations on UV-visible absorption spectra of the selenium nanoparticle sols synthesized by the reaction of sodium selenosulphate with  $2.0 \times 10^{-2} \text{ mol dm}^{-3}$  of different organic acids. From Figure 2(A), it is clear that the intensity of selenium nanoparticles increases with the increase in sodium selenosulphate concentration. However, it shows a shoulder at around 240 nm, when the reaction was carried out with acetic acid and oxalic acid. But it does not show any such kind of the behavior when the reaction was carried out with an aromatic acid (i.e., gallic acid and many more). This may be due to the overlapping of the absorption spectrum of aromatic system with the shoulder of the selenium nanoparticles, at lower wavelengths ( $<300 \text{ nm}$ ). Till now, none of the researchers have observed such a shoulder for selenium nanoparticles. However, the absorbance at lower wavelength region, increases significantly with acid concentration, only in the case of oxalic acid (Figure 2(B)). Whereas, from Figure 2(C), it is clear that, there is no significant effect of PVA concentration, in the concentration range from 0.01 to 0.1%, on the UV-visible absorption spectra of selenium nanoparticles sols. PVA was found to be a very efficient stabilizer for selenium nanoparticles, even at low concentration of 0.01%.

Further, the particle size was correlated with the nature of the UV-visible spectra, and if the particle size is about 100 nm or more, it shows a clear regular maxima in the visible region [20]. Comparison of the present spectra with those reported by Lin and Wang [20] shows that the selenium nanoparticles have an average size of about 80 nm, which is further supported by AFM images.

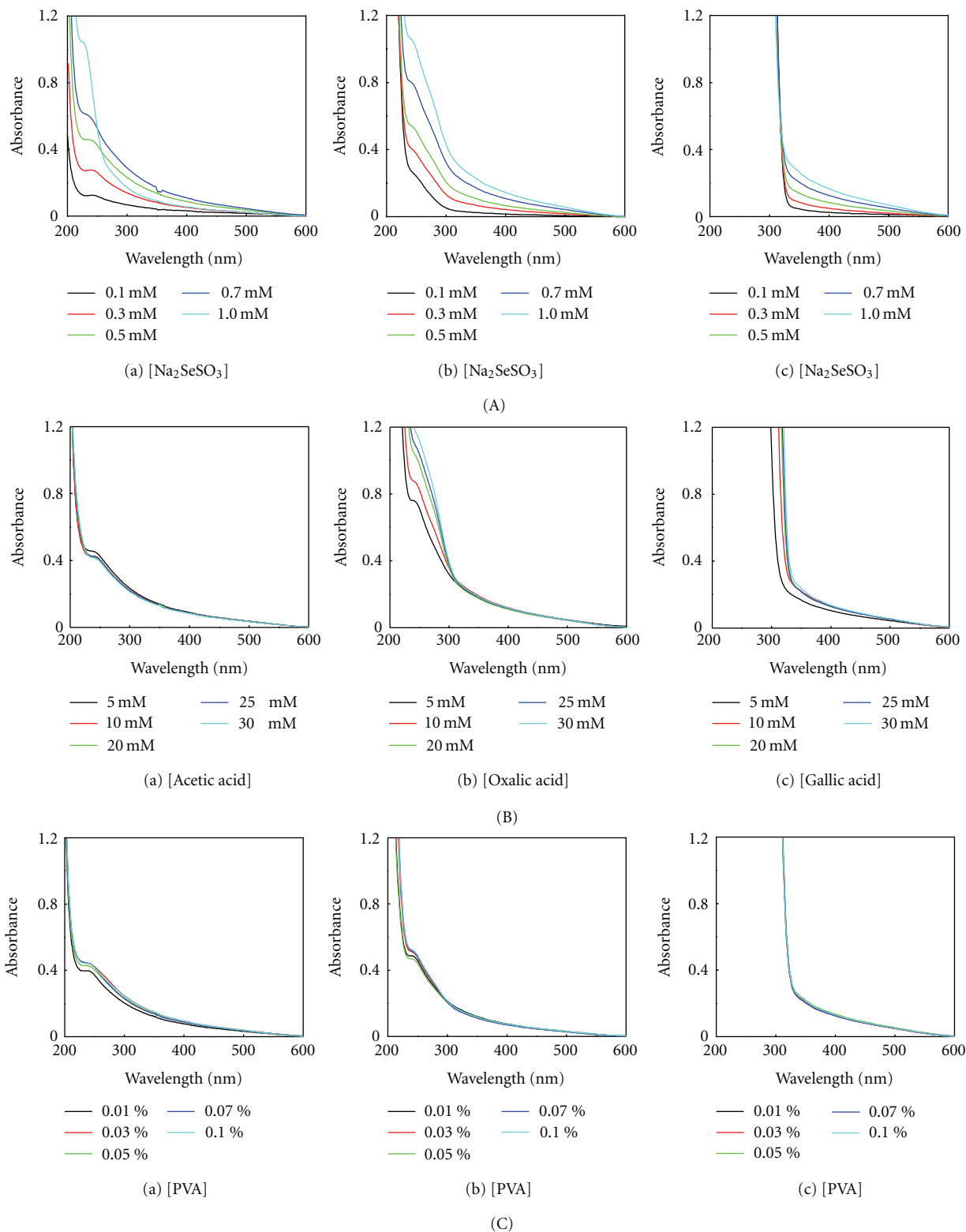


FIGURE 2: (A) Effect of sodium selenosulphate concentration on the UV-visible absorption spectra of the selenium sols produced by the reaction of sodium selenosulphate with  $5.0 \times 10^{-3} \text{ mol dm}^{-3}$  (a) acetic acid, (b) oxalic acid, and (c) gallic acid, at a fixed concentration of PVA (0.05%). (B) Effect of acid concentration, (a) acetic acid, (b) oxalic acid, and (c) gallic acid, on the absorption spectra of the selenium sols produced by reaction with  $5.0 \times 10^{-4} \text{ mol dm}^{-3}$  sodium selenosulphate, in the presence of 0.05% PVA. (C) Effect of PVA concentration on absorption spectra of the selenium sol produced by the reaction of  $5.0 \times 10^{-4} \text{ mol dm}^{-3}$  sodium selenosulphate with  $5.0 \times 10^{-3} \text{ mol dm}^{-3}$  (a) acetic acid, (b) oxalic acid, and (c) gallic acid.

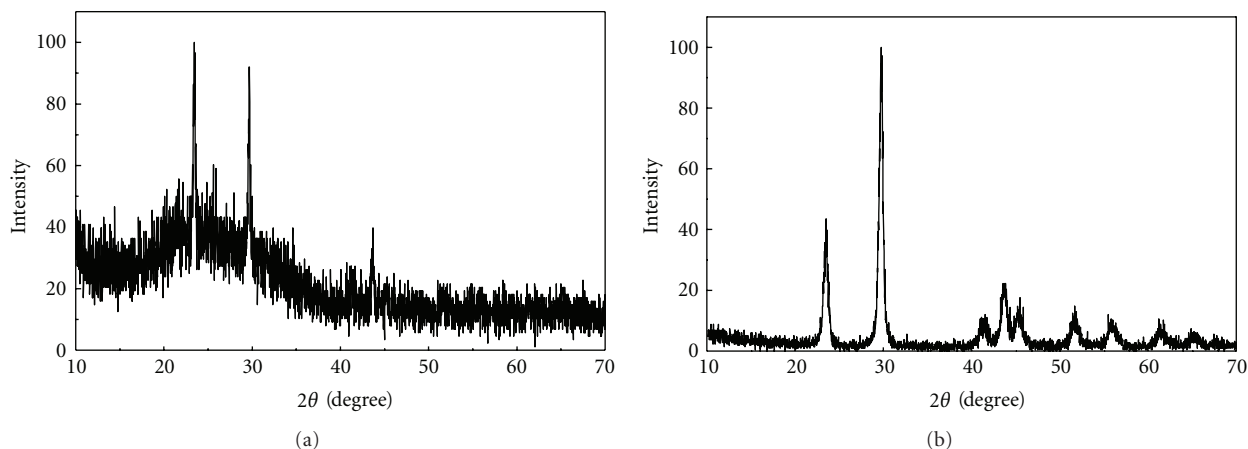


FIGURE 3: (a) XRD pattern of the synthesized selenium nanoparticles annealed at 130°C, for 6 hrs, and (b) commercial selenium sample. Selenium nanoparticles were synthesized by the reaction of  $1.0 \times 10^{-3}$  mol dm<sup>-3</sup> sodium selenosulphate with  $2.0 \times 10^{-2}$  mol dm<sup>-3</sup> acetic acid, in the presence of 0.01% PVA.

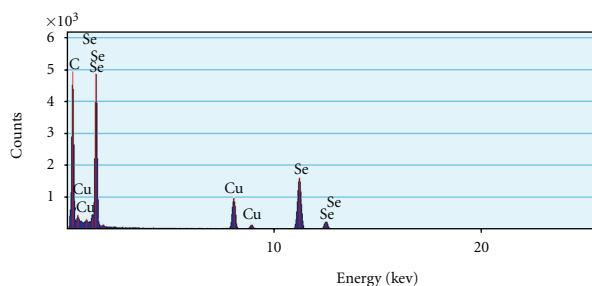


FIGURE 4: EDAX pattern of the selenium nanoparticles, synthesized by the reaction of  $1.0 \times 10^{-3}$  mol dm<sup>-3</sup> sodium selenosulphate with  $2.0 \times 10^{-2}$  mol dm<sup>-3</sup> acetic acid, in the presence of 0.01% PVA.

**3.2. X-Ray Diffraction Study and EDAX of the Synthesized Selenium Nanoparticles.** Crystal structure of the selenium nanoparticles was determined by XRD technique. The typical XRD patterns of the synthesized sample, after heat treatment at 130°C, for 6 hrs, and that of the commercially available selenium, are displayed in Figures 3(a) and 3(b), respectively. The XRD pattern of the synthesized selenium nanoparticles, without heat treatment, is much more noisy, with broader peaks (plot not shown), indicating amorphous nature of the particles. It is believed that amorphous selenium is red in colour, which is further confirmed by selenium sol presented in Figure 1. All the diffraction pattern peaks in Figure 3(a) correspond to trigonal phase, with lattice constants  $a = 4.362$  Å and  $c = 4.958$  Å, which match very well with the reported values (JCPDS file no. 06-362).

Further, chemical composition of the synthesized selenium nanoparticles was also confirmed by EDAX. The EDAX spectrum of the nanoparticles, shown in Figure 4, also indicates that the nanoparticles are of selenium only. The peak corresponding to copper and carbon arises due to carbon-coated copper grid, on which thin film of the sample was deposited for TEM analysis.

**3.3. Differential Scanning Calorimetry (DSC) Study.** DSC thermograms of the synthesized selenium nanoparticles and standard commercial selenium sample were recorded from 50° to 250°C. DSC thermogram of the synthesized selenium nanoparticles showed an exothermic transition at 90°C, along with endothermic melting peak at 217°C (Figure 5(a)). Enthalpy of the transition was found to be 45.2 J/g. The repeat DSC thermogram of the same selenium sample, recorded after bringing it to ambient temperature, did not show any exothermic peak at the mentioned temperature (plot not shown). This clearly indicates that the selenium particles lose their nanocrystalline nature in the first thermal run itself, and the transition could be assigned to increase in the crystallinity of the selenium nanoparticles. This observation is in corroboration with the XRD results obtained with the synthesized sample and that annealed at 130°C. DSC thermogram of the standard selenium powder sample also shows melting peak at 217°C, without any such exothermic peak, which is shown in Figure 5(b).

**3.4. AFM and TEM Studies.** AFM and TEM are very important techniques, which are used to get the information about particle size, shape, surface topography, and so forth. Therefore, morphology and structure of the synthesized selenium nanoparticles were also determined by these techniques. Typical 2D and 3D AFM images of the synthesized selenium nanoparticles are shown in Figure 6. The 2D image of the synthesized selenium nanoparticles shows smaller individual particles of about 10 nm size, along with larger agglomerates of sizes upto ~150 nm while the 3D image indicates the presence of individual spherical particles, with maximum height of 30 nm in the z-direction.

Transmission electron microscope image of the synthesized selenium nanoparticle is shown in Figure 7. Spherical shape of individual nanoparticles, with size in the range of 35–70 nm, is evident from the TEM image. AFM image is taken by suspending much higher concentration of the

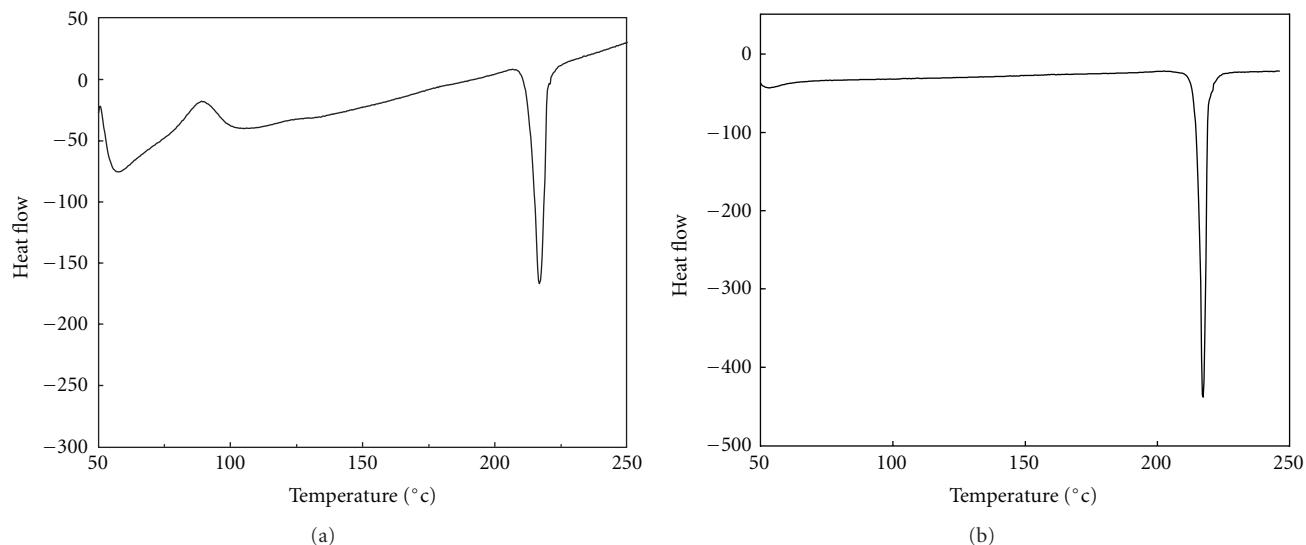


FIGURE 5: DSC thermogram of (a) the selenium nanoparticles synthesized by the reaction of  $1.0 \times 10^{-3} \text{ mol dm}^{-3}$  sodium selenosulphate with  $2.0 \times 10^{-2} \text{ mol dm}^{-3}$  acetic acid, in the presence of 0.01% PVA, and (b) standard commercial selenium sample.

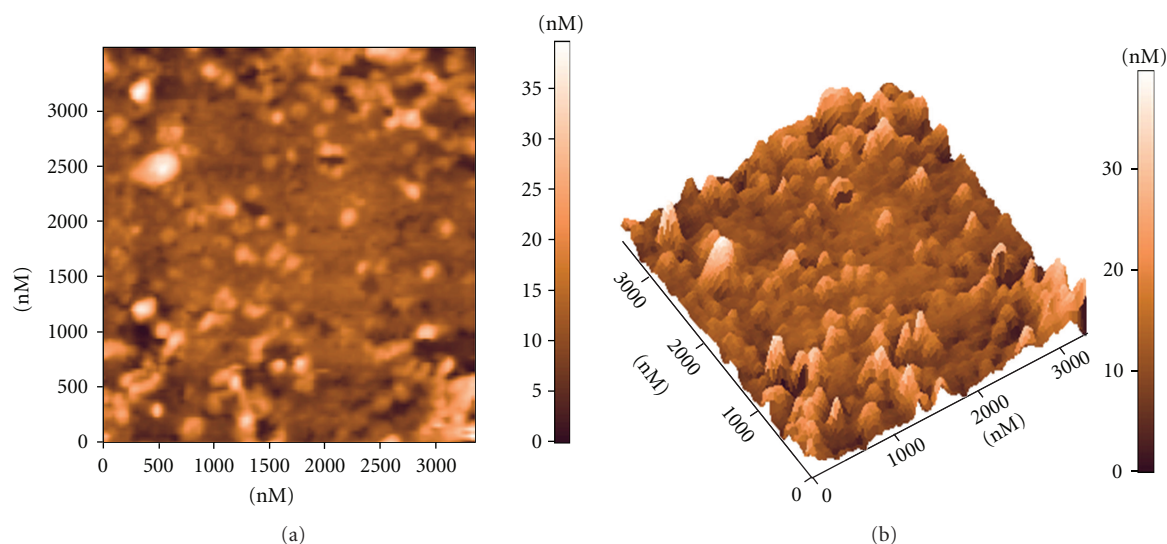


FIGURE 6: AFM images of the selenium nanoparticles formed by the reaction of  $1.0 \times 10^{-3} \text{ mol dm}^{-3}$  sodium selenosulphate with  $2.0 \times 10^{-2} \text{ mol dm}^{-3}$  acetic acid, in the presence of 0.01 % PVA, (a) 2D image and (b) 3D image.

selenium nanoparticles on the silicon wafer in the presence of the PVA stabilizer. It shows individual particles in the size range of 10–150 nm, along with some larger aggregates while the TEM image is taken at much higher magnification, with a dilute sample, after washing out the PVA stabilizer. Thus, it shows a specific portion of the sample deposited on the graphite-coated copper grid, having well-separated individual particles of size in the range of 35–70 nm. These differences in the two sample preparation methods are responsible for the observed difference in the particle sizes. The conclusions drawn from AFM and TEM studies are in corroboration with each other. Thus, the present method is capable of producing spherical selenium nanoparticles.

#### 4. Conclusions

Acid-induced synthesis of selenium nanoparticles has been found to be a simple and convenient method, which can be carried out under ambient conditions. PVA was used as a stabilizer for the selenium nanoparticles. The size of the selenium particles was found to increase with sodium selenosulphate concentration. The effects of higher concentration of PVA and organic acids were not that pronounced. Nanonature of the synthesized selenium particles and increase in their crystallinity on heating were confirmed by both XRD and DSC experiments. Spherical selenium nanoparticles of size about 35–70 nm, as determined by AFM and TEM techniques, could be produced. The

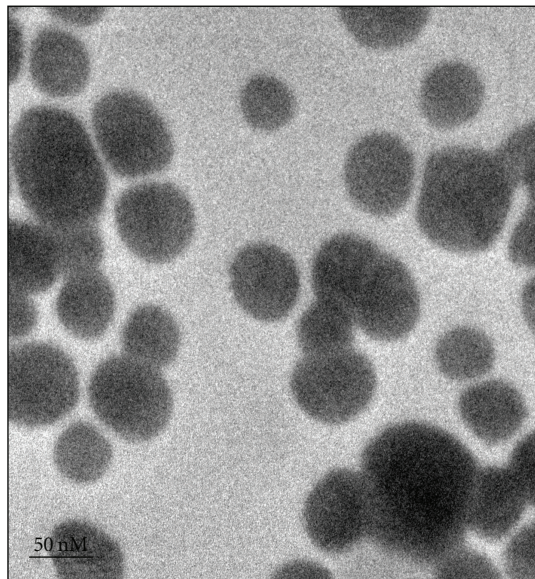


FIGURE 7: TEM images of the selenium nanoparticles, formed by the reaction of  $1.0 \times 10^{-3} \text{ mol dm}^{-3}$  sodium selenosulphate with  $2.0 \times 10^{-2} \text{ mol dm}^{-3}$  acetic acid, in the presence of 0.01% PVA.

selenium nanoparticles may serve as template, to generate other important nanomaterials, and find applications in fabrication of nanoscale optoelectronic devices.

### Acknowledgments

The author, C. Dwivedi, is grateful to Homi Bhabha National Institute, BRNS, and Department of Atomic Energy, for awarding research fellowship. The authors are thankful to Dr. P. A. Hassan, BARC, for AFM, Dr. S. C. Purandare and Mr. R. D. Bapat, TIFR, for TEM and EDAX, and Dr. L. Varshney, BARC, for DSC experiments. The authors also wish to acknowledge Dr. T. Mukherjee and Dr. S. K. Sarkar, for their encouragement during the course of the study.

### References

- [1] Y. Wang and N. Herron, "Nanometer-sized semiconductor clusters: materials synthesis, quantum size effects, and photo-physical properties," *Journal of Physical Chemistry*, vol. 95, no. 2, pp. 525–532, 1991.
- [2] M. Haase, H. Weller, and A. Henglein, "Photochemistry of colloidal semiconductors. 26. Photoelectron emission from CdS particles and related chemical effects," *Journal of Physical Chemistry*, vol. 92, no. 16, pp. 4706–4712, 1988.
- [3] R. Rossetti and L. E. Brus, "Picosecond resonance Raman scattering study of methylviologen reduction on the surface of photoexcited colloidal CdS crystallites," *Journal of Physical Chemistry*, vol. 90, no. 4, pp. 558–560, 1986.
- [4] S. Li, Y. Shen, A. Xie et al., "Rapid, room-temperature synthesis of amorphous selenium/protein composites using *Capsicum annuum* L extract," *Nanotechnology*, vol. 18, no. 40, Article ID 405101, 2007.
- [5] X. Cao, Y. Xie, S. Zhang, and F. Li, "Ultra-thin trigonal selenium nanoribbons developed from series-wound beads," *Advanced Materials*, vol. 16, no. 7, pp. 649–578, 2004.
- [6] P. Cherin and P. Unger, "The crystal structure of trigonal selenium," *Inorganic Chemistry*, vol. 6, no. 8, pp. 1589–1591, 1967.
- [7] P. Unger and P. Cherin, in *The Physics of Selenium and Tellurium*, W. C. Cooper, Ed., p. 223, Pergamon, Oxford, UK, 1969.
- [8] P. Cherin and P. Unger, "Refinement of crystal structure of  $\alpha$ -monoclinic Se," *Acta Crystallographica*, vol. 28, pp. 313–317, 1972.
- [9] H. Yin, Z. Xu, H. Bao, J. Bai, and Y. Zheng, "Single crystal trigonal selenium nanoplates converted from selenium nanoparticles," *Chemistry Letters*, vol. 34, no. 1, pp. 122–123, 2005.
- [10] J. Xu, F. Yang, L. Chen, Y. Hu, and Q. Hu, "Effect of selenium on increasing the antioxidant activity of tea leaves harvested during the early spring tea producing season," *Journal of Agricultural and Food Chemistry*, vol. 51, no. 4, pp. 1081–1084, 2003.
- [11] B. Zhang, X. Ye, W. Dai, W. Hou, F. Zuo, and Y. Xie, "Biomolecule-assisted synthesis of single-crystalline selenium nanowires and nanoribbons via a novel flake-cracking mechanism," *Nanotechnology*, vol. 17, no. 2, pp. 385–390, 2006.
- [12] P. Liu, Y. Ma, W. Cai et al., "Photoconductivity of single-crystalline selenium nanotubes," *Nanotechnology*, vol. 18, no. 20, Article ID 205704, 2007.
- [13] Q. Li and V. W. W. Yam, "High-yield synthesis of selenium nanowires in water at room temperature," *Chemical Communications*, no. 9, pp. 1006–1008, 2006.
- [14] Y. Zhu, Y. Qian, H. Huang, and M. Zhang, "Preparation of nanometer-size selenium powders of uniform particle size by  $\gamma$ -irradiation," *Materials Letters*, vol. 28, no. 1–3, pp. 119–122, 1996.
- [15] R. S. Oremland, M. J. Herbel, J. S. Blum et al., "Structural and Spectral Features of Selenium Nanospheres Produced by Se-Respiring Bacteria," *Applied and Environmental Microbiology*, vol. 70, no. 1, pp. 52–60, 2004.
- [16] B. Mishra, P. A. Hassan, K. I. Priyadarsini, and H. Mohan, "Reactions of biological oxidants with selenourea: formation of redox active nanoselenium," *Journal of Physical Chemistry B*, vol. 109, no. 26, pp. 12718–12723, 2005.
- [17] T. C. Franklin, W. K. Adeniyi, and R. Nnodimele, "Electro-oxidation of some insoluble inorganic sulfides, selenides, and tellurides in cationic surfactant-aqueous sodium hydroxide systems," *Journal of the Electrochemical Society*, vol. 137, no. 2, pp. 480–484, 1990.
- [18] C. P. Shah, M. Kumar, K. K. Pushpa, and P. N. Bajaj, "Acrylonitrile-induced synthesis of polyvinyl alcohol-stabilized selenium nanoparticles," *Crystal Growth and Design*, vol. 8, no. 11, pp. 4159–4164, 2008.
- [19] S. Gorer and G. Hodes, "Quantum size effects in the study of chemical solution deposition mechanisms of semiconductor films," *Journal of Physical Chemistry*, vol. 98, no. 20, pp. 5338–5346, 1994.
- [20] Z. H. Lin and C. R. C. Wang, "Evidence on the size-dependent absorption spectral evolution of selenium nanoparticles," *Materials Chemistry and Physics*, vol. 92, no. 2–3, pp. 591–594, 2005.

## Research Article

# Synthesis, Characterization and Catalytic Performance of $\text{H}_3\text{SiW}_{12}\text{O}_{40}/\text{SiO}_2$ Prepared by Sol-Gel Technique

W. N. R. W. Isahak,<sup>1,2</sup> M. Ismail,<sup>2</sup> N. M. Nordin,<sup>1</sup> J. M. Jahim,<sup>2</sup> and M. A. Yarmo<sup>1</sup>

<sup>1</sup>Department of Chemical and Process Engineering, Faculty of Engineering and Built Environment, Universiti Kebangsaan Malaysia, 43600 Bangi, Malaysia

<sup>2</sup>School of Chemical Sciences and Food Technology, Faculty of Science and Technology, Universiti Kebangsaan Malaysia, 43600 Bangi, Malaysia

Correspondence should be addressed to W. N. R. W. Isahak, wannorroslam@yahoo.com

Received 29 March 2011; Accepted 12 July 2011

Academic Editor: Mallikarjuna Nadagouda

Copyright © 2011 W. N. R. W. Isahak et al. This is an open access article distributed under the Creative Commons Attribution License, which permits unrestricted use, distribution, and reproduction in any medium, provided the original work is properly cited.

The purpose of this work is to study the synthesis, characterization, and catalytic performance of two types of solid heteropoly acid catalysts, namely, silicotungstic acid bulk (STAB) and STA-silica sol-gel (STA-SG) compared with sulfuric acid. From the XPS analyses, there was a significant formation of W-O-Si, W-O-W, and Si-O-Si bonding in STA-SG compared to that in STAB. The main spectra of O1s (90.74%, 531.5 eV) followed by other O1s peak (9.26%, 532.8 eV) were due to the presence of W-O-W and W-O-Si bonds, respectively. The STA-SG catalyst was found to be the more environmentally benign solid acid catalyst for the esterification reaction between oleic acid and glycerol due to its lower toxicity supported by silica via sol-gel technique. In addition, the ease of separation for STA-SG catalyst was attributed to its insoluble state in the product phase. The esterification products were then analysed by FTIR and HPLC. Both the  $\text{H}_2\text{SO}_4$  and the STAB gave high conversion of 100% and 98% but at a lower selectivity of GME with 81.6% and 89.9%, respectively. On the contrary, the STA-SG enabled a conversion of 94% but with a significantly higher GME selectivity of 95%, rendering it the more efficient solid acid catalyst.

## 1. Introduction

During the recent years, glycerol has been used as combustion materials around the world. The glycerol usage was expanded into many other high-quality products such as pharmaceutical, foods, and engine lubricant. To date, glycerol modification into glycerol monoester (GME) as lubrication materials that was based on the biosources was not really practised in the industry. The nature of the polar head group and the structure of the hydrocarbon tail of GME gave the strong impact as a friction reducer [1].

The GME is synthesized at present by acid catalyzed esterification of glycerol and fatty acids [2, 3]. Recently, list of studies involving alternative heterogeneous catalytic routes have been reported such as the glycerol esterification with lauric acid (LA) and oleic acid (OA) by using functionalized mesoporous materials [4], zeolitic molecular sieves [5, 6], and solid cationic resins [7, 8] as catalysts. In another work, the beta-zeolite catalyst gave the conversion of fatty acids

above 20% at optimum condition of glycerol:LA molar ratio of 1:1 at 100°C for 24 hours [9].

In this work, the usage and activities of the silicotungstic acid bulk (STAB) and the silicotungstic acid-silica sol-gel (STA-SG) have been studied. The STAB consists of two molecular structures, namely, Keggin and Dawson structures with four protons. The Dawson type STAB is formed by the combination of two Keggin molecules. The activity and stability of these catalysts depend on the structure and the type of the central atom along with the metal [10, 11]. The STAB is impregnated onto different supports such as polymers and silica [12] to achieve high surface area and stability in polar solvents.

## 2. Experimental

**2.1. Synthesis of the Catalyst.** The catalyst was prepared according to Izumi et al [13] methods with some modification. In this study, a mixture of water (2.0 mol), 1-butanol

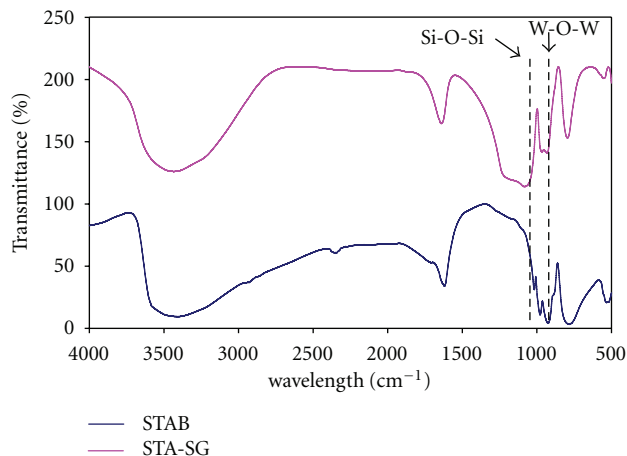


FIGURE 1: FTIR spectrum of STAB and STA-SG.

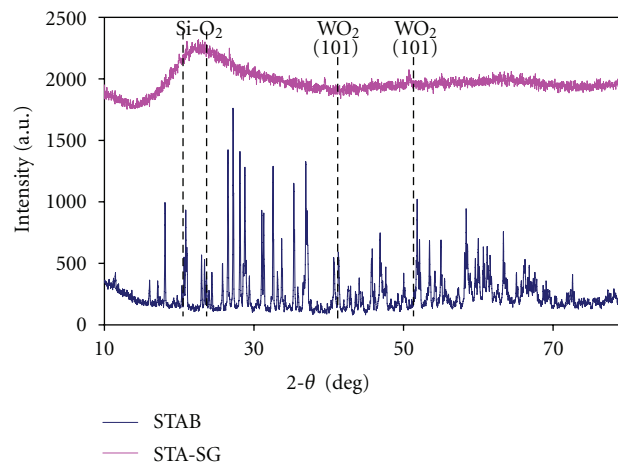


FIGURE 2: XRD diffractogram of STAB and STA-SG.

TABLE 1: BET surface area for STAB and STA-SG catalyst.

Type of catalyst	BET surface area (m <sup>2</sup> /g)
STAB	0.98
STA-SG	460.12

(0.2 mol), and heteropoly acid ( $5.0 \times 10^{-4}$  mol) was added to tetraethyl orthosilicate (0.2 mol) and stirred at 80°C for 3 hours. Then, the hydrogel obtained was dehydrated slowly at 80°C for 1.5 hours. The dried gel obtained was extracted in soxhlet apparatus with methanol as a solvent for 72 hours and dried for overnight. The heteropoly acid immobilised silica was dried at 100°C for 3 hours to use as catalytic materials and characterized by using BET, FTIR, TEM, and XPS methods.

**2.2. Characterization of the Catalyst.** The Brunauer, Emmett dan Teller (BET) analysis of the STAB and STA-SG catalysts was applied by using Micromeritics model ASAP 2010 and the physical nitrogen adsorption was done at liquid nitrogen temperature of 77 K. The XRD method was performed by using XRD's Bruker AXS D8 Advance type with x-ray radiation source of Cu K $\alpha$  (40 kV, 40 mA) to record the 2 $\theta$  diffraction angle from 10° to 60° at wavelength ( $\lambda = 0.154$  nm). TEM analysis was performed by using CM12 transmission electron microscope Philips type with electron gun at 200 kV. The X-ray photoelectron spectroscopy (XPS) measurement of the STAB and STA-SG catalysts were performed on XPS Axis Ultra from Kratos equipped with monochromatic Al K $\alpha$  radiation. The samples were analyzed at the analysis chamber pressure at about  $1 \times 10^{-10}$  Pa. The spectra referenced with respect to C1s line at 284.5 eV.

**2.3. Esterification Reaction.** The esterification process between purified glycerol (from the palm oil transesterification source) and oleic acid was carried out in the batch reactor with STAB and STA-SG as the catalysts. The reaction was performed at 100°C for 8 hours and connected to the pump system in order to remove water during the reaction.

The products were then separated from the unreacted reactants through centrifugation and analysed in the HPLC.

### 3. Results and Discussion

**3.1. Physical Surface Analysis (BET).** The analyses of BET showed that STAB has BET surface area of 0.98 m<sup>2</sup>/g while STA-SG of 460.11 m<sup>2</sup>/g as summarized in Table 1. The STA-SG catalyst gave a relatively higher surface area after sol-gel technique was applied. This could suggest that STA-SG has more active sites and high surface area towards higher activity and yield of GMO.

**3.2. FTIR Analysis.** The typical FTIR spectrum of STAB obtained at 1100 cm<sup>-1</sup> (Si-O-Si), 968 cm<sup>-1</sup> (W-O<sub>d</sub> terminal), 903 cm<sup>-1</sup> (W-O<sub>b</sub>-W edge shared) and 719 cm<sup>-1</sup> (W-O<sub>c</sub>-W) corner shared) corresponded to the primary structure [SiW<sub>12</sub>O<sub>40</sub>]<sup>-4</sup> of the catalyst [14] as can be seen in Figure 1. In the STA-SG catalyst, the Si-O-Si bond detected at 1100 cm<sup>-1</sup> was bigger and wider than STAB catalyst. It clearly demonstrated that Si-O-Si bend with higher composition in STA-SG affected Si and O from TEOS and that STAB was chemically bonded with each other.

**3.3. Catalysts Crystallinity by XRD.** From XRD analysis, STAB sample generated many peaks which clearly shown that the sample was formed as crystalline compound. However, STA-SG obtained by sol-gel technique gave the amorphous state due to the presence of the silica compounds. From Figure 2, there was a broader peak shown at 28° which was represented by the Si-O-Si bond as the main component in STA-SG catalyst. Subsequently, this would lead to a predicted analysis by XPS that there would be nearly 50% Si-O-Si bond in STA-SG catalyst.

**3.4. Surface Morphology by TEM.** From Figures 3(b) and 3(c), TEM analysis has shown the morphology of STA-SG catalyst. The STAB was assorted in the silica based on TEOS. The distribution of the catalyst in silica phase was depicted in Figure 3(b). The STA-SG catalyst was smaller in size in

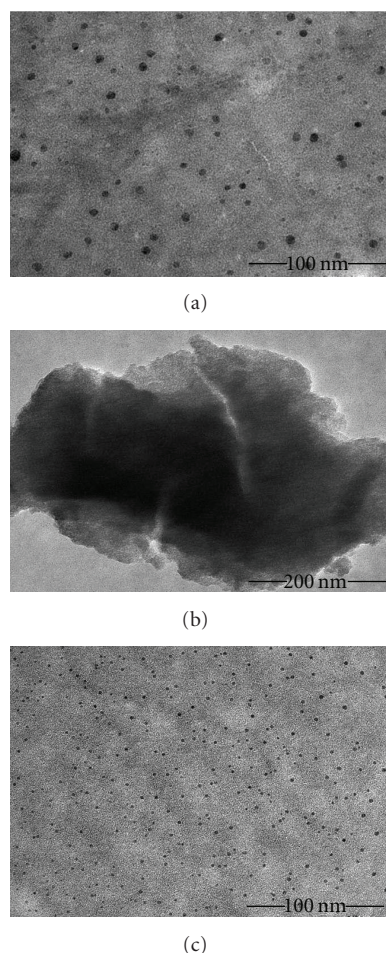


FIGURE 3: TEM micrograph for (a) STAB at 45KX, (b) STA-SG at 35KX, and (c) STA-SG at 45KX.

TABLE 2: Percentage of mass concentration (%) of C1s, O1s, Si2p and W4f elements from wide scan analyses for STAB and STA-SG catalysts.

Type of catalyst	C1s	O1s	Si 2p	W 4f
STAB	7.11	23.79	0.48	68.62
STA-SG	2.33	61.19	33.89	2.59

the range of 3.5–5.5 nm compared to STAB in the range of 17–20 nm.

From the analysis, it was noted that the equally shaped and smaller size of STA-SG particle was parallel to the BET characterization results that STA-SG has higher surface area compared to STAB. It was also affected by the additional of silica based on TEOS as sol gel technique.

**3.5. Surface Analysis by XPS.** The XPS investigation of binding energies (BE) and surface composition of silica supported STAB was investigated in detail. The XPS wide scan spectra of STAB and STA-SG was shown in Figure 4. The photoelectron peaks in the XPS spectra for STAB and STA-SG showed the presences of C1s, O1s, Si2p and W4f as expected. Percentages

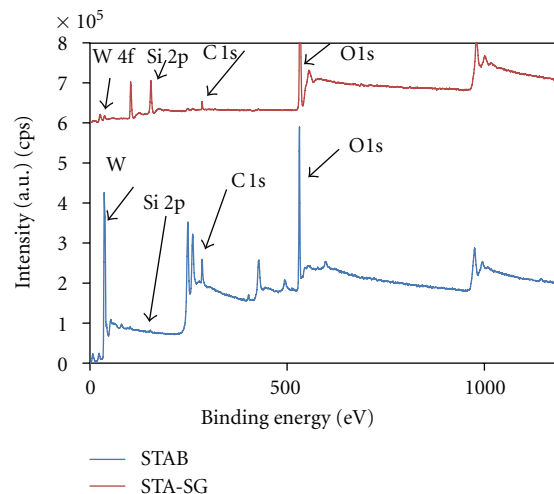


FIGURE 4: Wide scan for STAB and STA-SG.

of mass concentration for all the elements were summarized in Table 2.

From Figure 5(a), it was found that the bulk STA has Si2p binding energy at 102.5 and 103.3 eV, respectively. Meanwhile, the value of Si2p binding energy of STA-SG are 103.0, 103.7, and 104.5 eV (Figure 5(b)), indicating the formation of W-O-Si, Si-O-Si and  $\text{SiOH}_2^+$ , respectively. The Si2p-binding energy of 103.7 eV that represented of  $\text{SiO}_2$  was in agreement with the binding energy of silica found in the literature [15–18]. The O1s XPS narrow scan spectrum recorded from bulk STA was shown in Figure 6(a) and contained two distinct chemical states of O1s. This showed that the main (90.74%, 531.5 eV) and intermediate (9.26%, 532.8 eV) were the contributions of the presence of W-O-W and W-O-Si bonds, respectively [19].

The O1s spectra recorded from sample STA-SG (Figure 6(b)) was very different from the STAB (Figure 6(a)). The spectra consisted of the main signal at the 532.9 eV could be associated with Si-O-Si bond and a much weaker signals at the 532.1 and 533.7 eV, which might be represented by W-O-W and adsorbed water,  $\text{SiOH}_2^+$ . The W4f XPS spectra recorded from bulk STA (Figure 7(a)) composed of the spin-orbit doublet with binding energies for the  $W4f_{7/2}$  and  $W4f_{5/2}$  of 36.8 and 39.0 eV, respectively, with  $\Delta\text{BE} = 2.13$ . These values were typical of the presence of W (VI) [11]. The W4f spectra recorded from STA-SG is less well resolved than that of STAB (Figure 7(b)).

The W4f XPS also fitted on the basis of two different W contributions: a spin orbit doublet at 35.5 eV ( $W4f_{7/2}$  component) which accounted for bigger area of the total spectra and a second doublet at 37.7 eV ( $W4f_{5/2}$  component) accounting for the remaining area. The major component has a binding energy which was the same value as the STAB. The minor component appearing at the lower binding energy may represent the partial decomposition of STAB on the silica surface and the formation of an oxide of the type  $\text{WO}_x$  as  $\text{WO}_2$  in which W has an oxidation state lower than VI.

Based on other researchers finding [16, 19], we suggest that there are a few interactions between  $(\text{H}_3\text{SiW}_{12}\text{O}_{40})$ —

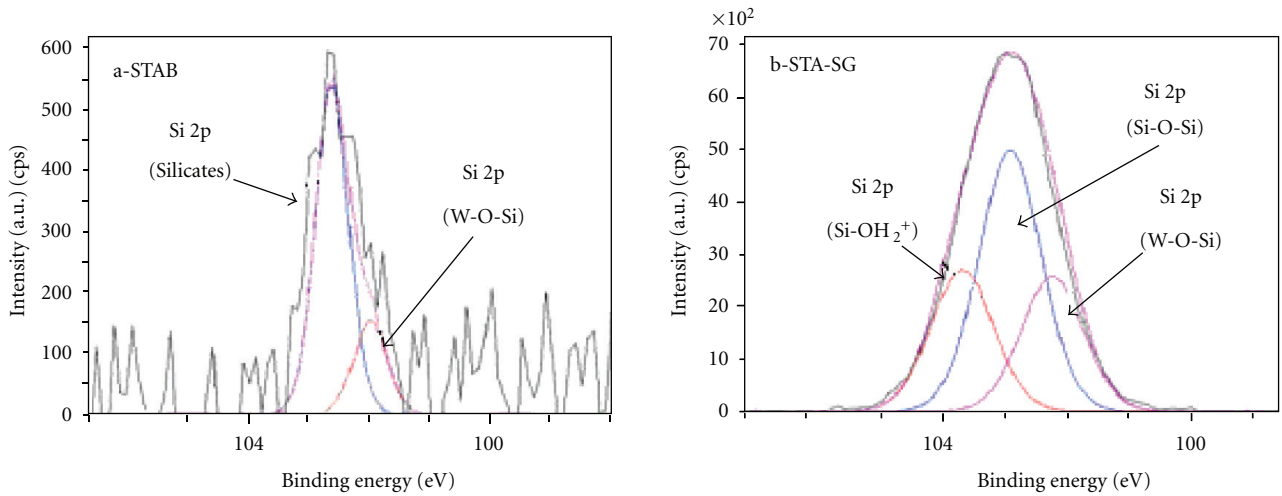


FIGURE 5: Narrow scan for Si2p (a) STAB and (b) STA-SG.

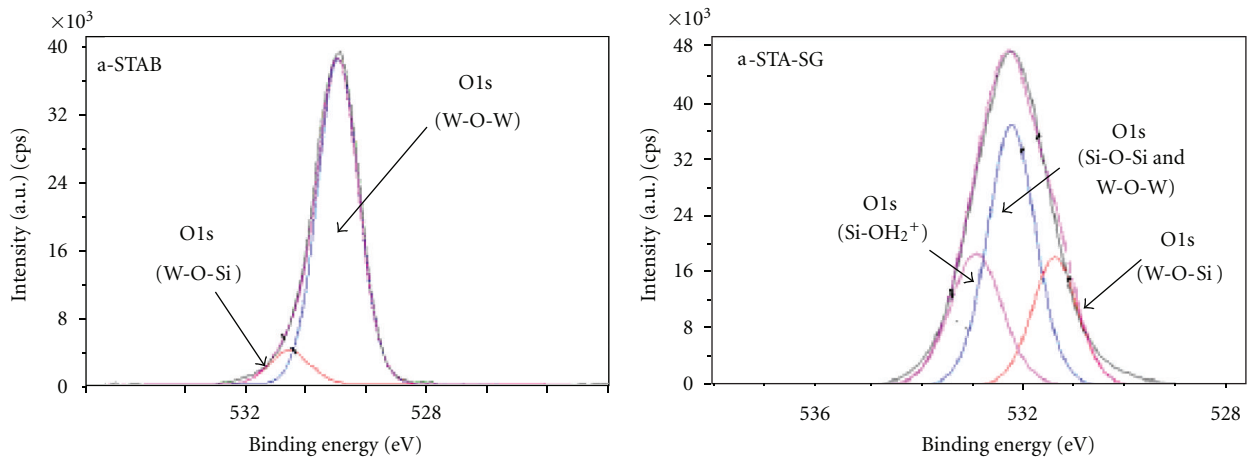


FIGURE 6: Narrow scan for O1s (a) STAB and (b) STA-SG.

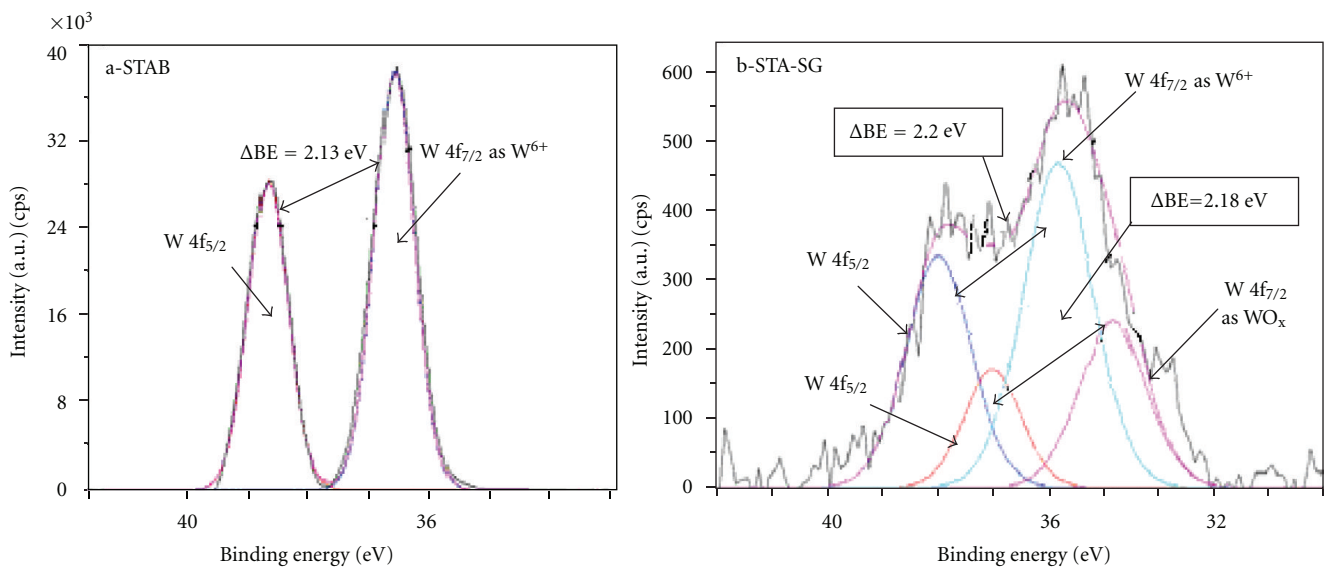


FIGURE 7: Narrow scan for W4f (a) STAB and (b) STA-SG.

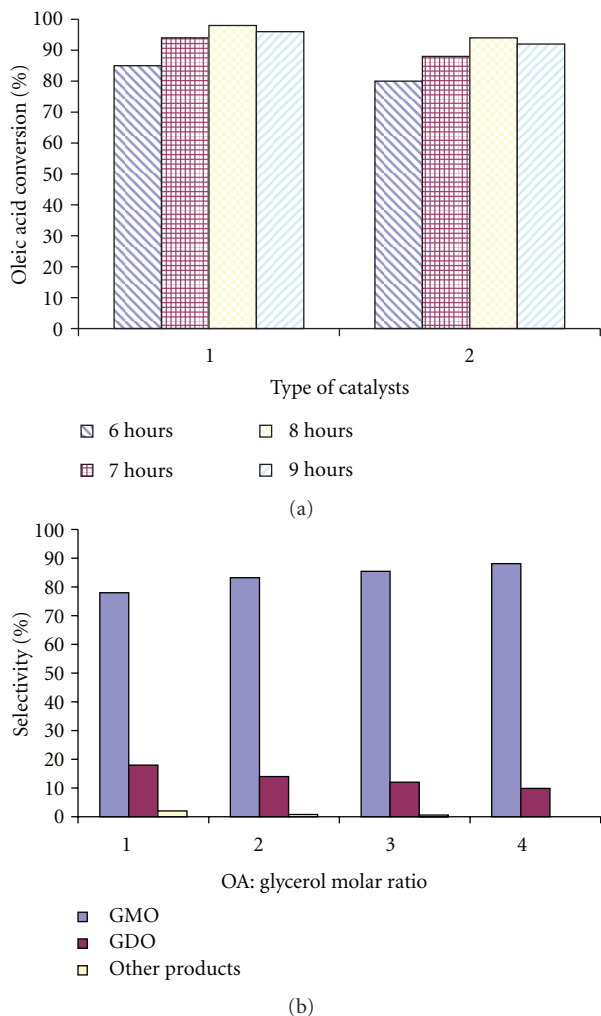


FIGURE 8: Catalytic activity in the esterification reaction (a) reaction time versus conversion for types of catalysts and (b) AO: glycerol molar ratio versus selectivity using STA-SG as the catalyst.

with the silanol groups at silica surface to give ion pairs in the form ( $\equiv\text{SiOH}_2^+$ ) ( $\text{H}_3\text{SiW}_{12}\text{O}_{40}$ ) from the reaction below:  $\equiv\text{Si-OH} + \text{H}_4\text{SiW}_{12}\text{O}_{40} \rightarrow [\equiv\text{Si-OH}_2]^+[\text{H}_3\text{SiW}_{12}\text{O}_{40}]^-$ .

**3.6. Esterification Reaction.** The activity of the catalysts was studied based on the three main parameters, namely, reaction time, OA: glycerol molar ratio, and type of catalysts. From Figure 8(a), STAB gave a higher conversion of oleic acid with 98% compared to STA-SG with 96% at 100°C and OA: glycerol molar ratio of 6:1 for 8 hours. At 9 hours of the reaction, it was shown that the conversion was reduced to about 1.5%. This indicated that the backward reaction occurred because of the catalysts inhibition. However, the STA-SG catalyst gave relatively higher selectivity of the glycerol monooleate (GMO) and glycerol dioleate (GDO), the byproduct, of 95% and 5%, respectively. It was typically higher than STAB that gave selectivity to GMO and GDO of 89.9% and 10.1%, respectively.

The reaction temperature of 100°C was chosen to study the other parameters on the basis that the higher temperature

would shift the reaction equilibrium to produce more side products such as GDO and acrolein but at a lower selectivity of GMO. However, the OA: glycerol molar ratio of 6:1 yielded higher selectivity of GMO of up to 95% at 100°C for 8 hours as depicted in Figure 8(b), hence the stronger parameter that promoted towards higher desired product. In other words, higher molar ratio of OA would increase the chances for higher GMO production, as the OA is three times easier to react with the glycerol compound.

## 4. Conclusion

The synthesized STA-SG catalyst that prepared by sol-gel technique has the good properties as well as catalytic materials. The  $\text{H}_2\text{SO}_4$  and STAB catalysts gave higher conversion of 100% and 98% compared to STA-SG of 96%. Even though there were no significant differences among the three catalysts in terms of the conversion capability, the STA-SG catalyst has an advantage of enabling a higher selectivity of GMO with 95% compared to 89.9% and 81.6% by using STAB and  $\text{H}_2\text{SO}_4$ , respectively. This indicated that the solid heteropoly acid type STA-SG has a better catalytic activity and higher number of active sites that contributed towards higher selectivity of the main product, namely, glycerol monooleate (GMO).

## Acknowledgments

The authors wish to thank Universiti Kebangsaan Malaysia (UKM) for funding this project under research Grant no. UKM-GUP-BTK-08-14-306 and Centre of Research and Innovation Management (CRIM).

## References

- [1] ATC Document 49. Lubricant Additives and the Environment, 2007.
- [2] A. Corma, S. Iborra, S. Miquel, and J. Primo, "Catalysts for the production of fine chemicals: production of food emulsifiers, monoglycerides, by glycerolysis of fats with solid base catalysts," *Journal of Catalysis*, vol. 173, no. 2, pp. 315–321, 1998.
- [3] N. O. V. Sonntag, "Glycerolysis of fats and methyl esters—status, review and critique," *Journal of the American Oil Chemists' Society*, vol. 59, no. 10, pp. 795a–802a, 1982.
- [4] W. D. Bossaert, D. E. de Vos, W. M. van Rhijn et al., "Mesoporous sulfonic acids as selective heterogeneous catalysts for the synthesis of monoglycerides," *Journal of Catalysis*, vol. 182, no. 1, pp. 156–164, 1999.
- [5] E. Heykants, W. H. Verrelst, R. F. Parton, and P. A. Jacobs, "Shape-selective zeolite catalysed synthesis of monoglycerides by esterification of fatty acids with glycerol," *Studies in Surface Science and Catalysis*, vol. 105, pp. 1277–1284, 1997.
- [6] Z. Chen, J. Zhong, Q. Li, Y. Li, and Z. Ou, *Science in China Series B*, vol. 32, p. 769, 1989.
- [7] S. Abro, Y. Pouilloux, and J. Barrault, *Comptes-Rendus de l'Académie des Sciences de Paris. Série II*, vol. 323, p. 493, 1996.
- [8] S. Abro, Y. Pouilloux, and J. Barrault, "Selective synthesis of monoglycerides from glycerol and oleic acid in the presence of solid catalysts," *Studies in Surface Science and Catalysis*, vol. 108, pp. 539–546, 1997.

- [9] M. D. S. Machado, J. Pérez-Pariente, E. Sastre, D. Cardoso, and A. M. de Guereñu, "Selective synthesis of glycerol monolaurate with zeolitic molecular sieves," *Applied Catalysis A*, vol. 203, no. 2, pp. 321–328, 2000.
- [10] N. Mizuno and M. Misono, "Heterogeneous catalysis," *Chemical Reviews*, vol. 98, no. 1, pp. 199–217, 1998.
- [11] G. Li, Y. Ding, J. Wang, X. Wang, and J. Suo, "New progress of Keggin and Wells-Dawson type polyoxometalates catalyze acid and oxidative reactions," *Journal of Molecular Catalysis A*, vol. 262, no. 1-2, pp. 67–76, 2007.
- [12] D. Varisli, T. Dogu, and G. Dogu, "Novel mesoporous nano-composite  $\text{WO}_x$ -silicate acidic catalysts: ethylene and diethyl-ether from ethanol," *Industrial and Engineering Chemistry Research*, vol. 48, no. 21, pp. 9394–9401, 2008.
- [13] Y. Izumi, K. Hisano, and T. Hida, "Acid catalysis of silica-included heteropolyacid in polar reaction media," *Applied Catalysis A*, vol. 181, no. 2, pp. 277–282, 1999.
- [14] M. Aparicio, Y. Castro, and A. Duran, "Synthesis and characterisation of proton conducting styrene-co-methacrylate-silica sol-gel membranes containing tungstophosphoric acid," *Solid State Ionics*, vol. 176, no. 3-4, pp. 333–340, 2005.
- [15] J. F. Moulder, P. E. Sobol, and K. D. Bomben, Eds., *Hand Book of X-Ray Photoelectron Spectroscopy (1992–1995)*, Physical Electronics Division.
- [16] A. D. Newman, D. R. Brown, P. Siril, A. F. Lee, and K. Wilson, "Structural studies of high dispersion  $\text{H}_3\text{SiW}_{12}\text{O}_{40}/\text{SiO}_2$  solid acid catalysts," *Physical Chemistry Chemical Physics*, vol. 8, no. 24, pp. 2893–2903, 2006.
- [17] F. J. Berry, G. R. Derrick, J. F. Marco, and M. Mortimer, "Silica-supported silicotungstic acid: a study by X-ray photoelectron spectroscopy," *Materials Chemistry and Physics*, vol. 114, no. 2-3, pp. 1000–1003, 2009.
- [18] T. Blasco, A. Corma, A. Martínez, and P. Martínez-Escolano, "Supported heteropolyacid (HPW) catalysts for the continuous alkylation of isobutane with 2-butene: the benefit of using MCM-41 with larger pore diameters," *Journal of Catalysis*, vol. 177, no. 2, pp. 306–313, 1998.
- [19] A. D. Newman, A. F. Lee, K. Wilson, and N. A. Young, "On the active site in  $\text{H}_3\text{SiW}_{12}\text{O}_{40}/\text{SiO}_2$  catalysts for fine chemical synthesis," *Catalysis Letters*, vol. 102, no. 1-2, pp. 45–50, 2005.

## Research Article

# Hydrothermal Synthesis of Ni/Al Layered Double Hydroxide Nanorods

Yun Zhao, Fenfei Xiao, and Qingze Jiao

School of Chemical Engineering and Environment, Beijing Institute of Technology, Beijing 100081, China

Correspondence should be addressed to Yun Zhao, zhaoyun@bit.edu.cn

Received 7 March 2011; Accepted 11 April 2011

Academic Editor: Mallikarjuna Nadagouda

Copyright © 2011 Yun Zhao et al. This is an open access article distributed under the Creative Commons Attribution License, which permits unrestricted use, distribution, and reproduction in any medium, provided the original work is properly cited.

Ni/Al layered double hydroxide (LDH) nanorods were successfully synthesized by the hydrothermal reaction. The crystal structure of the products was characterized by X-ray diffraction (XRD). The morphology of the products was observed using transmission electron microscopy (TEM) and field emission scanning electron microscopy (SEM). The influences of reaction time and pH value on the morphology of the Ni/Al LDHs were investigated. The result showed that the well-crystallized nanorods of Ni/Al LDHs could be obtained when the pH value was about 10.0 with a long reaction time (12–18 h) at 180°C.

## 1. Introduction

Layered double hydroxides (LDHs) or LDH-type compounds belong to a large class of anionic clays. They can be represented by the general formula  $[M(II)_{1-x}M(III)_x \cdot (OH)_2]^{x+} [A^{n-}]_{x/n} mH_2O$  [1], where M(II) is a divalent metal cation, such as Mg, Mn, Ni, Zn, and Cu; M(III) is a trivalent metal cation, such as Al, Fe, Co, and Cr;  $[A^{n-}]$  is an exchangeable anion, such as  $F^-$ ,  $Cl^-$ ,  $NO_3^-$ ,  $CO_3^{2-}$ ,  $SO_4^{2-}$ , and  $PO_4^{3-}$  [2, 3]. The value of  $x$  is between 0.2 and 0.34 generally. LDHs are a layered structure with positively charged brucite-like sheets, where M(II) and M(III) are octahedrally coordinated. The excess charge is balanced by anions in the interlayer, together with water molecules. Recently, LDHs have attracted much attention because of their unique applications in many fields. For example, they can be used as catalysts, catalyst supports, ion exchangers, adsorbents, and pigments and also be used in sensor and magnetic technologies [1, 4, 5]. Scotter and Ken B, prepared Ni/Al, Mg/Al, Co/Al, Cu/Al LDHs and used them as the catalysts of the steam reforming of methanol to produce hydrogen [6]. Alexandre et al. used Cu/Ni/Al LDHs as precursors of catalysts for the wet air oxidation of phenol aqueous solutions [7]. Most of these advanced functions depend strongly on the composition, size, and morphology. So nanostructures of LDHs will be of particular interest for the applications.

In the last decade, 1-D nanostructures have been paid more attention due to their unique physical and chemical properties and their potential applications in science and engineering. The successful synthesis of nanotubes such as BN,  $WS_2$ , and  $MoS_2$  has been reported [8]. Many hydroxide and oxide nanorods or nanotubes have also been prepared [9–15]. However, there is little report relating to LDH nanorods. A variety of Ni-based LDHs such as Ni/Al, Ni/Co, Ni/Fe, and Ni/Mn have been studied as cathode materials and catalysts [16, 17]. If Ni/Al LDHs were fabricated in the form of a one-dimensional (1-D) nanostructure, they would hold promise as highly functionalized materials.

In this paper, Ni/Al LDH nanorods were successfully synthesized by hydrothermal reaction. In particular, the effect factors on the morphology of the LDHs were investigated such as reaction time and pH value.

## 2. Experimental

A series of Ni/Al LDHs with nominal  $Ni^{2+}/Al^{3+}$  atomic ratio of 3/1 were prepared by hydrothermal reaction at 180°C. All of them were prepared as follows: appropriate amounts of  $NiSO_4 \cdot 6H_2O$  and  $Al_2(SO_4)_3 \cdot 18H_2O$  ( $Ni^{2+}/Al^{3+} = 3/1$  (molar ratio)) were dissolved in deionized water (40 mL). Then aqueous solution of ammonium hydroxide was added to the above solution drop by drop with vigorous stirring to adjust

TABLE 1: Chemical formulas and interlayer distances of Ni/Al LDH prepared at different pH values.

pH value	Interlayer distances (nm)	Ni/Al (molar ratio)	Composition of LDHs
5.5	1.0589	1.71	$[\text{Ni}_{0.63}\text{Al}_{0.37}(\text{OH})_2](\text{SO}_4^{2-})_{0.19} \cdot 0.88\text{H}_2\text{O}$
8.5	0.8401	2.86	$[\text{Ni}_{0.74}\text{Al}_{0.26}(\text{OH})_2](\text{SO}_4^{2-})_{0.13}(\text{CO}_3^{2-})_{0.04} \cdot 0.72\text{H}_2\text{O}$
10.0	0.8708	2.96	$[\text{Ni}_{0.75}\text{Al}_{0.25}(\text{OH})_2](\text{SO}_4^{2-})_{0.16}(\text{CO}_3^{2-})_{0.03} \cdot 0.84\text{H}_2\text{O}$

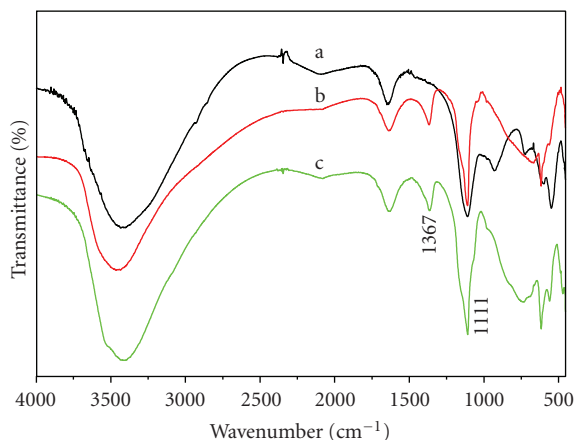


FIGURE 1: IR spectra of Ni/Al LDHs prepared at different pH values a: 5.5; b: 8.5; c: 10.0.

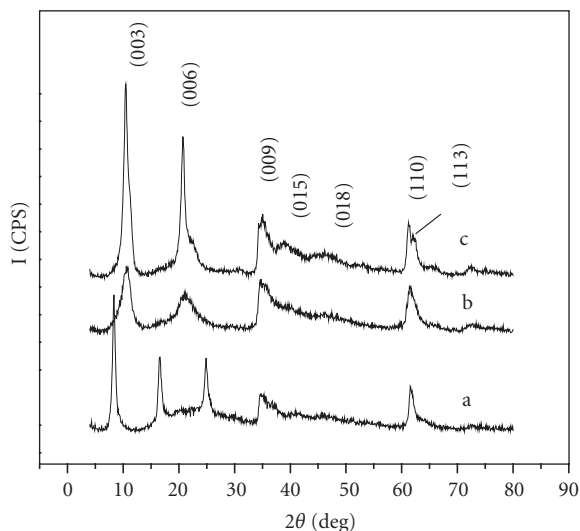


FIGURE 2: XRD powder patterns of the products prepared at different pH values a: 5.5, b: 8.5, c: 10.0.

the pH value of the solution. After that, the suspension was transferred into a 50 mL stainless Teflon-lined autoclave and heated at 180°C for appropriate time, then cooled to room temperature naturally. The resulting products were filtrated and washed several times with distilled water and absolute ethanol. The apple-green solid was then collected and dried at room temperature for 12 h.

XRD powder analysis was carried out with a Rigaku D/max-RB12KW X-ray diffractometer using Cu  $K_{\alpha 1}$  radiation ( $\lambda = 1.5418 \text{ \AA}$ ) in the  $2\theta$  range of 4–80° at room temperature.

The TEM micrographs were recorded on a Hitachi H-800 instrument. The SEM images were taken on a Hitachi S4800 field emission scanning electron microscopy. Metals and S analysis was performed on a Perkin-Elmer Optima 3300DV inductively coupled plasma-atomic emission spectrometer instrument. Microanalysis (% C, H, N) data were collected using a LECO CHN-900 analyzer. IR spectra were recorded on a Bruker Vector 22 spectrometer using KBr pellets.

### 3. Results and Discussion

**3.1. Influence of pH Value on the Structure and the Morphology of LDHs.** Chemical formulas for LDHs prepared at different pH are given in Table 1 based on the metals, S analysis, and microanalysis (% C, H, and N) data. A Ni/Al ratio of  $\sim 3$  for Ni/Al LDHs obtained at pH of 8.5 and 10.0 is consistent with the Ni/Al ratio used in the starting solutions. The Ni/Al ratio of 1.7, however, suggests the incomplete precipitation of  $\text{Ni}^{2+}$  ions at pH of 5.5. The elemental analyses indicated that the LDH samples prepared at pH of 8.5 and 10.0 contain both sulfate and carbonate anions within the interlayer, however, sulfate anions are the dominant interlayer anion. It can also be confirmed by IR spectrum (Figure 1). The band at  $1111 \text{ cm}^{-1}$  can be attributed to  $\nu_3$  vibration of  $\text{SO}_4^{2-}$ , and the band at  $1367 \text{ cm}^{-1}$  can be assigned to  $\nu_3$  vibration of  $\text{CO}_3^{2-}$ . The introduction of carbonate can be attributed to the  $\text{CO}_2$  in aqueous solution of ammonium hydroxide in the process of preparing LDHs. LDHs prepared at  $\text{pH} = 5.5$  contain only sulfate anions in the interlayer due to using the smallest amount of aqueous solution of ammonium hydroxide.

The powder XRD patterns for the Ni/Al LDHs prepared at different pH value are shown in Figure 2. All the XRD patterns exhibit the characteristic reflections of a LDHs material. They show two groups of very close (003), (006), and (009) reflections for LDHs prepared at pH of 8.5 and 10.0 due to containing both sulfate and carbonate anions within the interlayer. No impurity can be detected in the XRD analysis. Therefore pure Ni/Al LDHs must have been obtained at pH of 5.5, 8.5, and 10.0. The lower diffraction intensity for LDHs obtained at pH of 8.5 is observed. This indicates their lower crystallinity. The diffraction peaks of LDHs synthesized at pH of 10.0 are narrow and sharp, which suggest that Ni-Al LDHs prepared at  $\text{pH} = 10.0$  are well crystallized. Comparing the positions of 003 and 006 reflections of samples prepared at different pH value, we can see that they shift obviously toward lower  $2\theta$  angle with the decrease of pH value. This indicates that when the pH values decreases to 5.5, the distance from the center of one layer to the next for Ni/Al LDHs increases (see Table 1), which is related to the actual Ni/Al molar ratio of the LDHs samples.

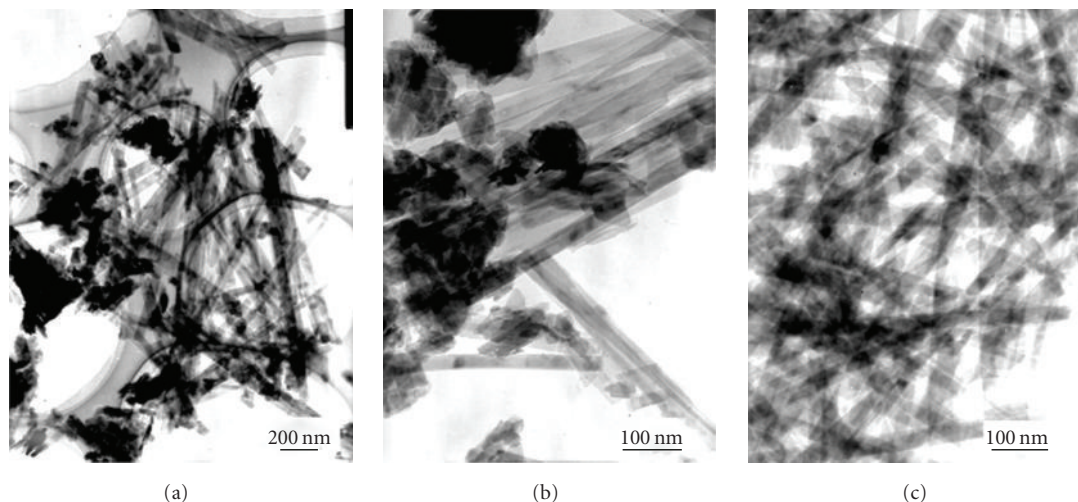


FIGURE 3: TEM images for Ni/Al LDHs synthesized at different pH values. (a) 5.5; (b) 8.5; (c) 10.0.

TABLE 2: Chemical formulas of Ni/Al LDH prepared at different reaction times.

Reaction times (h)	Ni/Al (molar ratio)	Composition of LDHs
2	2.57	$[\text{Ni}_{0.72}\text{Al}_{0.28}(\text{OH})_2](\text{SO}_4^{2-})_{0.13}(\text{CO}_3^{2-})_{0.05} \cdot 0.93\text{H}_2\text{O}$
6	2.70	$[\text{Ni}_{0.73}\text{Al}_{0.27}(\text{OH})_2](\text{SO}_4^{2-})_{0.12}(\text{CO}_3^{2-})_{0.09} \cdot 0.86\text{H}_2\text{O}$
12	2.96	$[\text{Ni}_{0.75}\text{Al}_{0.25}(\text{OH})_2](\text{SO}_4^{2-})_{0.16}(\text{CO}_3^{2-})_{0.03} \cdot 0.84\text{H}_2\text{O}$
18	2.93	$[\text{Ni}_{0.75}\text{Al}_{0.25}(\text{OH})_2](\text{SO}_4^{2-})_{0.16}(\text{CO}_3^{2-})_{0.10} \cdot 0.98\text{H}_2\text{O}$

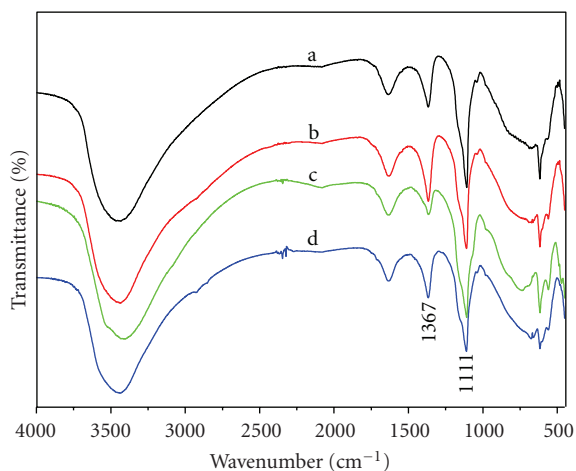


FIGURE 4: IR spectra of Ni/Al LDHs prepared with different reaction times a: 2 h; b: 6 h; c: 12 h; d: 18 h.

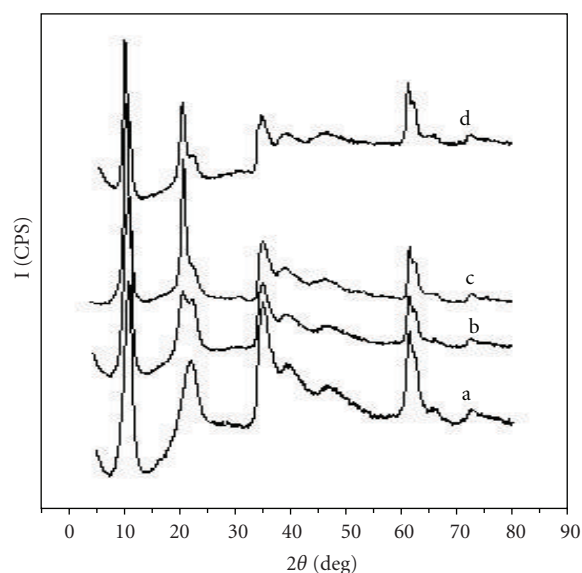


FIGURE 5: XRD patterns of the products prepared at different reaction times a: 2 h; b: 6 h; c: 12 h; d: 18 h.

As shown in Table 1, the real Ni/Al molar ratio of the LDHs samples decreases with decreasing pH value.

The morphologies of the as-prepared Ni/Al LDHs were examined with transmission electron microscopy (TEM). In Figure 3, the effect of pH value on the morphology of LDHs is demonstrated. It can be seen that nanoparticles and nanorods coexist in Ni/Al LDHs obtained at pH of 5.5 and 8.5. However, only nanorods were formed when the pH value was increased to 10.0. They are 20–40 nm in diameter and 600–1000 nm in length.

It is clear that the pH of 10.0 is suitable for the formation of well crystallized Ni/Al LDH nanorods. So the influence of reaction time on the structure and morphology of Ni/Al LDHs was investigated at pH of 10.0.

3.2. Influence of Reaction Time on the Structure and the Morphology of LDHs. Chemical formulas for LDHs prepared

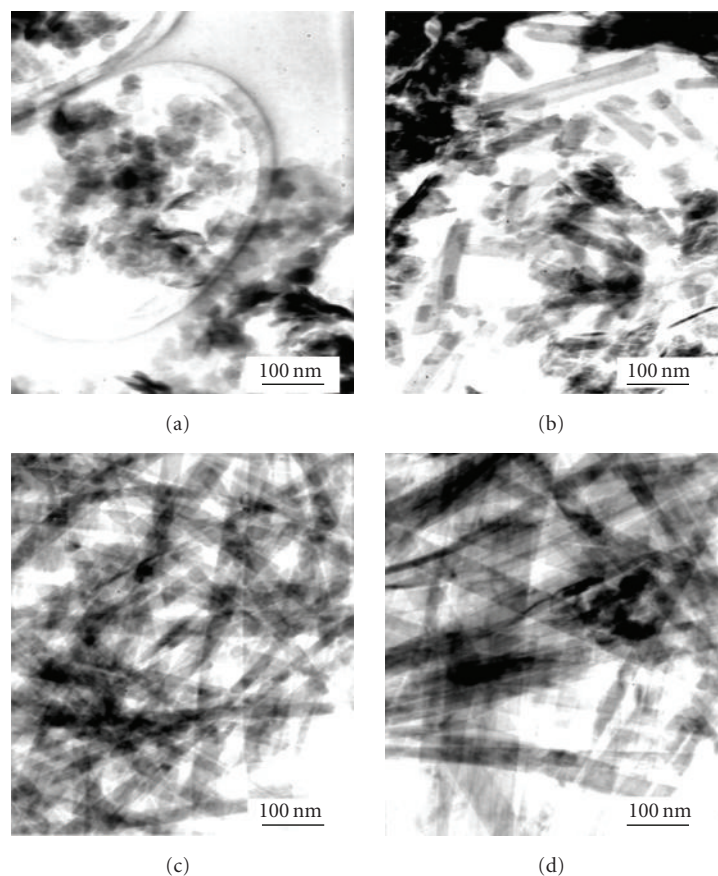


FIGURE 6: TEM images for Ni/Al LDHs with different reaction times, (a) 2 h; (b) 6 h; (c) 12 h; (d) 18 h.

at different times are given in Table 2 based on the metals, S analysis and microanalysis (% C, H, N) data. The elemental analyses, and IR spectrum (Figure 4) yield evidence of the formation of carbonate and sulfate-containing LDHs at different times: 2, 6, 12, and 18 h.

The powder XRD patterns for Ni/Al LDHs synthesized at 180°C for different reaction times (2, 6, 12 and 18 h) are shown in Figure 5. In each case, the XRD patterns exhibit the characteristic reflections of an LDHs material with a basal peak. They also show two groups of very close (003), (006), and (009) reflections for LDHs prepared at different times due to containing both sulfate and carbonate anions within the interlayer. The intensity of the LDH diffraction peaks increases with increasing the reaction time, indicating that, as expected, the crystallinity of the crystallites increase with increasing the reaction time.

From Figure 6, it can be found that the reaction time has a large effect on the morphology of Ni/Al LDHs. When the reaction time was lower than 2 h, only nanoparticles with the size of 15–40 nm were obtained. If the reaction time was up to 6 h, short nanorods were formed and the length was about 50–300 nm. With the increase of the reaction time, nanorods with a high aspect ratio were observed. As can be seen from Figure 4(c), nanorods of Ni/Al LDHs with reaction time of 12 h were 20–40 nm in diameter and 600–1000 nm in length. When the time was prolonged to 18 h, the nanorods

increased in length and width. They had a diameter of 30–70 nm and a length of 1–3  $\mu\text{m}$ .

Ni/Al LDHs prepared for 12 h and 18 h were also observed using SEM. As shown in Figure 7, a large amount of Ni/Al LDHs nanorods with much higher aspect ratios were obtained. It confirmed that Ni/Al LDHs nanorods were successfully prepared by hydrothermal reaction at 180°C and pH of 10.0 for a longer reaction time (12–18h).

On the basis of the reports [8, 10, 14], many 1-D nanostructures (nanotubes or nanorods) have been successfully synthesized from layered structures, the so-called 2-D structures such as  $\text{Ni}(\text{OH})_2$  and  $\text{Mg}(\text{OH})_2$ . Ni/Al LDHs are layered compounds, therefore, we may suppose that the formation of Ni/Al LDHs nanorods might be related to the nature of its lamellar 2-D structures. However the structure of Ni/Al LDHs is different from  $\text{Ni}(\text{OH})_2$  and  $\text{Mg}(\text{OH})_2$  with simple layered structures. The structure of Ni/Al layered double hydroxides (LDHs) can be described as containing brucite ( $\text{Mg}(\text{OH})_2$ )-like layers in which some of the divalent cations ( $\text{Ni}^{2+}$ ) have been replaced by trivalent ions ( $\text{Al}^{3+}$ ) giving positively charged sheets. This charge is balanced by intercalation of  $\text{CO}_3^{2-}$  or  $\text{SO}_4^{2-}$  anions in the hydrated interlayer regions. It is obvious that Ni/Al LDHs possess complicated layered structure.

Based on the report [18], highly symmetrical materials, which have hexagonal layered structures, can be grown

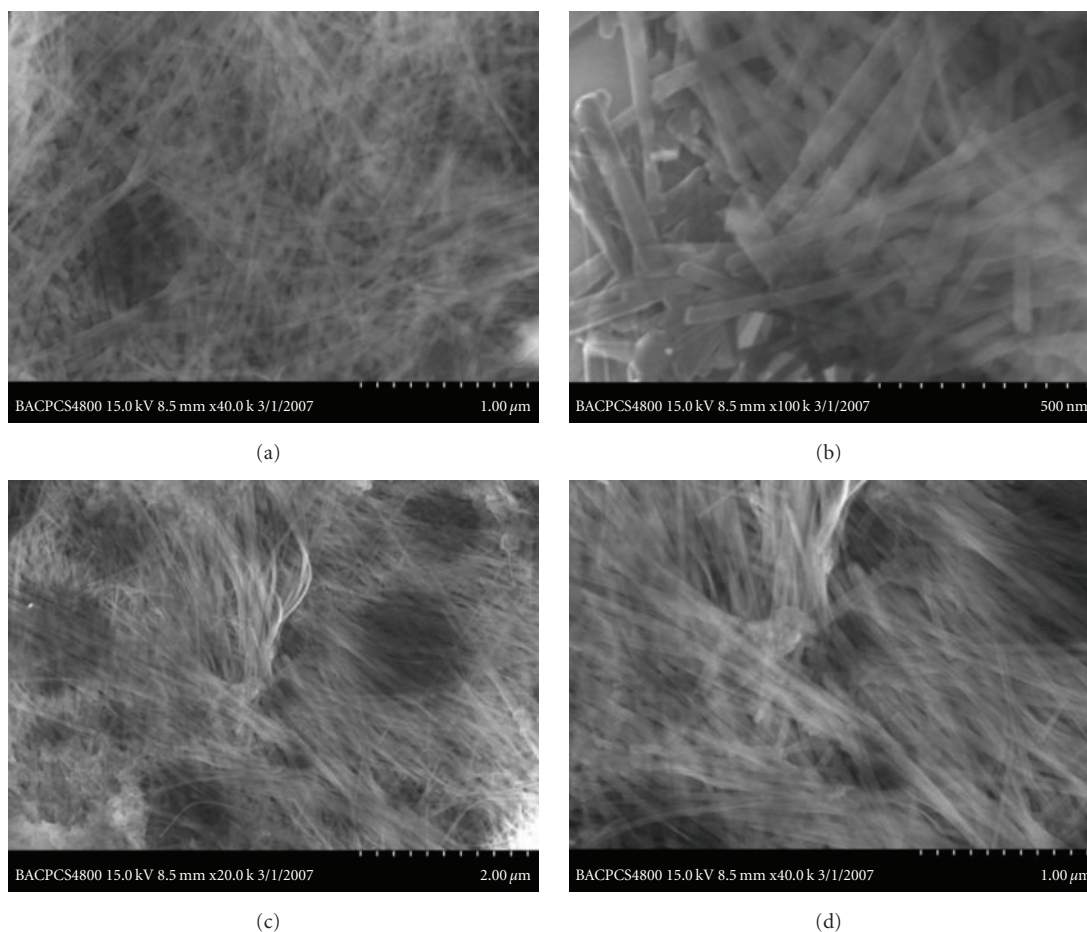


FIGURE 7: SEM images for Ni/Al LDHs with different reaction times. (a, b) 12 h; (c, d) 18 h.

into low-symmetrical crystallites such as one-dimensional nanorods. LDHs, whose basic layered unit possesses hexagonal symmetry, represent a group of highly symmetrical materials that show peculiar one-dimensional growth anisotropy. Under the present hydrothermal condition, the nucleation of LDHs would occur and there was an intrinsic tendency to grow into rod-like nanoparticles due to its antistropic hexagonal structure. So, formed LDH nanorods are stable geometrical morphologies in the surface chemistry context, because with this shape LDHs have a low system energy [15, 18]. The TEM images with different reaction times showed that the growth of Ni/Al LDH nanorods is forming nanoparticles first, then growing to short nanorods, and finally to long nanorods.

#### 4. Conclusions

In summary, nanoparticles and nanorods of Ni/Al LDHs with size and morphological controls have been synthesized by hydrothermal reaction. The effect factors such as pH value and reaction time on the morphology of the LDHs were investigated. Ni/Al LDH nanorods were successfully prepared by hydrothermal reaction at 180°C and pH of 10.0 for 12 h–18 h. Ni/Al LDH nanorods with reaction time of 12 h had a

diameter of 20–40 nm and a length of 600–1000 nm. When the time prolonged to 18 h, longer and wider nanorods were obtained with a diameter of 30–70 nm and a length of 1–3 μm. The successful growth of nanorods will provide a promising route to low-dimensional nanostructures of other LDHs.

#### Acknowledgment

This work was supported by Beijing Municipal Natural Science Foundation (Grant no. 2092026).

#### References

- [1] F. Cavani, F. Trifirò, and A. Vaccari, "Hydrotalcite-type anionic clays: preparation, properties and applications," *Catalysis Today*, vol. 11, no. 2, pp. 173–301, 1991.
- [2] S. Miyata, "Physico-chemical properties of synthetic hydrotalcites in relation to composition," *Clays and Clay Minerals*, vol. 28, no. 1, pp. 50–56, 1980.
- [3] A. Ookubo, K. Ooi, and H. Hayashi, "Preparation and phosphate ion-exchange properties of a hydrotalcite-like compound," *Langmuir*, vol. 9, no. 5, pp. 1418–1422, 1993.
- [4] S. Miyata, "Properties and adsorption characteristics of hydrotalcites," *Gypsum & Lime*, vol. 187, p. 333, 1983.

- [5] W. T. Reichle, "Anionic clay minerals," *Chemtech*, vol. 16, pp. 58–63, 1986.
- [6] R. Scotter and S. Ken B, "Low temperature steam reforming of methanol over layered double hydroxide-derived catalysts," *Applied Catalysis A*, vol. 231, no. 1-2, pp. 215–226, 2002.
- [7] A. Alejandre, F. Medina, X. Rodriguez, P. Salagre, Y. Cesteros, and J. E. Sueiras, "Cu/Ni/Al layered double hydroxides as precursors of catalysts for the wet air oxidation of phenol aqueous solutions," *Applied Catalysis B*, vol. 30, no. 1-2, pp. 195–207, 2001.
- [8] R. Tenne, "Fullerene-like materials and nanotubes from inorganic compounds with a layered (2-D) structure," *Colloids and Surfaces A*, vol. 208, no. 1–3, pp. 83–92, 2002.
- [9] A. W. Xu, L. P. Fang, and H. Q. Liu, "A simple method to synthesize  $\text{Dy}(\text{OH})_3$  and  $\text{Dy}_2\text{O}_3$  nanotubes," *Journal of the American Chemical Society*, vol. 125, no. 6, pp. 1494–1495, 2003.
- [10] J. Liang and Y. Li, "Synthesis and characterization of  $\text{Ni}(\text{OH})_2$  single-crystal nanorods," *Chemistry Letters*, vol. 32, no. 12, p. 1126, 2003.
- [11] B. Cheng and E. T. Samulski, "Hydrothermal synthesis of one-dimensional ZnO nanostructures with different aspect ratios," *Chemical Communications*, vol. 10, no. 8, pp. 986–987, 2004.
- [12] M. Cao, C. Hu, Y. Wang, Y. Guo, C. Guo, and E. Wang, "A controllable synthetic route to Cu, CuO, and CuO nanotubes and nanorods," *Chemical Communications*, vol. 9, no. 15, pp. 1884–1885, 2003.
- [13] F. S. Cai, G. Y. Zhang, J. Chen, X. L. Gou, H. K. Liu, and S. X. Dou, " $\text{Ni}(\text{OH})_2$  tubes with mesoscale dimensions as positive-electrode materials of alkaline rechargeable batteries," *Angewandte Chemie International Edition*, vol. 43, no. 32, pp. 4212–4216, 2004.
- [14] L. Yan, J. Zhuang, X. Sun, Z. Deng, and Y. Li, "Formation of rod-like  $\text{Mg}(\text{OH})_2$  nanocrystallites under hydrothermal conditions and the conversion to MgO nanorods by thermal dehydration," *Materials Chemistry and Physics*, vol. 76, no. 2, pp. 119–122, 2002.
- [15] X. L. Li, J. F. Liu, and Y. D. Li, "Low-temperature conversion synthesis of  $\text{M}(\text{OH})_2$  (M=Ni, Co, Fe) nanoflakes and nanorods," *Materials Chemistry and Physics*, vol. 80, no. 1, pp. 222–227, 2003.
- [16] R. S. Jayashree and P. Vishnu Kamath, "Layered double hydroxides of Ni with Cr and Mn as candidate electrode materials for alkaline secondary cells," *Journal of Power Sources*, vol. 107, no. 1, pp. 120–124, 2002.
- [17] Y. Zhao, Q. Z. Jiao, J. I. Liang, and C. H. Li, "Synthesis of Ni/Mg/Al layered double hydroxides and their use as catalyst precursors in the preparation of carbon nanotubes," *Chemical Research in Chinese Universities*, vol. 21, no. 4, pp. 471–475, 2005.
- [18] J. T. Sampanthar and H. C. Zeng, "Arresting butterfly-like intermediate nanocrystals of  $\beta\text{-Co}(\text{OH})_2$  via ethylenediamine-mediated synthesis," *Journal of the American Chemical Society*, vol. 124, no. 23, pp. 6668–6675, 2002.

## Research Article

# Optical, X-Ray Diffraction, and Magnetic Properties of the Cobalt-Substituted Nickel Chromium Ferrites ( $\text{CrCo}_x\text{Ni}_{1-x}\text{FeO}_4$ , $x = 0, 0.2, 0.4, 0.6, 0.8, 1.0$ ) Synthesized Using Sol-Gel Autocombustion Method

Sonal Singhal,<sup>1</sup> Santosh Bhukal,<sup>1</sup> Jagdish Singh,<sup>2</sup> Kailash Chandra,<sup>2</sup> and S. Bansal<sup>3</sup>

<sup>1</sup>Department of Chemistry, Panjab University, Chandigarh 160 014, India

<sup>2</sup>Institute Instrumentation Centre, IIT Roorkee, Roorkee 247 667, India

<sup>3</sup>School of Physics and Materials Science, Thapar University, Patiala 147004, India

Correspondence should be addressed to Sonal Singhal, sonal1174@gmail.com

Received 9 March 2011; Accepted 28 March 2011

Academic Editor: Mallikarjuna Nadagouda

Copyright © 2011 Sonal Singhal et al. This is an open access article distributed under the Creative Commons Attribution License, which permits unrestricted use, distribution, and reproduction in any medium, provided the original work is properly cited.

Cobalt-substituted nickel chromium ferrites ( $\text{CrCo}_x\text{Ni}_{1-x}\text{FeO}_4$ ,  $x = 0, 0.2, 0.4, 0.6, 0.8, 1.0$ ) have been synthesized using sol-gel autocombustion method and annealed at 400 °C, 600 °C, 800 °C, and 1000 °C. All the ferrite samples have been characterized using UV-VIS spectrophotometry, FT-IR spectroscopy, Transmission Electron Microscopy, powder X-Ray Diffraction, and magnetic measurements. Typical FT-IR spectra of the samples annealed at 400 °C, 600 °C, 800 °C, and 1000 °C exhibit two frequency bands in the range of  $\sim 480\text{ cm}^{-1}$  and  $\sim 590\text{ cm}^{-1}$  corresponding to the formation of octahedral and tetrahedral clusters of metal oxide, respectively. TEM images reveal that crystallite size increases from  $\sim 10\text{ nm}$  to  $\sim 45\text{ nm}$  as the annealing temperature is increased from 400 °C to 1000 °C. The unit cell parameter “a” is found to increase on increasing the cobalt concentration due to larger ionic radius of cobalt. Also, as the cobalt concentration increases, the saturation magnetization increases from 4.32 to 19.85 emu/g. This is due to the fact that cobalt ion replaces the less magnetic nickel ions. However, the coercivity decreases with increase in cobalt concentration due to the decrease in anisotropy field. The band gap has been calculated using UV-VIS spectrophotometry and has been found to decrease with the increase of particle size.

## 1. Introduction

Magnetic nanoferrite particles have generated diverse technological interests because of their potential applications in magnetic fluids, high frequency magnets, magnetic bulk cores, microwave absorbers, and high-density data storage [1, 2]. Among the various ferrites, nickel ferrites and cobalt ferrites have been extensively used in electronic devices because of their large permeability at high frequency, remarkably high electrical resistivity, mechanical hardness, chemical stability, and cost-effectiveness [3, 4]. Substituted nickel ferrites are widely used as magnetic materials due to their high electrical resistivity, low eddy current, and dielectric losses [5, 6].

The magnetic properties of materials are strongly affected when the particle size approaches a critical diameter, below

which each particle is a single domain. As a result the influence of thermal energy over the magnetic moment ordering leads to super paramagnetic relaxation [7, 8]. Cobalt and nickel, both the ferrites, belong to the category of inverse spinel ferrites. Therefore, by substituting the  $\text{Co}^{2+}$ ,  $\text{Ni}^{2+}$ , and/or  $\text{Fe}^{3+}$  ions by suitable cations, their structures undergo a change from inverse spinel to mixed spinel, leading to a corresponding change in the magnetic properties. Thus, by the choice of the cations as well as their distribution in tetrahedral and octahedral sites of the lattice, interesting and useful magnetic properties can be obtained [9].

The effect of substitution of  $\text{Fe}^{3+}$  by  $\text{Cr}^{3+}$  in  $\text{NiFe}_2\text{O}_4$  has been studied by various workers [10–12], and it has been reported that  $\text{Cr}^{3+}$  always seeks to the octahedral sites. Lee et al. [10] suggested that  $\text{Ni}^{2+}$  moves to tetrahedral site within the range  $0.2 < x < 0.6$  and the magnetic moment and Curie

temperature decrease with the chromium substitution. Fayek and Ata Allah [11] reported that  $\text{Cr}^{3+}$  occupies the octahedral sites for a maximum of  $x = 0.6$  and the excess  $\text{Cr}^{3+}$  replaces the  $\text{Fe}^{3+}$  at the tetrahedral site. Gismelseed and Yousif [12] studied the  $\text{Cr}^{3+}$  substituted  $\text{NiCr}_x\text{Fe}_{1-x}\text{O}_4$  ( $0 < x < 1.4$ ) prepared through conventional double sintering ceramic technique and suggested that as the  $\text{Cr}^{3+}$  substitution increases, the system is slowly converted into a normal spinel structure.

Chae et al. [13] reported the magnetic properties of chromium substituted cobalt ferrites prepared using sol-gel method and suggested that the coercivity decreases fast but saturation magnetization decreases slowly with the chromium content. Gabal and Al Angari [14] reported the effect of chromium ion substitution on the electromagnetic properties of nickel ferrite and observed that coercivity increases, whereas the saturation magnetization decreases linearly with the Cr content. They also reported that the Neel's magnetic moments calculated from expected cation distribution are in confirmation with those obtained from the hysteresis loops for ferrites up to  $x = 0.8$ .

The present work deals with the synthesis of nanoparticles of cobalt-substituted nickel chromium ferrites ( $\text{CrCo}_x\text{Ni}_{1-x}\text{FeO}_4$ , where  $x = 0, 0.2, 0.4, 0.6, 0.8$  &  $1.0$ ) via sol-gel autocombustion method and investigation of their optical, X-ray diffraction, and magnetic properties by means of FT-IR, UV-Vis spectrophotometry, Powder X-ray diffraction, and magnetic measurements.

## 2. Experimental

**2.1. Preparation of  $\text{CrCo}_x\text{Ni}_{1-x}\text{FeO}_4$  Nanoparticles.** Nanoparticles of  $\text{CrCo}_x\text{Ni}_{1-x}\text{FeO}_4$  ( $x = 0, 0.2, 0.4, 0.6, 0.8$  &  $1.0$ ) have been synthesized by sol-gel autocombustion method [15–17]. AR Grade  $\text{Fe}(\text{NO}_3)_3 \cdot 9\text{H}_2\text{O}$ ,  $\text{Co}(\text{NO}_3)_2 \cdot 6\text{H}_2\text{O}$ ,  $\text{Cr}(\text{NO}_3)_3 \cdot 9\text{H}_2\text{O}$ ,  $\text{Ni}(\text{NO}_3)_2 \cdot 6\text{H}_2\text{O}$  and citric acid have been used for the synthesis of these ferrites. The nitrates and citric acid were weighed in desired stoichiometric proportions and dissolved separately in minimum amount of distilled water. The individual solutions were then mixed together and the pH value of the solution was adjusted to about 6 by adding 1 M  $\text{NH}_4\text{OH}$  solution. The solution was then slowly heated and stirred using a hot plate magnetic stirrer till gels were formed, which were ignited and burnt in a self-propagating combustion manner to obtain loose powder. The powders were annealed at  $400^\circ\text{C}$ ,  $600^\circ\text{C}$ ,  $800^\circ\text{C}$ , and  $1000^\circ\text{C}$  in a muffle furnace for 2 hours.

**2.2. Physical Measurements.** Fourier Transform infrared (FT-IR) spectra have been recorded using Perkin Elmer RX-1 FT-IR spectrophotometer with KBr pellets in the range  $4000\text{--}400\text{ cm}^{-1}$ . Powder X-ray diffraction studies have been carried out using a Bruker AXS, D8 Advance spectrophotometer with  $\text{Cu-K}\alpha$  radiation. Hitachi (H-7500) TEM, operated at 120 kV was used to record the micrographs of the samples. The magnetic properties have been measured at room temperature by a vibrating sample magnetometer (VSM) (155, PAR) up to a magnetic field of  $\pm 10\text{ kOe}$ . UV-Visible spectrum was recorded using a Hitachi 330 UV-VIS-NIR spectrophotometer.

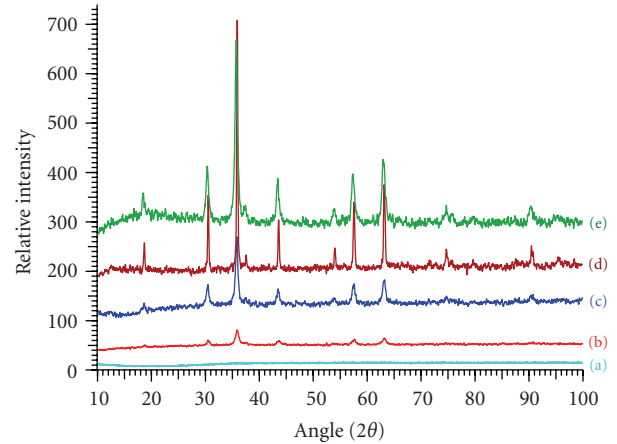


FIGURE 1: X-ray diffraction patterns of  $\text{CrCo}_{0.6}\text{Ni}_{0.4}\text{FeO}_4$  (a) as obtained and annealed at (b)  $400^\circ\text{C}$ , (c)  $600^\circ\text{C}$ , (d)  $800^\circ\text{C}$ , and (e)  $1000^\circ\text{C}$ .

## 3. Results and Discussion

**3.1. FT-IR Characterization.** The FT-IR spectra for all the samples annealed at  $400^\circ\text{C}$ ,  $600^\circ\text{C}$ ,  $800^\circ\text{C}$ , and  $1000^\circ\text{C}$  exhibit two main absorption bands below  $1000\text{ cm}^{-1}$ , corresponding to the vibrational modes of the metal oxides of ferrites. The band in the range of  $\sim 590\text{ cm}^{-1}$  is attributed to the stretching mode of the tetrahedral clusters, whereas that in the range of  $\sim 470\text{ cm}^{-1}$  is attributed to the stretching mode of the octahedral clusters [18, 19]. The vibrational mode of the tetrahedral cluster is higher than that of octahedral mode due to shorter edge length of the tetrahedral clusters.

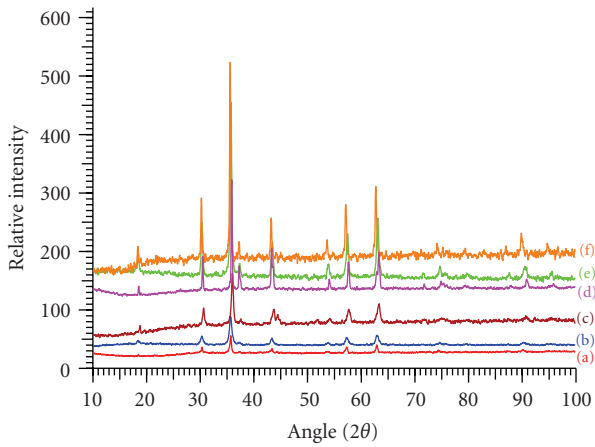
**3.2. TEM Characterization.** The TEM micrographs of all the samples exhibit highly agglomerated particles because of the interfacial surface tension as reported in our earlier studies [20–22]. As the annealing temperature increases from  $400^\circ\text{C}$  to  $1000^\circ\text{C}$ , the particle size increases from  $\sim 10\text{ nm}$  to  $\sim 45\text{ nm}$ . Such an increase in grain size has also been reported earlier [23, 24]. It is widely believed that the net decrease in the solid-solid and solid-vapour interface free energy provides the driving force for grain growth during annealing process.

**3.3. X-Ray Diffraction Studies.** The typical X-ray diffraction patterns of the as-obtained  $\text{CrCo}_{0.6}\text{Ni}_{0.4}\text{FeO}_4$  and those annealed at  $400^\circ\text{C}$ ,  $600^\circ\text{C}$ ,  $800^\circ\text{C}$ , and  $1000^\circ\text{C}$  for 2 hours are shown in Figure 1. The absence of any peak in the X-ray diffractograph of the as-obtained sample indicates the amorphous nature of the samples. However, the annealed samples exhibit characteristic diffraction peaks of the ferrite. The broad peaks at  $400^\circ\text{C}$  signify lower crystallite size of the synthesized sample and as the annealing temperature is increased, the peaks become sharp due to increase in the grain size.

The average crystallite size for all the samples has been calculated from the line broadening of the most intense peak corresponding to (3 1 1) plane of the spinel structure using the classical Scherrer equation [25]. It is observed that the particle size increases as the annealing temperature is raised

TABLE 1: Lattice parameters, saturation magnetization, coercivity, and energy band gap of the ferrites after annealing at 1000°C.

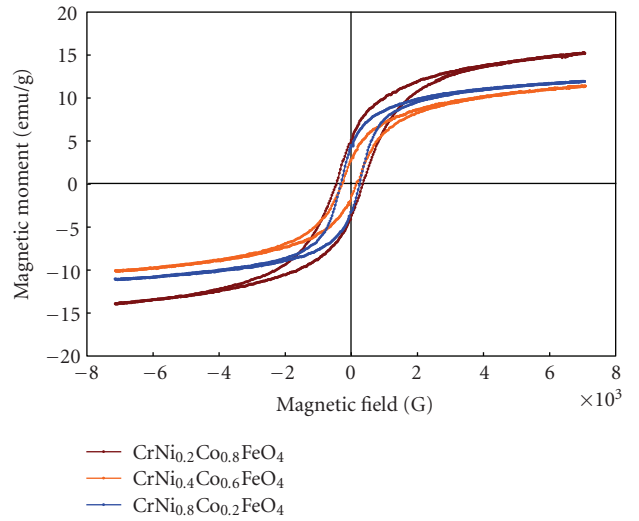
Ferrites composition	Lattice parameter, $a$ (Å)	Volume (Å <sup>3</sup> )	Saturation magnetization, $M_s$ (emu/g)	Coercivity $H_c$ (Oe)	Energy band gap, $E_g$ (eV)
CrNiFeO <sub>4</sub>	8.2974	571.24	4.32	1500	2.30
CrNi <sub>0.8</sub> Co <sub>0.2</sub> FeO <sub>4</sub>	8.3026	572.32	9.75	290	2.27
CrNi <sub>0.6</sub> Co <sub>0.4</sub> FeO <sub>4</sub>	8.3143	574.75	14.86	240	2.73
CrNi <sub>0.4</sub> Co <sub>0.6</sub> FeO <sub>4</sub>	8.3321	578.45	17.70	190	2.82
CrNi <sub>0.2</sub> Co <sub>0.8</sub> FeO <sub>4</sub>	8.3567	583.59	19.85	130	2.62
CrCoFeO <sub>4</sub>	8.3736	587.13	13.28	38	2.50

FIGURE 2: X-ray diffraction patterns of (a) CrNi<sub>0.2</sub>Co<sub>0.8</sub>FeO<sub>4</sub>, (b) CrNi<sub>0.4</sub>Co<sub>0.6</sub>FeO<sub>4</sub>, (c) CrNi<sub>0.6</sub>Co<sub>0.4</sub>FeO<sub>4</sub>, (d) CrNi<sub>0.8</sub>Co<sub>0.2</sub>FeO<sub>4</sub>, (e) CrNiFeO<sub>4</sub>, and (f) CrCrFeO<sub>4</sub> annealed at 1000°C.

from 400°C to 1000°C, which is also confirmed by the TEM studies.

Typical X-ray diffraction patterns for all the ferrites annealed at 1000°C for 2 hours are shown in Figure 2. All the samples have been found to be face centred cubic (fcc) with Fd-3m space group. The lattice parameters, calculated using Powley as well as Le-Bail refinement methods (built in TOPAS V2.1 of BRUKER AXS), are listed in Table 1. The lattice parameter “ $a$ ” has been found to increase with cobalt concentration; this may be due to smaller ionic radius of nickel.

**3.4. Magnetic Measurements.** Hysteresis loops for all the samples annealed at 600°C and 1000°C are shown in Figures 3 and 4, respectively. It is observed that the saturation magnetization ( $M_s$ ) increases with the annealing temperature due to increase in particle size [26]. From Table 1, it can be seen that the saturation magnetization,  $M_s$ , increases from 4.32 emu/g to 19.85 emu/g on increasing the cobalt concentration from 0 to 0.8. This increase can be understood because of the less magnetic behavior of nickel. However,

FIGURE 3: B-H loops of some typical CrCo <sub>$x$</sub> Ni<sub>1- $x$</sub> FeO<sub>4</sub> ferrites annealed at 600°C.

the saturation magnetisation decreases to 13.28 emu/g, with further increase of cobalt concentration to  $x = 1.0$ .

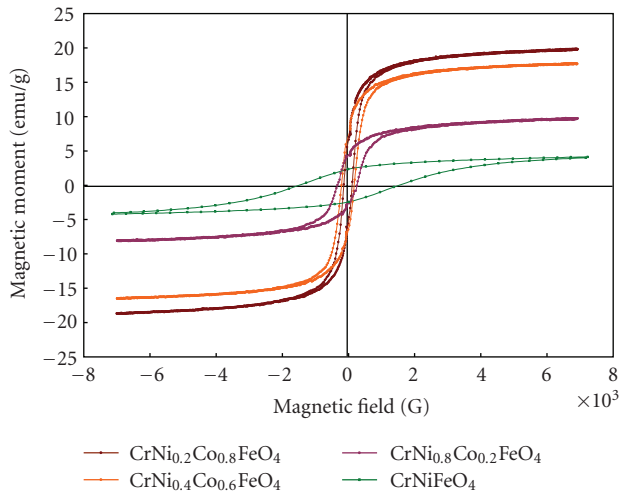
This behaviour can be explained on the basis of the super exchange interaction mechanism. In a cubic system of ferromagnetic spinels, the magnetic order is mainly due to super exchange interactions occurring between the metal ions in the  $A$  and  $B$  sublattices. Therefore, it is possible to vary magnetic properties of the samples by varying the cations. According to Neel’s two sublattice model of ferrimagnetism, the magnetic moment per formula unit (in  $\mu_B$ ),  $n_B^N(x)$  is expressed as [27]

$$n_B^N(x) = M_B(x) - M_A(x), \quad (1)$$

where  $M_B$  and  $M_A$  are the  $B$ - and  $A$ -sublattice magnetic moments in  $\mu_B$ , respectively. Cation distribution of the ferrites has been estimated using this model and is listed in Table 1, which suggests that cobalt and chromium ions predominantly occupy the octahedral sites, which is consistent with their preference for large octahedral site energy. This causes an increase in the saturation magnetization of the substituted ferrites up to  $x = 0.8$ . However, in the case

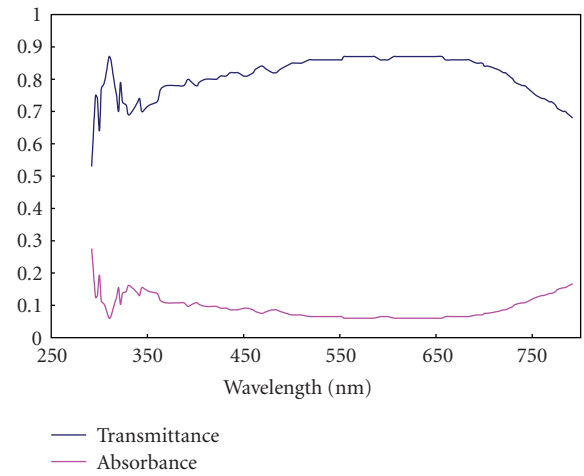
TABLE 2: Cation distribution for  $\text{CrCo}_x\text{Ni}_{1-x}\text{FeO}_4$  annealed at  $1000^\circ\text{C}$ .

Ferrites Composition	Observed magnetic moment, ( $n_B$ )	Cation distribution	Calculated magnetic moment
$\text{CrNiFeO}_4$	0.18	$(\text{Fe}_{0.8}\text{Cr}_{0.2})^A[\text{NiCr}_{0.8}\text{Fe}_{0.2}]^B\text{O}_4$	0.20
$\text{CrNi}_{0.8}\text{Co}_{0.2}\text{FeO}_4$	0.40	$(\text{Fe}_{0.95}\text{Co}_{0.05})^A[\text{CrNi}_{0.8}\text{Co}_{0.15}\text{Fe}_{0.05}]^B\text{O}_4$	0.40
$\text{CrNi}_{0.6}\text{Co}_{0.4}\text{FeO}_4$	0.62	$(\text{Fe}_{0.95}\text{Co}_{0.05})^A[\text{CrNi}_{0.6}\text{Co}_{0.35}\text{Fe}_{0.05}]^B\text{O}_4$	0.60
$\text{CrNi}_{0.4}\text{Co}_{0.6}\text{FeO}_4$	0.73	$(\text{Fe}_{0.97}\text{Co}_{0.03})^A[\text{CrNi}_{0.4}\text{Co}_{0.57}\text{Fe}_{0.03}]^B\text{O}_4$	0.72
$\text{CrNi}_{0.2}\text{Co}_{0.8}\text{FeO}_4$	0.82	$(\text{Fe}_{0.99}\text{Co}_{0.01})^A[\text{CrNi}_{0.2}\text{Co}_{0.79}\text{Fe}_{0.01}]^B\text{O}_4$	0.84
$\text{CrCoFeO}_4$	0.58	$(\text{Fe})^A[\text{CoCr}]^B\text{O}_4$	1.00

FIGURE 4: B-H loops of some typical  $\text{CrCo}_x\text{Ni}_{1-x}\text{FeO}_4$  ferrites annealed at  $1000^\circ\text{C}$ .

of  $\text{CoCrFeO}_4$  saturation magnetization decreases because all the iron enters in to the  $A$  site. This may be due to the fact that the exchange interaction between  $A$  and  $B$  sites gets lowered resulting in strengthening of  $B$ - $B$  interaction and weakening of  $A$ - $B$  interaction, which leads to decrease of saturation magnetization. Therefore in  $\text{CoCrFeO}_4$  Neel's magnetic moments calculated from expected cation distribution in comparison with that from the hysteresis loop do not give the satisfactory result.

The variation of the coercivity with average grain size has also been studied. It is observed that as the grain size increases, the value of coercivity ( $H_c$ ), reaches a maximum value and then decreases. This variation of  $H_c$  with grain size can be explained on the basis of domain structure, critical diameter, and the anisotropy of the crystal [28, 29]. From Table 1, it is clear that the coercivity decreases with the decrease of nickel concentration. This may be attributed to the decrease in anisotropy field, which in turn decreases the domain wall energy [30, 31]. In the case of  $\text{CrNiFeO}_4$ ,

FIGURE 5: Plot of absorbance and transmittance as a function of wavelength  $\lambda$  (nm) for  $\text{CrCo}_{0.6}\text{Ni}_{0.4}\text{FeO}_4$  annealed at  $1000^\circ\text{C}$ .

the coercivity value is very high 1500 G. This behaviour in coercivity may be understood as described by the Banerjee and O'Reilly [32] on the basis of a new model for cation distribution. This may be due to the fact that the chromium ions enter into the tetrahedral site when  $x > 0.8$ . According to the cation distribution model [32] when  $\text{Cr}^{3+}$  ions occupy tetrahedral sites, they cause a negative trigonal field to be superimposed on the octahedral  $\text{Cr}^{3+}$  ions. Due to this a twofold degeneracy of the orbital ground state results in an unquenched orbital angular momentum and a large anisotropy.

**3.5. Optical Studies.** The energy band gaps of all the ferrites have been calculated with the help of optical absorption and percentage transmission data. The absorption and transmission spectra of  $\text{CrCo}_{0.6}\text{Ni}_{0.4}\text{FeO}_4$  annealed at  $1000^\circ\text{C}$  are shown in Figure 5. The absorption coefficient,  $\alpha$  of the nanoparticles has been calculated using the fundamental

relationships [33]

$$I = I_0 e^{-\alpha t},$$

$$A = \log \left( \frac{I_0}{I} \right), \quad \alpha = 2.303 (A/t), \quad (2)$$

where  $A$  is the absorbance and  $t$  is the thickness of the sample. To estimate the energy band gap for all the samples, the graph of  $(\alpha h\nu)^2$  versus  $h\nu$  has been plotted. The intercept of the line at  $\alpha = 0$  gives the value of energy band gap. The values of energy band gap for all the samples annealed at 1000°C has been found to be in the range of 2.3–2.8 eV listed in Table 1. It is observed that as the particle size decreases, the energy band gap increases. This may be explained on the basis of Bras' effective mass model [34, 35] according to which the measured band gap,  $E_g$  can be expressed as a function of particle size as

$$E_g^* \cong E_g^{\text{bulk}} + \frac{\hbar^2 \pi^2}{2er^2} \left( \frac{1}{m_e} + \frac{1}{m_h} \right) - \frac{1.8e^2}{4\pi\epsilon\epsilon_0 r}, \quad (3)$$

where  $E_g^{\text{bulk}}$  is the bulk energy gap,  $r$  is the particle size,  $m_e$  is the effective mass of electrons,  $m_h$  is the effective mass of holes,  $\epsilon$  is the relative permittivity,  $\epsilon_0$  is the permittivity of free space,  $\hbar$  is the planck's constant divided by  $2\pi$ , and  $e$  is the charge on electron.

#### 4. Conclusion

$\text{CrCo}_x\text{Ni}_{1-x}\text{FeO}_4$ ,  $x = 0, 0.2, 0.4, 0.6, 0.8$  &  $1.0$  have been synthesized using the sol-gel autocombustion method. The formation of the ferrite powders has been confirmed by FT-IR and XRD studies. The TEM studies confirm that as the annealing temperature increases particle size increases up to 45 nm. The values of saturation magnetization increases and coercivity decreases with increasing  $\text{Co}^{3+}$  content. The values of energy band gap have been found to range ~2.5 eV. However, the band gap increases up to ~3.0 eV with the decrease of the particle size from ~45 nm to ~10 nm.

#### References

- [1] Y. Qi, Y. Yang, X. Zhao et al., "Controllable magnetic properties of cobalt ferrite particles derived from layered double hydroxide precursors," *Particuology*, vol. 8, pp. 207–211, 2010.
- [2] Y. Cedeño-Mattei and O. Perales-Pérez, "Synthesis of high-coercivity cobalt ferrite nanocrystals," *Microelectronics Journal*, vol. 40, no. 4-5, pp. 673–676, 2009.
- [3] J. Smit and H. P. J. Wijn, *Ferrites*, Philips Technical Library, Eindhoven, The Netherlands, 1959.
- [4] K. Ishino and Y. Narumiya, "Development of magnetic ferrites: control and application of losses," *American Ceramic Society Bulletin*, vol. 66, no. 10, pp. 1469–1474, 1987.
- [5] P. I. Slick, in *Ferromagnetic Materials*, E. P. Wohlfarth, Ed., vol. 2, p. 196, North-Holland, Amsterdam, The Netherlands, 1980.
- [6] T. Abraham, "Economics of ceramic magnets," *American Ceramic Society Bulletin*, vol. 73, no. 8, pp. 62–65, 1994.
- [7] D. Fiorani, in *Magnetic Properties of Fine Particles*, J. L. Dormann and D. Fiorani, Eds., North-Holland Delta Series, Elsevier, London, UK, 1992.
- [8] D. K. Kim, Y. Zhang, W. Voit, K. V. Rao, and M. Muhammed, "Synthesis and characterization of surfactant-coated superparamagnetic monodispersed iron oxide nanoparticles," *Journal of Magnetism and Magnetic Materials*, vol. 225, no. 1-2, pp. 30–36, 2001.
- [9] J. Smit and H. P. J. Wijn, *Ferrites*, John Wiley & Sons, London, UK, 1959.
- [10] S. H. Lee, S. J. Yoon, G. J. Lee et al., "Electrical and magnetic properties of  $\text{NiCr}_x\text{Fe}_{2-x}\text{O}_4$  spinel ( $0 \leq x \leq 0.6$ )," *Materials Chemistry and Physics*, vol. 61, p. 147, 1999.
- [11] M. K. Fayek and S. S. Ata-Allah, "Fe Mössbauer and electrical studies of the (NiO)-(CrO)-(FeO) system," *Physica Status Solidi (A)*, vol. 198, no. 2, pp. 457–464, 2003.
- [12] A. M. Gismelseed and A. A. Yousif, "Mössbauer study of chromium-substituted nickel ferrites," *Physica B: Condensed Matter*, vol. 370, no. 1–4, pp. 215–222, 2005.
- [13] K. P. Chae, Y. B. Lee, J. G. Lee, and S. H. Lee, "Crystallographic and magnetic properties of  $\text{CoCr}_x\text{Fe}_{2-x}\text{O}_4$  ferrite powders," *Journal of Magnetism and Magnetic Materials*, vol. 220, no. 1, pp. 59–64, 2000.
- [14] M. A. Gabal and Y. M. A. Angari, "Effect of chromium ion substitution on the electromagnetic properties of nickel ferrite," *Materials Chemistry and Physics*, vol. 118, no. 1, pp. 153–160, 2009.
- [15] N. A. Chen, K. Yang, and M. Gu, "Microwave absorption properties of La-substituted M-type strontium ferrites," *Journal of Alloys and Compounds*, vol. 490, no. 1-2, pp. 609–612, 2010.
- [16] S. E. Jacobo, C. Herme, and P. G. Bercoff, "Influence of the iron content on the formation process of substituted Co-Nd strontium hexaferrite prepared by the citrate precursor method," *Journal of Alloys and Compounds*, vol. 495, no. 2, pp. 513–515, 2010.
- [17] Q. Fang, H. Cheng, K. Huang, J. Wang, R. Li, and Y. Jiao, "Doping effect on crystal structure and magnetic properties of chromium-substituted strontium hexaferrite nanoparticles," *Journal of Magnetism and Magnetic Materials*, vol. 294, no. 3, pp. 281–286, 2005.
- [18] A. Pradeep and G. Chandrasekaran, "FTIR study of Ni, Cu and Zn substituted nano-particles of  $\text{MgFe}_2\text{O}_4$ ," *Materials Letters*, vol. 60, no. 3, pp. 371–374, 2006.
- [19] P. N. Vasambekar, C. B. Kolekar, and A. S. Vaingankar, "Magnetic behaviour of Cd and Cr substituted cobalt ferrites," *Materials Chemistry and Physics*, vol. 60, no. 3, pp. 282–285, 1999.
- [20] S. Singhal, A. N. Garg, and K. Chandra, "Evolution of the magnetic properties during the thermal treatment of nanosize  $\text{BaMFeO}$  ( $M = \text{Fe, Co, Ni}$  and  $\text{Al}$ ) obtained through aerosol route," *Journal of Magnetism and Magnetic Materials*, vol. 285, no. 1-2, pp. 193–198, 2005.
- [21] S. Singhal, J. Singh, S. K. Barthwal, and K. Chandra, "Preparation and characterization of nanosize nickel-substituted cobalt ferrites ( $\text{CoNiFeO}$ )," *Journal of Solid State Chemistry*, vol. 178, no. 10, pp. 3183–3189, 2005.
- [22] S. Singhal and K. Chandra, "Cation distribution and magnetic properties in chromium-substituted nickel ferrites prepared using aerosol route," *Journal of Solid State Chemistry*, vol. 180, no. 1, pp. 296–300, 2007.
- [23] A. C. F. M. Costa, A. P. Diniz, V. J. Silva et al., "Influence of calcination temperature on the morphology and magnetic properties of Ni-Zn ferrite applied as an electromagnetic energy absorber," *Journal of Alloys and Compounds*, vol. 483, no. 1-2, pp. 563–565, 2009.
- [24] J. E. Burke and D. Turnbull, "Recrystallization and grain growth," *Progress in Metal Physics*, vol. 3, p. 220, 1952.

- [25] B. D. Cullity, *Elements of X-Ray Diffraction*, chapter 14, Addison-Wesley, Reading, Mass, USA, 1976.
- [26] B. S. Chauhan, R. Kumar, K. M. Jadhav, and M. Singh, "Magnetic study of substituted mg-mn ferrites synthesized by citrate precursor method," *Journal of Magnetism and Magnetic Materials*, vol. 283, no. 1, pp. 71–81, 2004.
- [27] L. Neel, *Comptes Rendus de l'Académie des Sciences*, vol. 230, p. 375, 1950.
- [28] S. Singhal, T. Namgyal, S. Bansal, and K Chandra, "Effect of Zn Substitution on the Magnetic Properties of Cobalt Ferrite Nano Particles Prepared Via Sol-Gel Route," *Journal of Electromagnetic Analysis and Application*, vol. 2, p. 376, 2010.
- [29] B. D. Cullity, *Introduction to Magnetic Materials*, Addison-Wesley, Reading, Mass, USA, 1972.
- [30] Y. M. Yakovlev, E. V. Rubalikaya, and N. Lapovok, "Ferromagnetic Resonance in Lithium Ferrite," *Soviet Physics-Solid State*, vol. 10, p. 2301, 1969.
- [31] K. S. Rao, A. M. Kumar, M. C. Varma, G. S. V. R. K. Choudary, and K. H. Rao, "Cation distribution of titanium substituted cobalt ferrites," *Journal of Alloys and Compounds*, vol. 488, no. 1, pp. L6–L9, 2009.
- [32] S. K. Banerjee and W. O'Reilly, *IEEE Transactions on Magnetics*, vol. 3, p. 463, 1966.
- [33] M. Srivastava, A. K. Ojha, S. Chaubey, and A. Materny, "Synthesis and optical characterization of nanocrystalline NiFeO structures," *Journal of Alloys and Compounds*, vol. 481, no. 1-2, pp. 515–519, 2009.
- [34] K. F. Lin, H. M. Cheng, H. C. Hsu, LI. J. Lin, and W. F. Hsieh, "Band gap variation of size-controlled ZnO quantum dots synthesized by sol-gel method," *Chemical Physics Letters*, vol. 409, no. 4-6, pp. 208–211, 2005.
- [35] O. S. Polezhaeva, N. V. Yaroshinskaya, and V. K. Ivanov, "Synthesis of nanosized ceria with controlled particle sizes and bandgap widths," *Russian Journal of Inorganic Chemistry*, vol. 52, no. 8, pp. 1184–1188, 2007.

## Research Article

# Structure and Magnetic Properties of $Y_{3-x}Er_xFe_5O_{12}$ ( $x = 0.2, 1.0, \text{ and } 2.0$ ) Thin Films Prepared by Sol-Gel Method

Ramadan Shaiboub, Noor Baa'yah Ibrahim, Mustaffa Abdullah, and Ftema Abdulhade

School of Applied Physics, Faculty of Science and Technology, Universiti Kebangsaan Malaysia, Selangor, 43600 Bangi, Malaysia

Correspondence should be addressed to Noor Baa'yah Ibrahim, baayah@ukm.my

Received 18 February 2011; Accepted 9 March 2011

Academic Editor: Mallikarjuna Nadagouda

Copyright © 2011 Ramadan Shaiboub et al. This is an open access article distributed under the Creative Commons Attribution License, which permits unrestricted use, distribution, and reproduction in any medium, provided the original work is properly cited.

Nanoparticles  $Y_{3-x}Er_xFe_5O_{12}$  ( $x = 0.2, 1.0, \text{ and } 2.0$ ) thin films were prepared by sol-gel method and treated at 800, 900, and 1000°C, respectively, for 2 h. The films have single phase garnet structure and the sizes of particles are in the range of 44 to 83 nm. The magnetic measurements show that the saturation magnetization decreased with increasing of Er concentration for all samples treated at different annealing temperatures. The saturation magnetization increased with the particle size due to the enhancement of the surface spin effect. The coercivity initially decreased for  $x = 1.0$  and then increased for  $x = 2.0$  with increasing annealing temperature.

## 1. Introduction

The rare-earth iron garnets (RIGs) have the general unit formula as  $R_3Fe_5O_{12}$ , where R is either a trivalent rare-earth ion or yttrium. The garnets have eight formula units in a cubic unit cell. The cubic unit cells of RIGs have approximately the same lattice constant of the order of 12 Å [1], due to similar ionic radii of  $R^{3+}$  ions. Ionic distribution in garnet is represented as  $\{R_3^{3+}\}[Fe_2^{3+}](Fe_3^{3+})O_{12}$ . The interaction between the  $Fe^{3+}$  ions in [a] and (d) sites is strongly antiferromagnetic due to a strong superexchange interaction. The magnetic moment of the rare-earth ions in the {c} sublattice couples antiparallel with the resultant moment of  $Fe^{3+}$  ions. YIG ( $Y_3Fe_5O_{12}$ ) is one of the common RIGs, which has attracted much attention in telecommunications and data storage industries due to their interesting magnetic and magneto-optic properties [2]. The resulting magnetic moment in YIG is due to the unequal distribution of  $Fe^{3+}$  ions in two different sublattices of [a] and (d). YIGs are also of scientific importance because of the wide variety of magnetic properties that can be obtained by substituting yttrium with a rare-earth (RE) metal [3–9]. Most of the previous studies have concentrated on the preparation of Bi- and Ce-doped YIG powders and films because of their high

Faraday rotation coefficient [10–17]. Some studies have been carried out on Er-YIG powder nanoparticles [18–27].

In this paper erbium is chosen because its ionic radius (1.03 Å) is slightly less than ionic radius of yttrium (1.04 Å). Also, it has an extremely high verdet constant ( $\sim -11 \times 10^{-2}$  min/Oe·cm) at ( $\lambda = 600$  nm) and large Bohr magneton ( $9.6 \mu_B$ ) [28]. This paper reports the influence of low and high concentration of  $Er^{3+}$  on the structure and magnetic properties of YIG thin films.

## 2. Experimental Method

The YIG precursor sol was prepared by a sol-gel method using reagent grade nitrates purchased from Aldrich, Milwaukee, Wis, USA. Yttrium nitrate hexahydrate ( $Y(NO_3)_3 \cdot 6H_2O$ , 99.95% purity), iron(III) nitrate nonohydrate ( $Fe(NO_3)_3 \cdot 9H_2O$ , 98% purity), and Erbium nitrate pentahydrate ( $Er(NO_3)_3 \cdot 5H_2O$ ) were used as the raw materials. 2-methoxyethanol and acetic acid were used as solvents.  $Fe(NO_3)_3 \cdot 9H_2O$  and  $Y(NO_3)_3 \cdot 6H_2O$  were dissolved in the 2-methoxyethanol and refluxed at 80°C for 3 hours. The  $Er(NO_3)_3 \cdot 5H_2O$  dissolved in acetic acid was added gradually into the Fe-Y solution. Then the refluxing

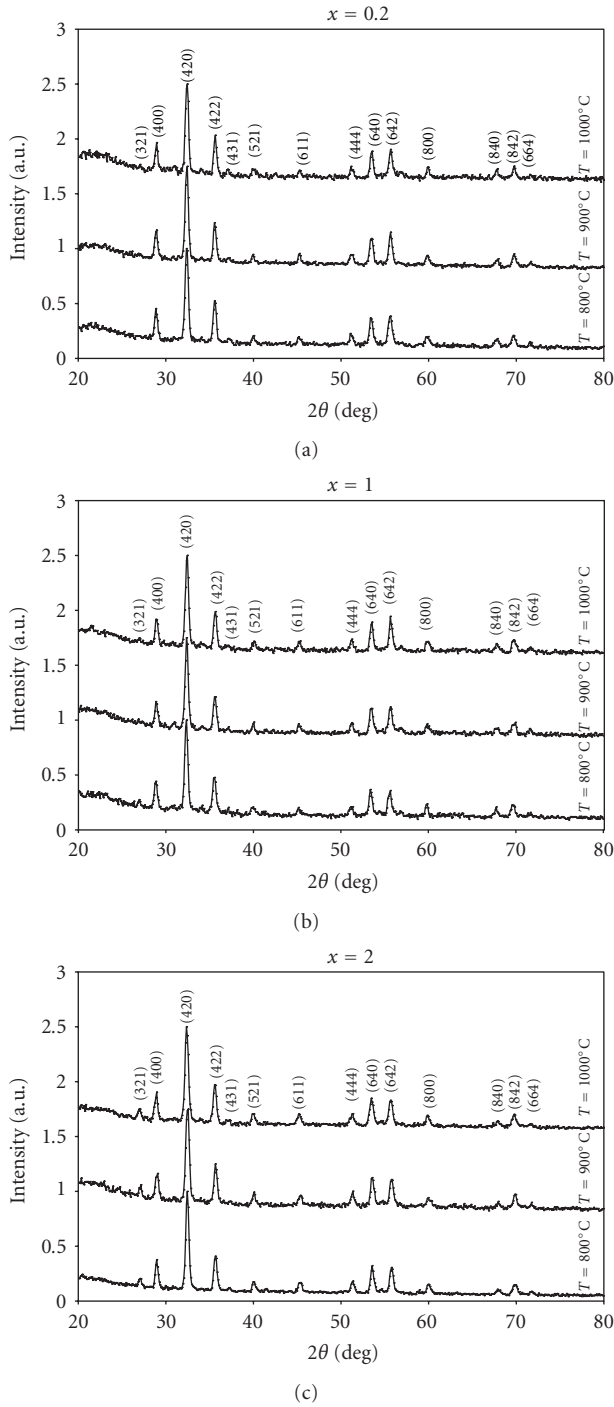


FIGURE 1: XRD patterns of  $\text{Y}_{3-x}\text{Er}_x\text{Fe}_5\text{O}_{12}$  films heated from 800 to  $1000^\circ\text{C}$  (a)  $x = 0.2$ , (b)  $x = 1.0$ , and (c)  $x = 2.0$ .

process was continued for 3 hours. The pH value was adjusted in the range of 2-3. After cooling down to room temperature, the solution was stirred for 3 days. The gel was transformed into film on a quartz substrate using the spin coating technique. The rate of the spinning process was 3500 rpm, and it was done for 30 seconds. After the spinning process, the film was dried at room temperature. Then the

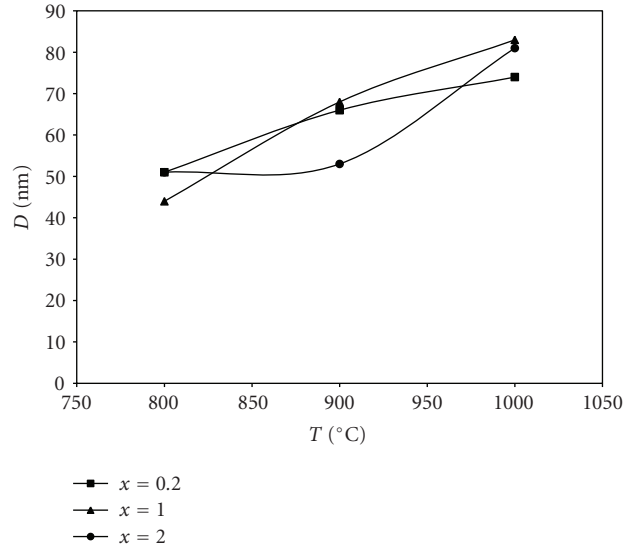


FIGURE 2: Particle size dependence on the heating treatment for  $\text{Y}_{3-x}\text{Er}_x\text{Fe}_5\text{O}_{12}$  films.

heat treatment was carried out: initial heating at  $350^\circ\text{C}$  for 15 min to burn off the organic materials followed by heating at  $800^\circ\text{C}$ ,  $900^\circ\text{C}$ , and  $1000^\circ\text{C}$  for 2 hours to crystallise the films.

The characterizations were carried out using an X-ray diffractometer (Philips model Pw 3020 MRD x'pert pro) with a  $\text{CuK}\alpha$  radiation ( $\lambda = 1.54056 \text{ \AA}$ ) to identify the phases and field emission scanning electron microscopic (FE-SEM model Zeiss Supra 55 vp) to determine the particle size and films thicknesses. The magnetic properties of the films were measured at room temperature using a vibrating sample magnetometer (VSM, LakeShore Cryotronics and 7400 Series).

### 3. Results and Discussion

**3.1. Structural Properties.** Figure 1 shows the spectra for all samples. The XRD patterns reveal a single phase garnet structure and the crystallization had completely occurred at  $800^\circ\text{C}$  due to the good homogeneity of the gel prepared at  $\text{pH} = 2-3$ . This temperature is lower than that reported by Xu et al. [29]. However, increasing the temperature up to  $1000^\circ\text{C}$  does not give great influence to the sample crystallization. This is proved by the intensities ratio calculation shown in Table 1.

The average crystallite size was calculated according to the Scherrer's formula

$$D = \frac{k\lambda}{\beta \cos\theta}, \quad (1)$$

where  $D$  is the mean crystallite size,  $k$  (0.89) is the Scherrer constant,  $\lambda$  is X-ray wavelength (0.154252 nm), and  $\beta$  is the relative value of the full width at half maximum (FWHM) of the diffraction peak (420).

The crystallite size for samples with the same  $x$  but treated at different temperature increased with increasing

TABLE 1: The average intensity ratios calculations for  $Y_{3-x}Er_xFe_5O_{12}$  films.

$x = 0.2$										
Temp. ( $^{\circ}C$ )	$I^*$	$I_{o1}$	$I_{o2}$	$I_{o3}$	$I_{o4}$	$I_{o1}/I^*$	$I_{o2}/I^*$	$I_{o3}/I^*$	$I_{o4}/I^*$	$(I_o/I^*)$ average
800	1356	615	709	498	521	0.45	0.52	0.37	0.38	0.43
900	1464	613	711	501	585	0.42	0.49	0.34	0.40	0.41
1000	1047	488	558	406	423	0.47	0.53	0.39	0.40	0.45
$x = 1.0$										
Temp. ( $^{\circ}C$ )	$I^*$	$I_{o1}$	$I_{o2}$	$I_{o3}$	$I_{o4}$	$I_{o1}/I^*$	$I_{o2}/I^*$	$I_{o3}/I^*$	$I_{o4}/I^*$	$(I_o/I^*)$ average
800	1082	478	516	397	387	0.44	0.48	0.37	0.36	0.41
900	1236	517	570	440	456	0.42	0.46	0.36	0.37	0.40
1000	1313	548	640	515	584	0.42	0.49	0.39	0.44	0.54
$x = 2.0$										
Temp. ( $^{\circ}C$ )	$I^*$	$I_{o1}$	$I_{o2}$	$I_{o3}$	$I_{o4}$	$I_{o1}/I^*$	$I_{o2}/I^*$	$I_{o3}/I^*$	$I_{o4}/I^*$	$(I_o/I^*)$ average
800	1579	637	742	550	520	0.40	0.47	0.35	0.33	0.39
900	1178	486	589	441	422	0.41	0.50	0.37	0.36	0.41
1000	1966	743	804	633	602	0.38	0.41	0.32	0.31	0.36

$I^*$ : highest intensity;  $I_{o1}$ ,  $I_{o2}$ ,  $I_{o3}$ , and  $I_{o4}$ : other peak intensities.

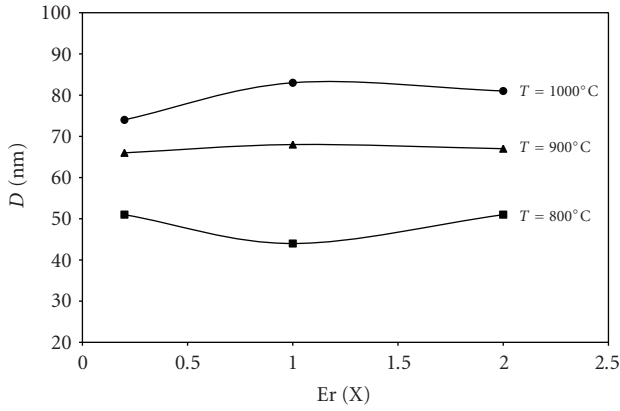


FIGURE 3: Particle size as a function of the Er concentration for  $Y_{3-x}Er_xFe_5O_{12}$  films treated at different temperatures.

annealing temperature (Figure 2). It is observed that the films crystallites sizes are about the same at the same annealing temperatures as shown in Figure 3. The result is probably due to the similar ionic radii of  $Er^{3+}$  (1.03 Å) and  $Y^{3+}$  (1.04 Å) ions.

### 3.2. Magnetization

**3.2.1. In-Plane Saturation Magnetization ( $M_s$ ) versus Particle Size ( $D$ ).** Figure 4 shows the variation in  $M_s$  with the average particle size for all samples. The results show that the  $M_s$  decreases with decreasing particle size for samples with the same  $x$ . A similar reduction in the magnetization was also reported for small particles of iron [30],  $\alpha-Fe_2O_3$  [31],  $BaFe_{12}O_9$  [32], and  $MnFe_2O_4$  [33]. This reduction can be related to the higher surface-to-volume ratio in the smaller particles, which results in the existence of nonmagnetic surface layer. Therefore, the  $M_s$  of the particles decreased as the particle sizes is reduced.

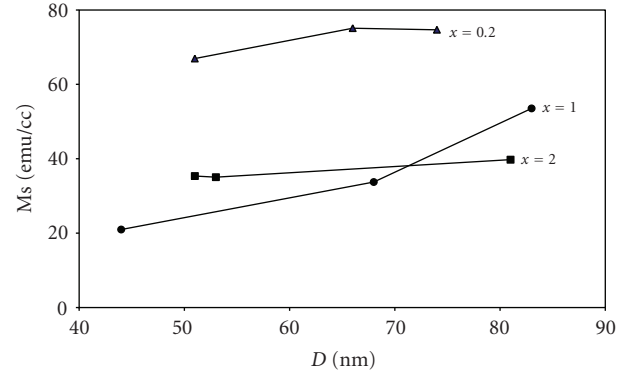


FIGURE 4: Saturation magnetization with the average particle size for all films treated at different temperatures.

**3.2.2. Saturation Magnetization ( $M_s$ ) versus Er Concentration ( $x$ ).** The tetrahedral and octahedral cavities in YIG are occupied by  $Fe^{3+}$  ions and dodecahedral cavities are occupied by  $Y^{3+}$  ions. In this experiment, we substituted some  $Er^{3+}$  ions for  $Y^{3+}$  ions, so the ionic distribution can be written as  $\{Y_{3-x}^{3+}Er_x^{3+}\}[Fe_2^{3+}](Fe_3^{3+})O_{12}^{2-}$ , where,  $\{ \}$  = c sub lattice,  $[ \ ]$  = a sub-lattice, and  $( \ )$  = d sub-lattice.  $Er^{3+}$  ion is magnetic (magnetic moment  $9.6\mu_B$ ) and  $Y^{3+}$  ion is nonmagnetic (magnetic moment  $0\mu_B$ ), so there are three magnetic sub-lattices: one (c) forms by the  $Er^{3+}$  ions occupying the dodecahedral sites, another [a] forms by  $Fe^{3+}$  ions occupying the octahedral sites, and the third (d) forms by the  $Fe^{3+}$  ions occupying the tetrahedral sites. The two iron sub-lattices are coupled antiferromagnetically by the superexchange interaction via the intervening  $O^{2-}$  ions. The {c} sub-lattice is coupled antiferromagnetically with the tetrahedral sub-lattice. At room temperature, the three sub-lattice moments align along the  $[111]$  direction [34]. The net magnetic moment is  $M = M_c - |M_d - M_a|$ .

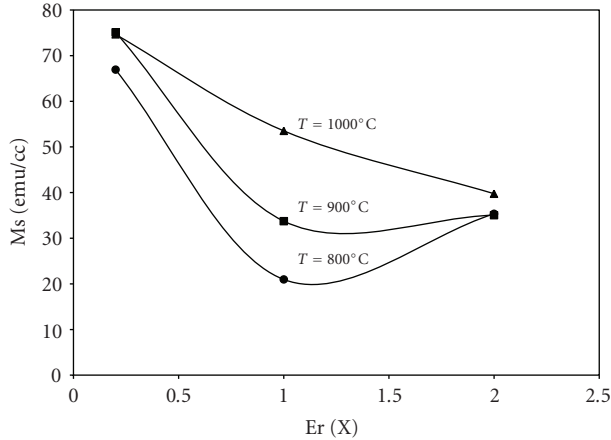


FIGURE 5: Saturation magnetization with Er concentration for all films treated at different temperatures.

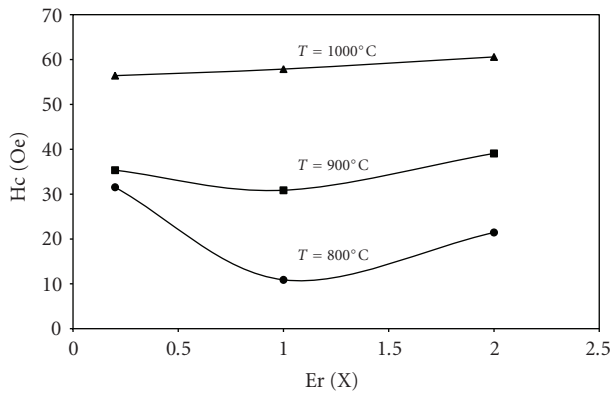


FIGURE 6: Coercivity with Er concentration for all films treated at different temperatures.

The variation of  $M_s$  with the  $x$  is shown in Figure 5. At different temperatures,  $M_s$  decreased with increasing  $x$ , which could be related to the fact that the magnetic moment of  $\text{Er}^{3+}$  ions aligns opposite to the effective moments formed by  $\text{Fe}^{3+}$  ions. With decreasing annealing temperatures the coercivity is initially decreased for  $x = 1.0$  and then increases for  $x = 2.0$  as shown in Figure 6.

#### 4. Conclusion

The structure and magnetic properties of  $\text{Y}_{3-x}\text{Er}_x\text{Fe}_5\text{O}_{12}$  films ( $x = 0.2, 1.0$  and  $2.0$ ) prepared by a sol-gel method have been reported. All the samples have only single phase garnet. The crystallization begins at  $800^\circ\text{C}$ , and as the heating temperature increases the obtained crystallite size is increased. At the same Er concentration, the saturation magnetization decreased as the particle size is reduced due to the influence of the magnetic domain structure and surface spin effect. The saturation magnetization decreased as the Er concentration is increased due to the opposite alignment between  $\text{Er}^{3+}$  ions and  $\text{Fe}^{3+}$  ions.

#### Acknowledgment

The authors are grateful to the Malaysian Ministry of Science, technology and innovation for the science fund Grant 03-01-02-SF0538.

#### References

- [1] M. Lahoubi, M. Guillot, A. Marchand, F. Tcheou, and E. Roudault, "Double umbrella structure in terbium iron garnet," *IEEE Transactions on Magnetics*, vol. 20, no. 5, pp. 1518–1520, 1984.
- [2] Y. Konishi, *Microwave Integrated Circuit*, Marcel-Dekker, New York, NY, USA, 1991.
- [3] M. Gilleo, "Ferromagnetic insulators: garnets," in *Ferromagnetic Materials*, E. P. Wohlfarth, Ed., vol. 2, chapter 1, North-Holland, Amsterdam, The Netherlands, 1980.
- [4] S. Thongmee, P. Winotai, and I. M. Tang, "Local field fluctuations in the substituted aluminum iron garnets,  $\text{Y}_3\text{Fe}_{5-x}\text{Al}_x\text{O}_{12}$ ," *Solid State Communications*, vol. 109, no. 7, pp. 471–476, 1999.
- [5] M. S. Lataifeh, "Magnetic study of Al-substituted holmium iron garnet," *Journal of the Physical Society of Japan*, vol. 69, no. 7, pp. 2280–2282, 2000.
- [6] M. J. Geselbracht, A. M. Cappellari, A. B. Ellis, M. A. Rzeznik, and B. J. Johnson, "Rare earth iron garnets: their synthesis and magnetic properties," *Journal of Chemical Education*, vol. 71, no. 8, pp. 696–703, 1994.
- [7] M. S. Lataifeh and A. Al-sharif, "Magnetization measurements on some rare-earth iron garnets," *Applied Physics A*, vol. 61, no. 4, pp. 415–418, 1995.
- [8] M. S. Lataifeh, A. D. Lehlooh, and S. Mahmood, "Mössbauer spectroscopy of Al substituted Fe in holmium iron garnet," *Hyperfine Interactions*, vol. 122, no. 3-4, pp. 253–258, 1999.
- [9] M. Inoue, K. Arai, T. Fujii, and M. Abe, "Magneto-optical properties of one-dimensional photonic crystals composed of magnetic and dielectric layers," *Journal of Applied Physics*, vol. 83, no. 11, pp. 6768–6770, 1998.
- [10] M. Gomi, K. Satoh, and M. Abe, "Giant Faraday rotation of Ce-substituted YIG films epitaxially grown by RF sputtering," *Japanese Journal of Applied Physics*, vol. 27, pp. L1536–L1538, 1988.
- [11] T. Shintaku and T. Uno, "Preparation of Ce-substituted yttrium iron garnet films for magneto-optic waveguide devices," *Japanese Journal of Applied Physics, Part 1*, vol. 35, no. 9A, pp. 4689–4691, 1996.
- [12] A. Tate, T. Uno, S. Mino, A. Shibukawa, and T. Shintaku, "Crystallinity of Ce substituted YIG films prepared by RF sputtering," *Japanese Journal of Applied Physics, Part 1*, vol. 35, no. 6, pp. 3419–3425, 1996.
- [13] T. Shintaku, A. Tate, and S. Mino, "Ce-substituted yttrium iron garnet films prepared on  $\text{Gd}_3\text{Sc}_2\text{Ga}_3\text{O}_{12}$  garnet substrates by sputter epitaxy," *Applied Physics Letters*, vol. 71, no. 12, pp. 1640–1642, 1997.
- [14] C. Y. Tsay, C. Y. Liu, K. S. Liu, I. N. Lin, L. J. Hu, and T. S. Yeh, "Low temperature sintering of microwave magnetic garnet materials," *Journal of Magnetism and Magnetic Materials*, vol. 239, no. 1–3, pp. 490–494, 2002.
- [15] H. Hayashi, S. Iwasa, N. J. Vasa et al., "Fabrication of Bi-doped YIG optical thin film for electric current sensor by pulsed laser deposition," *Applied Surface Science*, vol. 197-198, pp. 463–466, 2002.

- [16] M. Huang and S. Zhang, "Growth and characterization of rare-earth iron garnet single crystals modified by bismuth and ytterbium substituted for yttrium," *Materials Chemistry and Physics*, vol. 73, no. 2-3, pp. 314–317, 2002.
- [17] M. C. Sekhar, J. -Y. Hwang, M. Ferrera et al., "Strong enhancement of the Faraday rotation in Ce and Bi comodified epitaxial iron garnet thin films," *Applied Physics Letters*, vol. 94, no. 18, Article ID 181916, 2009.
- [18] H. Xu, H. Yang, and L. Lu, "Effect of erbium oxide on synthesis and magnetic properties of yttrium-iron garnet nanoparticles in organic medium," *Journal of Materials Science: Materials in Electronics*, vol. 19, no. 6, pp. 509–513, 2008.
- [19] N. I. Tsidaeva, "The magneto-optical activity of rare-earth ion in Y-substituted erbium and neodymium iron garnets," *Journal of Alloys and Compounds*, vol. 408–412, pp. 164–168, 2006.
- [20] J. Ostoréro and M. Guillot, "High field induced magnetic anisotropy of Al-substituted erbium iron garnet single crystals," *IEEE Transactions on Magnetics*, vol. 37, no. 4, pp. 2441–2444, 2001.
- [21] P. Novák, V. A. Borodin, V. D. Doroshev, M. M. Savosta, and T. N. Tarasenko, "NMR of Fe in erbium-yttrium iron garnets," *Hyperfine Interactions*, vol. 59, no. 1–4, pp. 427–430, 1990.
- [22] P. Feldmann, M. Guillot, H. Le Gall, and A. Marchand, "Faraday rotation in erbium-yttrium iron garnet," *IEEE Transactions on Magnetics*, vol. 17, no. 6, pp. 3217–3219, 1981.
- [23] N. Tsidaeva and V. Abaeva, "The investigation of mechanisms of the magneto-optical activity of rare-earth iron garnet single crystals," *Journal of Alloys and Compounds*, vol. 418, no. 1-2, pp. 145–150, 2006.
- [24] N. I. Tsidaeva, "The magnetic and magneto-optical properties of Y-substituted erbium iron garnet single crystals," *Journal of Alloys and Compounds*, vol. 374, no. 1-2, pp. 160–164, 2004.
- [25] P. Feldmann, H. Le Gall, M. Guillot, and A. Marchand, "Anisotropy of the Faraday rotation in erbium-yttrium iron garnet below the compensation temperature," *Journal of Applied Physics*, vol. 53, no. 3, pp. 2486–2488, 1982.
- [26] J. Ostoréro and M. Guillot, "Magneto-optical properties of Sc-substituted erbium-iron-garnet single crystals," *Journal of Applied Physics*, vol. 83, no. 11, pp. 6756–6758, 1998.
- [27] P. Feldmann, H. Le Gall, J. M. Desvignes, M. Guillot, and A. Marchand, "Faraday rotation in single crystal erbium iron garnet," *Journal of Magnetism and Magnetic Materials*, vol. 21, no. 3, pp. 280–284, 1980.
- [28] A. Di Biccari, *Sol-gel processing of  $RxY_{3-x}Al_yFe_5-yO_{12}$  magneto-optical films*, M.S. thesis, Materials Science & Engineering Department, Blacksburg, Va, USA, 2002.
- [29] H. Xu, H. Yang, and L. Lu, "Effect of erbium oxide on synthesis and magnetic properties of yttrium-iron garnet nanoparticles in organic medium," *Journal of Materials Science: Materials in Electronics*, vol. 19, no. 6, pp. 509–513, 2008.
- [30] S. Gangopadhyay, G. C. Hadjipanayis, B. Dale et al., "Magnetic properties of ultrafine iron particles," *Physical Review B*, vol. 45, no. 17, pp. 9778–9787, 1992.
- [31] D. H. Han, J. P. Wang, and H. L. Luo, "Crystallite size effect on saturation magnetization of fine ferrimagnetic particles," *Journal of Magnetism and Magnetic Materials*, vol. 136, no. 1-2, pp. 176–182, 1994.
- [32] X. Batlle, X. Obradors, M. Medarde, J. Rodríguez-Carvajal, M. Pernet, and M. Vallet-Regí, "Surface spin canting in  $BaFe_{12}O_{19}$  fine particles," *Journal of Magnetism and Magnetic Materials*, vol. 124, no. 1-2, pp. 228–238, 1993.
- [33] Z. X. Tang, C. M. Sorensen, K. J. Klabunde, and G. C. Hadjipanayis, "Size-dependent Curie temperature in nanoscale  $MnFe_2O_4$  particles," *Physical Review Letters*, vol. 67, no. 25, pp. 3602–3605, 1991.
- [34] S. Thongmee, P. Winotai, and I. M. Tang, "Local field fluctuations in the substituted aluminum iron garnets,  $Y_3Fe_{5-x}Al_xO_{12}$ ," *Solid State Communications*, vol. 109, no. 7, pp. 471–476, 1999.

## Research Article

# Magnetic Properties of $\text{Co}_{0.5}\text{Zn}_{0.5}\text{Fe}_2\text{O}_4$ Nanoparticles Synthesized by a Template-Assisted Hydrothermal Method

H. Y. He

Key Laboratory of Auxiliary Chemistry and Technology for Chemical Industry,  
Shaanxi University of Science and Technology, Ministry of Education, 710021 Xi'an, China

Correspondence should be addressed to H. Y. He, hehy@sust.edu.cn

Received 7 March 2011; Accepted 5 April 2011

Academic Editor: Mallikarjuna Nadagouda

Copyright © 2011 H. Y. He. This is an open access article distributed under the Creative Commons Attribution License, which permits unrestricted use, distribution, and reproduction in any medium, provided the original work is properly cited.

In the present paper, nickel cobalt ferrite ( $\text{Co}_{0.5}\text{Zn}_{0.5}\text{Fe}_2\text{O}_4$ ) nanoparticles were synthesized using a template-assisted hydrothermal method. Carboxymethyl cellulose was used as the templating agent for controlling the morphology of the  $\text{Co}_{0.5}\text{Zn}_{0.5}\text{Fe}_2\text{O}_4$  nanoparticles. The synthesized nanoparticles were characterized using X-ray diffraction, scanning electron microscopy, and a vibrating sample magnetometer. The results indicated that the morphology of the nanoparticles changed from granular and superparamagnetic to platelike and ferromagnetic with the addition of the template. The  $\text{Co}_{0.5}\text{Zn}_{0.5}\text{Fe}_2\text{O}_4$  nanoparticles synthesized without the template exhibited a saturation magnetization and coercivity 2.81 T and  $0.2 \text{ kA}\cdot\text{m}^{-1}$ , while when the template was used, the saturation magnetization and coercivity increased to 3.13 T and  $76.6 \text{ kA}\cdot\text{m}^{-1}$  as the template proportion increased to 0.3.

## 1. Introduction

Over recent decades, the fabrication of spinel ferrite nanoparticles has been intensively investigated due to their excellent magnetic and electrical properties, and their potential uses in many areas, such as magnetic devices, recording tapes or disks, microwave absorbers, and active components of ferrofluids [1–5]. Among spinel ferrites,  $\text{Zn}^{2+}$  substituted  $\text{CoFe}_2\text{O}_4$  nanoparticles ( $\text{Co}_{1-x}\text{Zn}_x\text{Fe}_2\text{O}_4$ ) exhibit improved properties such as excellent chemical stability, high corrosion resistivity, magnetocrystalline anisotropy, magnetostriction, and magneto-optical properties [6–8].

Since the magnetic property of spinel ferrites is associated with their morphology and size, modern data storage, microwave protection, and biomedical applications require strict control over the morphology of the particles and a considerable reduction in their dimensions to the single domain and superparamagnetic size [9].

To date, many methods have been developed to prepare  $\text{Co}_{1-x}\text{Zn}_x\text{Fe}_2\text{O}_4$  nanopowders, such as the coprecipitation method [6, 8, 10], the standard solid-state reaction technique [7, 11], the forced hydrolysis method [12], the microwave-hydrothermal method [13], and the hydrothermal method

[14]. However, research on the template-assisted synthesis of  $\text{Co}_{1-x}\text{Zn}_x\text{Fe}_2\text{O}_4$  nanoparticles is comparatively limited. In the current study, focus was placed on development of a synthesis route for  $\text{Co}_{0.5}\text{Zn}_{0.5}\text{Fe}_2\text{O}_4$  nanoparticles via a template-assisted hydrothermal method and examining the magnetic properties (magnetization and coercivity) and morphology dependence on the template.

## 2. Experimental

$\text{Co}_{0.5}\text{Zn}_{0.5}\text{Fe}_2\text{O}_4$  powders were synthesized from cobalt chloride, zinc acetate, and iron (III) nitrate with carboxymethyl cellulose (CMC) as a template. The chemicals were weighted according to the required stoichiometric proportions, and three solutions of cobalt chloride, zinc acetate, and iron (III) nitrate were prepared in deionized water with continuous stirring. The template was added to the solutions with constant stirring to achieve molar ratios of CMC monomer:metal ions (CMC:M) of 0:1, 0.1:1, and 0.3:1. When the template was dissolved, the solutions were heated to  $80^\circ\text{C}$  and held for 8 h. The solutions were then adjusted to  $\text{pH} > 9$  with aqueous NaOH and transferred into autoclaves

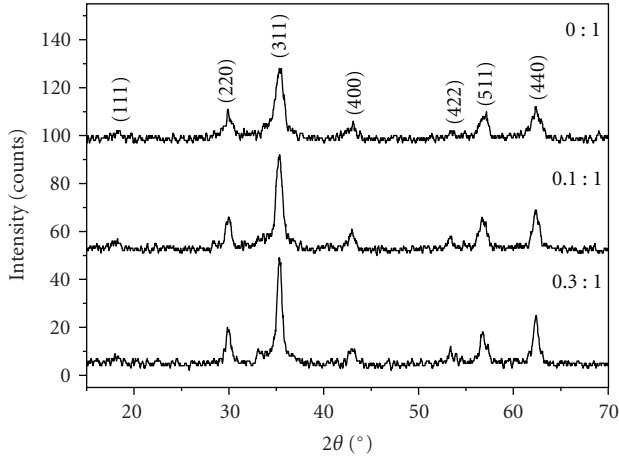


FIGURE 1: XRD patterns of the powders synthesized with different molar ratios of CMC monomer to metal ions.

TABLE 1: Lattice parameters, density, and orientation degree ( $O_{hk_0}$ ) of the  $\text{Co}_{0.5}\text{Zn}_{0.5}\text{Fe}_2\text{O}_4$  particles determined with XRD data analysis.

CMC:M	$a$ (Å)	$c$ (Å)	$c/a$	$D$ ( $\text{g}\cdot\text{cm}^{-1}$ )	$O_{hk_0}$
0:1	8.3913	8.6038	1.0253	5.214	1.260
0.1:1	8.4210	8.1811	0.9715	5.445	1.337
0.3:1	8.4204	8.2398	0.9685	5.407	1.359

(volume: 100 mL, degree of filling: 80% V). After sealing, the hydrothermal reaction was then carried out in hydrothermal ovens at 170°C for 30 h, the heating rate was about 20  $\text{K}\cdot\text{min}^{-1}$ . After natural cooling in the furnace, the products were washed repeatedly with distilled water and then dried for 24 h at ambient temperature.

The crystalline structure of the synthesized  $\text{Co}_{0.5}\text{Zn}_{0.5}\text{Fe}_2\text{O}_4$  powders was identified at room temperature using X-ray diffractometry (XRD, Cu- $\text{K}\alpha_1$ ,  $\lambda = 0.15406$  nm, Model no. D/Max-2200PC, Rigaku, Japan). The morphology of the particles was analyzed using scanning electron microscopy (SEM, Model no. JXM-6700F, Japan). The magnetic property was measured with a vibrating sample magnetometer (VSM, Model no. Versa Lab, Quantun Design, USA)

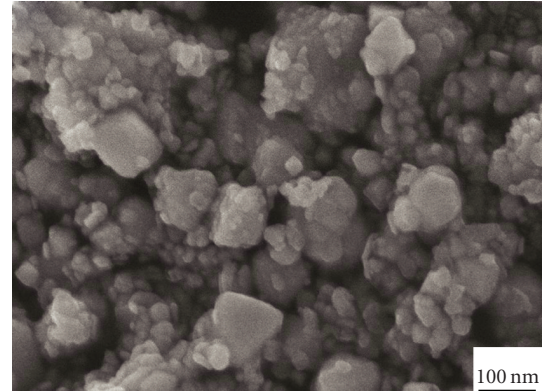
### 3. Results and Discussion

Figure 1 shows the XRD patterns of the synthesized powders. All the diffraction peaks were indexed to zinc cobalt ferrite with spinel structure, indicating that the final products consisted of single-phase  $\text{Co}_{0.5}\text{Zn}_{0.5}\text{Fe}_2\text{O}_4$  without any other impurities.

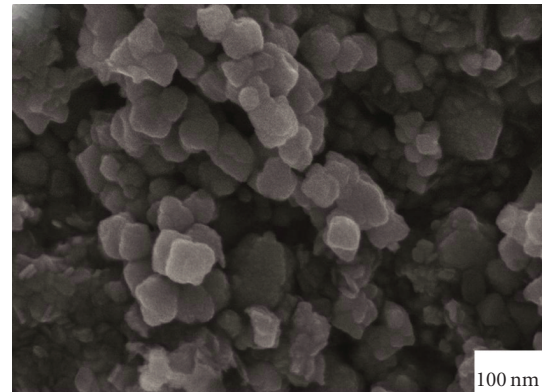
The lattice parameters of the powders were calculated with the relation for tetragonal structures using:

$$\frac{1}{d^2} = \frac{h^2 + k^2}{a^2} + \frac{l^2}{c^2}. \quad (1)$$

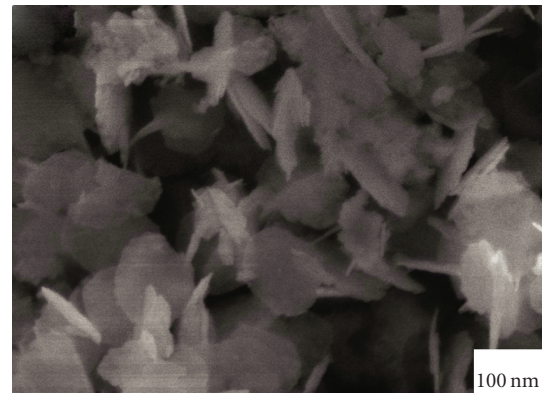
A  $c/a = 1$  ratio would indicate a perfect cubic structure in the powder, but the calculated results (Table 1) show that



(a)



(b)



(c)

FIGURE 2: SEM micrographs of the powders synthesized with molar ratios of CMC monomer to metal ions to (a) 0:1, (b) 0.1:1, and (c) 0.3:1.

the powders had varying anisotropies depending on the amount of template that was added. Without any template, the  $c/a$  ratio was greater than 1, but as the template was added, the ratio decreased below 1. This is a common occurrence for structures prepared through special synthesis processes. For example, the  $c/a$  ratios of some films with  $c$ -orientation texture, are all relatively large as reported in literature [15–17]. Each lattice cell contains eight

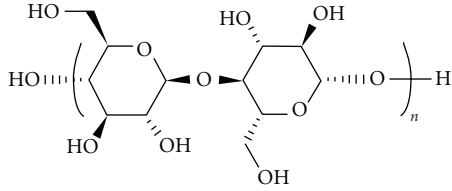


FIGURE 3: Molecular structure of the carboxymethyl cellulose (CMC).

$\text{Co}_{0.5}\text{Zn}_{0.5}\text{Fe}_2\text{O}_4$  molecules. With these lattice parameters, the density of the powders ( $D$ ,  $\text{g}\cdot\text{cm}^{-3}$ ) can be calculated by the following:

$$D = \frac{8G_m N_a}{a^2 b \cdot 10^{24}}, \quad (2)$$

where  $G_m$  is gram molecular weight (236.300 for the  $\text{Co}_{0.5}\text{Zn}_{0.5}\text{Fe}_2\text{O}_4$ ) and  $N_a$  is Avogadro constant ( $6.022 \cdot 10^{23}$ ). As-calculated densities are also listed in Table 1.

The orientation degree of the  $(hk_0)$  plane was calculated from (3) deduced from a formula in literature [15]

$$O_{hk_0} = \frac{(I_{220} + I_{440})/I_{311\text{sample}}}{(I_{220} + I_{440})/I_{311\text{standard}}}. \quad (3)$$

The larger the  $O_{hk_0}$  value, the larger the abundance of crystallites oriented in the  $(hk_0)$  direction. The calculated results (Table 1) indicate that the template obviously affected the orientation degree of  $(hk_0)$  plane, and the  $O_{hk_0}$  increased with the increase in template proportion from 0 : 1 to 0.3 : 1.

From the SEM micrographs of the powders (Figure 2), the average grain size was  $\sim 35\text{--}45$  nm, and the grain morphology changed from granular to platelike with increasing template proportion. This change in the morphology was consistent with the variation of orientation degree with the template proportion.

The change in morphology can be related to the structure of the CMC monomer, which contained two substituted cyclohexane hexagonal rings with some substituted radicals (Figure 3). The substituted radicals were composed of a hydroxyl radical and a sodium acetate radical on two sides of the hexagonal ring. By partial substitution of the radicals, the CMC molecules could react with each other or with the as-produced polymer at appropriate temperatures. Polymerization in two dimensions may take place because the cyclohexane hexagonal ring appears a platelike morphology. The substituted radicals then could adsorb, before and after the polymerization, the metal hydroxides through hydrogen bonding and substituting sodium ions with Co, Zn, and Fe ions to polymerize into platelike hydroxide layers. In the hydrothermal reaction, the hydroxide layers transformed into the  $(hk_0)$ -oriented  $\text{Co}_{0.5}\text{Zn}_{0.5}\text{Fe}_2\text{O}_4$  particles.

Figure 4 shows the room temperature hysteresis loops of the  $\text{Co}_{0.5}\text{Zn}_{0.5}\text{Fe}_2\text{O}_4$  powders. The powder synthesized without the template was superparamagnetic, while the powders become ferromagnetic with the addition of the template. As the template proportion increased from 0 to 0.1 and 0.3, the saturation magnetization of the powder

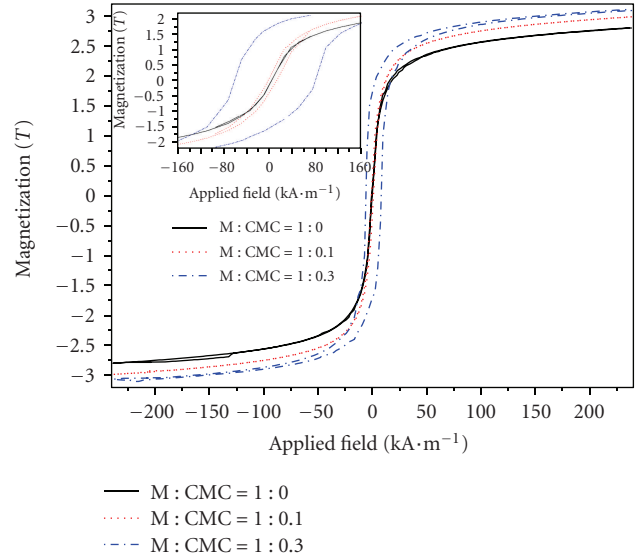


FIGURE 4: Variation of magnetization with applied field. The insert shows the part of the curve near the origin.

increased from 2.81 T to 3.00 T and 3.13 T ( $60.3 \text{ emu}\cdot\text{g}^{-1}$ ), while the coercivity markedly increased from  $0.2 \text{ kA}\cdot\text{m}^{-1}$  to  $7.6 \text{ kA}\cdot\text{m}^{-1}$  and  $76.6 \text{ kA}\cdot\text{m}^{-1}$  (Figure 5). These variations in the magnetic nature could be attributed to the corresponding change in the structural morphology.

The magnetization of the  $\text{Co}_{0.5}\text{Zn}_{0.5}\text{Fe}_2\text{O}_4$  nanoparticles increased with increasing applied field, but it did not reach the saturation state, even under high magnetic fields of  $239 \text{ kA}\cdot\text{m}^{-1}$  (30 kOe). This characteristic was also reported for the  $\text{Co}_{0.5}\text{Zn}_{0.5}\text{Fe}_2\text{O}_4$  nanospheres prepared via the solvothermal method, and the saturation magnetization of the nanoparticles was close to that observed for the nanospheres at an applied field of 5 kOe ( $64.6 \text{ emu}\cdot\text{g}^{-1}$ ) [18]. The saturation magnetization of these samples was smaller than that observed for the bulk material though ( $\sim 80 \text{ emu}\cdot\text{g}^{-1}$ ) [12, 14]. These differences in the magnetization value (such as saturation magnetization, remanent magnetization, and coercivity) between the nanosized ferrites and bulk ferrites can be attributed to the finite size effect [19]. Additionally, the lack of oxygen to mediate the superexchange mechanism between nearest iron ions on the surface can lead to a decrease in exchange coupling, resulting in slanted spins and a decrease in the nanoparticles' saturation magnetization [20]. They can also be attributed to the enhancement of the surface barrier potential due to distortion of the crystal lattice caused by the atoms deviating from normal positions in the surface layers [21].

#### 4. Conclusions

$\text{Co}_{0.5}\text{Zn}_{0.5}\text{Fe}_2\text{O}_4$  ferrites were synthesized using a template-assisted hydrothermal method with CMC as the templating agent. The average particle size was found to be  $\sim 35\text{--}45$  nm, and room temperature X-ray diffraction confirmed the formation of single-phase Zn–Co ferrite at  $170^\circ\text{C}$  for all

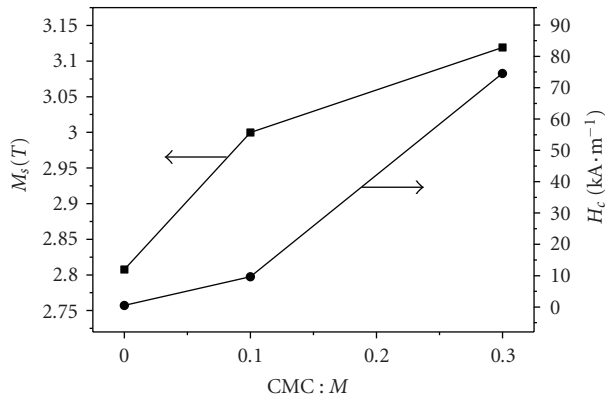


FIGURE 5: Variations of saturation magnetisation and coercivity with molar ratio of CMC monomer : metal ions (CMC : M).

template proportions used in this experiment. The FE-SEM results showed that the morphology of the  $\text{Co}_{0.5}\text{Zn}_{0.5}\text{Fe}_2\text{O}_4$  powder changed from granular to platelike with increasing template proportion, and the room temperature VSM results showed that the  $\text{Co}_{0.5}\text{Zn}_{0.5}\text{Fe}_2\text{O}_4$  nanoparticles synthesized without the template exhibited superparamagnetic behavior with a saturation magnetization of 2.81 T. The addition of the template resulted in the powder becoming ferromagnetic with the saturation magnetization and coercivity being 3.13 T and  $76.6 \text{ kA}\cdot\text{m}^{-1}$  when the template proportion was 0.3. Additionally, the morphology and magnetic properties of the  $\text{Co}_{0.5}\text{Zn}_{0.5}\text{Fe}_2\text{O}_4$  nanoparticle could be controlled by using low template proportions. The synthesized  $\text{Co}_{0.5}\text{Zn}_{0.5}\text{Fe}_2\text{O}_4$  would be useful in several technological applications such as soft magnets, low loss materials at high frequencies, and magnetic fluids.

## Acknowledgments

The authors thank the Mr. Z. Miao of the Northwest Institute for Non-Ferrous Metal Research for his kind assistance in SEM measurement and Mr. S. Liu of the Advanced Material Analysis and Test Center of the Xi'an University of Technology for his kind assistance in magnetic property measurements.

## References

- [1] M. Kaiser, "Effect of nickel substitutions on some properties of Cu—Zn ferrites," *Journal of Alloys and Compounds*, vol. 468, no. 1-2, pp. 15–21, 2009.
- [2] M. J. Iqbal and M. R. Siddiquah, "Electrical and magnetic properties of chromium-substituted cobalt ferrite nanomaterials," *Journal of Alloys and Compounds*, vol. 453, no. 1-2, pp. 513–518, 2008.
- [3] M. Srivastava, A. K. Ojha, S. Chaubey, and A. Materny, "Synthesis and optical characterization of nanocrystalline  $\text{NiFe}_2\text{O}_4$  structures," *Journal of Alloys and Compounds*, vol. 481, no. 1-2, pp. 515–519, 2009.
- [4] I. H. Gul and A. Maqsood, "Structural, magnetic and electrical

- properties of cobalt ferrites prepared by the sol-gel route," *Journal of Alloys and Compounds*, vol. 465, no. 1-2, pp. 227–231, 2008.
- [5] Y. Köseoğlu, A. Baykal, M. S. Toprak, F. Gözüak, A. C. Başaran, and B. Aktaş, "Synthesis and characterization of  $\text{ZnFe}_2\text{O}_4$  magnetic nanoparticles via a PEG-assisted route," *Journal of Alloys and Compounds*, vol. 462, no. 1-2, pp. 209–213, 2008.
- [6] G. Vaidyanathan and S. Sendhilnathan, "Characterization of  $\text{Co}_{1-x}\text{Zn}_x\text{Fe}_2\text{O}_4$  nanoparticles synthesized by co-precipitation method," *Physica B*, vol. 403, no. 13-16, pp. 2157–2167, 2008.
- [7] A. K. M. Akther Hossain, H. Tabata, and T. Kawai, "Magnetoresistive properties of  $\text{Zn}_{1-x}\text{Co}_x\text{Fe}_2\text{O}_4$  ferrites," *Journal of Magnetism and Magnetic Materials*, vol. 320, no. 6, pp. 1157–1162, 2008.
- [8] M. U. Islam, F. Aen, S. B. Niazi et al., "Electrical transport properties of CoZn ferrite- $\text{SiO}_2$  composites prepared by coprecipitation technique," *Materials Chemistry and Physics*, vol. 109, no. 2-3, pp. 482–487, 2008.
- [9] G. V. Kurlyandskaya, J. Cunanan, S. M. Bhagat, J. C. Apesteguy, and S. E. Jacobo, "Field-induced microwave absorption in  $\text{Fe}_3\text{O}_4$  nanoparticles and  $\text{Fe}_3\text{O}_4$ /polyaniline composites synthesized by different methods," *Journal of Physics and Chemistry of Solids*, vol. 68, no. 8, pp. 1527–1532, 2007.
- [10] R. Arulmurugan, G. Vaidyanathan, S. Sendhilnathan, and B. Jayadevan, "Thermomagnetic properties of  $\text{Co}_{1-x}\text{Zn}_x\text{Fe}_2\text{O}_4$  ( $x = 0.1 - 0.5$ ) nanoparticles," *Journal of Magnetism and Magnetic Materials*, vol. 303, no. 1, pp. 131–137, 2006.
- [11] A. Tawfik, I. M. Hamada, and O. M. Hemeda, "Effect of laser irradiation on the structure and electromechanical properties of Co—Zn ferrite," *Journal of Magnetism and Magnetic Materials*, vol. 250, pp. 77–82, 2002.
- [12] G. V. Duong, N. Hanh, D. V. Linh et al., "Monodispersed nanocrystalline  $\text{Co}_{1-x}\text{Zn}_x\text{Fe}_2\text{O}_4$  particles by forced hydrolysis: synthesis and characterization," *Journal of Magnetism and Magnetic Materials*, vol. 311, no. 1, pp. 46–50, 2007.
- [13] C. K. Kim, J. H. Lee, S. Katoh, R. Murakami, and M. Yoshimura, "Synthesis of Co-, Co—Zn and Ni—Zn ferrite powders by the microwave-hydrothermal method," *Materials Research Bulletin*, vol. 36, no. 12, pp. 2241–2250, 2001.
- [14] F. Gözüak, Y. Köseoğlu, A. Baykal, and H. Kavas, "Synthesis and characterization of  $\text{Co}_x\text{Zn}_{1-x}\text{Fe}_2\text{O}_4$  magnetic nanoparticles via a PEG-assisted route," *Journal of Magnetism and Magnetic Materials*, vol. 321, no. 14, pp. 2170–2177, 2009.
- [15] R. W. Schwartz, P. G. Clem, J. A. Voigt et al., "Control of microstructure and orientation in solution-deposited  $\text{BaTiO}_3$  and  $\text{SrTiO}_3$  thin films," *Journal of the American Ceramic Society*, vol. 82, no. 9, pp. 2359–2367, 1999.
- [16] S. Hoffmann, U. Hasenkox, R. Waser, C. L. Jia, and K. Urban, "Chemical solution deposited  $\text{BaTiO}_3$  and  $\text{SrTiO}_3$  thin films with columnar microstructure," in *Proceedings of the MRS Spring Meeting*, pp. 9–15, February 1997.
- [17] H. Y. He, "Effect of heating rate on microstructure of  $(\text{Ba}_{0.99}\text{Bi}_{0.01})\text{TiO}_3$  thin films prepared by sol-gel deposition process," *Materials Research Innovations*, vol. 12, no. 2, pp. 66–68, 2008.
- [18] C. Hou, H. Yu, Q. Zhang, Y. Li, and H. Wang, "Preparation and magnetic property analysis of monodisperse Co-Zn ferrite nanospheres," *Journal of Alloys and Compounds*, vol. 491, no. 1-2, pp. 431–435, 2010.
- [19] M. Sertkol, Y. Köseoğlu, A. Baykal, H. Kavas, and A. C. Başaran, "Synthesis and magnetic characterization of

Zn<sub>0.6</sub>Ni<sub>0.4</sub>Fe<sub>2</sub>O<sub>4</sub> nanoparticles via a polyethylene glycol-assisted hydrothermal route,” *Journal of Magnetism and Magnetic Materials*, vol. 321, no. 3, pp. 157–162, 2009.

- [20] T. Ozkaya, M. S. Toprak, A. Baykal, H. Kavas, Y. Köseoğlu, and B. Aktaş, “Synthesis of Fe<sub>3</sub>O<sub>4</sub> nanoparticles at 100°C and its magnetic characterization,” *Journal of Alloys and Compounds*, vol. 472, no. 1-2, pp. 18–23, 2009.
- [21] M. Sertkol, Y. Köseoğlu, A. Baykal, H. Kavas, A. Bozkurt, and M. S. Toprak, “Microwave synthesis and characterization of Zn-doped nickel ferrite nanoparticles,” *Journal of Alloys and Compounds*, vol. 486, no. 1-2, pp. 325–329, 2009.

## Research Article

# Green Synthesis of Silver Nanoparticles Using *Polyalthia longifolia* Leaf Extract along with D-Sorbitol: Study of Antibacterial Activity

S. Kaviya,<sup>1</sup> J. Santhanalakshmi,<sup>1</sup> and B. Viswanathan<sup>2</sup>

<sup>1</sup>Department of Physical Chemistry, University of Madras, Chennai 600 025, India

<sup>2</sup>National Center for Catalysis Research, Indian Institute of Technology, Chennai 600 036, India

Correspondence should be addressed to S. Kaviya, kaviyahere@gmail.com

Received 23 March 2011; Accepted 16 June 2011

Academic Editor: Mallikarjuna Nadagouda

Copyright © 2011 S. Kaviya et al. This is an open access article distributed under the Creative Commons Attribution License, which permits unrestricted use, distribution, and reproduction in any medium, provided the original work is properly cited.

Synthesis of silver nanoparticles (AgNPs) using *Polyalthia longifolia* leaf extract as reducing and capping agent along with D-sorbitol used to increase the stability of the nanoparticles has been reported. The reaction is carried out at two different concentrations ( $10^{-3}$  M and  $10^{-4}$  M) of silver nitrate, and the effect of temperature on the synthesis of AgNPs is investigated by stirring at room temperature (25°C) and at 60°C. The UV-visible spectra of NPs showed a blue shift with increasing temperature at both concentrations. FT-IR analysis shows that the biomolecules played an important role in the reduction of Ag<sup>+</sup> ions and the growth of AgNPs. TEM results were utilized for the determination of the size and morphology of nanoparticles. The synthesized silver nanoparticles are found to be highly toxic against Gram-positive bacteria than Gram-negative bacteria.

## 1. Introduction

An important area of research in nanotechnology is the synthesis of nano silver particles. Silver has long been recognized as having an inhibitory effect towards many bacterial strains and microorganisms [1]. Antibacterial activity of the silver-containing materials used in medicine to reduce infections in burn treatment [2] and arthroplasty [3], as well as to prevent bacteria colonization on prostheses [4], catheters [5], vascular grafts, dental materials [6], stainless steel materials [7], and human skin [8]. Silver nanoparticles also exhibit a potent cytoprotective activity towards HIV-infected cells [9]. Because of such wide range of applications, numerous synthetic methods have been developed [10]. Biological routes of nanoparticles synthesis using microorganism [11–13], enzyme [14] and plant or plant extract [15–21] have been suggested as possible ecofriendly alternatives to chemical and physical methods. Using plant for nanoparticles synthesis can be advantageous over other biological processes by eliminating the elaborate process of maintaining cell cultures [22]. It can also be suitably scaled up for large-scale synthesis of nanoparticles. Specific surface area is relevant for catalytic

reactivity and other related properties such as antimicrobial activity in silver nanoparticles.

*Polyalthia longifolia* is a lofty evergreen tree, native to India, commonly planted due to its effectiveness in alleviating noise pollution. Methanolic extract of *Polyalthia longifolia* have yielded 20 known and 2 new organic compounds, some of which show cytotoxic properties [23]. Here in, we report for the first time synthesis of silver nanoparticles using aqueous extract derived from *Polyalthia longifolia* leaves with D-sorbitol and their catalytic and antibacterial activity of the synthesized NPs is described.

## 2. Experimental

The *Polyalthia longifolia* leaves were collected from University of Madras Campus located at Chennai, India. All the chemicals were obtained from Aldrich and experiments done in triplicates. Double-distilled water was used for the experiments. Fresh leaves of *Polyalthia longifolia* were collected, washed thoroughly with double-distilled water, and incised into small pieces. About 4 g of finely cut *Polyalthia longifolia* leaves were weighed and transferred into

a 250 mL beaker containing 40 mL double-distilled water, mixed well, and boiled for 2 min. The extract obtained was filtered through Whatman number 1 filter paper, and the filtrate was collected in 250 mL Erlenmeyer flask and stored at 4°C for further use.

Aqueous solution of  $10^{-3}$  M and  $10^{-4}$  M silver nitrate ( $\text{AgNO}_3$ ) and  $10^{-2}$  M of D-sorbitol was prepared and used for the synthesis of silver nanoparticles. 3 mL of extract and 1 mL of D-sorbitol were added to 40 mL of  $\text{AgNO}_3$  solution. The effect of temperature on the synthesis of silver nanoparticles was carried out at room temperature (25°C) and 60°C. The silver nanoparticles synthesized using *Polyalthia longifolia* leaf extract was tested for antimicrobial activity by agar well diffusion method against pathogenic bacteria *Escherichia coli*, *Pseudomonas aeruginosa* (Gram negative), and *Staphylococcus aureus* (Gram positive). The pure cultures of bacteria were subcultured on nutrient agar medium. Each strain was swabbed uniformly onto the individual plates using sterile cotton swabs. Wells of 10 mm diameter were made on nutrient agar plates using gel puncture. Using a micropipette, 50  $\mu\text{L}$  of nanoparticle solution was poured onto each well on all plates. After incubation at 37°C for 24 hours, the different levels of zone of inhibition of bacteria were measured.

The bioreduction of  $\text{Ag}^+$  ion in solution was monitored using UV-visible spectrometer (Techomp 8500 spectrometer). Further characterization was done using FTIR (Bruker tensor 27) spectrometer. The extract was centrifuged at 5000 rpm for 30 min and the resulting suspension was redispersed in 10 mL sterile distilled water. The centrifuging and redispersing process was repeated three times. Finally, the dried form of extract was palletized with KBr and analyzed using FTIR. The morphology of the AgNPs was examined using transmission electron microscopy (JEOL 3010 TEM). The films of the samples were prepared on a carbon coated copper grid by dropping a small amount of the sample and then allowing it to dry.

### 3. Results and Discussion

The time of addition of extract into the metal ion solution was considered as the start of the reaction. It is well known that silver nanoparticles exhibit yellowish brown color in aqueous solution due to excitation of surface plasmon vibrations in silver nanoparticles [15]. As the *Polyalthia longifolia* leaf extract was mixed in the aqueous solution of the silver ion complex and D-sorbitol, initially the color changed from watery to yellowish brown due to the reduction of silver ion. The reduction rate is found to increase with the reaction temperature [24]. For  $10^{-3}$  M solution the addition of 3 mL of extract to the reaction mixture, the reaction completed by 1.30 h, 1 h while  $10^{-4}$  M solution the reaction completed by 1 h, 40 min at 25°C and 60°C, respectively.

UV-vis spectroscopy could be used to examine size and shape controlled nanoparticles in aqueous suspensions [25]. Figure 1 shows the UV-vis spectra which are recorded after the completion of the reaction. For  $10^{-3}$  M solution, the silver nanoparticles have absorbance peak at 451 nm and 435 nm, and  $10^{-4}$  M solution has peak at 425 nm and 422 nm

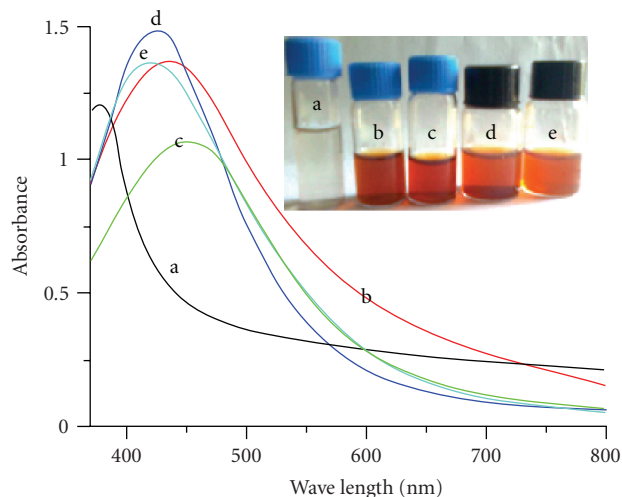


FIGURE 1: UV-vis absorption spectrum of (a) *Polyalthia longifolia* leaf extract, biosynthesized silver nanoparticles of different concentration ( $10^{-3}$  M and  $10^{-4}$  M) at (b and d) 25°C, (c and e) 60°C.

for reaction at 25°C and 60°C, respectively. The frequency and width of the surface plasmon absorption depend on the size and shape of the metal nanoparticles as well as on the dielectric constant of the metal itself and the surrounding medium [24]. Supposing the same particle shape, medium dielectric constant and temperature, the mean diameter of the nanoparticles strongly influence the SPR band in aqueous solution [25]. The spectrum shows the blue shift with raising temperature. This blue shift indicates the reduction of mean diameter of the biogenic silver nanoparticles [24, 26, 27].

FT-IR measurements were carried out to identify the possible biomolecules responsible for the reduction of the  $\text{Ag}^+$  ions and capping of the bioreduced silver nanoparticles synthesized by *Polyalthia longifolia* leaf extract along with D-sorbitol. Figure 2(b) represents the FTIR spectrum of D-sorbitol and shows bands at  $2938\text{ cm}^{-1}$  (C–H stretching in alkanes) and  $1645\text{ cm}^{-1}$  (C=O stretch of carbonyls). Figure 2(a) represents the FTIR spectrum of the leaf extract and shows peaks at  $1637$ ,  $1418$ , and  $1063\text{ cm}^{-1}$ . These peaks are known to be associated with the amide I arise due to carbonyl stretch in proteins ( $1637\text{ cm}^{-1}$ ), –C–C–stretch (in ring) aromatic ( $1418\text{ cm}^{-1}$ ) [28], and C–N stretching vibration of amine ( $1063\text{ cm}^{-1}$ ) [29], respectively. Proteins present in the extract can bind to AgNP through either free amino or carboxyl groups in the proteins [30]. Experimentally, D-sorbitol does not have the potential to reduce the silver ions in the solution, but it may cap the formed silver nanoparticles through electrostatic attraction or bind to the protein groups in the extract via hydrogen bond and increase the stability of the silver nanoparticles. It indicates that the functional groups in biomolecules are mainly responsible for the reduction of silver ions.

The silver nanoparticles are spherical in shape and are not aggregated in solution with raising temperature (Figure 3). This is due to the binding force between the AgNPs and the capping molecules that may get decreased with increasing temperature even though the size of the

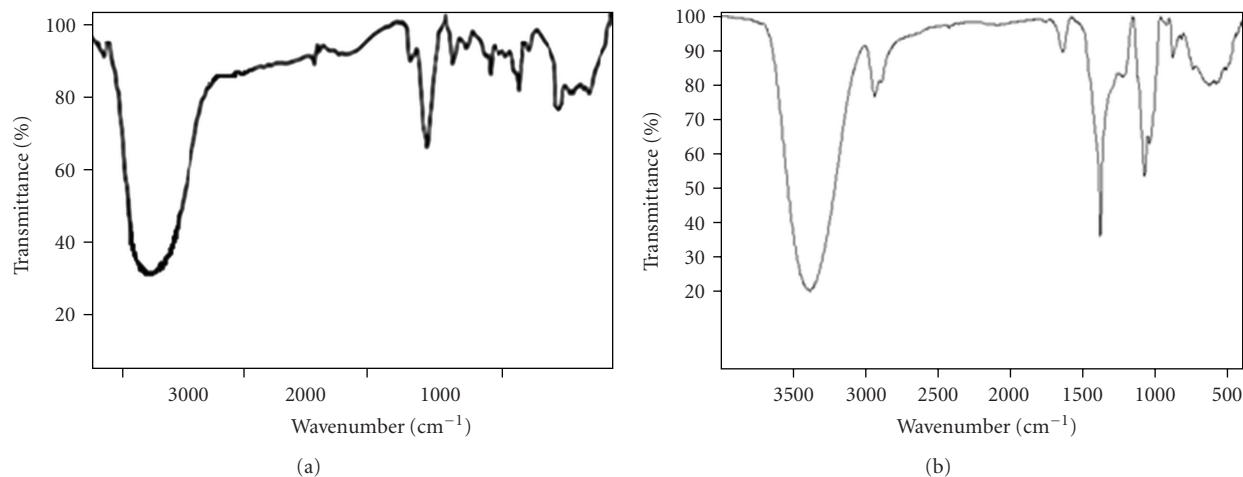


FIGURE 2: FTIR spectrum of (a) *Polyalthia longifolia* leaf extract and (b) D-sorbitol.

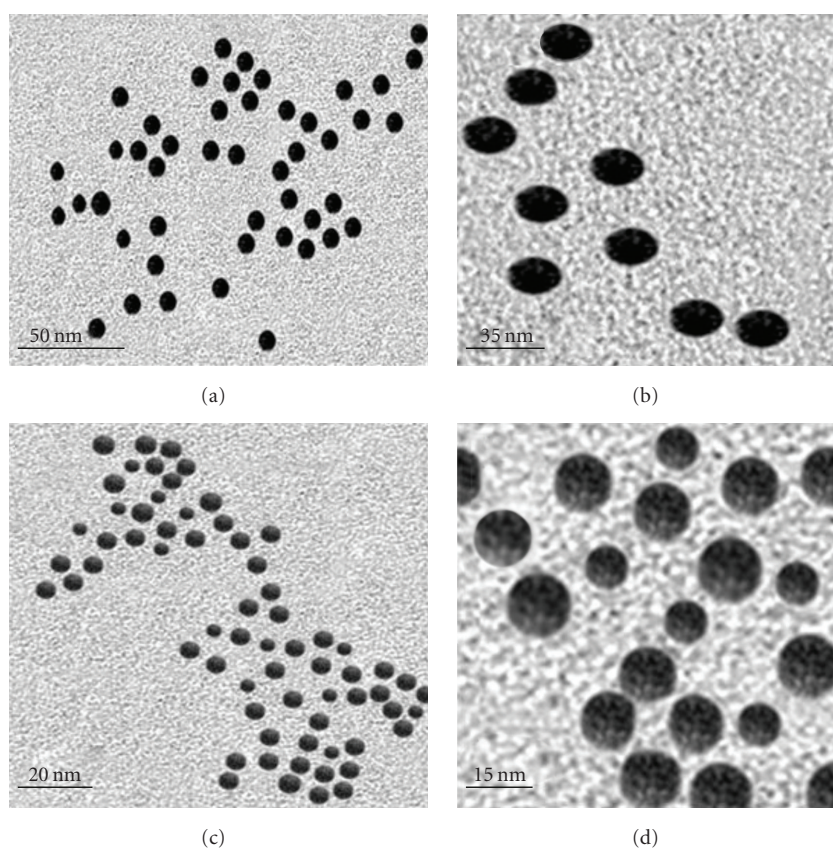


FIGURE 3: HRTEM image of the biosynthesized silver nanoparticles showing various particle sizes at (a and c) 25°C, (b and d) 60°C.

nanoparticles is reduced. In the  $10^{-3}$  M, the size of the synthesized nanoparticle is 50 nm and 35 nm at 25°C and 60°C, respectively. Similarly, in the case of  $10^{-4}$  M, the size of the synthesized nanoparticle is 20 nm and 15 nm at 25°C and 60°C, respectively.

The biologically synthesized silver nanoparticles exhibited excellent antibacterial activity against the bacterial pathogens *Staphylococcus aureus* (Gram positive), *Escherichia*

*coli*, and *Pseudomonas aeruginosa* (Gram negative) [31]. It has been reported that antibacterial effect was size and dose dependant and was more pronounced against Gram-negative bacteria than Gram-positive bacteria. But the present study clearly indicates that the synthesized silver nanoparticles have good antibacterial action against Gram-positive organism than Gram-negative organisms (Figure 4 and Table 1). The antimicrobial activities of colloidal silver particles are

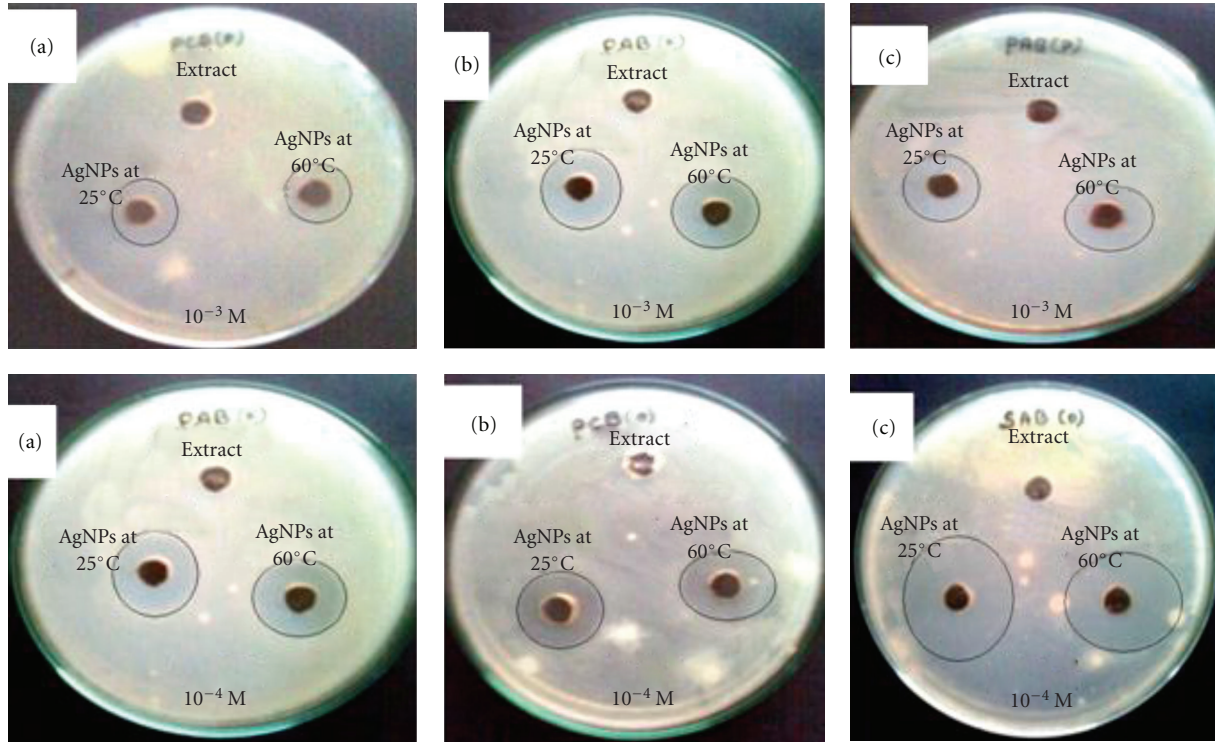


FIGURE 4: Zone of inhibition of silver nanoparticles against (a) *Escherichia coli*, (b) *Pseudomonas aeruginosa*, and (c) *Staphylococcus aureus*.

TABLE 1: Zone of inhibition (mm) of biologically synthesized silver nanoparticles against bacterial pathogens.

S. NO	Test organism	$10^{-3}$ M AgNPs synthesized at		$10^{-4}$ M AgNPs synthesized at	
		25°C	60°C	25°C	60°C
(1)	<i>Escherichia coli</i>	7.3	7.7	7.3	8
(2)	<i>Pseudomonas aeruginosa</i>	8.3	9	8.8	9.5
(3)	<i>Staphylococcus aureus</i>	14	16	14.6	16.4

influenced by the dimensions of the particles. The smaller particles lead to the greater antimicrobial effects [32]. The effect of antibacterial activity is higher in the case of silver nanoparticles synthesized at 60°C compared to 25°C because of being smaller in size [31, 33].

It is necessary to emphasize that the tested silver nanoparticles have bactericidal effects resulting not only in inhibition of bacterial growth but also in killing bacteria. Experiments conducted using the scanning tunneling electron microscopy (STEM) and X-ray energy dispersive spectrometer (EDS) showed that silver nanoparticles not only at the surface of cell membrane, but also inside the bacteria [34]. This suggests the possibility that the silver nanoparticles may also penetrate inside the bacteria and cause damage by interacting with phosphorus and sulfur containing compounds such as DNA [35]. The exact of inhibition of bacterial growth reported in

this study is dependent on the concentration and number of nanoparticles in medium.

#### 4. Conclusions

Silver nanoparticles were synthesized by *Polyalthia longifolia* leaves extract along with D-sorbitol. The spectroscopic characterization from UV-visible, FTIR, and TEM supports the stability of the biosynthesized nanoparticles. The nanosilver was found to have wider antimicrobial activity in Gram positive than Gram negative organisms. We believe that the silver nanoparticle has great potential for applications in catalysis, biomedical, and pharmaceutical industries.

#### References

- [1] H. Jiang, S. Manolache, A. C. L. Wong, and F. S. Denes, "Plasma-enhanced deposition of silver nanoparticles onto polymer and metal surfaces for the generation of antimicrobial characteristics," *Journal of Applied Polymer Science*, vol. 93, no. 3, pp. 1411–1422, 2004.
- [2] D. V. Parikh, T. Fink, K. Rajasekharan et al., "Antimicrobial silver/sodium carboxymethyl cotton dressings for burn wounds," *Textile Research Journal*, vol. 75, no. 2, pp. 134–138, 2005.
- [3] V. Alt, T. Bechert, P. Steinrücke et al., "An in vitro assessment of the antibacterial properties and cytotoxicity of nanoparticulate silver bone cement," *Biomaterials*, vol. 25, no. 18, pp. 4383–4391, 2004.
- [4] G. Gosheger, J. Harges, H. Ahrens et al., "Silver-coated megaendoprostheses in a rabbit model—an analysis of the

- infection rate and toxicological side effects," *Biomaterials*, vol. 25, no. 24, pp. 5547–5556, 2004.
- [5] M. E. Rupp, T. Fitzgerald, N. Marion et al., "Effect of silver-coated urinary catheters: efficacy, cost-effectiveness, and antimicrobial resistance," *American Journal of Infection Control*, vol. 32, no. 8, pp. 445–450, 2004.
- [6] S. Ohashi, S. Saku, and K. Yamamoto, "Antibacterial activity of silver inorganic agent YDA filler," *Journal of Oral Rehabilitation*, vol. 31, no. 4, pp. 364–367, 2004.
- [7] M. Bosetti, A. Masse, E. Tobin, and M. Cannas, "Silver coated materials for external fixation devices: in vitro biocompatibility and genotoxicity," *Biomaterials*, vol. 23, no. 3, pp. 887–892, 2002.
- [8] H. J. Lee and S. H. Jeong, "Bacteriostasis and skin innocuousness of nanosize silver colloids on textile fabrics," *Textile Research Journal*, vol. 75, no. 7, pp. 551–556, 2005.
- [9] R. W. Y. Sun, R. Chen, N. P. Y. Chung, C. M. Ho, C. L. S. Lin, and C. M. Che, "Silver nanoparticles fabricated in hepes buffer exhibit cytoprotective activities toward HIV-1 infected cells," *Chemical Communications*, no. 40, pp. 5059–5061, 2005.
- [10] M. Gutierrez and A. Henglein, "Formation of colloidal silver by "push-pull" reduction of  $\text{Ag}^+$ ," *Journal of Physical Chemistry*, vol. 97, no. 44, pp. 11368–11370, 1993.
- [11] T. Klaus, R. Joerger, E. Olsson, and C. G. Granqvist, "Silver-based crystalline nanoparticles, microbially fabricated," *Proceedings of the National Academy of Sciences of the United States of America*, vol. 96, no. 24, pp. 13611–13614, 1999.
- [12] Y. Konishi, K. Ohno, N. Saitoh et al., "Bioreductive deposition of platinum nanoparticles on the bacterium *Shewanella algae*," *Journal of Biotechnology*, vol. 128, no. 3, pp. 648–653, 2007.
- [13] B. Nair and T. Pradeep, "Coalescence of nanoclusters and formation of submicron crystallites assisted by *Lactobacillus*," *Crystal Growth and Design*, vol. 2, no. 4, pp. 293–298, 2002.
- [14] I. Willner, R. Baron, and B. Willner, "Growing metal nanoparticles by enzymes," *Advanced Materials*, vol. 18, no. 9, pp. 1109–1120, 2006.
- [15] S. S. Shankar, A. Rai, B. Ankamwar, A. Singh, A. Ahmad, and M. Sastry, "Biological synthesis of triangular gold nanoprisms," *Nature Materials*, vol. 3, no. 7, pp. 482–488, 2004.
- [16] D. Philip, C. Unni, S. Aromal, and V. K. Vidhu, "Murraya Koenigii leaf-assisted rapid green synthesis of silver and gold nanoparticles," *Spectrochimica Acta Part A*, vol. 78, no. 2, pp. 899–904, 2011.
- [17] R. Veerasamy, T. Z. Xin, S. Gunasagaran et al., "Biosynthesis of silver nanoparticles using mangosteen leaf extract and evaluation of their antimicrobial activities," *Journal of Saudi Chemical Society*, vol. 15, no. 2, pp. 113–120, 2011.
- [18] D. Philip, "Mangifera Indica leaf-assisted biosynthesis of well-dispersed silver nanoparticles," *Spectrochimica Acta Part A*, vol. 78, no. 1, pp. 327–331, 2011.
- [19] S. P. Dubey, M. Lahtinen, and M. Sillanpaa, "Tansy fruit mediated greener synthesis of silver and gold nanoparticles," *Process Biochemistry*, vol. 45, no. 7, pp. 1065–1071, 2010.
- [20] S. L. Smitha, D. Philip, and K. G. Gopchandran, "Green synthesis of gold nanoparticles using *Cinnamomum zeylanicum* leaf broth," *Spectrochimica Acta Part A*, vol. 74, no. 3, pp. 735–739, 2009.
- [21] A. R. V. Nestor, V. S. Mendieta, M. A. C. Lopez, R. M. G. Espinosa, M. A. C. Lopez, and J. A. Alatorre, "Solventless synthesis and optical properties of Au and Ag nanoparticles using *Camellia sinensis*," *Materials Letters*, vol. 62, no. 17–18, pp. 3103–3105, 2008.
- [22] S. S. Shankar, A. Rai, A. Ahmad, and M. Sastry, "Rapid synthesis of Au, Ag, and bimetallic Au core—Ag shell nanoparticles using neem (*Azadirachta indica*) leaf broth," *Journal of Colloid and Interface Science*, vol. 275, no. 2, pp. 496–502, 2004.
- [23] C. Y. Chen, F. R. Chang, Y. C. Shih et al., "Cytotoxic constituents of *Polyalthia longifolia* var. *pendula*," *Journal of Natural Products*, vol. 63, no. 11, pp. 1475–1478, 2000.
- [24] A. Rai, A. Singh, A. Ahmad, and M. Sastry, "Role of halide ions and temperature on the morphology of biologically synthesized gold nanotriangles," *Langmuir*, vol. 22, no. 2, pp. 736–741, 2006.
- [25] B. J. Wiley, S. H. Im, Z. Y. Li, J. McLellan, A. Siekkinen, and Y. Xia, "Maneuvering the surface plasmon resonance of silver nanostructures through shape-controlled synthesis," *Journal of Physical Chemistry B*, vol. 110, no. 32, pp. 15666–15675, 2006.
- [26] J. Y. Song and B. S. Kim, "Rapid biological synthesis of silver nanoparticles using plant leaf extracts," *Bioprocess and Biosystems Engineering*, vol. 32, no. 1, pp. 79–84, 2009.
- [27] A. M. Fayaz, K. Balaji, P. T. Kalaichelvan, and R. Venkatesan, "Fungal based synthesis of silver nanoparticles—an effect of temperature on the size of particles," *Colloids and Surfaces B*, vol. 74, no. 1, pp. 123–126, 2009.
- [28] H. Bar, D. K. Bhui, G. P. Sahoo, P. Sarkar, S. P. De, and A. Misra, "Green synthesis of silver nanoparticles using latex of *Jatropha curcas*," *Colloids and Surfaces A*, vol. 339, no. 1–3, pp. 134–139, 2009.
- [29] K. B. Narayanan and N. Sakthivel, "Coriander leaf mediated biosynthesis of gold nanoparticles," *Materials Letters*, vol. 62, no. 30, pp. 4588–4590, 2008.
- [30] A. Gole, C. Dash, V. Ramakrishnan et al., "Pepsin-gold colloid conjugates: preparation, characterization, and enzymatic activity," *Langmuir*, vol. 17, no. 5, pp. 1674–1679, 2001.
- [31] M. Singh, S. Singh, S. Prasad, and I. S. Gambhir, "Nanotechnology in medicine and antibacterial effect of silver nanoparticles," *Digest Journal of Nanomaterials and Biostructures*, vol. 3, no. 3, pp. 115–122, 2007.
- [32] C. Baker, A. Pradhan, L. Pakstis, J. Pochan Darrin, and S. S. Ismat, "Synthesis and antibacterial properties of silver nanoparticles," *Journal of Nanoscience and Nanotechnology*, vol. 5, no. 2, pp. 244–249, 2005.
- [33] C. Carlson, S. M. Hussein, A. M. Schrand et al., "Unique cellular interaction of silver nanoparticles: size-dependent generation of reactive oxygen species," *Journal of Physical Chemistry B*, vol. 112, no. 43, pp. 13608–13619, 2008.
- [34] J. R. Morones, J. L. Elechiguerra, A. Camacho et al., "The bactericidal effect of silver nanoparticles," *Nanotechnology*, vol. 16, no. 10, pp. 2346–2353, 2005.
- [35] D. W. Hatchett and H. S. White, "Electrochemistry of sulfur adlayers on the low-index faces of silver," *Journal of Physical Chemistry*, vol. 100, no. 23, pp. 9854–9859, 1996.

## Research Article

# Selective Oxidation Using Flame Aerosol Synthesized Iron and Vanadium-Doped Nano-TiO<sub>2</sub>

Zhong-Min Wang,<sup>1</sup> Endalkachew Sahle-Demessie,<sup>2</sup> and Ashraf Aly Hassan<sup>2</sup>

<sup>1</sup> Environmental Health Laboratory, California Department of Public Health, 850 Marina Bay Parkway, EHLB/G365, Richmond, CA 94804, USA

<sup>2</sup> U.S. Environmental Protection Agency, Office of Research and Development, National Risk Management Research Laboratory, Cincinnati, OH 45268, USA

Correspondence should be addressed to Endalkachew Sahle-Demessie, sahle-demessie.endalkachew@epa.gov

Received 20 December 2010; Accepted 13 April 2011

Academic Editor: Mallikarjuna Nadagouda

Copyright © 2011 Zhong-Min Wang et al. This is an open access article distributed under the Creative Commons Attribution License, which permits unrestricted use, distribution, and reproduction in any medium, provided the original work is properly cited.

Selective photocatalytic oxidation of 1-phenyl ethanol to acetophenone using titanium dioxide (TiO<sub>2</sub>) raw and doped with Fe or V, prepared by flame aerosol deposition method, was investigated. The effects of metal doping on crystal phase and morphology of the synthesized nanostructured TiO<sub>2</sub> were analyzed using XRD, TEM, Raman spectroscopy, and BET nitrogen adsorbed surface area measurement. The increase in the concentration of V and Fe reduced the crystalline structure and the anatase-to-rutile ratios of the synthesized TiO<sub>2</sub>. Synthesized TiO<sub>2</sub> became fine amorphous powder as the Fe and V concentrations were increased to 3 and 5%, respectively. Doping V and Fe to TiO<sub>2</sub> synthesized by the flame aerosol increased photocatalytic activity by 6 folds and 2.5 folds, respectively, compared to that of pure TiO<sub>2</sub>. It was found that an optimal doping concentration for Fe and V were 0.5% and 3%, respectively. The type and concentration of the metal dopants and the method used to add the dopant to the TiO<sub>2</sub> are critical parameters for enhancing the activity of the resulting photocatalyst. The effects of solvents on the photocatalytic reaction were also investigated by using both water and acetonitrile as the reaction medium.

## 1. Introduction

Titanium dioxide (TiO<sub>2</sub>) is a photocatalyst that is used for various applications; such as wastewater and air treatments, virus disinfection and water splitting due to its low cost and its high activity and stability under irradiation. However, TiO<sub>2</sub> has a large band gap energy (3.2 eV) that prohibits the use of visible light to activate it and requires UV light of wavelength ranging 320~400 nm to generate electron-hole pairs. Searching for semiconductors that absorbs large portion of solar spectrum reaching the earth has been intensified. Recently, there has been increasing interest in doping TiO<sub>2</sub> with transition metal or nonmetal species, such as nitrogen and sulfur, to narrow or shift the band gap in order to activate the catalyst using visible light [1–6]. Doping metals in TiO<sub>2</sub> matrix could increase the photocatalytic performance of TiO<sub>2</sub> with irradiation both UV and visible light because of better conducting characteristics. Metal doping

can also change the physical properties, such as lifetime of electron-hole pair and adsorption characteristics. Various transition metals have been used as doping materials [7–11], and many systems have been tested for potential commercial applications [1, 6] as well as improving photocatalyst activity of TiO<sub>2</sub> in visible light range [12–18].

However, the effects of metal doping on catalytic properties of the TiO<sub>2</sub> are not conclusive. There are also no general guidelines to be followed in the selection of metal species or the methods of photocatalyst preparation that would result in improved activity. Although doping with transition metals at low concentrations has positive effects on the photocatalytic activity of TiO<sub>2</sub> [19, 20], some dopants have shown adverse effects [1, 21]. There is a progressive shift of the light absorption threshold toward the visible light range when increasing amounts of cations M<sup>+n</sup> (M: Cr, V, Fe, Co), but no improvement of the photoactivity of the system was observed [22]. Metal doping of TiO<sub>2</sub> with Cr<sup>3+</sup> and Mo<sup>5+</sup>

ions have shown to narrow the band gap of  $\text{TiO}_2$ , change other physical properties such as the lifetime of electron-hole pairs and adsorption characteristics of the catalyst [23]. The presence of doping species either on the surface or in the lattice and the method how the metal species is deposited or combined with the  $\text{TiO}_2$  are critical to photocatalytic activity. Doping metal species in the matrix has been suggested to create a hole-trap or an electron-hole recombination center rather than an electron trap. Dvoranová et al. [24] suggested that transition metals should be coated mainly on the surface of the photocatalyst to form an electron trap and hence promote photocatalysis, although their results are inconclusive. The difference in results could be derived from differences in preparation methods, synthesis conditions, and position of doped species on the surface or in the crystal lattice structure of  $\text{TiO}_2$  [25]. Overload metal species on  $\text{TiO}_2$  promote either phase change [26] or recombination of the electron-holes by dramatically changing conductivity of materials [27], becoming detrimental to the photocatalytic activity. Therefore, optimal dopant concentration is usually reported for the best photocatalyst performance [27–32].

Flame aerosol synthesis of nanoparticles have been used for large-scale manufacturing of ceramic powders such as pigmentary  $\text{TiO}_2$ , fumed silica, and alumina [33]. Advances in this field has allowed the production of more complex products with high functionality including molecular doping of small quantities of materials in the preparation of ceramic materials [34]. The technology has been used to produce highly active nanostructured coatings with closely controlled morphology and composition [33, 35, 36]. Flame synthesis technology could be a more effective way to make versatile and low cost nanostructured materials, such as carbon nano-tubes [37]. This study aims to synthesize metal-doped nanostructured catalysts using the flame aerosol technology and test the effect of doping on photo-activities of the resulted nanostructured catalysts. In this study photocatalytic performance of Fe or V doped  $\text{TiO}_2$  synthesized using flame aerosol process in addition to further characteristics are presented. Iron was chosen because of its low toxicity and the wide availability of data as a doping material. Studies indicated that V is one of the promising doping materials [34, 38, 39], therefore it is a good choice as a doping material.

Selective catalytic oxidation of alcohols to carbonyls is one of the most important chemical transformations in chemical industry. Acetophenone is the simplest aromatic ketone with a melting point of  $20^\circ\text{C}$  and has low water solubility. It is an important intermediate in chemical and pharmaceutical industries. It is used for fragrance in soaps and perfumes, as a flavoring agent in food, and as a solvent for plastics and resins. In addition, it is used as a polymerization catalyst for the manufacture of olefins, as an intermediate for pharmaceuticals, agrochemicals, and other organic compounds as well as a drug to induce sleep.

Commercial acetophenone production involves Friedel-Crafts acylation of benzene with acetic anhydride or acetyl chloride. Friedel-Craft alkylation is commonly condensed using homogeneous acid catalysts such as aluminum chloride at more than stoichiometric amounts with acetyl chloride as the acylating agent. This process may create

pollution problems related to the disposal of the catalyst and treatment of acidic effluent. It can be also obtained by air oxidation of ethyl benzene, as a by-product of cumene or from acrylonitrile.

Dehydrogenation of secondary alcohol is usually carried out using chromic acid or sulfuric acid with potassium dichromate. However, in the current work, a simple process was developed based on the utilization of heterogeneous catalysts to produce acetophenone by photocatalytic oxidation of 1-phenylethanol. The photooxidation process is cleaner than the conventional synthetic method since the reaction by-product is water, and the photocatalyst can be easily recycled back to the reaction system. The oxidation of 1-Phenylethanol was selected as a probe molecule for this study. There are studies that have shown that the preparation methods of meta-doped  $\text{TiO}_2$  can be critical in promoting the photoactivity [40].

## 2. Experimental

*2.1. Materials and Preparation of Metal-Doped  $\text{TiO}_2$  using Flame Aerosol Methods.* Schematic diagram of the flame aerosol synthesis system for preparing the pure and vanadium doped- $\text{TiO}_2$  is shown in Figure 1(a). The system consists of a diffusion burner, an atomizer for generating aerosol from the titanium (IV) Isopropoxide (TTIP) (97% Aldrich Chemical) a precursor for  $\text{TiO}_2$ , a water-cooled stainless steel plate for collecting the products. Mass flow controllers were used to adjust the flow rates of methane, oxygen, and air. The organic form of the vanadium, vanadium (V) oxy-triisopropoxide (98%, Aldrich Chemical), was easily dissolved in TTIP in the atomizer at preset ratios. The mixture of precursors flowed to the flame through the center port of the diffusion burner. Methane and oxygen were fed through the second and outer ports, respectively. Schematic diagram of the flame aerosol reactor system for preparing iron-doped titanium dioxide is shown in Figure 1(b). A solution of  $\text{Fe}(\text{NO}_3)_3$  was used as the iron source since it is more stable and less volatile than Fe carbonyl. Varying concentrations of the iron nitrate water solution were used to obtain desired amounts of Fe doping. Water was removed from the flow via diffusion dryer before aerosols reach the flame reactor to avoid quenching and allow better control of the flame temperature that may result in forming big clump in the transport tube. Earlier experiments indicated that in the case of Fe doping the stream bearing precursor material has to flow through the out port of the burner to generate higher anatase-to-rutile ratio in the  $\text{TiO}_2$ . The  $\text{TiO}_2$  precursor and oxygen were introduced through the center port of the burner and methane flowed through the middle annular tube. The precursor oxidized in the flame and metal-doped  $\text{TiO}_2$  was deposited on a water-cooled stainless steel plate placed above the flame and controlled by an automatic rotating frame support. The flame temperatures were controlled by adjusting the gas flow rates and controlling the fuel-to-air ratios. The quench temperature profile was adjusted by controlling the rotating speed and the cooling water flow rate into the cooling plate. The quenching temperature affected the particle size and the morphology of

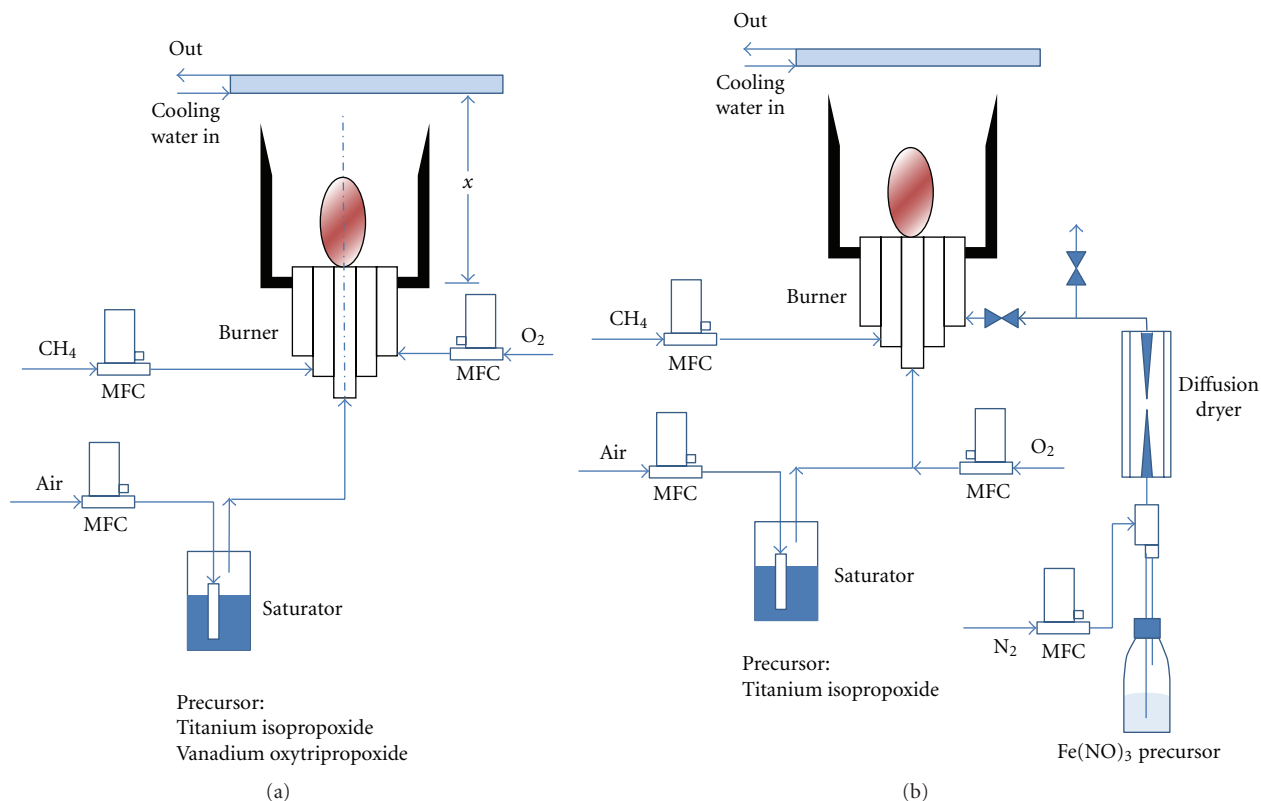


FIGURE 1: Multiannular coflow diffusion burner for synthesizing nanostructured  $\text{TiO}_2$  with (a) vanadia doped, (b) Fe doped.

TABLE 1: Typical flame synthesis condition for the metal doped  $\text{TiO}_2$ .

Flow	Pure $\text{TiO}_2$	V-doped $\text{TiO}_2$	Fe-doped $\text{TiO}_2$
$\text{CH}_4$ (L/m)	1.00	1.00	1.13
$\text{O}_2$ (L/m)	1.00	1.00	1.00
Air (L/m)	3.88	3.88	3.88
Doping flow (L/m)	—	—	0.30

the  $\text{TiO}_2$  particles. The position of the cooling plate above the flame determined the reaction time of the  $\text{TiO}_2$  precursor in the flame, which is a critical parameter to determine the primary particle size and the characteristics of the flame-synthesized  $\text{TiO}_2$ . A large number of preliminary tests, XRD, and Raman spectroscopy measurements were conducted to determine suitable operation conditions that afforded for desired crystalline structure, form, particle size, and doping concentrations of  $\text{TiO}_2$ . The typical experiment conditions for the flame aerosol synthesis process are shown in Table 1.

**2.2. Characterization of the Synthesized Samples.** X-ray diffraction pattern of powder samples of metal-doped  $\text{TiO}_2$  were characterized by XRD (Rigaku D-2000) for recording and for determining the crystal structure. Transmission Electron Microscopy (TEM) (Philips, PW6060) was used to determine the surface morphology and particle size of

the doped catalysts. The BET surface area was measured by AutoChem 2920 (Micromeritics, Atlanta, GA). Bulk doping concentrations of the metal species in the synthesized photocatalysts were determined by inductively coupled plasma (ICP) emission spectroscopy (Perkin Elmer Optima 3300 DV).

**2.3. Photocatalytic Reaction.** Photocatalytic activities of neat, vanadium, or Fe-doped  $\text{TiO}_2$  were evaluated using oxidation of a probe molecule, 1-phenylethanol to acetophenone in two different solvents. All experiments employed the same light source. The reactions were performed in a 20 mL microbatch reactor equipped with Pen-Ray 5.5 Watts UV lamp (TM UVP, Inc. San Gabriel, CA). The irradiance at the reactor surface was  $15 \text{ mW/cm}^2$  as measured with a photometer (International Light Inc. model IL 1400A). The schematic diagram of the microreactor system is shown in Figure 2. Neat and doped  $\text{TiO}_2$  (0.05 g/L) were suspended in the microreactor that contained 20 mL reaction medium with substrate concentration at 20 ppm. Water or acetonitrile were used as the reaction medium to study the effect of solvents. The mixture was well stirred during the reaction process using a magnetic stirrer. The UV lamp was placed at the center of the reactor, and oxygen was supplied for the oxidation. Since adsorbed oxygen served as a trap for the photogenerated conduction band electron in many heterogeneous photocatalytic reactions [41], solvents were saturated with  $\text{O}_2$  prior to the reaction study. The reactions

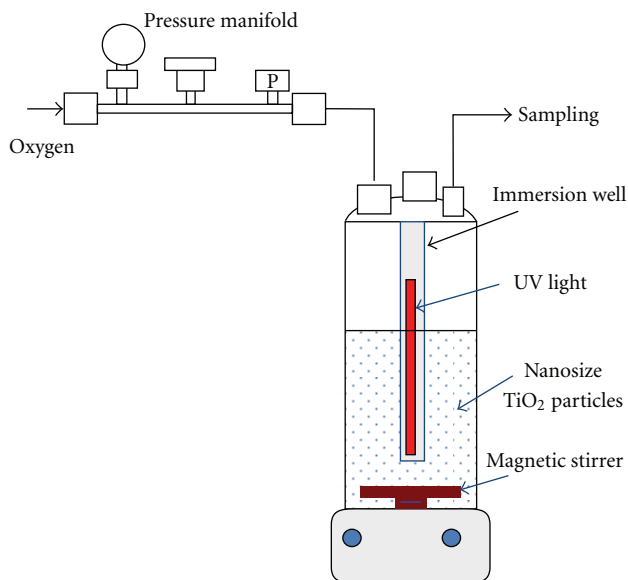


FIGURE 2: Schematic of the micro reactor system for photooxidation.

were conducted at room temperature and at atmospheric pressure. Control studies were made to measure the photocatalytic activity of neat flame synthesized anatase phase TiO<sub>2</sub> and commercially available TiO<sub>2</sub> from Degussa (P25). Liquid samples were collected through the reactor sample port at selected time intervals, and the mixtures were analyzed using a Hewlett-Packard 6890 gas chromatograph with a low-bleed HP-5MS (30 m × 0.25 mm × 0.25 mm) column and a split/splitless injector. A mass selective detector equipped with a quadrupole mass filter (Hewlett-Packard 5973) was used for detection of the samples. Quantification of the oxygenated products was obtained using a multipoint calibration curve for each product.

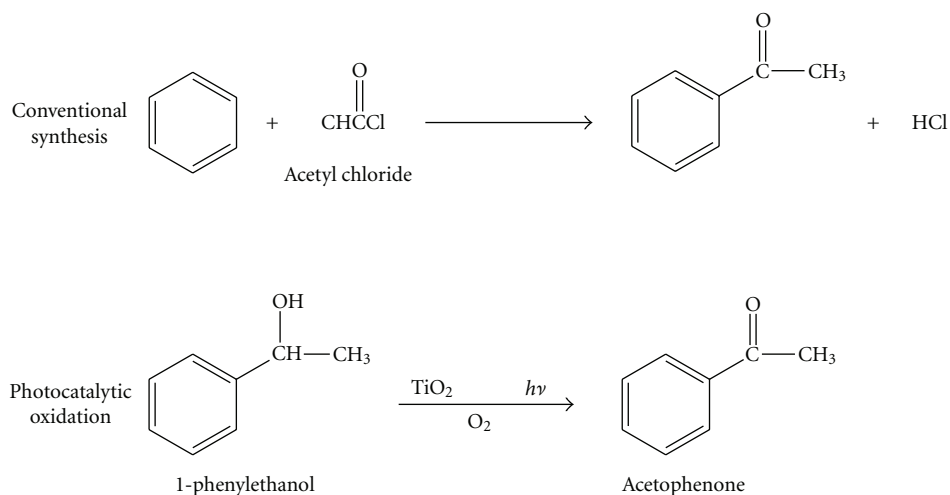
### 3. Results and Discussion

**3.1. Structural Characteristics of Metal-Doped TiO<sub>2</sub>.** The X-ray diffraction patterns for neat TiO<sub>2</sub> samples and for Fe-doped TiO<sub>2</sub> with different Fe concentrations are shown in Figure 3. The primary crystalline structure of the pure TiO<sub>2</sub> was the anatase phase. As the doped Fe concentration increased, the anatase TiO<sub>2</sub> phase fraction decreased, reaching almost amorphous structure and losing its catalytic activity as the Fe concentration exceeded 2% in atom ratio. Similar XRD patterns were observed when the vanadium concentrations of the doped TiO<sub>2</sub> increased beyond 4 wt%. However, the concentrations of vanadium can reach as much high as 5% wt. before major changes in the crystal structure was detected. Other researchers have observed that niobium and vanadium stabilize the anatase crystalline form of TiO<sub>2</sub> [27, 42]. No diffraction peaks originating from V<sub>2</sub>O<sub>5</sub> crystallite were detected from the vanadium dispersed on the TiO<sub>2</sub>, which could be due to the presence of vanadyl groups (V<sup>4+</sup>) or polymeric vanadates (V<sup>5+</sup>). A previous study [26] has shown that the increase in the doped metal ion concentrations interferes in flame synthesis of TiO<sub>2</sub>

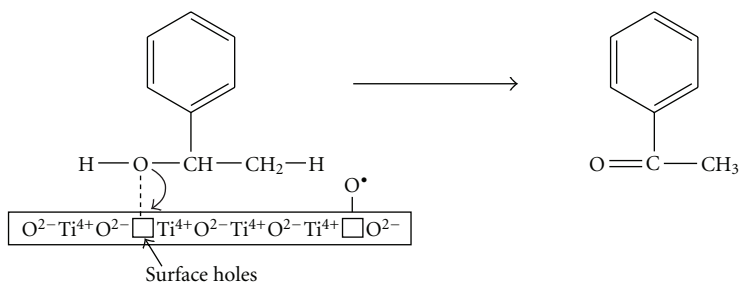
converting some of the anatase phase to rutile, and finally it became amorphous.

The Raman spectrum for the neat and Fe-doped TiO<sub>2</sub> are shown in Figure 4. A well-resolved Raman peak is seen at 153 cm<sup>-1</sup>, and three broader features are found in the high-frequency region located at around 415, 515, and 630 cm<sup>-1</sup>. In spite of their lower intensity and broader line width, all the Raman features observed in the spectra are close to those in the bulk anatase phase. The Raman spectra of the nanophase TiO<sub>2</sub> after different amounts of Fe were doped is shown in Figure 4. One significant observation of these spectra is the reduced intensity of the lowest-frequency Eg mode with increased amounts of Fe and a shift in peak position of the 153 cm<sup>-1</sup>, indicating the decrease in the crystalline quality of the TiO<sub>2</sub>. Therefore, the result confirms XRD data that the neat TiO<sub>2</sub> possesses higher degree of long-range order of anatase phase. However, with increase in Fe concentration the peak intensity attenuated gradually, and the weak overlapped broader peaks in the high-frequency region indicate that the short-range order is poor and optical phonons may decay as imperfect sites. Table 2 summarizes surface area changes for different doping concentrations of flame-synthesized Fe-doped TiO<sub>2</sub>. As the doped Fe concentrations increased, the particles gradually lost crystalline structure and the products surface area increased. The surface area of vanadium-doped TiO<sub>2</sub> also increased with increase in the amount of doping, shown in Table 3. Comparison of TEM images of pure TiO<sub>2</sub>, and V- or Fe- doped TiO<sub>2</sub> suggested that the doped metal ions to be present on the top layers of the TiO<sub>2</sub> particles shown as Figure 5. Ranjit and Viswanathan [31] have reported that the solid solution of TiO<sub>2</sub> with doping materials in the top few layers of the surface promote the photocatalytic activity of the catalyst. Shah et al. [43] confirmed that photocatalytic efficiency of TiO<sub>2</sub> can be enhanced by homogeneous doping of Nd<sup>3+</sup>, Pd<sup>2+</sup>, and Pt<sup>4+</sup>, but Fe<sup>3+</sup> doping resulted in little or no improvements. TEM images show that when the doping concentration is not relatively high, both of the Fe- and V-doped TiO<sub>2</sub> have similar spherical shapes and uniform particle sizes ranging from 10 to 50 nm. As the doping concentration increases the TiO<sub>2</sub> particle sizes become smaller, more agglomerated, and resulting in larger surface areas and change of crystallinity.

**3.2. Photocatalytic Oxidation of Aromatic Alcohol.** In this study, the photocatalytic conversion oxidation of 1-phenylethanol to acetophenone was tested using undoped TiO<sub>2</sub> prepared by flame aerosol method and from Degussa, Fe- and V-doped TiO<sub>2</sub>. Gas phase oxidation of 1-phenyl ethanol produced multiple products such as benzaldehyde, styrene, toluene, and acetophenone; however, in liquid phase acetophenone was the main product observed [44]. Therefore, the yield of acetophenone that is acetophenone produced/1-phenyl-ethanol consumed is more than 95%. The initial reaction of photocatalytic oxidation 1-phenylethanol takes place on the surface of TiO<sub>2</sub>, where the primary hole reaches the surface and interacts with the surface hydroxyl groups followed by an electron transfer to the hole to form species like OH<sup>·</sup> and ≡TiO<sup>·</sup> [45]. These species react via a mediated pathway. At high alcohol



SCHEME 1

SCHEME 2: Photocatalytic oxidation of 1-phenyl ethanol to acetophenone over  $\text{TiO}_2$  ( $\square$  = surface hole).TABLE 2: BET surface area of codeposited Fe-doped  $\text{TiO}_2$  prepared with flame aerosol method.

Photocatalyst	Fe concentration (wt.%)	BET surface area ( $\text{m}^2/\text{g}$ )	% anatase
Degussa	0	51.0	82
Flame-synthesized	0	73.0	95
Pure $\text{TiO}_2$			
Fe-doped I	0.55	83.4	80
Fe-doped II	1.18	94.6	52
Fe-doped III	3.0	143.6	Amorphous
Fe-doped IV	5.0	198.3	Amorphous

TABLE 3: BET surface area of codeposited Vanadium-doped  $\text{TiO}_2$  prepared with flame aerosol synthesis.

Photocatalyst	V concentration (%)	BET surface area ( $\text{M}^2/\text{g}$ )	% anatase
Degussa	0	51	82
Flame-synthesized	0	73	95
Pure $\text{TiO}_2$			
V-doped I	1.78	64.7	90
V-doped II	3.00	68.3	86
V-doped III	4.47	90.6	63
V-doped IV	4.84	96.2	57
V-doped V	4.95	120.7	Amorphous

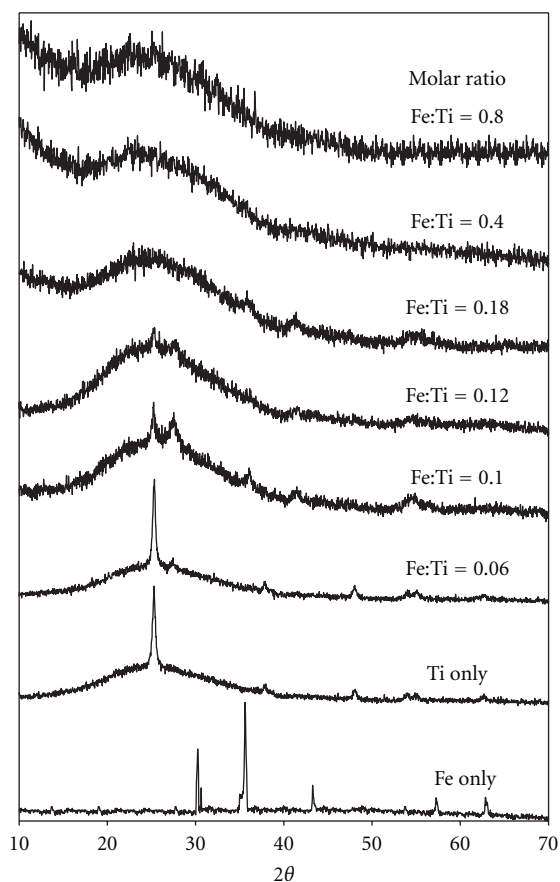


FIGURE 3: X-ray diffraction patterns of flame aerosol prepared iron deposited  $\text{TiO}_2$  at different doping concentrations.

concentration, which is the case, there could also be a direct interaction of the surface hole with the hydroxyl group of the alcohol [46]. In addition, alcohols may undergo dehydration on the catalyst surface during photocatalytic oxidation reaction [47, 48].

The initial photooxidation step here may be the interaction of a surface hole with the hydroxyl group of the alcohol forming a metal-oxo species with the removal of a proton (Scheme 2) [45]. This proton removal step becomes easier with increased carbon chain branching as well as with increased carbon chain length, because of the increased availability of adjacent removable protons. The higher the number of adjacent hydrogen atoms present, the easier is the removal and the greater would be the conversion. It was observed that presence of a benzene ring enhanced the conversion. The linking of phenyl rings of 1-phenylethanol to the  $\text{TiO}_2$  surface via a  $\pi$ -OH interaction, an inhibition effect may be produced, preventing phenyl group migration; the formation of phenyl ethanol hydroperoxide species, which may give acetophenone and water. This can be attributed to the electron-deficient nature of the benzene ring, which results in a reduced electron density at oxygen-hydrogen bond, thereby making the proton abstraction relatively easier. In gas phase processes, styrene has been formed from 1-phenylethanol due to the photocatalytic-induced dehydration of the alcohol [41].

Photooxidation of cumene to acetophenone in acetonitrile has been reported [49], where IR and XPS analysis of cumene adsorption on  $\text{TiO}_2$  have shown that an interaction of the benzene ring with surface OH groups takes place without appreciable dehydration or dehydroxylation of the surface. Acetophenone and  $\text{CO}_2$  were the only reaction products detected, and the reaction proceeds with the intermediate of a hydroperoxide.

**3.3. Influence of Doping Concentration.** Photocatalytic oxidation of 1-phenylethanol over raw nano-phase  $\text{TiO}_2$  in aqueous medium (pH = 6.4) after 3 hours of run gave only 4% conversion. No significant difference in photoactivity was observed between the  $\text{TiO}_2$  prepared using flame aerosol method and the Degussa (P25). Reaction using both V and Fe-doped  $\text{TiO}_2$  gave higher conversions than the reaction with neat  $\text{TiO}_2$ . Other studies have shown that metal-doped  $\text{TiO}_2$  have faster electron-hole recombination rate than the raw neat  $\text{TiO}_2$  including those doping on  $\text{TiO}_2$  surface by impregnation method [50]. The yield of acetophenone formed as a function of the amount of Fe- and V-doped on the  $\text{TiO}_2$  are shown in Figures 7 and 8, respectively. For both of Fe- and V-doped  $\text{TiO}_2$  there were doping concentrations that gave optimal yields of acetophenone at the reaction time of 3 hours (Figures 7 and 8). The optimal doping amount for Fe is about 0.6% wt, and 15% yield of acetophenone, whereas the optimal concentration for V-doped  $\text{TiO}_2$  of about 3 wt% gave 40% yield of acetophenone. Increasing or decreasing the metal-doping concentration lowered the catalyst activity. Vanadium doping greatly improved the photoactivity compared to those of pure or Fe-doped  $\text{TiO}_2$ . Previous studies indicated that the formation of the photoactive complex by  $\text{Fe}^{3+}$  with organics play a key role in promoting photocatalytic reaction. Increasing  $\text{Fe}^{2+}$  of nano- $\text{TiO}_2$  attenuate the photocatalytic activity [51].

One of the possible reasons for the optimal doping concentration is the competing effects between the recombination rate of the electron and hole pairs on the catalyst surface, and the hole capture rate by the substrate. At low metal concentrations, the metal ions do not affect the bulk electronic structure of the semiconductor and its electron-hole generation and separation capacity. As a result, the photoactivity slowly increases with doped metal concentration. At excess metal concentration, the metal ions may sharply increase the conductivity of the resulted materials and the recombination rate of the photogenerated electron-hole pairs. Further increase of the doping concentration did not favor enhanced activity. It has been previously observed that incorporating cations of valence higher than that of the parent cation, such as  $\text{W}^{6+}$ ,  $\text{Ta}^{5+}$ , and  $\text{Nb}^{5+}$ , into the crystal matrix of  $\text{TiO}_2$  resulted in enhanced rates of water cleavage while the opposite is observed upon doping with cations of lower valence, such as  $\text{In}^{3+}$ ,  $\text{Zn}^{2+}$ , and  $\text{Li}^+$  [52]. The change in the photocatalytic activity is found to be dependent on the concentration and valence of the doping cations. Those results are explained in terms of alteration of the bulk electronic structure of the semiconductor, which influences its electron-hole generation and separation capacity under illumination.

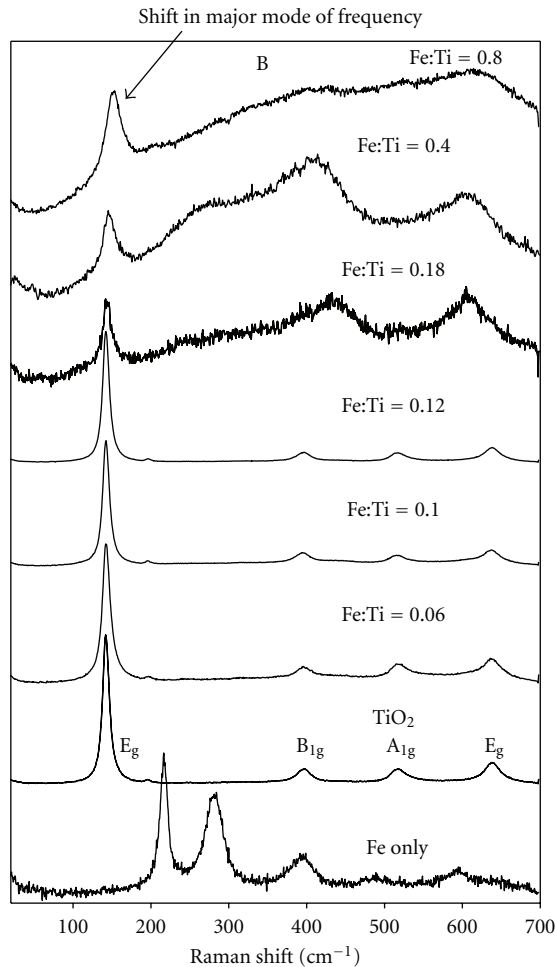


FIGURE 4: Raman spectra of nanostructured  $\text{TiO}_2$  flame aerosol synthesized doped with increasing amounts of Fe.

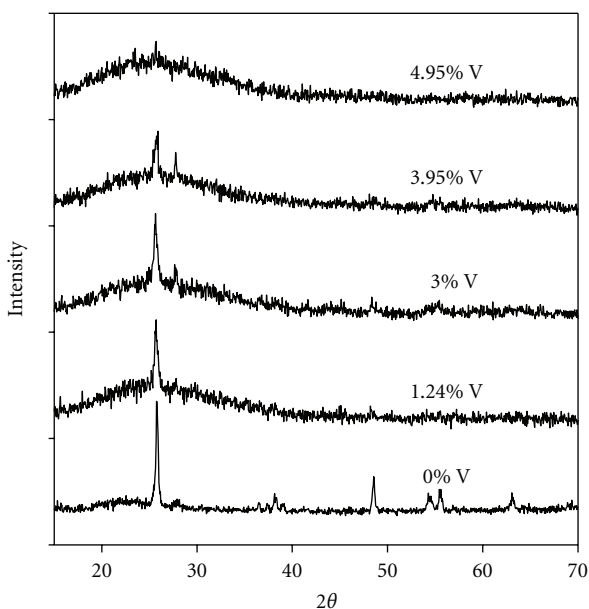
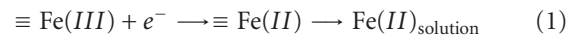
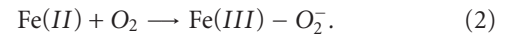


FIGURE 5: X-Ray diffraction patterns of flame aerosol prepared vanadium-deposited  $\text{TiO}_2$  at different doping concentrations.

Studies have also indicated problems concerning the stability of  $\text{Fe-TiO}_2$  photocatalysts [53]. One major cause of a decrease in activity was photocorrosion leading to loss of Fe from the doped material



competing with the activation of oxygen



With increased doping concentrations of both Fe and V, the crystal structure and the morphology of catalyst have changed, and the size of catalyst particles decreased. As particle size decreased, the total catalyst surface area increased and the photogenerated electron density on the surface of each particle increased. This could have enhanced the photocatalytic reaction. However, with increase in the density of the electron-hole pairs, the possibility of the recombination of the electrons and holes also increases, which could be one of the reason that there is an optimal particles size that allowed highest conversion for the photocatalytic reaction.

Doping of metal ions in  $\text{TiO}_2$  can alter its bulk electronic structure, which influences its electron-hole generation and separation capacity under light illumination. Compared to Fe-doped samples, higher concentrations of vanadium were doped to the  $\text{TiO}_2$  while maintaining the anatase crystal structure. On the other hand, V-doped photocatalyst has shown higher photocatalytic activity compared to Fe-doped and neat  $\text{TiO}_2$  samples. One of the possible reasons for the significant difference in the photocatalytic activity in the  $\text{TiO}_2$  doped with the two metals is that iron has larger electric conductivity than vanadium. Higher amounts of Fe allowed easier recombination of the electrons and holes which resulted in deleterious effects on the photoactivity of the doped  $\text{TiO}_2$ . Vanadium has lower conductivity than iron therefore its concentration could be higher in the doped  $\text{TiO}_2$  and with little change in the catalytic materials' conductivity. Higher valence of  $\text{V}^{5+}$  could also help the photoactivity of the resulted catalyst [52].

**3.4. Solvent Effect.** The reaction in acetonitrile gave higher conversions than in water. The effects of using either water or acetonitrile as solvents on photocatalytic oxidation of 1-phenylethanol studied are shown in Figures 7 and 8. For V-doped  $\text{TiO}_2$ , the increase in conversion of 1-phenylethanol with dopant concentration was 5 to 6 times higher in acetonitrile compared to the reaction in aqueous medium. Acetonitrile afforded much higher conversions compared to that in an aqueous medium because of the higher solubility of 1-phenylethanol in acetonitrile limiting the availability of the reactants in water leading to the low reaction rate [54]. The lower activity of the photocatalyst in water could also be attributable to the hydrophobic nature of  $\text{TiO}_2$  limiting the adsorption of 1-phenylethanol. Water molecules cover most of the titanium dioxide slurry surface due to their polarity, and the available surface for 1-phenylethanol directly interacts with the catalyst becoming less and the diffusion resistance is increased for both of the reactant and products.

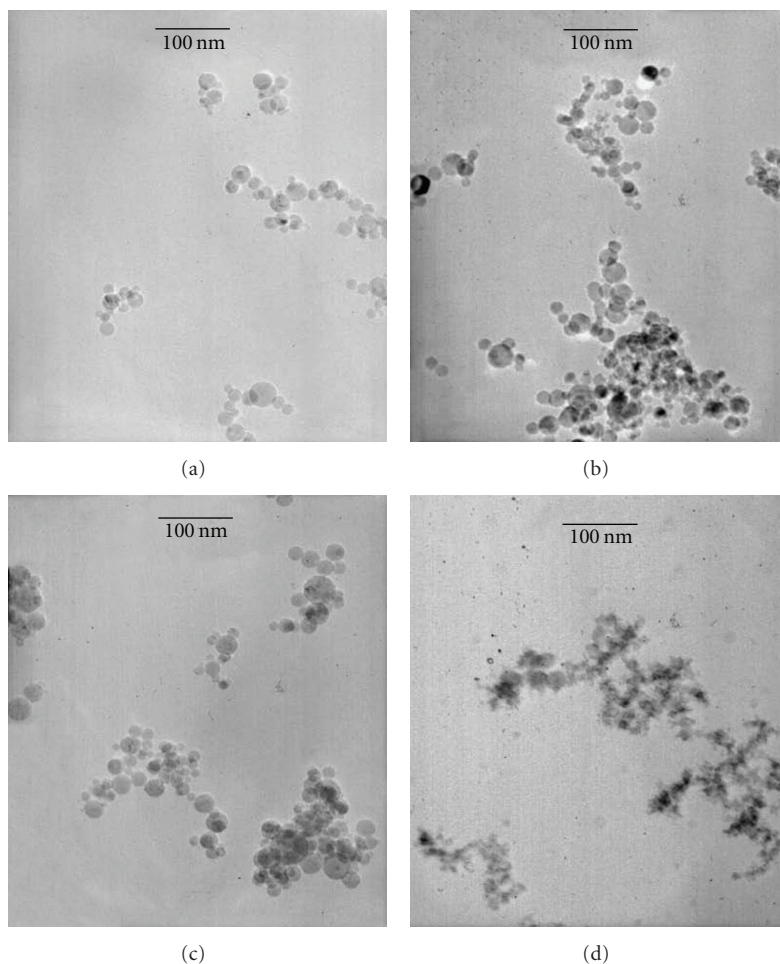


FIGURE 6: Transmission electron micrograph of the pure or doped  $\text{TiO}_2$  particles: (a) pure  $\text{TiO}_2$  particles using the TTIP Precursor; (b) 0.6 wt% Fe-doped  $\text{TiO}_2$  particles; (c) 2 wt% V-doped  $\text{TiO}_2$  particles; and (d) 2 wt% Fe-doped  $\text{TiO}_2$ .

Selective adsorption of reactants on the  $\text{TiO}_2$  surface was found to account for differences in product selectivity [55]. Solvents such as chloroform strongly inhibit the photooxidation process due to the fact that it could compete with the hydrocarbon for oxidation and with  $\text{O}_2$  for reduction. Differences in reaction rates and chemoselectivity of products was also observed when aqueous medium was compared to those of organic solvents [56]. Solvent effects have been attributed to the stabilization of cation radicals intermediates. A highly efficient photocatalytic process of linear olefins epoxidation by molecular oxygen, using  $\text{TiO}_2$  suspensions, has been reported [57]. The yield (epoxide produced/olefin consumed) increased with a decrease of chain length and in solvents with high donor number as follows: hexane < nitromethane < acetonitrile < butyronitrile. This effect may well be able to also be explained by a process that is mediated by the solvent hydroperoxides.

As the reaction time increased from three to six hours, the yield of oxidation product increased 25% using Fe-doped  $\text{TiO}_2$  and 40% for V-doped  $\text{TiO}_2$ . The yield for the vanadium doped catalyst system has higher conversion rate than the iron-doped catalyst system for the longer reaction time. This

confirms the experimental data, as vanadium-doped  $\text{TiO}_2$  has higher activity.

#### 4. Conclusion

The effects of metal doping on flame synthesized nanostructured  $\text{TiO}_2$  have been studied in order to extend its response to illumination with visible light. A flame aerosol codeposition method was used for the preparation of V- and Fe-doped  $\text{TiO}_2$ . Partial oxidation of 1-phenylethanol to acetophenone was used as a probe reaction to study photocatalytic activity. The type and concentration of dopant have strong influence in improving or inhibiting photocatalytic activity partial photooxidation. Although Fe- and V-doped  $\text{TiO}_2$  did not show enhanced response to visible light, there are improvements in photoactivity of doped catalyst. The photocatalytic activity of V and Fe- $\text{TiO}_2$  materials depends markedly on the doping level. Relatively high amounts of iron (5 wt% in  $\text{Fe}^{3+}$ ) and vanadium (6 wt% in  $\text{V}^{5+}$ ) had adverse effect on the activity of  $\text{TiO}_2$  for 1-phenylethanol oxidation. However, positive effects are observed with a lower  $\text{Fe}^{3+}$  concentration (0.5 wt%) and  $\text{V}^{5+}$  concentrations

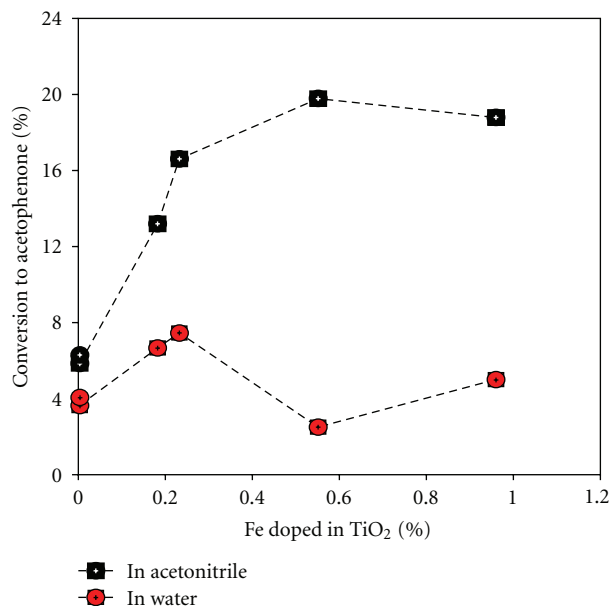


FIGURE 7: Conversion for yield of ketone formation and conversion of Fe-doped TiO<sub>2</sub> for the different doping concentrations.

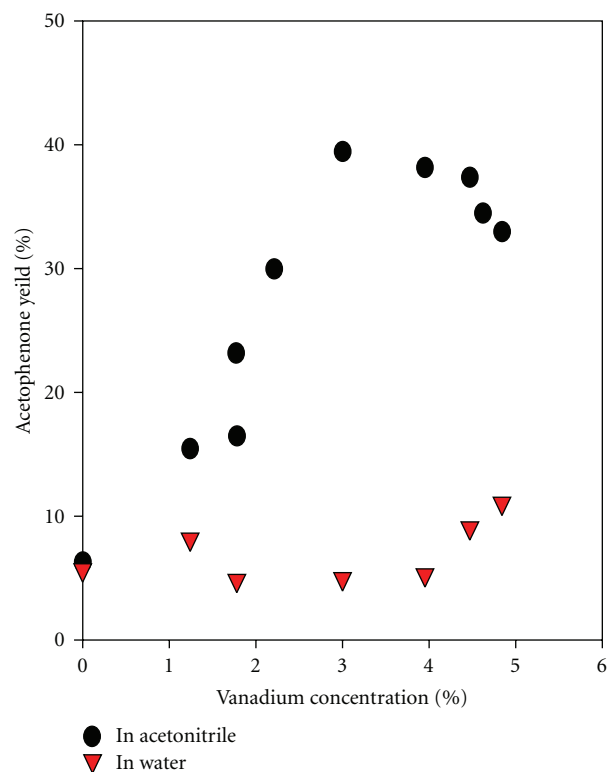


FIGURE 8: Conversion rate for ketone formation and conversion of vanadium-doped TiO<sub>2</sub> for the different doping concentrations.

(3 wt%), where the conversion of 1-phenylethanol increased by 2.5 and 6 folds, respectively, compared to undoped TiO<sub>2</sub>.

With the increase of the metal doping amount, the crystallinity of titanium dioxide decreased and the ratio of anatase-to-rutile in the product decreased. As the doping

concentration increased, the resulting product from the flame process became amorphous fine powders, and the crystal patterns could not be detected by XRD, and Raman spectroscopy. These changes in physical properties of the TiO<sub>2</sub> resulted in unique adsorption properties of organic substrates and allowed controlling the photocatalytic properties of the catalyst. Vanadium-doped TiO<sub>2</sub> showed higher activity than that of iron-doped TiO<sub>2</sub>. An optimal doping concentration existed for both of the doping species in the applied photocatalytic reaction systems. The optimum doping concentration also depended on the type of solvent used for the photocatalytic reaction. The possible reasons for the optimal doping concentration have also been discussed. For the studied system, the one using acetonitrile as solvent has much higher conversions compared to the system using water as solvent.

## References

- [1] J. M. Herrmann, "Heterogeneous photocatalysis: fundamentals and applications to the removal of various types of aqueous pollutants," *Catalysis Today*, vol. 53, no. 1, pp. 115–129, 1999.
- [2] M. R. Hoffmann, S. T. Martin, W. Choi, and D. W. Bahnemann, "Environmental applications of semiconductor photocatalysis," *Chemical Reviews*, vol. 95, no. 1, pp. 69–96, 1995.
- [3] J. A. Navío, G. Colón, M. I. Litter, and G. N. Bianco, "Synthesis, characterization and photocatalytic properties of iron-doped titania semiconductors prepared from TiO<sub>2</sub> and iron (III) acetylacetonate," *Journal of Molecular Catalysis A: Chemical*, vol. 106, no. 3, pp. 267–276, 1996.
- [4] S. Sakthivel, M. Janczarek, and H. Kisch, "Visible light activity and photoelectrochemical properties of nitrogen-doped TiO<sub>2</sub>," *Journal of Physical Chemistry B*, vol. 108, no. 50, pp. 19384–19387, 2004.
- [5] Y. Suda, H. Kawasaki, T. Ueda, and T. Ohshima, "Preparation of nitrogen-doped titanium oxide thin film using a PLD method as parameters of target material and nitrogen concentration ratio in nitrogen/oxygen gas mixture," *Thin Solid Films*, vol. 475, no. 1–2, pp. 337–341, 2005.
- [6] J. C. Yu, W. Ho, J. Yu, H. Yip, K. W. Po, and J. Zhao, "Efficient visible-light-induced photocatalytic disinfection on sulfur-doped nanocrystalline titania," *Environmental Science and Technology*, vol. 39, no. 4, pp. 1175–1179, 2005.
- [7] F. Fresno, C. Guillard, J. M. Coronado et al., "Photocatalytic degradation of a sulfonamide herbicide over pure and tin-doped TiO<sub>2</sub> photocatalysts," *Journal of Photochemistry and Photobiology A: Chemistry*, vol. 173, no. 1, pp. 13–20, 2005.
- [8] T. I. Halkides, D. I. Kondarides, and X. E. Verykios, "Catalytic reduction of NO by C<sub>3</sub>H<sub>6</sub> over Rh/TiO<sub>2</sub> catalysts effect of W-cation doping of TiO<sub>2</sub> on morphological characteristics and catalytic performance," *Applied Catalysis B: Environmental*, vol. 41, no. 4, pp. 415–426, 2003.
- [9] S. M. Karvinen, "The effects of trace element doping on the optical properties and photocatalytic activity of nanostructured titanium dioxide," *Industrial and Engineering Chemistry Research*, vol. 42, no. 5, pp. 1035–1043, 2003.
- [10] K. Palmisano, V. Augugliaro, A. Sclafani, and M. Schiavello, "Activity of chromium-ion-doped titania for the dinitrogen photoreduction to ammonia and for the phenol photodegradation," *Journal of Physical Chemistry*, vol. 92, no. 23, pp. 6710–6713, 1988.

- [11] T. Umabayashi, T. Yamaki, H. Itoh, and K. Asai, "Analysis of electronic structures of 3d transition metal-doped TiO<sub>2</sub> based on band calculations," *Journal of Physics and Chemistry of Solids*, vol. 63, no. 10, pp. 1909–1920, 2002.
- [12] J. I. Choi, J. H. Han, and D. Y. Kim, "Effect of titania and lithia doping on the boundary migration of alumina under an electric field," *Journal of the American Ceramic Society*, vol. 86, no. 2, pp. 347–350, 2003.
- [13] V. Guidi, M. C. Carotta, M. Ferroni, G. Martinelli, and M. Sacerdoti, "Effect of dopants on grain coalescence and oxygen mobility in nanostructured titania anatase and rutile," *Journal of Physical Chemistry B*, vol. 107, no. 1, pp. 120–124, 2003.
- [14] S. Jeon and P. V. Braun, "Hydrothermal synthesis of Er-doped luminescent TiO<sub>2</sub> nanoparticles," *Chemistry of Materials*, vol. 15, no. 6, pp. 1256–1263, 2003.
- [15] H. Jiang and L. Gao, "Enhancing the UV inducing hydrophilicity of TiO<sub>2</sub> thin film by doping Fe ions," *Materials Chemistry and Physics*, vol. 77, no. 3, pp. 878–881, 2003.
- [16] A. Kumbhar and G. Chumanov, "Synthesis of iron(III)-doped titania nanoparticles and its application for photodegradation of sulforhodamine-B pollutant," *Journal of Nanoparticle Research*, vol. 7, no. 4-5, pp. 489–498, 2005.
- [17] S. Mozia et al., "Decomposition of nonionic surfactant on a nitrogen-doped photocatalyst under visible-light irradiation," *Applied Catalysis B-Environmental*, vol. 55, no. 3, pp. 195–200, 2005.
- [18] S. Yin, Y. Aita, M. Komatsu, J. Wang, Q. Tang, and T. Sato, "Synthesis of excellent visible-light responsive TiO<sub>2</sub>—<sub>x</sub>N<sub>y</sub> photocatalyst by a homogeneous precipitation- solvothermal process," *Journal of Materials Chemistry*, vol. 15, no. 6, pp. 674–682, 2005.
- [19] H. Luo, T. Takata, Y. Lee, J. Zhao, K. Domen, and Y. Yan, "Photocatalytic activity enhancing for titanium dioxide by co-doping with bromine and chlorine," *Chemistry of Materials*, vol. 16, no. 5, pp. 846–849, 2004.
- [20] H. Wittmer, "Apparent band shift of Cr<sup>3+</sup>-doped titania as observed by photoacoustic and impedance spectroscopy," *Zeitschrift Fur Physikalische Chemie-International Journal of Research in Physical Chemistry & Chemical Physics*, vol. 214, pp. 709–720, 2000.
- [21] Y. Ma, X. T. Zhang, ZI. S. Guan, YA. A. Cao, and J. N. Yao, "Effects of zinc(II) and iron(III) doping of titania films on their photoreactivity to decompose rhodamine B," *Journal of Materials Research*, vol. 16, no. 10, pp. 2928–2933, 2001.
- [22] F. Gracia, J. P. Holgado, A. Caballero, and A. R. Gonzalez-Elipse, "Structural, optical, and photoelectrochemical properties of M<sup>+</sup>-TiO<sub>2</sub> model thin film photocatalysts," *Journal of Physical Chemistry B*, vol. 108, no. 45, pp. 17466–17476, 2004.
- [23] K. Wilke and H. D. Breuer, "The influence of transition metal doping on the physical and photocatalytic properties of titania," *Journal of Photochemistry and Photobiology A: Chemistry*, vol. 121, no. 1, pp. 49–53, 1999.
- [24] D. Dvoranová, V. Brezová, M. Mazúr, and M. A. Malati, "Investigations of metal-doped titanium dioxide photocatalysts," *Applied Catalysis B: Environmental*, vol. 37, no. 2, pp. 91–105, 2002.
- [25] E. Piera, M. I. Tejedor-Tejedor, M. E. Zorn, and M. A. Anderson, "Relationship concerning the nature and concentration of Fe(III) species on the surface of TiO<sub>2</sub> particles and photocatalytic activity of the catalyst," *Applied Catalysis B: Environmental*, vol. 46, no. 4, pp. 671–685, 2003.
- [26] Z. M. Wang, G. Yang, P. Biswas, W. Bresser, and P. Boolchand, "Processing of iron-doped titania powders in flame aerosol reactors," *Powder Technology*, vol. 114, no. 1-3, pp. 197–204, 2001.
- [27] J. J. Sene, W. A. Zeltner, and M. A. Anderson, "Fundamental photoelectrocatalytic and electrophoretic mobility studies of TiO<sub>2</sub> and V-doped TiO<sub>2</sub> thin-film electrode materials," *Journal of Physical Chemistry B*, vol. 107, no. 7, pp. 1597–1603, 2003.
- [28] P. Falaras, I. M. Arabatzis, T. Stergiopoulos, and M. C. Bernard, "Enhanced activity of silver modified thin-film TiO<sub>2</sub> photocatalysts," *International Journal of Photoenergy*, vol. 5, no. 3, pp. 123–130, 2003.
- [29] C. Li, J. Wang, X. Wang, H. Chen, and W. Su, "Nonlinear electrical properties of Ta-doped titania capacitor-varistor ceramics," *Materials Chemistry and Physics*, vol. 74, no. 2, pp. 187–191, 2002.
- [30] T. V. Nguyen, S. Kim, and O. B. Yang, "Water decomposition on TiO<sub>2</sub>-SiO<sub>2</sub> and RuS<sub>2</sub> /TiO<sub>2</sub>-SiO<sub>2</sub> photocatalysts: the effect of electronic characteristics," *Catalysis Communications*, vol. 5, pp. 59–62, 2004.
- [31] K. T. Ranjit and B. Viswanathan, "Photocatalytic reduction of nitrite and nitrate ions over doped TiO<sub>2</sub> catalysts," *Journal of Photochemistry and Photobiology A: Chemistry*, vol. 107, no. 1–3, pp. 215–220, 1997.
- [32] Z. H. Yuan, J. H. Jia, and LI. D. Zhang, "Influence of co-doping of Zn(II) + Fe(III) on the photocatalytic activity of TiO<sub>2</sub> for phenol degradation," *Materials Chemistry and Physics*, vol. 73, no. 2-3, pp. 323–326, 2002.
- [33] E. Sahle-Demessie, M. Gonzalez, Z. M. Wang, and P. Biswas, "Synthesizing alcohols and ketones by photoinduced catalytic partial oxidation of hydrocarbons in TiO<sub>2</sub> film reactors prepared by three different methods," *Industrial and Engineering Chemistry Research*, vol. 38, no. 9, pp. 3276–3284, 1999.
- [34] M. Anpo, T. Kawamura, S. Kodama, K. Maruya, and T. Onishi, "Photocatalysis on Ti-Al binary metal oxides: enhancement of the photocatalytic activity of TiO<sub>2</sub> species," *Journal of Physical Chemistry*, vol. 92, no. 2, pp. 438–440, 1988.
- [35] W. J. Stark and S. E. Pratsinis, "Aerosol flame reactors for manufacture of nanoparticles," *Powder Technology*, vol. 126, no. 2, pp. 103–108, 2002.
- [36] K. Wegner and S. E. Pratsinis, "Flame synthesis of nanoparticles," *Chimica Oggi*, vol. 22, no. 9, pp. 27–29, 2004.
- [37] M. J. Height, J. B. Howard, J. W. Tester, and J. B. V. Sande, "Flame synthesis of single-walled carbon nanotubes," *Carbon*, vol. 42, no. 11, pp. 2295–2307, 2004.
- [38] W. Choi, A. Termin, and M. R. Hoffmann, "The role of metal ion dopants in quantum-sized TiO<sub>2</sub>—correlation between photoreactivity and charge carrier recombination dynamics," *Journal of Physical Chemistry*, vol. 98, no. 51, pp. 13669–13679, 1994.
- [39] S. Klosek and D. Raftery, "Visible light driven V-doped TiO<sub>2</sub> photocatalyst and its photooxidation of ethanol," *Journal of Physical Chemistry B*, vol. 105, no. 14, pp. 2815–2819, 2002.
- [40] M. Shui, L. H. Yue, and Z. D. Xu, "Photocatalytic activity of iron doping TiO<sub>2</sub> prepared by several methods," *Acta Physico-Chimica Sinica*, vol. 17, no. 3, pp. 282–285, 2001.
- [41] M. A. Fox and M. T. Dulay, "Heterogeneous photocatalysis," *Chemical Reviews*, vol. 93, no. 1, pp. 341–357, 1993.
- [42] H. Kikkawa, B. O'Regan, and M. A. Anderson, "Photoelectrochemical properties of Nb-doped TiO<sub>2</sub> semiconductor ceramic membrane," *Journal of Electroanalytical Chemistry and Interfacial Electrochemistry*, vol. 309, no. 1-2, pp. 91–101, 1991.

- [43] S. I. Shah, W. Li, C. P. Huang, O. Jung, and C. Ni, "Study of Nd, Pd, Pt, and Fe dopant effect on photoreactivity of TiO<sub>2</sub> nanoparticles," *Proceedings of the National Academy of Sciences of the United States of America*, vol. 99, no. 9, pp. 6482–6486, 2002.
- [44] U. R. Pillai and E. Sahle-Demessie, "Selective oxidation of alcohols in gas phase using light-activated titanium dioxide," *Journal of Catalysis*, vol. 211, no. 2, pp. 434–444, 2002.
- [45] C. Minero, G. Mariella, V. Maurino, and E. Pelizzetti, "Photocatalytic transformation of organic compounds in the presence of inorganic anions. 1. Hydroxyl-mediated and direct electron-transfer reactions of phenol on a titanium dioxide-fluoride system," *Langmuir*, vol. 16, no. 6, pp. 2632–2641, 2000.
- [46] V. Brezová, M. Čeppan, E. Brandšteterová, M. Breza, and L. Lapčík, "Photocatalytic hydroxylation of benzoic acid in aqueous titanium dioxide suspension," *Journal of Photochemistry and Photobiology, A: Chemistry*, vol. 59, no. 3, pp. 385–391, 1991.
- [47] P. Calza, C. Minero, and E. Pelizzetti, "Photocatalytically assisted hydrolysis of chlorinated methanes under anaerobic conditions," *Environmental Science and Technology*, vol. 31, no. 8, pp. 2198–2203, 1997.
- [48] N. Djeghri and S. J. Teichner, "Heterogeneous photocatalysis: the photooxidation of 2-methylbutane," *Journal of Catalysis*, vol. 62, no. 1, pp. 99–106, 1980.
- [49] R. Wittenberg, M. A. Pradera, and J. A. Navio, "Cumene photo-oxidation over powder TiO<sub>2</sub> catalyst," *Langmuir*, vol. 13, no. 8, pp. 2373–2379, 1997.
- [50] A. Di Paola, E. García-López, S. Ikeda, G. Marc, B. Ohtani, and L. Palmisano, "Photocatalytic degradation of organic compounds in aqueous systems by transition metal doped polycrystalline TiO<sub>2</sub>," *Catalysis Today*, vol. 75, no. 1–4, pp. 87–93, 2002.
- [51] J. Araña, O. González Díaz, M. Miranda Saracho, J. M. Doña Rodríguez, J. A. Herrera Melián, and J. Pérez Peña, "Maleic acid photocatalytic degradation using Fe-TiO<sub>2</sub> catalysts. Dependence of the degradation mechanism on the Fe catalysts content," *Applied Catalysis B: Environmental*, vol. 36, no. 2, pp. 113–124, 2002.
- [52] K. E. Karakitsou and X. E. Verykios, "Effects of altermvalent cation doping of TiO<sub>2</sub> on its performance as a photocatalyst for water cleavage," *Journal of Physical Chemistry*, vol. 97, no. 6, pp. 1184–1189, 1993.
- [53] M. I. Litter and J. A. Navío, "Photocatalytic properties of iron-doped titania semiconductors," *Journal of Photochemistry and Photobiology A: Chemistry*, vol. 98, no. 3, pp. 171–181, 1996.
- [54] G. J. Ten Brink, I. W. C. E. Arends, and R. A. Sheldon, "Green, catalytic oxidation of alcohols in water," *Science*, vol. 287, no. 5458, pp. 1636–1639, 2000.
- [55] C. B. Almqvist and P. Biswas, "The photo-oxidation of cyclohexane on titanium dioxide: an investigation of competitive adsorption and its effects on product formation and selectivity," *Applied Catalysis A: General*, vol. 214, no. 2, pp. 259–271, 2001.
- [56] F. Soana, M. Sturini, L. Cermenati, and A. Albini, "Titanium dioxide photocatalyzed oxygenation of naphthalene and some of its derivatives," *Journal of the Chemical Society. Perkin Transactions 2*, no. 4, pp. 699–704, 2000.
- [57] T. Ohno, K. Nakabeya, and M. Matsumura, "Epoxidation of olefins on photoirradiated titanium dioxide powder using molecular oxygen as an oxidant," *Journal of Catalysis*, vol. 176, no. 1, pp. 76–81, 1998.

## Research Article

# Nano-Scale Hydroxyapatite: Synthesis, Two-Dimensional Transport Experiments, and Application for Uranium Remediation

S. R. Kanel,<sup>1</sup> T. P. Clement,<sup>2</sup> M. O. Barnett,<sup>2</sup> and M. N. Goltz<sup>1</sup>

<sup>1</sup> Department of Systems and Engineering Management, Air Force Institute of Technology, 2950 Hobson Way, WPAFB, Fairborn, OH 45433, USA

<sup>2</sup> Department of Civil Engineering, Auburn University, Auburn, AL 36849, USA

Correspondence should be addressed to S. R. Kanel, sushil.kanel.ctr@afit.edu

Received 31 October 2010; Accepted 9 December 2010

Academic Editor: Mallikarjuna Nadagouda

Copyright © 2011 S. R. Kanel et al. This is an open access article distributed under the Creative Commons Attribution License, which permits unrestricted use, distribution, and reproduction in any medium, provided the original work is properly cited.

Synthetic nano-scale hydroxyapatite (NHA) was prepared and characterized using X-ray diffraction (XRD) and scanning electron microscopy (SEM) methods. The XRD data confirmed that the crystalline structure and chemical composition of NHA correspond to  $\text{Ca}_5\text{OH}(\text{PO}_4)_3$ . The SEM data confirmed the size of NHA to be less than 50 nm. A two-dimensional physical model packed with saturated porous media was used to study the transport characteristics of NHA under constant flow conditions. The data show that the transport patterns of NHA were almost identical to tracer transport patterns. This result indicates that the NHA material can move with water like a tracer, and its movement was neither retarded nor influenced by any physicochemical interactions and/or density effects. We have also tested the reactivity of NHA with 1 mg/L hexavalent uranium (U(VI)) and found that complete removal of U(VI) is possible using 0.5 g/L NHA at pH 5 to 6. Our results demonstrate that NHA has the potential to be injected as a dilute slurry for *in situ* treatment of U(VI)-contaminated groundwater systems.

## 1. Introduction

Groundwater systems can be contaminated by uranium discharged from ore mining and processing activities and from various nuclear weapons or fuel manufacturing activities. Uranium contamination can cause serious diseases including bone cancer, nonspecific malignant neoplasms, and lung cancer [1]. Therefore, the US Environmental Protection Agency (USEPA) standard for uranium in drinking water is set at 30  $\mu\text{g}/\text{L}$  [2].

A number of materials have been used as adsorbents or reductants for removing hexavalent uranium from groundwater. These include reactive sorbents such as activated carbon, zero-valent iron, phosphate rocks, zeolites, and various types of apatites [3]. Among available sorbent materials, apatites are one of the most promising candidates for adsorbing and immobilizing dissolved uranium from groundwater [4, 5]. This is because the apatite group of minerals have been found to be stable across a wide range of

geological conditions for hundreds of years [6, 7]. The solubility product of uranium-apatite minerals ( $K_{sp}$ ) can vary from about  $10^{-20}$  to  $10^{-150}$  [7, 8]. Furthermore, apatite is an ideal material for long-term sequestration of metals due to its high affinity for actinides and heavy metals [9]. Therefore, apatite has been widely used for immobilizing heavy metals such as Pb [10], actinides such as plutonium [11] and U, Cr, Co, Ni, Al, Cu, Fe, Pu, Cd, Zn, As, Sb, and V [5, 12–14].

In the literature, several researchers have studied uranium removal by apatite using batch-scale [4, 5, 15–19] and column-scale experiments [20]. Several researchers have also attempted to apply hydroxyapatite (HA) to treat contaminant plumes at field sites. For example, commercial HA,  $\text{Ca}_5(\text{PO}_4)_3\text{OH}$ , has been used in a permeable reactive barrier (PRB) in a shallow alluvial aquifer at Fry Canyon, Utah to remove uranium [4]. However, almost all previous studies reported in the literature have focused on evaluating the feasibility for HA use in permeable reactive barrier (PRB)-type applications.

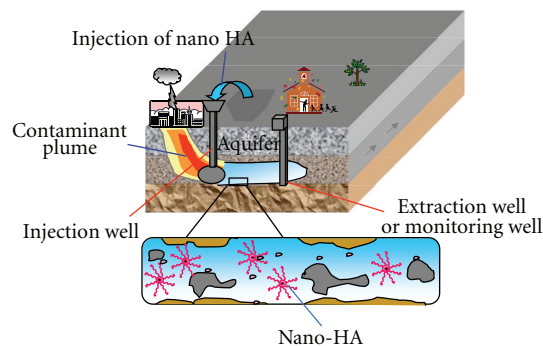


FIGURE 1: Schematic diagram of *in situ* groundwater remediation by injection of nano-HA.

The focus of this study is to demonstrate the feasibility of a novel *in situ* remediation technology that can treat uranium using nano-scale HA that can be directly delivered *in situ* and transported to the contaminated zone via injection wells. HA reacting with hexavalent uranium (U(VI)) has been shown to produce stable minerals such as chernikovite and autunite [5]. Use of injection wells would help avoid construction of expensive barriers, and also the method can target deep plumes at locations where trenching to construct a PRB is infeasible or cost prohibitive. Furthermore, a methodology that involves injection of HA would allow for repetitive treatments to ensure that sufficient quantities of U(VI) were immobilized to protect the environment.

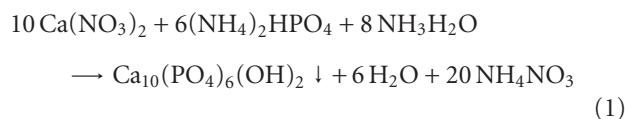
A conceptual schematic diagram illustrating the concept of injecting nano-HA to remediate a dissolved contaminant plume is shown in Figure 1. The overall goal of this study is to develop experimental datasets to investigate the feasibility of the remediation methodologies illustrated in this figure. The specific objectives of this study are to (1) synthesize and characterize nano-scale HA particles in laboratory, (2) investigate the transport characteristics of the synthesized nano-scale HA, and (3) demonstrate the reactivity of the nano-HA for treating U(VI) at different pH conditions.

## 2. Experimental

**2.1. Material and Methods.** All the chemicals used in the experiments were reagent grade. Chemicals used in this study, which include O-phosphoric acid, sodium nitrate, sodium bicarbonate, sodium hydroxide, and nitric acid, were purchased from Fisher Chemical Company (Fisher Scientific, Fairlawn, NJ, USA). Calcium nitrate ( $\text{CaN}_2\text{O}_6 \cdot 4\text{H}_2\text{O}$ ) was purchased from Acros Organic (Morris Plains, NJ, USA). Ammonium hydroxide (6N) was purchased from Ricca Chemical Company (Arlington, TX, USA). The acids were trace metal grade, and the uranium standards and stock solutions were prepared from plasma-grade uranium standard (using depleted uranium).

**2.2. Nano-HA Synthesis.** Nano hydroxyapatite (NHA) was synthesized by reacting  $\text{Ca}(\text{NO}_3)_2 \cdot 4\text{H}_2\text{O}$  (0.1 M), and  $(\text{NH}_4)_2\text{HPO}_4$  (0.06 M) with ammonium hydroxide (1 M).

The  $\text{Ca}(\text{NO}_3)_2$  solution was vigorously stirred at room temperature and phosphate solution was added dropwise to the solution. The  $\text{NH}_4\text{OH}$  was then slowly added dropwise to this mixture for about 30 min to produce a milky gelatinous hydroxyapatite precipitate ( $\text{Ca}_{10}(\text{PO}_4)_6(\text{OH})_2$ ), which was washed with deionized water three times. The overall precipitation reaction for synthesizing hydroxyapatite can be written as



The reaction process described above is a modified version of an HA synthesis method described in previous studies [21, 22].

**2.3. Batch Experiments.** Batch adsorption experiments were conducted at room temperature ( $\sim 295 \text{ K}$ ) in 50 mL polycarbonate centrifuge tubes, each tube yielding one data point. Experiments were performed in duplicates to verify the reproducibility of the results. The samples are prepared by mixing an appropriate amount of the HA, ionic strength adjuster (0.01 M  $\text{NaNO}_3$ ), acidified U(VI) stock solution ( $\text{UO}_2(\text{NO}_3)_2$ ), and distilled deionized water. In all the batch experiments, the pH of the solution was adjusted using 1 M  $\text{NaOH}$  or  $\text{HNO}_3$ . The reacted samples were removed from the shaker and centrifuged to aid in filtration. The samples were opened and an aliquot of the supernatant was withdrawn and immediately filtered with a  $0.45 \mu\text{m}$  syringe filter, and the pH of the remaining suspension was measured. The filtrate was analyzed to measure the values of aqueous U(VI) concentration levels using a kinetic phosphorescence analyzer (KPA) (model KPA-11, Chemchek Instruments, Richland, WA) after acidifying the filtrate to a pH value of 1. The level of uncertainty associated with the U(VI) analysis method is  $\pm 3\%$  [23, 24].

**2.4. Details of Porous Media Transport Experiments.** A two-dimensional aquifer model packed with A-110 silica beads (Potters Industries, USA) was used in this study. A uniform flow field was established by maintaining a constant hydraulic gradient across the flow tank. Experimental details of the two-dimensional experiments are summarized in our previous work [25, 26]. Briefly, the dimensions of the flow container were 41 cm (length)  $\times$  1.1 cm (width)  $\times$  30 cm (height). Two chambers (each 5.5 cm wide) were situated at the left and right ends of the tank. A series of overflow orifices were used to control the water level (head) at either side of the flow tank. In all the transport experiments the ambient freshwater flowed by establishing a head difference of 0.7 cm across the chamber. The flow field was allowed to reach steady state for a period of 10 min before starting the nanoparticle injection experiments.

The freshwater supply source was marked with a small amount of nonsorbing red dye, and hence the entire tank appeared red prior to any injection. After establishing steady-state flow conditions, 20 mL of uncolored freshwater was

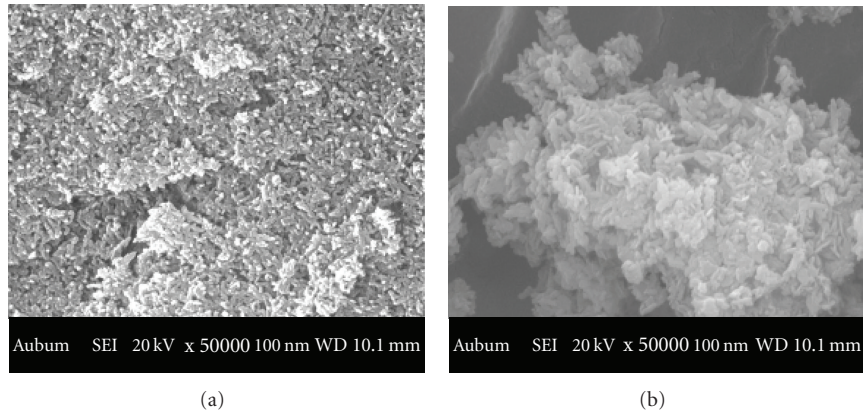


FIGURE 2: SEM images of (a) lab synthesized nano-HA and (b) commercial Aldrich-HA.

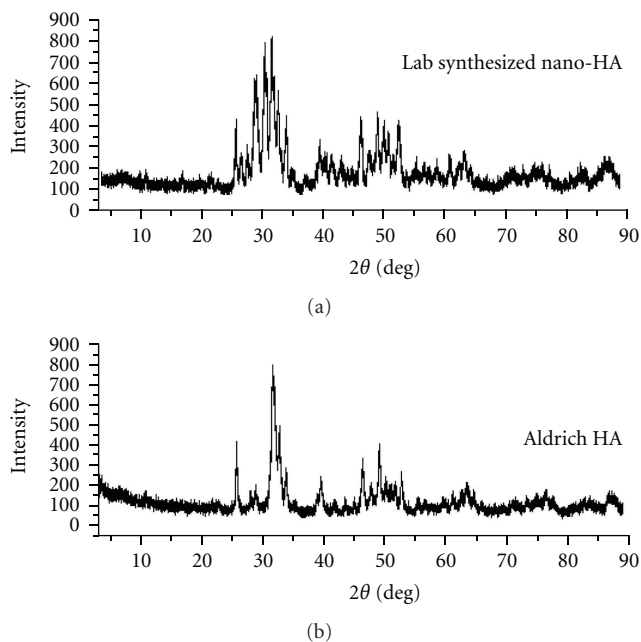


FIGURE 3: Lab synthesized nano-HA and Aldrich HA.

injected into the porous media tank to characterize tracer transport through the physical system. The location of the injection point was approximately 11.2 cm from the left end and 17 cm from the bottom of the flow container. It took approximately 10 s to manually inject the 20 mL tracer slug. The movement of the tracer was recorded for about 15 min by taking high-resolution digital pictures at regular intervals. After completing the tracer study, we injected similar volume of nano-HA and recorded its migration patterns and compared it with the tracer data.

### 3. Results and Discussion

**3.1. Characterization of NHA.** SEM images of synthesized nano-HA particles and commercial HA powder purchased

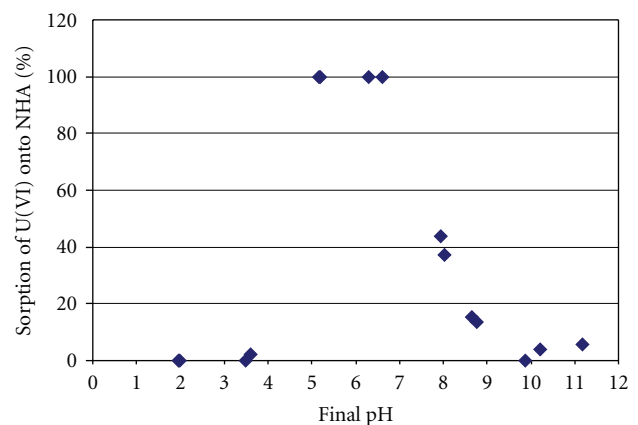


FIGURE 4: Influence of pH on U(VI) removal by synthetic NHA; experimental conditions: U(VI): 1 mg/L and NHA: 0.5 g/L.

from Aldrich Chemicals are shown in Figure 2. The image confirms that the particles are on the order of 20 to 50 nanometers and are needle shaped.

The XRD data for nano-HA and a commercial HA powder are shown in Figure 3. The XRD data confirm that the lab synthesized nano-HA has peaks that correspond to the peaks of commercial crystalline HA.

**3.2. Reactivity of Nano-HA with U(VI).** The percent removal of U(VI) by NHA was investigated using  $1 \text{ mg L}^{-1}$  of the U(VI) at different pH values, and the results are presented in Figure 4. The data show that almost 100% of U(VI) (at a concentration of 1 mg/L) can be removed by 0.5 g/L NHA at pH 5 to 6 (see Figure 4). The U(VI) removal capacity and the pH dependence pattern of the synthesized NHA were comparable to the commercial HA (data not shown here).

**3.3. Transport of NHA in Porous Media Systems.** The transport patterns of the tracer and NHA observed at different times are shown in Figure 5. The pictures at 0 min present

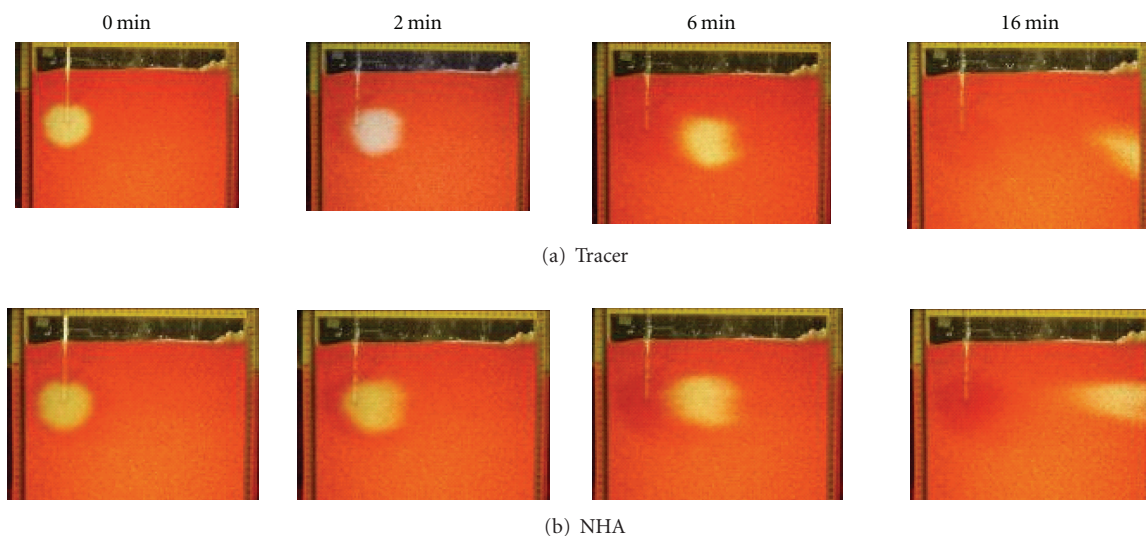


FIGURE 5: Transport of (a) tracer (uncolored deionized water) and (b) NHA plumes in the two-dimensional flow container.

the location of the plumes immediately after injection. Other pictures shown in the figure were taken at 2, 6, and 16 minutes. The data indicate that the freshwater tracer (deionized water) plume dispersed and moved horizontally and reached the right boundary after approximately 16 minutes of transport (see Figure 5(a)). The NHA plume also moved horizontally toward the right boundary at a rate nearly identical to the tracer transport rate (see Figure 5(b)).

Colloidal suspensions can be removed by the porous medium due to various physical and chemical processes including charge interaction, filtration, diffusion, interception, and/or sedimentation [27]. However, in the case of NHA, the transport was observed to be similar to that of a tracer plume. This implies that the transport of dilute NHA solutions will be controlled primarily by advection and dispersion processes. A mass balance analysis that compared the mass of injected NHA with the mass recovered in the effluent indicated that about 85% of NHA was transported through the system. The mass balance discrepancy of 15% is attributed to experimental errors; however, it is possible that an unrecoverable fraction of NHA particles remain trapped in the porous medium. Extraction of porous media samples obtained near the injection zone did not yield any recoverable amount of NHA.

In the published literature, no datasets are available that document the transport patterns of NHA in a two-dimensional (2D) flow tank packed with porous media. In an earlier report we studied the 2D transport of stabilized and unstabilized zero-valent iron nanoparticles through porous media [26] and found that density effects can play a significant role in transporting surface-modified iron nanoparticles. Such density effects were not observed in these NHA transport experiments. Since NHA moved like a tracer, this material could be used either for extracting contaminants or for *in situ* stabilization of contaminants, depending on site-specific needs and conditions.

#### 4. Conclusions

The findings of this study demonstrate that nano-scale hydroxyapatite (NHA) materials could be used for developing treatment approaches for removing and/or immobilizing highly toxic radionuclides such as U(VI) in subsurface groundwater systems. These approaches would allow remediation of U(VI) without the need to excavate. Since HA has the potential to immobilize U(VI) to stable minerals such as autunite and chernikovite [5, 6], this process has important implication for *in situ* U(VI) remediation. Our flow tank data indicate that the transport characteristics of NHA are similar to tracer transport characteristics. The reactivity data show that NHA has a strong affinity to efficiently remove U(VI) around pH 5 to 6. More studies are, however, needed to further understand and scale up these processes to field-specific transport conditions.

#### Acknowledgments

This research was, in part, supported by the office of science (BER), US Department of Energy Grant no. DE-FG02-06ER64213, and the experiments were completed when the first author was employed at the Department of Civil Engineering, Auburn University, AL, USA. The first author is currently employed at the Air Force Institute of Technology (AFIT), Wright Patterson Air Force Base, OH, USA and is supported by a National Research Council Research Associateship Award.

#### References

- [1] L. J. Kosarek, "Radionuclide removal from water," *Environmental Science and Technology*, vol. 13, no. 5, pp. 522–525, 1979.
- [2] D. E. Giammar and J. G. Hering, "Time scales for sorption—desorption and surface precipitation of uranyl on goethite,"

- Environmental Science and Technology*, vol. 35, no. 16, pp. 3332–3337, 2001.
- [3] R. Han, W. Zou, Y. Wang, and L. Zhu, “Removal of uranium(VI) from aqueous solutions by manganese oxide coated zeolite: discussion of adsorption isotherms and pH effect,” *Journal of Environmental Radioactivity*, vol. 93, no. 3, pp. 127–143, 2007.
- [4] C. C. Fuller, J. R. Bargar, and J. A. Davis, “Molecular-scale characterization of uranium sorption by bone apatite materials for a permeable reactive barrier demonstration,” *Environmental Science and Technology*, vol. 37, no. 20, pp. 4642–4649, 2003.
- [5] C. C. Fuller, J. R. Bargar, J. A. Davis, and M. J. Piana, “Mechanisms of uranium interactions with hydroxyapatite: implications for groundwater remediation,” *Environmental Science and Technology*, vol. 36, no. 2, pp. 158–165, 2002.
- [6] J. L. Conca and J. Wright, “An apatite II permeable reactive barrier to remediate groundwater containing Zn, Pb and Cd,” *Applied Geochemistry*, vol. 21, no. 8, pp. 1288–1300, 2006.
- [7] J. O. Nriagu, “Lead orthophosphates-IV Formation and stability in the environment,” *Geochimica et Cosmochimica Acta*, vol. 38, no. 6, pp. 887–898, 1974.
- [8] M. Mannecki, P. A. Maurice, and S. J. Traina, “Kinetics of aqueous Pb reaction with apatites,” *Soil Science*, vol. 165, no. 12, pp. 920–933, 2000.
- [9] X. Chen, J. V. Wright, J. L. Conca, and L. M. Peurrung, “Effects of pH on heavy metal sorption on mineral apatite,” *Environmental Science and Technology*, vol. 31, no. 3, pp. 624–631, 1997.
- [10] QI. Y. Ma, S. J. Traina, T. J. Logan, and J. A. Ryan, “In situ lead immobilization by apatite,” *Environmental Science and Technology*, vol. 27, no. 9, pp. 1803–1810, 1993.
- [11] R. C. Moore, M. Gasser, N. Awwad et al., “Sorption of plutonium(VI) by hydroxyapatite,” *Journal of Radioanalytical and Nuclear Chemistry*, vol. 263, no. 1, pp. 97–101, 2005.
- [12] J. Gómez del Río, P. Sanchez, P. J. Morando, and D. S. Cicerone, “Retention of Cd, Zn and Co on hydroxyapatite filters,” *Chemosphere*, vol. 64, no. 6, pp. 1015–1020, 2006.
- [13] A. Krestou, A. Xenidis, and D. Panyas, “Mechanism of aqueous uranium(VI) uptake by hydroxyapatite,” *Minerals Engineering*, vol. 17, no. 3, pp. 373–381, 2004.
- [14] J. S. Arey, J. C. Seaman, and P. M. Bertsch, “Immobilization of uranium in contaminated sediments by hydroxyapatite addition,” *Environmental Science and Technology*, vol. 33, no. 2, pp. 337–342, 1999.
- [15] J. Rakovan, R. J. Reeder, E. J. Elzinga, D. J. Cherniak, C. D. Tait, and D. E. Morris, “Structural characterization of U(VI) in apatite by X-ray absorption spectroscopy,” *Environmental Science and Technology*, vol. 36, no. 14, pp. 3114–3117, 2002.
- [16] S. Saxena, M. Prasad, and S. F. D’Souza, “Radionuclide sorption onto low-cost mineral adsorbent,” *Industrial and Engineering Chemistry Research*, vol. 45, no. 26, pp. 9122–9128, 2006.
- [17] J. C. Seaman, J. S. Arey, and P. M. Bertsch, “Immobilization of nickel and other metals in contaminated sediments by hydroxyapatite addition,” *Journal of Environmental Quality*, vol. 30, no. 2, pp. 460–469, 2001.
- [18] J. C. Seaman, T. Meehan, and P. M. Bertsch, “Immobilization of cesium-137 and uranium in contaminated sediments using soil amendments,” *Journal of Environmental Quality*, vol. 30, no. 4, pp. 1206–1213, 2001.
- [19] B. M. Thomson, C. L. Smith, R. D. Busch, M. D. Siegel, and C. Baldwin, “Removal of metals and radionuclides using apatite and other natural sorbents,” *Journal of Environmental Engineering*, vol. 129, no. 6, pp. 492–499, 2003.
- [20] F. G. Simon, V. Biermann, and B. Peplinski, “Uranium removal from groundwater using hydroxyapatite,” *Applied Geochemistry*, vol. 23, no. 8, pp. 2137–2145, 2008.
- [21] S. Deb, J. Giri, S. Dasgupta, D. Datta, and D. Bahadur, “Synthesis and characterization of biocompatible hydroxyapatite coated ferrite,” *Bulletin of Materials Science*, vol. 26, no. 7, pp. 655–660, 2003.
- [22] L. B. Kong, J. Ma, and F. Boey, “Nanosized hydroxyapatite powders derived from coprecipitation process,” *Journal of Materials Science*, vol. 37, no. 6, pp. 1131–1134, 2002.
- [23] T. Cheng, M. O. Barnett, E. E. Roden, and J. Zhuang, “Effects of phosphate on uranium(VI) adsorption to goethite-coated sand,” *Environmental Science and Technology*, vol. 38, no. 22, pp. 6059–6065, 2004.
- [24] T. Cheng, M. O. Barnett, E. E. Roden, and J. Zhuang, “Effects of solid-to-solution ratio on uranium(VI) adsorption and its implications,” *Environmental Science and Technology*, vol. 40, no. 10, pp. 3243–3247, 2006.
- [25] R. R. Goswami and T. P. Clement, “Laboratory-scale investigation of saltwater intrusion dynamics,” *Water Resources Research*, vol. 43, no. 4, Article ID W04418, 2007.
- [26] S. R. Kanel, R. R. Goswami, T. P. Clement, M. O. Barnett, and D. Zhao, “Two dimensional transport characteristics of surface stabilized zero-valent iron nanoparticles in porous media,” *Environmental Science and Technology*, vol. 42, no. 3, pp. 896–900, 2008.
- [27] N. Tufenkji and M. Elimelech, “Correlation equation for predicting single-collector efficiency in physicochemical filtration in saturated porous media,” *Environmental Science and Technology*, vol. 38, no. 2, pp. 529–536, 2004.

## Research Article

# Microwave-Assisted Combustion Synthesis of Nano Iron Oxide/Iron-Coated Activated Carbon, Anthracite, Cellulose Fiber, and Silica, with Arsenic Adsorption Studies

Mallikarjuna N. Nadagouda and Darren A. Lytle

Water Supply and Water Resources Division, National Risk Management Research Laboratory, United States Environmental Protection Agency, 26 West Martin Luther King Drive, Cincinnati, OH 45268, USA

Correspondence should be addressed to Mallikarjuna N. Nadagouda, nadagouda.mallikarjuna@epa.gov

Received 9 March 2011; Accepted 18 April 2011

Academic Editor: Thomas F. Speth

Copyright © 2011 M. N. Nadagouda and D. A. Lytle. This is an open access article distributed under the Creative Commons Attribution License, which permits unrestricted use, distribution, and reproduction in any medium, provided the original work is properly cited.

Combustion synthesis of iron oxide/iron coated carbons such as activated carbon, anthracite, cellulose fiber, and silica is described. The reactions were carried out in alumina crucibles using a Panasonic kitchen microwave with inverter technology, and the reaction process was completed within a few minutes. The method used no additional fuel and nitrate, which is present in the precursor itself, to drive the reaction. The obtained samples were then characterized with X-ray mapping, scanning electron microscopy (SEM), energy dispersive X-ray analysis (EDS), selected area diffraction pattern (SAED), transmission electron microscopy (TEM), X-ray diffraction (XRD), and inductively coupled plasma (ICP) spectroscopy. The size of the iron oxide/iron nanoparticle-coated activated carbon, anthracite, cellulose fiber, and silica samples were found to be in the nano range (50–400 nm). The iron oxide/iron nanoparticles mostly crystallized into cubic symmetry which was confirmed by SAED. The XRD pattern indicated that iron oxide/iron nano particles existed in four major phases. That is,  $\gamma$ -Fe<sub>2</sub>O<sub>3</sub>,  $\alpha$ -Fe<sub>2</sub>O<sub>3</sub>, Fe<sub>3</sub>O<sub>4</sub>, and Fe. These iron-coated activated carbon, anthracite, cellulose fiber, and silica samples were tested for arsenic adsorption through batch experiments, revealing that few samples had significant arsenic adsorption.

## 1. Introduction

Arsenic (As) contamination is one of the most challenging environmental problems today. Millions of people worldwide are exposed to naturally occurring As-contaminated groundwater, which they use as their sole source of drinking water. Increased use of groundwater as a source for drinking water has caused serious health problems such as neurological, dermatological, gastrointestinal, and cardiorenal diseases; arsenic is also a suspected carcinogen. Furthermore, recent research has suggested that As acts as an endocrine disruptor at extremely low concentrations. Recently, because of its high nuisance value, The U.S. Environmental Protection Agency has revised the maximum contaminant level (MCL) of arsenic in drinking water from 50 to 10  $\mu\text{g/L}$ . As a result, there is a need to develop simple, low-cost methods for the removal of As from groundwater used as a source for drinking water.

Numerous materials have been used for arsenic adsorption such as rice husk (1), calcined and uncalcined layered double hydroxides (2), low-cost sorbents (3), aluminium oxide and phyllosilicate mineral surfaces in smelter-impacted soils (4), natural soil (5), waste biomass with a high fibrous protein content obtained from chicken feathers (6), nanocrystalline anatase form of titanium dioxide prepared by hydrolysis of titanium sulfate solution (7), and activated carbons prepared from solvent extracted olive pulp and olive stones (8).

There is now a growing interest, however, in using iron and its oxide form for their superior adsorption capability, when compared with the above mentioned alternatives [1–14]. Zhang et al. [1] reported that a novel Fe-Mn binary oxide adsorbent was developed for effective As (III) removal, which is more difficult to remove from drinking water and much more toxic to humans than As (V). The synthetic adsorbent

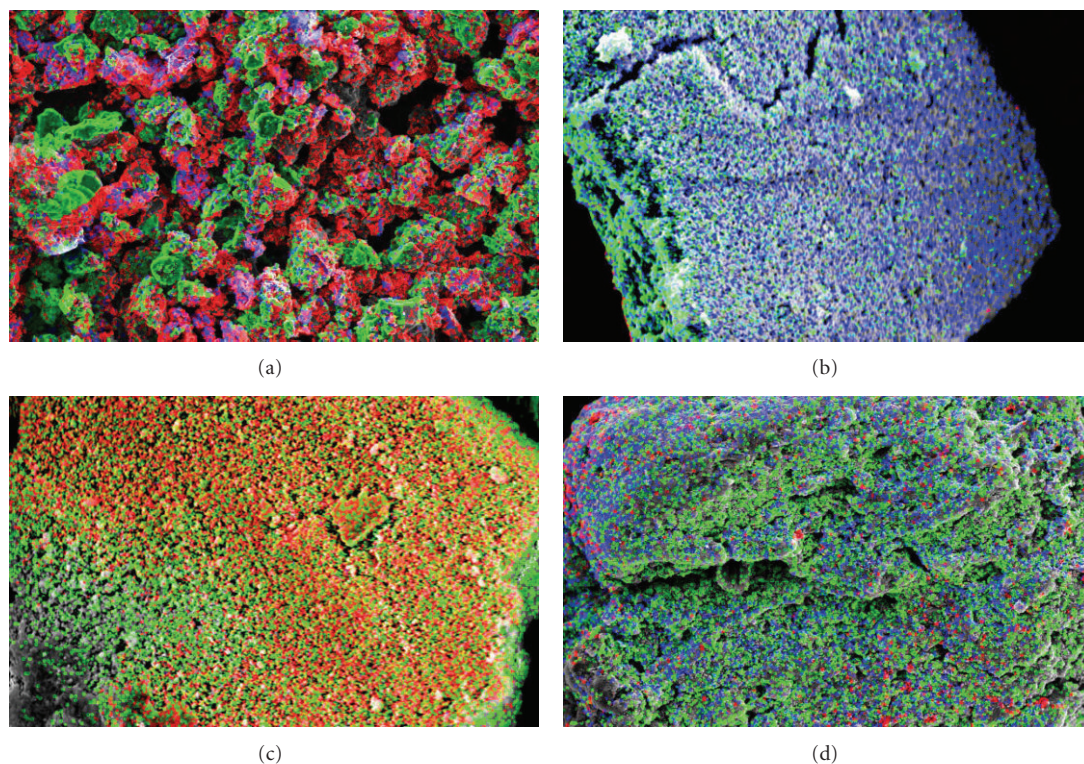


FIGURE 1: X-ray mapping images of (a) MN-1 (red-Fe, green-C, and blue-O), (b) MN-2 (blue-Fe, green-O, and red-C), (c) MN-3 (green-Fe, red-O, and blue-C), and (d) MN-4 (red-Silica, green-Fe, and blue-O).

showed a significantly higher As (III) uptake than As (V). Zhang et al. [2] showed that the bimetal oxide adsorbent showed a significantly higher As (V) adsorption capacity than the referenced Ce and Fe oxides ( $\text{CeO}_2$  and  $\text{Fe}_3\text{O}_4$ ) prepared by the same procedure, and some other arsenate adsorbents reported recently. Adsorption kinetics of arsenate and dimethylarsinate (DMA) on goethite ( $\alpha\text{-FeOOH}$ ) were investigated at different pH values and inert electrolyte concentrations. Their adsorption kinetics were described and compared using Elovich plots [4].

Nanoscale zero-valent iron was tested for the removal of As (III) in anoxic groundwater. Arsenic (III) adsorption kinetics were rapid and occurred on a scale of minutes following a pseudo-first-order rate expression with observed reaction rate constants of  $0.07\text{--}1.3\text{ min}^{-1}$ , and these values were about 1000 times higher than literature values for As (III) adsorption on micron-sized Iron [6]. New adsorbent, bead cellulose loaded with iron oxyhydroxide was applied for the adsorption and removal of arsenate and arsenite from aqueous systems. The adsorption capacity for arsenite and arsenate was 99.6 and 33.2 mg/g bead cellulose loaded with iron oxyhydroxide at pH 7.0, with an Fe content of 220 mg/mL. Kinetic data suggests a pseudo-second-order reaction model. Arsenate elimination was favored at acidic pH, whereas the adsorption of arsenite by bead cellulose loaded with iron oxyhydroxide was found to be effective in a wide pH range of 5–11 [12]. Effort from our laboratory to develop simple, low-cost methods for the removal of As from groundwater used as a source for drinking water herein,

we report on studies of iron oxide/iron nanoparticle-coated activated carbon, anthracite, cellulose fiber, and silica sample preparation using microwave-assisted combustion synthesis and their application in arsenic removal. The reaction occurs within a few minutes, uses no additional fuel, and is easy to process.

## 2. Experimental

The experimental procedure was carried out using  $\text{Fe}(\text{NO}_3)_3 \cdot 9\text{H}_2\text{O}$  (Aldrich, 99%) with various different carbons, and the composition ratio is shown in Table 1. The different ratio of  $\text{Fe}(\text{NO}_3)_3 \cdot 9\text{H}_2\text{O}$  to activated carbon, anthracite, cellulose fiber, and silica was mixed using a pestle and mortar, and then transferred to an alumina crucible. The mixtures were then heated under microwave irradiation (Panasonic kitchen microwave oven with inverter technology) for one to three minutes (Table 1).

Batch experiments were conducted for arsenic adsorption at room temperature. A stock arsenic solution was prepared by dissolution of 0.12 g  $\text{Na}_2\text{HAsO}_4$  into 4.0 L  $\text{H}_2\text{O}$  resulting in an initial concentration of 10 mg/L. Additionally, dissolved inorganic carbon was added by dissolving 1.40 g  $\text{NaHCO}_3$  into the stock solution resulting in a dissolved inorganic carbon level. Subsequently, the pH was adjusted to 7.0 by computer-controlled automatic titration. To high-density polyethylene bottles, 300 mL of stock solution and 0.25 g of synthesized adsorption media (MN-1 to MN-7)

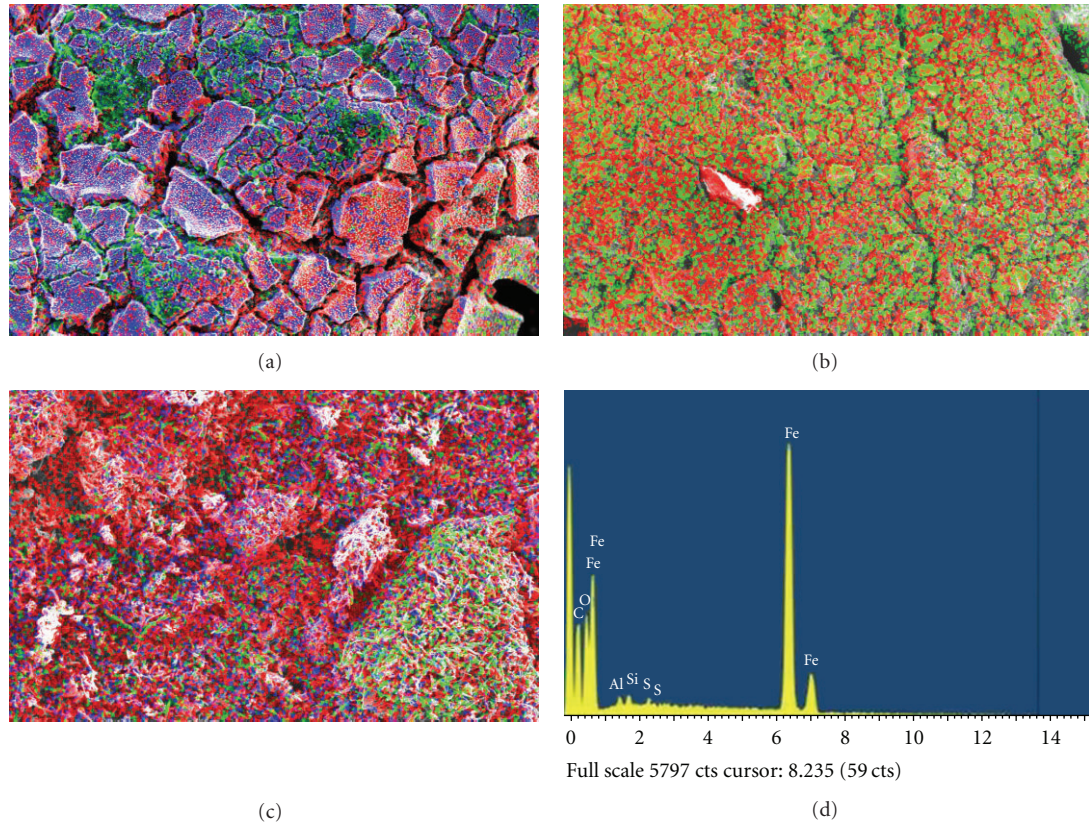


FIGURE 2: X-ray mapping images of (a) MN-5 (red-Fe, green-C, and blue-O), (b) MN-6 (blue-Fe, green-O, and red-C), (c) MN-7 (green-Fe, red-O, and blue-C), and (d) EDS spectrum of MN-7.

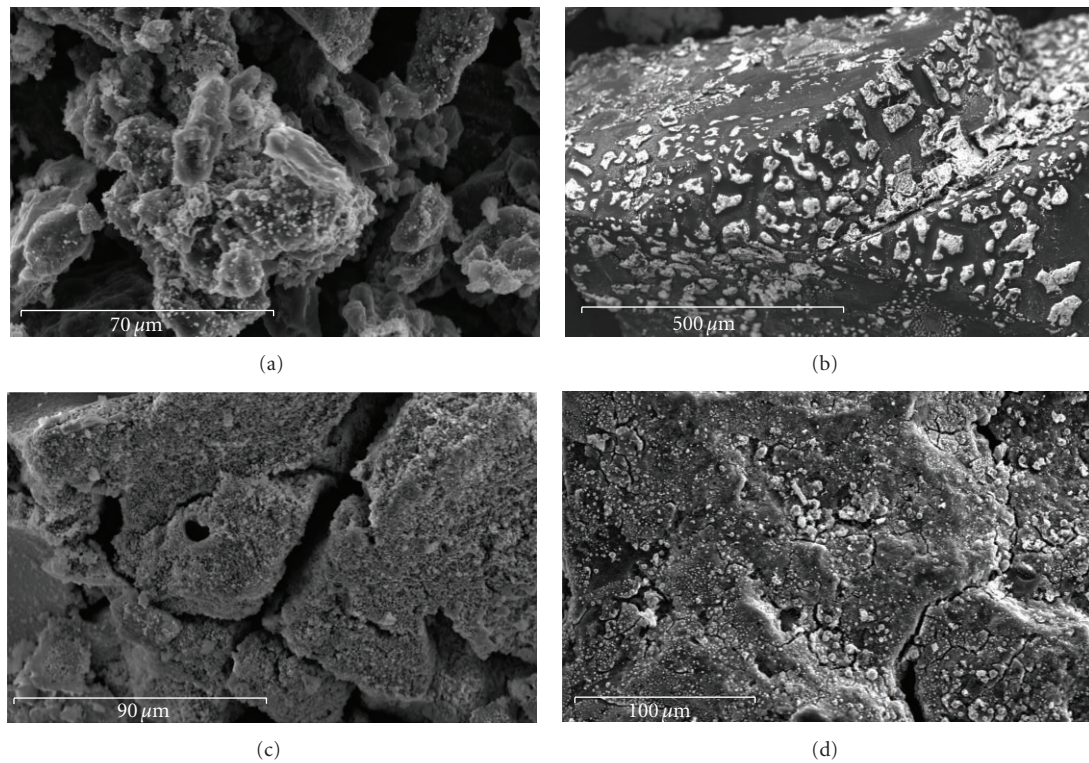


FIGURE 3: SEM images of iron coated (a) MN-1, (b) MN-2, (c) MN-3, and (d) MN-4.

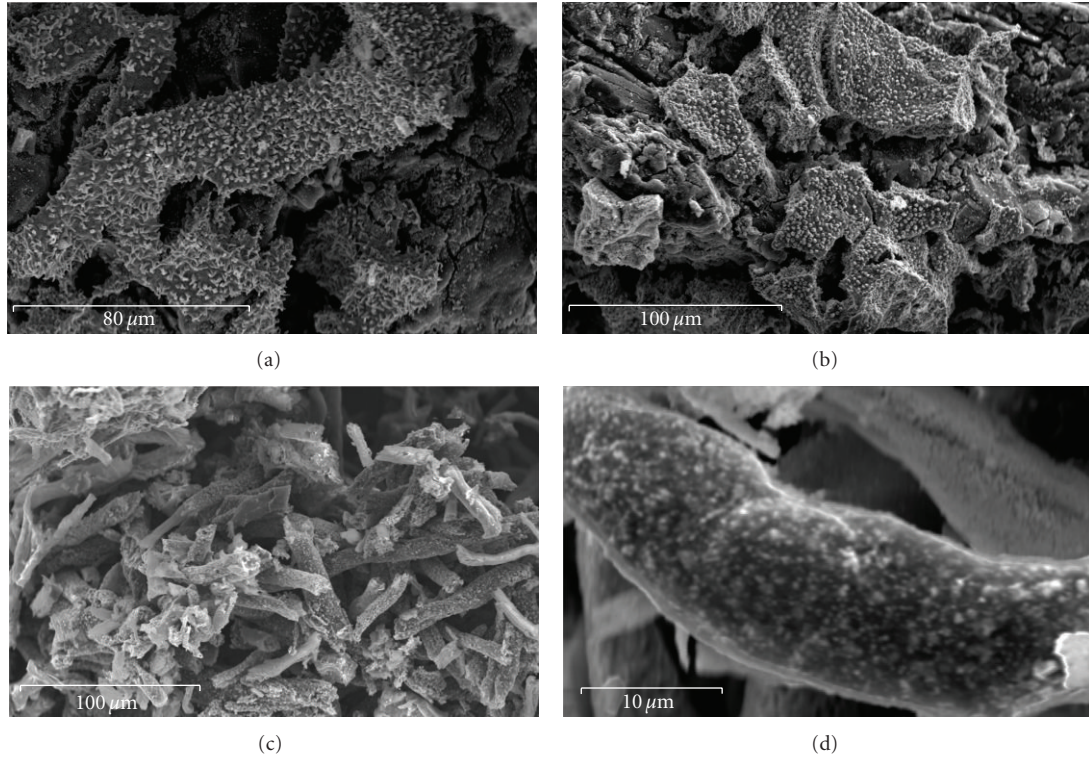


FIGURE 4: SEM Images of iron coated (a) MN-5, (b) MN-6, and (c-d) MN-7.

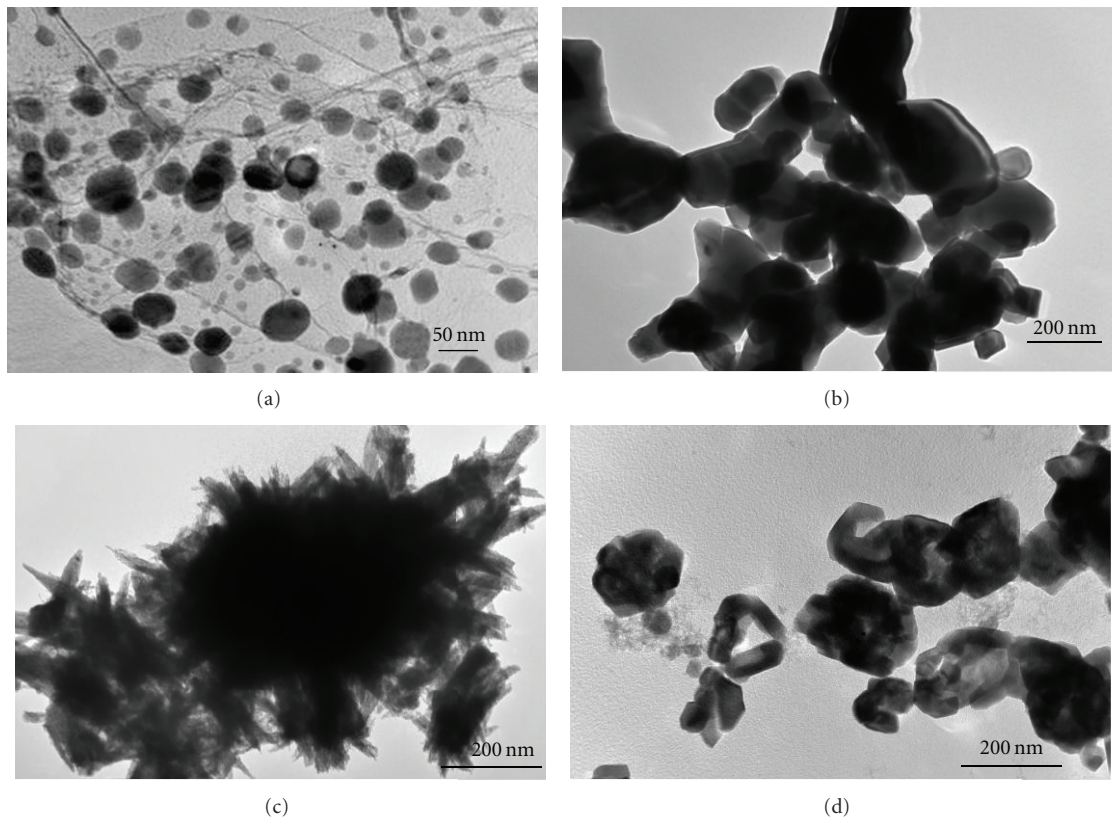


FIGURE 5: TEM images of iron coated (a) MN-1, (b) MN-2, (c) MN-3, and (d) MN-4.

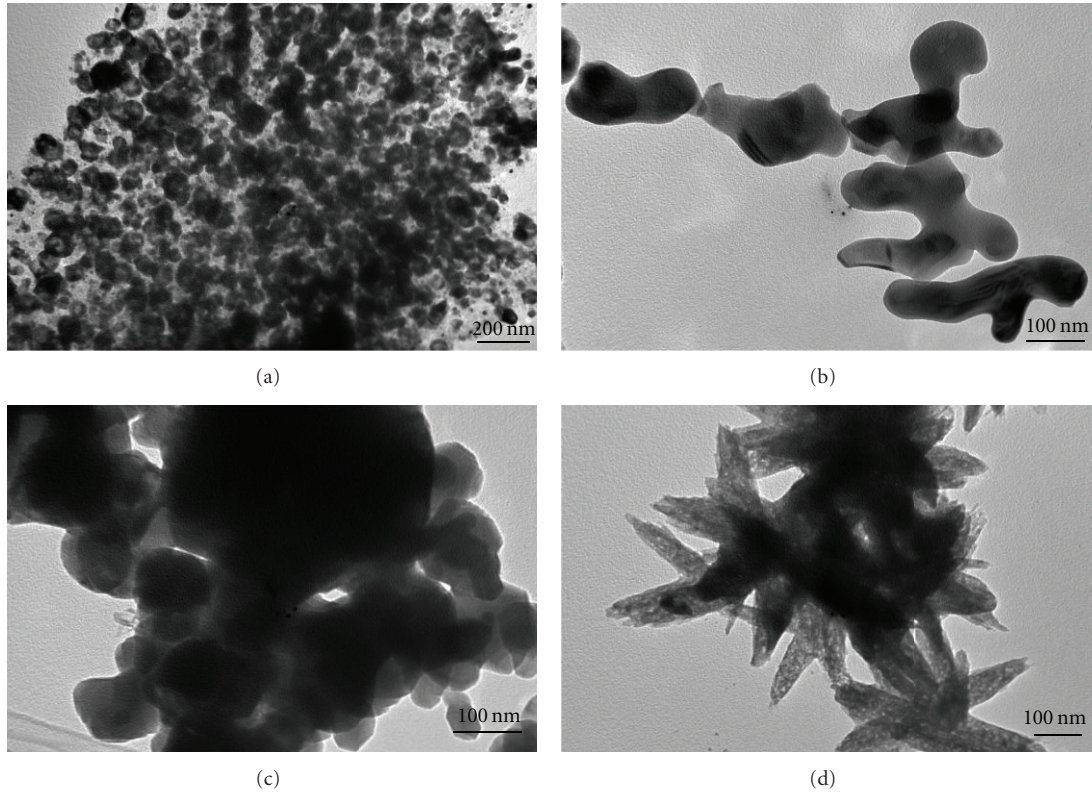


FIGURE 6: TEM images of iron coated (a) MN-5, (b) MN-6, (c) MN-7, and (d) MN-8 samples.

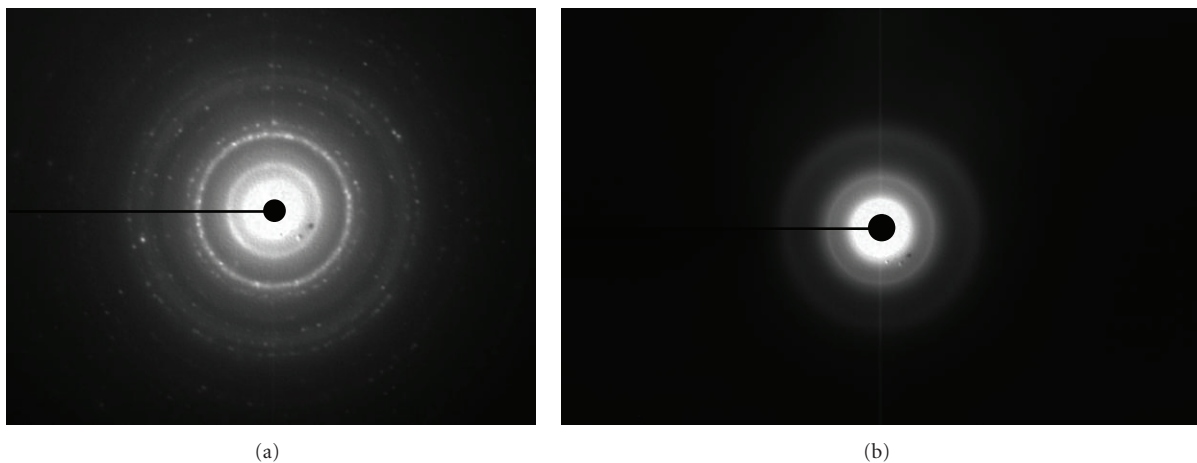


FIGURE 7: Selected area diffraction pattern (SAED) of (a) MN-1, and (b) MN-5 samples.

were added. Sample bottles were agitated by continuous tumbling for 48 hours. Approximately 60 mL of supernatant was extracted, filtered by 0.20  $\mu\text{m}$  syringe filter, and analyzed by inductively coupled plasma (ICP), and results are given in Figure 11 and Table 2.

A JEOL-1200EXII TEM with a side-mounted Gatan digital camera was used for the imaging of activated carbon, anthracite, cellulose fiber, and silica coated iron oxide/iron nanoparticles. Fifteen  $\mu\text{L}$  of iron oxide/iron nanoparticle coated activated carbon, anthracite, cellulose fiber, and silica

samples were dispersed in acetone, placed on a formvar-carbon coated copper grid, and allowed to air dry. Images were captured at an accelerating voltage of 120 kV and collected using Gatan software. For SEM, a JEOL-6490LV with an Oxford X-Act EDS system was used for imaging and elemental analysis. Images and EDS spectra were captured using an accelerating voltage of 15 to 30 kV. Spectra were collected for 50 live seconds using a process time of 5 percent, and a 30 to 50 percent dead-time. A Panalytical (Expert) 2-theta diffractometer with a copper  $K\alpha$  source was

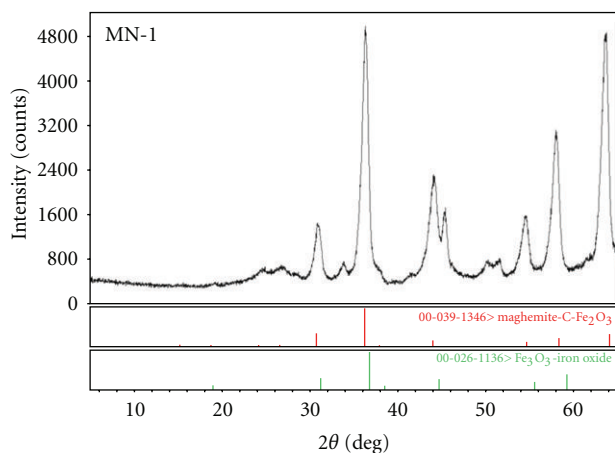


FIGURE 8: XRD pattern of maghemite coated anthracite synthesized using combustion reaction (MN-1 sample).

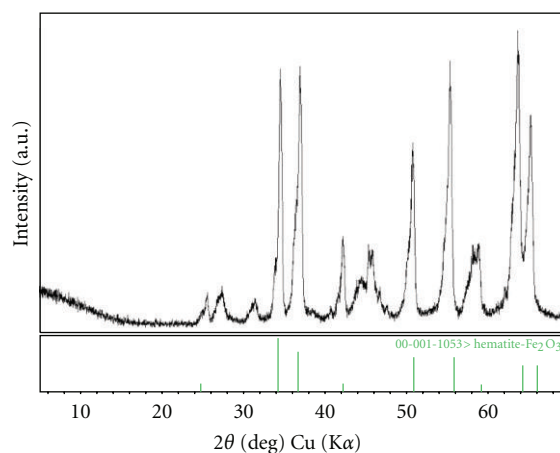


FIGURE 10: XRD pattern of hematite coated cellulose fibers synthesized using combustion reaction (MN-7 sample).

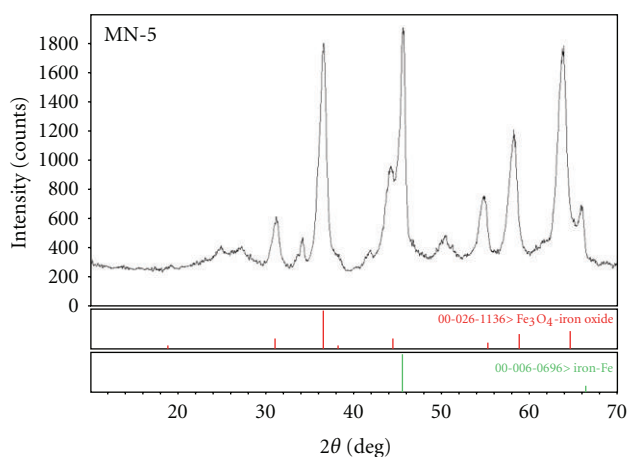


FIGURE 9: XRD pattern of maghemite coated commercial carbon synthesized using combustion reaction (MN-5 sample).

used to identify crystalline phases of the iron oxide/iron nanoparticle-coated activated carbon, anthracite, cellulose fiber, and silica samples. Scans were performed over a 2-theta ranging from 5 to 70°

### 3. Results and Discussion

Combustion synthesis or self-propagating high-temperature synthesis (SHS) provides striking realistic alternative to the conventional methods of producing advanced materials, such as ceramics, composites, and intermetallic compounds. The combustion procedure involves the decomposition of a reduction/oxidation reaction system, which then proceeds as a self-sustaining front throughout the reactant gel mixture. The reaction conditions and the large amount of heat evolved during the reaction make possible the direct fabrication of a large number of single or multicomponent powders that are crystalline and homogeneous and have a narrow particle size distribution.

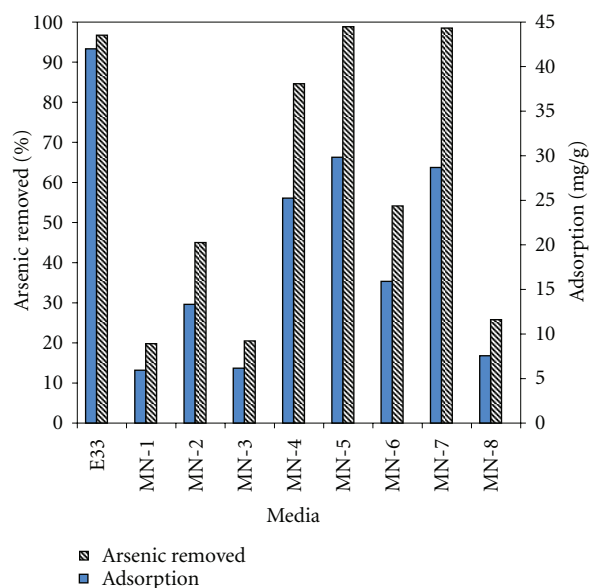


FIGURE 11: Arsenic adsorption study results.

The combustion synthesis of iron oxide/iron coated activated carbon, anthracite, cellulose fiber and silica samples were carried out in a kitchen microwave oven. The reaction uses activated carbon, anthracite, cellulose fiber and silica obtained from different vendors, and iron nitrate as precursor material for iron oxide/iron nanoparticle-coating. Nitrate, which was present in the precursor,  $\text{Fe}(\text{NO}_3)_3 \cdot 9\text{H}_2\text{O}$ , can be used as a fuel for obtaining the desired materials. The different concentrations of iron nitrate with activated carbon, anthracite, cellulose fiber and silica were ignited using the microwave oven, in highly exothermic reactions completed within one to three minutes. A uniform coating of iron oxide/iron nanoparticles was observed (see Figures 1(a)–1(d) and Figures 2(a)–2(c)). X-ray mapping images of MN-1 (red-Fe, green-C, and blue-O), MN-2 (blue-Fe, green-O, and red-C), MN-3 (green-Fe, red-O, and blue-C), and MN-4 (red-Silica, green-Fe and blue-O) samples

TABLE 1: Code, composition, and time of exposure of the reaction mixture.

Sample number	Sample code	Sample composition	Time exposed to microwave irradiation (Min)
1	NM1	5.4 gm activated carbon + 8.8 gm of Fe (NO <sub>3</sub> ) <sub>3</sub> ·9H <sub>2</sub> O	1 + 1.5 + 3
2	NM2	9.9 gm anthracite + 4.9 gm of Fe (NO <sub>3</sub> ) <sub>3</sub> ·9H <sub>2</sub> O + 0.5 mL H <sub>2</sub> O	2
3	NM3	9.9 gm anthracite + 11.12 gm of Fe (NO <sub>3</sub> ) <sub>3</sub> ·9H <sub>2</sub> O + 0.5 mL H <sub>2</sub> O	2
4	NM4	5 gm carbon (Hydrotarco 4000, lot No. 873812) + 11 gm of Fe (NO <sub>3</sub> ) <sub>3</sub> ·9H <sub>2</sub> O + 0.5 ml H <sub>2</sub> O	2
5	NM5	5 gm carbon (Norit, GAC 1240 lot. 30212-6) + 11.2 gm of Fe (NO <sub>3</sub> ) <sub>3</sub> ·9H <sub>2</sub> O + 0.5 mL H <sub>2</sub> O	2
6	NM6	5 gm activated carbon + 11.1 gm of Fe (NO <sub>3</sub> ) <sub>3</sub> ·9H <sub>2</sub> O + 0.5 mL H <sub>2</sub> O	2
7	NM7	4.92 gm cellulose fibrous long (sigma batch.047k0142) + 11.98 Fe (NO <sub>3</sub> ) <sub>3</sub> ·9H <sub>2</sub> O + 0.5 mL H <sub>2</sub> O	1 + 1
8	NM8	24.8 gm of sand coarse + 9.8 Fe (NO <sub>3</sub> ) <sub>3</sub> ·9H <sub>2</sub> O + 0.5 mL H <sub>2</sub> O	2

TABLE 2: Arsenic adsorption study results.

Sample name	As removed (%)	Adsorption (mg/g)
E33	96.7	42.0
MN-1	19.8	5.9
MN-2	45.0	13.3
MN-3	20.5	6.2
MN-4	84.6	25.3
MN-5	98.8	29.8
MN-6	54.1	15.9
MN-7	98.5	28.7
MN-8	25.8	7.6

are shown in Figures 1(a)–1(d), respectively. X-ray mapping studies indicate that iron nanoparticles are coated uniformly on the surface of carbon, anthracite, and silica. Similar coatings were observed for the MN-5 (red-Fe, green-C, and blue-oxygen), MN-6 (blue-Fe, green-O, and red-C), and MN-7 (green-Fe, red-O, and blue-C) samples. The energy dispersive spectrum (EDS) indicates the presence of iron in each case, and a representative EDS image of MN-7 is shown in Figure 2(d).

In order to understand the surface morphology, crystal shape and size, SEM analysis performed on MN-1 to MN-8 samples, and the results are shown in Figures 3 and 4. Figure 3 shows the SEM images of the iron-coated MN-1, MN-2, MN-3, and MN-4 samples. The iron oxide/iron nanoparticle coating varies from particles to flake depending upon the material used for preparation (see Figure 3). MN-1, MN-3, and MN-4 samples exhibit a spherical iron oxide/iron

nanoparticle coating whereas MN-2 displays a flake-like coating. The flake-like iron oxide/iron structures may result from insufficient fuel energy to break the iron into particles. Highly dispersed iron oxide/iron coatings appear on MN-5, MN-6, and MN-7 samples as shown in Figure 4. Notably, the MN-7 sample carbon, which was obtained from cellulose fiber, retained its parent structure even after modification with iron oxide/iron coating.

These fiber-based, carbon-coated iron oxide/iron materials exhibit numerous practical applications, including serving as membranes for arsenic removal. TEM studies confirm that nanoscale iron oxide/iron particles are achieved regardless of the material used for preparation (see Figures 5 and 6). MN-1 and MN-2 samples yielded spherical particles, while MN-3 yielded brush-like structures and MN-4 yielded ring-like structures (see Figure 5).

In the case of MN-5, MN-6, and MN-7, spherical-shaped structures were formed, while brush-like structures were formed on the MN-8 sample. For the selected samples, SAED results are shown in Figure 7. The samples crystallize in cubic symmetry. XRD was performed on all the synthesized samples and representative data are shown in Figures 8–10 (also see Figure S1–S5). Depending on the substrate and concentration of Fe(NO<sub>3</sub>)<sub>3</sub> used, four major phase were identified, namely, maghemite ( $\gamma$ -Fe<sub>2</sub>O<sub>3</sub>), Fe<sub>3</sub>O<sub>4</sub>, hematite ( $\alpha$ -Fe<sub>2</sub>O<sub>3</sub>), and Fe metal. Generally, broad XRD peaks indicate the coated iron particles of nanometer size.

Commercially available Bayoxide E33 (Bayer) is compared to these synthesized media for arsenic adsorption studies, and the data is shown in Figure 11 and Table 2. MN-4, MN-5, and MN-7 show comparable arsenic removal capabilities at tested time interval.

## 4. Conclusions

Combustion synthesis of iron oxide/iron nanoparticle-coated carbons such as activated carbon, anthracite, and silica is described. The reactions were carried out in alumina crucibles using a kitchen microwave oven, and the reaction completes within a few minutes. The method uses no additional fuel and uses a nitrate which is present in the precursor itself to drive the reaction. Depending upon the source of carbon used for the preparation, the formation of iron oxide/iron is observed. The coated iron oxide/iron nanoparticles were mostly spherical in nature, with size ranging from 50 to 400 nm. In a few cases, however, such as MN-3 and MN-8, brush-like structures were observed. Samples MN-4, MN-5, and MN-7 had significant arsenic adsorption when compared with samples MN-1, MN-2, MN-3, MN-6, MN-8, and the E-33 control sample. The synthesized iron oxide/iron nanoparticle-coated activated carbon, anthracite, cellulose fiber, and silica samples may serve as a part of practical applications for environmental remediation, catalysis, membrane design, and other technological solutions.

## Disclaimer

The U.S. Environmental Protection Agency, through its Office of Research and Development, funded and managed, or partially funded and collaborated in, the research described herein. It has been subjected to the Agency's peer and administrative review and has been approved for external publication. Any opinions expressed are those of the author(s) and do not necessarily reflect the views of the Agency, therefore, no official endorsement should be inferred. Any mention of trade names or commercial products does not constitute endorsement or recommendation for use.

## Acknowledgment

The authors thank Christina Bennet-Stamper for the SEM images and Carlo Cruz for arsenic adsorption studies.

## References

- [1] G. S. Zhang, J. H. Qu, H. J. Liu, R. P. Liu, and G. T. Li, "Removal mechanism of As(III) by a novel Fe-Mn binary oxide adsorbent: oxidation and sorption," *Environmental Science and Technology*, vol. 41, no. 13, pp. 4613–4619, 2007.
- [2] Y. Zhang, M. Yang, X. M. Dou, H. He, and D. S. Wang, "Arsenate adsorption on an Fe-Ce bimetal oxide adsorbent: role of surface properties," *Environmental Science and Technology*, vol. 39, no. 18, pp. 7246–7253, 2005.
- [3] A. Violante, S. D. Gaudio, M. Pigna, M. Ricciardella, and D. Banerjee, "Coprecipitation of arsenate with metal oxides. 2. Nature, mineralogy, and reactivity of iron(III) precipitates," *Environmental Science and Technology*, vol. 41, no. 24, pp. 8275–8280, 2007.
- [4] J. Zhang and R. Stanforth, "Slow adsorption reaction between arsenic species and goethite ( $\alpha$ -FeOOH): diffusion or heterogeneous surface reaction control," *Langmuir*, vol. 21, no. 7, pp. 2895–2901, 2005.
- [5] A. B. M. Giasuddin, S. R. Kanel, and H. Choi, "Adsorption of humic acid onto nanoscale zerovalent iron and its effect on arsenic removal," *Environmental Science and Technology*, vol. 41, no. 6, pp. 2022–2027, 2007.
- [6] S. R. Kanel, B. Manning, L. Charlet, and H. Choi, "Removal of arsenic(III) from groundwater by nanoscale zero-valent iron," *Environmental Science and Technology*, vol. 39, no. 5, pp. 1291–1298, 2005.
- [7] Y. Jia, L. Xu, Z. Fang, and G. P. Demopoulos, "Observation of surface precipitation of arsenate on ferrihydrite," *Environmental Science and Technology*, vol. 40, no. 10, pp. 3248–3253, 2006.
- [8] Y. Jia and G. P. Demopoulos, "Adsorption of arsenate onto ferrihydrite from aqueous solution: influence of media (sulfate vs nitrate), added gypsum, and pH alteration," *Environmental Science and Technology*, vol. 39, no. 24, pp. 9523–9527, 2005.
- [9] X. Guo and F. Chen, "Removal of arsenic by bead cellulose loaded with iron oxyhydroxide from groundwater," *Environmental Science and Technology*, vol. 39, no. 17, pp. 6808–6818, 2005.
- [10] B. J. Lafferty and R. H. Loeppert, "Methyl arsenic adsorption and desorption behavior on iron oxides," *Environmental Science and Technology*, vol. 39, no. 7, pp. 2120–2127, 2005.
- [11] M. Jang, S. H. Min, T. H. Kim, and J. K. Park, "Removal of arsenite and arsenate using hydrous ferric oxide incorporated into naturally occurring porous diatomite," *Environmental Science and Technology*, vol. 40, no. 5, pp. 1636–1643, 2006.
- [12] D. Mishra and J. Farrell, "Evaluation of mixed valent iron oxides as reactive adsorbents for arsenic removal," *Environmental Science and Technology*, vol. 39, no. 24, pp. 9689–9694, 2005.
- [13] K. J. Bisceglia, K. J. Rader, R. F. Carbonaro, K. J. Farley, J. D. Mahony, and D. M. Di Toro, "Iron(II)-catalyzed oxidation of arsenic(III) in a sediment column," *Environmental Science and Technology*, vol. 39, no. 23, pp. 9217–9222, 2005.
- [14] Z. Gu, J. Fang, and B. Deng, "Preparation and evaluation of GAC-based iron-containing adsorbents for arsenic removal," *Environmental Science and Technology*, vol. 39, no. 10, pp. 3833–3843, 2005.